A Numerical Study of Inertia and Streamline Curvature Effects on Peristaltic Flows

By
Bilal Ahmed
19-FBAS/PHDMA/F12

Department of Mathematics and Statistics
Faculty of Basic and Applied Sciences
International Islamic University Islamabad,
Pakistan

2018

Numerical analysis

Mathematics

A Numerical Study of Inertia and Streamline Curvature Effects on Peristaltic Flows

Submitted By:
Bilal Ahmed
19-FBAS/PHDMA/F12

Supervised by:
Dr. Tariq Javed

Co- Supervised by:
Prof. Dr. Muhammad Sajid T.I.

Department of Mathematics and Statistics
Faculty of Basic and Applied Sciences
International Islamic University Islamabad,
Pakistan
2019

A Numerical Study of Inertia and Streamline Curvature Effects on Peristaltic Flows

Submitted By
Bilal Ahmed
19-FBAS/PHDMA/F12

A Dissertation
Submitted in the Partial Fulfillment of the
Requirements for the Degree of
DOCTOR OF PHILOSOPHY
In
MATHEMATICS

Supervised By
Dr. Tariq Javed

Co- Supervised by
Prof. Dr. Muhammad Sajid T.I.

Department of Mathematics and Statistics
Faculty of Basic and Applied Sciences
International Islamic University Islamabad,
Pakistan
2018

Author's Declaration

"I, **Bilal Ahmed** Reg. No. **19-FBAS/PHDMA/F12** hereby state that my Ph.D. thesis titled: **A Numerical Study of Inertia and Streamline Curvature Effects on Peristaltic Flows** is my own work and has not been submitted previously by me for taking any degree from this university, **International Islamic University, Sector H-10, Islamabad, Pakistan** or anywhere else in the country/world.

At any time if my statement is found to be incorrect even after my Graduation the university has the right to withdraw my Ph.D. degree."

Name of Student: ***(Bilal Ahmed)***
Reg. No. **19-FBAS/PHDMA/F12**
Dated: **09/08/2018**

Plagiarism Undertaking

"I solemnly declare that research work presented in the thesis titled: **A Numerical Study of Inertia and Streamline Curvature Effects on Peristaltic Flows** is solely my research work with no significant contribution from any other person. Small contribution/help wherever taken has been duly acknowledged and that complete thesis has been written by me.

I understand the zero tolerance policy of the HEC and University, **International Islamic University, Sector H-10, Islamabad, Pakistan** towards plagiarism. Therefore, I as an Author of the above titled thesis declare that no portion of my thesis has been plagiarized and any material used as reference is properly referred/cited.

I undertake that if I am found guilty of any formal plagiarism in the above titled thesis even after award of Ph.D. degree, the university reserves the rights to withdraw/revoke my Ph.D. degree and that HEC and the University has the right to publish my name on the HEC/University Website on which names of students are placed who submitted plagiarized thesis."

Student/Author Signature: _____

Name: **(Bilal Ahmed)**

Certificate of Approval

"This is to certify that the research work presented in this thesis, entitled: **A Numerical Study of Inertia and Streamline Curvature Effects on Peristaltic Flows** was conducted by **Mr. Bilal Ahmed,** Reg. No. **19-FBAS/PHDMA/F12** under the supervision of **Dr. Tariq Javed**, no part of this thesis has been submitted anywhere else for any other degree. This thesis is submitted to the **Department of Mathematics & Statistics, FBAS, IIU, Islamabad** in partial fulfillment of the requirements for the degree of **Doctor of Philosophy in Mathematics, Department of Mathematics & Statistics, Faculty of Basic & Applied Science, International Islamic University, Sector H-10, Islamabad, Pakistan."**

Student Name: Bilal Ahmed **Signature:** _____

Examination Committee:

a) **External Examiner 1:**
(Name/Designation/Office Address) **Signature:** Saleem Asghar

Prof. Dr. Saleem Asghar
Professor of Mathematics,
Department of Mathematics,
COMSATS, IIT, Park Road, Chak Shahzad, Islamabad.

b) **External Examiner 2:**
(Name/Designation/Office Address) **Signature:** _____

Prof. Dr. Tasawar Hayat
Professor of Mathematics,
Department of Mathematics,
QAU, Islamabad

c) **Internal Examiner:**
(Name/Designation/Office Address) **Signature:** _____

Dr. Ahmer Mehmood
Associate Professor

Supervisor Name:
Dr. Tariq Javed **Signature:** _____

Co-Supervisor Name:
Prof. Dr. Muhammad Sajid, T.I. **Signature:** _____

Name of Dean/HOD:
Prof. Dr. Muhammad Sajid, T.I. **Signature:** _____

Acknowledgement

To begin with the name of Almighty **ALLAH,** the creator of the universe, who bestowed his blessing on me to complete this dissertation. I offer my humblest, sincerest and million Darood to the **Holy Prophet Hazrat MUHAMMAD (s.a.w)** who exhorts his followers to seek for knowledge from cradle to grave.

I wish to acknowledge the kind help, valuable instructions, intellectual suggestions and beneficial remarks of my sincere and kind-hearted supervisor **Dr. Tariq Javed,** without his generous encouragement and patient guidance, it would have been difficult for me to complete the assigned task.

I also want to thanks to my co-supervisor **Prof. Dr. Muhammad Sajid TI** who give me a lot of help during the research. He gives me a time and attention whenever I need him. No dought, he is very kind hearted and comparative with me in making of this dissertation. Also acknowledged **Dr. Nasir Ali** because support given by him works like a symbol of hope which enlightened my path towards success and made me able to come upon this benchmark. He gave me new ideas and direction to explore new versions of my research fields.

I must pay my heartily thanks to foreign external examiners, local external examiners and internal examiner for giving precise time from their busy routine to have a keen look on my PhD dissertation and examine the viva examination. The feedback given by them is highly acknowledgeable which improves the quality my PhD dissertation and encourages me in my future research.

I especially owe a debt of gratitude to **my father, mother, brother, sisters** and **Naveed Farooq** as they made an indirect special contribution to the success and completion of this dissertation. I would have been incompetent to this challenge without their prayers and utmost support which worked as instilling a great confidence and courage in me to complete my work successfully.

It gives me immense pleasure to express my most vigorously, deep gratitude and heartfelt wishes to **my wife** who always cared and guided me in all aspects of life whenever I needed her help.

I must mention a very supporting person **Brig. Muhammad Aslam (Retd)** in my PhD tenure. He gave me a support which enables me to spent more time on my research work and achieve my goal and complete my PhD degree.

My respected seniors **Dr. Hussain Ahmed (Late), Dr. Irfan Mustafa, Dr. Abuzar Gaffari, Dr. Abid Majeed** and **Dr. Saleem Iqbal** has been always there to listen and give me advice. I am deeply grateful to him for the long discussions that helped me to sort out the technical details of my work.

My acknowledgement will remain incomplete if I do not mention the companionship of my all friends especially **Ziafat Mehmood, Muhammad Arshad Siddique** and **Abdul Haleem Hamid** and my entire colleague for their help in my course and research work.

Zealous and sincerest thanks to my university friends **Sohail Ahmad Channar, Muhammad Usman, Wasi-ur-Rehman, Waqas Nazeer, Muhammad Shoaib, Dr. Mubbashar Nazir Mehar, Zeeshan Asghar, Raheel Ahmed, Iqrar Raza** and **Atif** for their kind cooperation and loving attitude.

Last not least I am thankful to my sincere and honorable friends and relatives **Zeeshan Haider, Zahid Mehmood, Nayyer Saleem, Waseem Bari, Naeem Bari, Nadeem Bari, Asim Hafeez, Umer Farooq, Umer Farooq (China), Raheel Ahmed Janjua, Jahangir Khan Tanoli, Khalid Mehmood, Tayyasr ul Arfeen, Muhammad Shafique, Arslan Tasleem, Amjad Iqbal Falak** and anyone I forgot for their unbeatable help and guidance to achieve my highest education.

Here, I would like to thanks to Higher Education Commission, Pakistan, (HEC), for providing me financial support under the scholarship program "Indigenous PhD Fellowship for 5000 Scholars, HEC (Phase II) Batch V, **PIN # 112-25367-2PSI-311**".

At the end, I am highly obliged to everyone who put in their altruistic efforts, enabling me to complete this task and prayed for my success

Bilal Ahmed

Dedicated
To
My Mother

Preface

In fluid mechanics, peristaltic flows gain considerable attention in the last couple of decades because of its numerous applications not only in biomedical science but also in the manufacturing industry. Peristaltic motion is kind of the fluid transportation which occurred due to the contraction and expansion of the progressive wave along the tube/channel occupying the fluid. In large number of physiological circumstances, the body uses a peristaltic mechanism to push or blend the innards of the tube, like in gastrointestinal tract, ureter, bile duct, esophagus and some other glandular ducts. Peristaltic pumping has valuable advantages in the manufacturing the biomedical devices that includes heart-lung machine in which the critical part of maintaining the pumping of the blood is performed on the principles of peristaltic pumping and similarly in many other devices. The peristaltic mechanism also involves in plant physiology and in various other pumping situations where it is necessary to avoid the interaction of internal moving parts like pistons etc. It is noted through literature survey that lubrication theory is widely used in the study of peristaltic flows which buried important features. It is therefore, the main objective of this dissertation is to study the peristaltic flows in different physical situations for different types of fluid passing through the channel or tube without using the assumptions of lubrication theory that are long wavelength and low Reynolds number assumption. By ignoring these assumptions, the results presented are valid for all wavelengths and non-zero moderate values of Reynolds number. The stream-vorticity function formulation is adopted to simulate in terms of modeled nonlinear partial differential equations by using finite element method based on Galerkin's residual technique to obtain the numerical results. The contribution of inertial forces along with other participated parameters in the modelled governing equation are presented through the contours of streamlines, vorticity, isothermal lines wherever, graphs of longitudinal velocity, pressure rise per wavelength and temperature distribution wherever.

Broadly, the thesis compose of three parts in which first part contains some basic definitions and preliminaries given in chapter one which can help the readers to understand the succeeding parts of the thesis. The second part contains the peristaltic flows passing through the channel in the different flow situation for Newtonian/non-Newtonian fluids that occupies next four chapters. The third part contains last four chapters in which the peristaltic flows passing through the tube in different flow

situation for Newtonian and non-Newtonian fluids. The main objective of each chapter is as follow:

Chapter two describes the peristaltic motion through a porous saturated channel under the influence of applied magnetic field of uniform strength. The modelled equations are solved by using the finite element method after converting into stream vorticity formulation. The results are presented without applying the lubrication theory and compared with existing literature. The obtained results are presented graphically for different values of Reynolds number, porosity parameter, Hartmann number and other participated parameters. It is noted that the streamlines are highly affected by the change in Reynolds number and Hartmann number. The diffusion of vorticity from the boundaries to the center of the channel increases with increasing both the permeability of the porous medium through permeability parameter and Reynolds number while an opposite trend is noted with increasing Hartmann number. Moreover, the pressure rise per wavelength in pumping region also decreases by increasing both permeability of the porous medium and strength of the magnetic field. These results are published in **Journal of Porous Media, 20(9) (2017), 841-857**.

In chapter three, mixed convective heat transfer analysis is presented in the study of peristaltic flow passing through the vertical channel. Mathematical modeling of governing equations are presented in which heat generation term is introduced in the energy equation. The set of nonlinear partial differential equations are exposed to Galerkin's formulated finite element method to present the numerical results. The assumptions of long wavelength and low Reynolds number are neglected to present the role of inertial forces in the heat transfer analysis of peristaltic flow. The obtained results for different values of Reynolds number, Grashof number and other participated parameters. It is noted that variation in Prandlt number and heat generation parameter effects the isothermal lines. Increase in heat generation reduces the velocity near the central region and improves the velocity in the vicinity of peristaltic wall. Heat generation is also responsible to enhance the size of bolus and curvature effect on isothermal lines and to drop the pressure in the flow region. Increase in time mean flow rate supports the enhancement of velocity, temperature and size of bolus while increase in wave number increases the size of bolus, reduces curvature effect of isotherms and rises the pressure. These results are published in **Journal of Applied Fluid Mechanics, 10(6) (2017), 1813-1827**.

Since previous both chapters cover the study of peristaltic flow of Newtonian fluid under different physical conditions, therefore chapter four contains the mathematical modeling and simulation of peristaltic flow of non-Newtonian fluid. In this chapter, Casson fluid is consider in peristaltic motion under the impact of applied magnetic field. Governing equation are modeled without applying the assumptions of lubrication theory which arrives to set of nonlinear partial differential equations. Galerkin's formulated finite element method is applied after discretizing the domain into mesh of quadratic triangular elements. It is noted that the Casson fluid parameter upsurge the curvature effects and flow is observed slower for Casson fluid as compared to that of Newtonian fluid. The increasing values of Hartmann and Reynolds numbers cause increase in volume of the bolus while increase in velocity is noted near the center of the channel and opposite behavior is observed near the peristaltic wall. These observations are published in the journal, **Nonlinear Engineering – Modeling and Application, DOI: 10.1515/nleng-2017-0098**.

Chapter five is dedicated to study the behavior of contours of streamlines and curvature effects in the peristaltic motion of micropolar fluid passing through the porous saturated medium under the influence of magnetic field. Finite element method is implemented to the governing equations that are modeled by dropping the assumptions of theory of lubrication i.e. long wavelength and low Reynolds number which arrives to a coupled nonlinear partial differential equations. To ensure the accuracy of the developed code, obtained results are compared with the results available in the literature and found in excellent agreement. It is concluded that at low Reynolds number, the trapped bolus are symmetrical while increasing Reynolds number magnifying the size of the boluses, increases the pressure rise per wavelength and reduces the velocity. Peristalsis mixing can be enhanced by increasing Hartmann number while it reduces by increasing permeability of the porous medium in the peristaltic transportation of the micropolar fluid. Increasing micropolar parameter supports the pressure rise per wave length and it is noted greater as compared to that of Newtonian case in pumping region while its behavior is opposite in augmented region and enhancing the coupling parameter gives improved pumping performance. These findings were published in **AIP Advances, 8, 015319 (2018)**.

In chapter six, the investigation of peristaltic transportation through the tube filled with porous medium under the influence of magnetic field is presented. The

governing equations for the peristaltic flow in tube are modelled in axisymmetric coordinates by dropping the assumptions of lubrication theory. The modified Laplacian operator is appeared in stream vorticity formulation. The effects of moderate values of Reynolds number, wave number, porosity parameter and time mean flow rate on the streamlines, velocity and pressure rise per wavelength are presented graphically. The obtained results evaluated by developed code is compared with the available results in literature to ensure the validation. Circulation of trapped bolus increases with magnification in the Reynolds and Hartmann numbers. The increase in velocity and consequently decrease in pressure in the central part of the tube is predicted by increasing the the permeability of the porous medium. The material given in this chapter are submitted for publication after revision in the journal **AIP Advances**.

Chapter seven contains comprehensive study of peristaltic flow passing through vertical channel to incorporate the buoyancy forces to analyze the heat transfer analysis through mixed convection in presence of heat generation parameter. The governing equations contains energy equation which includes heat generation parameter. The assumptions of lubrication theory are dropped in mathematical modelling the constitutive equations which arrives the model to set of nonlinear partial differential equations. The present model can be deduce to creeping flow to get the result of long wavelength. Galerkin's formulated finite element method is incorporated to solve the modeled equations and obtain numerical results that are presented in the form of contours of streamlines and isothermal lines, velocity and temperature profiles for variation of different involved parameters. It is observed that circulation of bolus increases by increasing the values of the wave and Reynolds numbers. Furthermore, Isothermal lines are symmetric at low time mean flow rates and saturation is observed in the lower part is reported by increasing rate of time mean flow. At the center of the tube, increasing value of Reynolds number decreases the longitudinal velocity while increases the temperature but increasing wave number enhances the velocity and reduces the temperature. The decrease in velocity is noted at center due to increasing values of Grashof number, Prandtl number and heat generation parameter, while the slight increase is also observed far away from the center. The decrease in temperature is noted for increasing values of Grashof number while, Prandtl number, heat generation and time-mean flow rate supported the

enhancement in temperature. Pressure rise per wavelength can be enhanced by increasing both the Reynolds and Grashof numbers. These results are published in **Communications in Theoretical Physics 69(4) (2018), 449-460**.

In chapter eight, peristaltic flow of a blood flow model is investigated by considering Casson fluid as a blood passing through the tube since it is widely shown that blood behaves similar to Casson fluid in narrow arteries. The magnetic field is applied perpendicular to the flow with uniform strength to predict the effect of electromagnetic forces on the blood flow model. The governing equations for blood flow model of Casson fluid are formulated to a system of nonlinear coupled partial differential equations, which are exposed to Galerkin's finite element method. The assumptions of lubrication theory are neglected, due to which the effects of moderate Reynolds number and wave number along with other parameters are presented. It is observed that velocity of the fluid is an increasing function of both Reynolds number and strength of applied magnetic field. The contours of streamlines, graphs of longitudinal velocity and pressure rise per wavelength are also plotted for different values of Casson fluid parameter and wave number. The dominant inertial forces caused by the increase in Reynolds number increases the magnitude, number of trapped boluses and vorticity exhibit the generation of the flow field in the narrow part of the tube in this case. These results are accepted for publication in **Journal of Quality Measurement and Analysis 14(1) (2018), 101-113**.

Chapter nine deals with the peristaltic transportation of micropolar fluid passing through the saturated porous medium under the influence of applied magnetic field. The flow problem is modelled without applying the long wavelength and low Reynolds number approximation that makes the governing equations as a set of nonlinear partial differential equations. The domain is discretize into mesh of quadratic six nodal triangular elements and finite element method is implemented to obtained numerical result. The obtained results are presented by plotting the graphs of longitudinal velocity, pressure rise per wavelength, contours of streamlines, vorticity andmicrorotation and discuss in detail. It is found that peristaltic mixing is supported by Reynolds number and permeability parameter of porous medium while Hartmann number reduces the number and size of the bolus. The pressure rise per wavelength for micropolar fluid is noted greater as compared to that of Newtonian fluid. These

contents given in ninth chapter has been submitted for possible publication in **European International Journal of Science and Technology**.

Contents

Nomenclature

$\boldsymbol{A}$	Unknown nodal vector
a	Half width of the channel
b	Wave amplitude
B_0	Magnetic field parameter
$\boldsymbol{B}$	Magnetic field vector
$\boldsymbol{b}$	Infinitesimal modification in Magnetic field
c	Velocity of wave train lab frame
c_p	Specific heat at constant pressure
D	Modified Laplacian
E_0	Electric field
$\boldsymbol{e}$	Infinitesimal modification in electric field
$\boldsymbol{F}$	Global forcing vector
F	Lorentz force
f	Forcing Function
$\boldsymbol{G^*}$	Microrotation vector
Gr	Grashof number
g	Acceleration caused by the gravity
H	Wave in lab frame
h	Wave in wave frame
J_0	Current density
J^*	Microgyration parameter in dimensional form
J	Microgyration parameter in non-dimensional form
$\boldsymbol{j}$	Infinitesimal modification in current density
k	Permeability of porous medium in dimensional form
K	Permeability of porous medium in non-dimensional form
$\boldsymbol{K}$	Global stiffness matrix
L	Differential operator
M	Hartmann Number
m	Micropolar parameter
N	Coupling parameter

N_k	Interpolation shape function
n	Behavior index
p^*	Dimensional pressure in wave frame
Pr	Prandtl number
P	Pressure in lab frame
p_y	Yield stress
p	Pressure in dimensionless form in wave frame
ΔP_λ	Pressure rise per wavelength
Q_0	Heat generation in dimensional form
Q^*	Time mean flow rate in dimensional form
Q	Time mean flow rate in non-dimensional form
q	Flow rate in non-dimensional form
q^*	Flow rate in dimensional form
R	Axial component in fixed frame
Re	Reynolds number
R_m	Magnetic Reynolds number
r	Non-dimensional radial component in wave frame
r^*	Radial coordinate in dimensional form in wave frame
T^*	Temperature of the fluid in dimensional form
T	Temperature of the fluid
T_1	Temperature at the wall
t	Time dependent variable
u_i	Nodal variable
$\tilde{u}$	Approximate nodal variable
u^*	Component of velocity in x^* direction in wave frame
U	Component of velocity in X direction in lab frame
v^*	Component of velocity in y^* direction in wave frame
V	Component of velocity in Y direction in lab frame
$\mathbf{V}$	Velocity vector
u, v	Dimensionless velocity components
W_i	Weight function
w_1, w_2, w_3	Weight functions
x^*, y^*	Dimensional rectangular coordinates in wave frame

X, Y	Dimensional rectangular coordinates in lab frame
x, y	Non- dimensional coordinates in wave frame
z	Non-dimensional axial component in wave frame
Z	Axial component in fixed frame
z^*	Dimensional axial coordinate in wave frame of reference

Greek symbols

α	Inclined angle of channel with horizontal
β	Heat generation parameter
β_T	Coefficient of thermal expansion
$\bar{\alpha}, \bar{\beta}, \bar{\gamma}$	Coefficients of spin gradient viscosity for micropolar fluids
ϵ	Residual error
ε_ψ	Error in approximate stream function
ε_ω	Error in approximate vorticity function
ε_θ	Error in approximate temperature function
Ω	Domain of the area integral
κ^*	Thermal conductivity
$\bar{\kappa}$	Coefficient of vortex viscosity
κ	Consistency index
Γ	Domain of the line integral
η	Dimensionless wave in wave frame
η^*	Dimensional wave in wave frame
λ	Wave length in lab frame
ϕ	Amplitude ratio
ψ	Stream function in non-dimensionl form
ψ^*	Stream function in dimensional form
ψ_k	Element nodal approximation of stream function
δ	Wave Number
θ	Dimensionless temperature
θ_k	Element nodal approximation of temperature function
π_c	Critical value of the π based on non-Newtonian modal
μ	Dynamic viscosity

ζ	Casson parameter
ν	Kinematic viscosity
ρ	Density
σ	Electrical conductivity
ω	Non-dimensionl vorticity
ω_k	Element nodal approximation of vorticity function
τ_{yx}	Shear stress

Subscript symbols

(ele)	Restriction to the relevant variable/function to the element
k	Index of the node

Chapter 1

Preliminaries

This chapter is devoted to discuss some basic definitions, concepts and equations also discussed by (Fox et al. (2003); White (2003)) which helps the readers for understanding the details in succeeding chapters. The governing equations representing the conservation of mass, momentum and energy conservation are also presented.

1.1 Fluid Mechanics

The branch of engineering or applied mechanics that examines the nature and properties of fluids both in motion and at rest. It simply deals with the study of gases, liquids and plasmas. Broadly speaking, it can be allocated to categories:

1.1.1 Fluid kinematics

1.1.2 Fluid dynamics

1.1.1 Fluid kinematics

When the fluid motion is considered in the absence of applied forces, we call it as fluid kinematics.

1.1.2 Fluid dynamics

In contrast to the fluid kinematics, when the effect of forces are incorporated to discuss the fluid motion, the study is treated as fluid dynamics. Fluid dynamics can also be further divided into two brand namely

(a) Fluid statics
(b) Fluid kinetics

(a) Fluid statics

When the effect of forces are considered on the fluid that is either static or stationary, the branch which deals with this phenomenon is called fluid statics.

(b) Fluid kinetics

If the effect of forces is also considered on the fluid which is in motion, the branch dealing with such phenomenon is called fluid kinetics.

1.2 Types of Fluids

Fluids are broadly categorized into two major groups

1.2.1 Ideal fluids

1.2.2 Real fluids

1.2.1 Ideal fluids

Fluids having no viscosity fall in the category of ideal fluids. In this case fluid offers no resistance to the applied shear stress.

1.2.2 Real fluids

All real fluids have some non-zero value of viscosity, and offers resistance to the flow. Real fluids are further divided into two main classes.

(a) Newtonian Fluids

(b) Non-Newtonian Fluids

(a) Newtonian Fluids

The fluids relates two quantities i.e. shear stress and deformation rate in the direct relation with linearly proportional are called Newtonian fluids. Mathematically,

$$\tau_{yx} = \mu \frac{du}{dy}, \tag{1.1}$$

gives the relation between shear stress and deformation rate for Newtonian fluids.

(b) Non-Newtonian Fluids

Fluids that do not obey relates two quantities i.e. shear stress and deformation rate in the direct relation with linearly proportional, thus violated the Newton's law of viscosity given in Eq. (1.1) are non-Newtonian fluids. For non-Newtonian, fluids shear stress and rate of deformation obeys power law model

$$\tau_{yx} = \kappa \left(\frac{du}{dy}\right)^n, \tag{1.2}$$

in which κ is the consistency index where as he symbol n is the behavior index. Eq. (1.2) can also be written as

$$\tau_{yx} = \eta \left(\frac{du}{dy}\right), \tag{1.3}$$

where

$$\eta = \kappa \left(\frac{du}{dy}\right)^{n-1}, \tag{1.4}$$

is the apparent viscosity. The numerical values of the apparent viscosities of most of the non-Newtonian fluids are relatively high when compared to the viscosity of water. Paint is an example of non-Newtonian fluid having a shear dependent viscosity and become less viscous when the applied shear stress is increased. Casson fluid and Micropolar are the other examples of non-Newtonian fluids.

1.3 Peristaltic Flow

The circumferential progressive wave of either contraction or/and expansion generated laterally to the channel/tube is known as a mechanism of peristalsis. Peristalsis can be found in several organisms, in a variety of organs and in a number of industrial processes. Peristalsis is now getting more interest by engineers, scientists as well as the researchers of biomedical sciences due to its vast applications. Physiologists considered peristalsis as one of the key mechanism of the fluid transportation in biological structures. It includes transportation/movement of urine in a body, movement of chime, transportation of spermatozoa in the cervical canal, vasomotion in small blood vessels and in the movement of lymph in the lymphatic vessels. The study of peristaltic flows give more effective mechanism for transportation in a sanitary fluid, industrial peristaltic pumping and in preparation of medical devices. In the printing industry, transporting of viscous fluids in mechanical roller pump and shifting of noxious fluids are good examples of peristaltic flows. Now a days, many medical devices are manufactured on the basis of peristaltic mechanism to transport fluid without moving internal machinery parts such as heart-lung machine and dialysis system etc.

1.3.1 Pumping Regions

The peristaltic flow is discretized into four types of flow regions or quadrants known as adverse pressure if pressure rise $\Delta P_\lambda > 0$ while pressure rise $\Delta P_\lambda < 0$ is for favorable pressure gradient. These regions are characterized on the basis of pressure difference with the time mean flow rate.

(a) Peristaltic pumping

The quadrant I corresponds to the flow in which time mean flow is positive with adverse pressure is known as peristaltic/positive pumping quadrant.

(b) Retrograde pumping

The quadrant II corresponds to the flow in which time mean flow is negative with adverse pressure is known as retrograde/backward pumping quadrant.

(c) Co-pumping

The quadrant III corresponds to the flow in which time mean flow is negative with $\Delta P_\lambda < 0$, is known as co- pumping quadrant.

(d) Augmented pumping

The quadrant IV corresponds to the flow in which time mean flow is positive with $\Delta P_\lambda < 0$, is known as augmented pumping quadrant. Furthermore, in quadrant IV, the free pumping region exist when $\Delta P_\lambda = 0$ with $Q > 0$.

1.3.2 Trapping phenomena

Trapping is one of the important physical phenomena in peristalsis. It depends on the formation of contours of streamlines. Sometimes, streamlines are not moving on the path similar to that of the peristaltic wall rather splits and moves in circular trajectories thus encloses a bolus of fluid in closed streamlines and circulating region arises. The trapped bolus and their movement along with the wave in the flow exhibit the trapping phenomenon for the peristaltic flow.

1.4 Dimensionless Parameters

This section is dedicated for understanding and definitions of some basic parameters involves in the flow of the fluids (Newtonian/non-Newtonian).

(a) Reynolds number

It is the ratio that corresponds to the inertial forces over the forces causes by viscosity of the fluid that known as Reynolds number. The low Reynolds number corresponds to the creeping flow while significantly high values of Reynolds number corresponds to the turbulence of the flow. In fact, Reynolds number at nonzero range predicts the dominance of the inertial forces depending upon the considered values and thus the nature of the fluid that whether it is laminar or turbulent.

(b) Wave number

The ratio that corresponds to the width of the channel/tube over the length of the wave is known as wave number.

(c) Amplitude ratio

The ratio that corresponds the relation between the amplitude of the wave in peristaltic motion and the radius of the channel/tube in which fluid is flowing is known as amplitude ratio.

(d) Hartmann number

The Hartmann number corresponds to the ratio of electromagnetic forces to viscous forces. It predicts the performance of magnetic field on the profile of the longitudinal

velocity of the fluid that takes apart in the shape of Lorentz force in the modelled governing equations.

(e) Prandtl number

Prandtl number involves the phenomena where heat transfer between the moving fluid and boundary of the channel/tube or surface on which fluid is moving is taken into account. It is the ratio of the rate of viscous diffusion to the rate of thermal diffusion.

(f) Grashof number

Grashof number Gr is the ratio of the buoyancy forces that appears due to gravitational force to the viscous forces and arises in the study of the fluid dynamics where heat transfer is takes place by convection mechanism.

(g) Casson fluid parameter

It is the parameter which involves in the momentum equation in the model of Casson fluid. The viscosity of the Casson fluid is zero at an infinite shear rate and infinite at zero shear rate. The viscosity of the Casson fluid in any flow situation can be organized by setting the strength of Casson fluid parameter in different ranges. The relation of Casson fluid parameter ζ and viscosityμ is $\zeta = \mu\sqrt{2\pi_c/p_y}$ where π_c is the critical value of the π (in case of Casson fluid π must be greater than π_c) and p_y represents the yield stress as mentioned by Animasaun et al. (2015).

(h) Porosity parameter

The coefficient is the porosity parameter which is not dependent of the nature and behavior of the fluid but it totally depends upon the medium of the geometry. It is also identified as intrinsic permeability of the medium or simpy specific permeability. It is called permeability in a single phase flow.

(i) Heat generation parameter

Heat generation parameter is defined as the amount of heat flux entering to the system.

(j) Micropolar parameter

Micropolar parameter describes the spin of the micro particles contained in the micropolar fluids.

(k) Coupling number

Coupling number is a non-dimensional parameter that relates or couples the equations of the linear momentum with the angular momentum to exhibits the microrotational

effects of the particles contained in micropolar fluids as mentioned by Chetti (2011). The value of the coupling number ranges from 0 to 1

1.5 Mechanisms of Heat Transfer

Heat is form of energy which is defined as the total amount of kinetic energy of the molecules of the system and can be transferred form one system to another depending upon the temperature difference of the systems. Broadly, heat is transferred in following three different ways from a system at high temperature to a system at low temperature.

1.5.1 Conduction

In this mode of heat transfer energy is transmitted between the bodies in direct contact. The heat transfer takes place due to temperature difference and it flows from a high temperature region to low temperature region until both regions become at same temperature.

1.5.2 Convection

Convection is the process in which heat moves through a gas or a liquid. In other words, the mode of heat transfer in liquids and gases is known as convection. Transfer of heat through convection is categorized in three different types, each one is explained below.

(a) Natural convection

Natural convection or free convection is mechanism of energy transfer that involves fluid motion due to density variation in fluid caused by temperature gradient.

(b) Forced convection

This mode of energy transmission involves fluid motion caused by some external agent e.g. fan or pumps. Forced convection may happen by natural means. For example, fluid radiator, heating and cooling of body-parts caused by blood circulation etc. are examples of forced convection.

(c) Mixed convection

There are the situations when both the above defined mechanism of natural and forced convection occurs together to cause the transfer of heat. In this phenomenon pressure forces and as well as buoyant forces takes a part.

1.5.3 Radiation

The mechanism that depends upon the heat transfer by electromagnetic waves occurred in the thermal band of any electromagnetic spectrum. Heat transfer due to radiation is

independent to medium i.e. it requires no medium and heat can be exchange through vacuum.

In this thesis, mixed convection mode of heat transfer is analyzed in peristaltic flow passing through vertical channel and tube considering of heat generation phenomenon. The analysis is made by incorporating the additional energy equation in the set of governing equations that describes the flow as well as the heat transfer characteristics of the model. The term representing the heat generation is takes apart in the energy equation.

1.6 Porous Medium

In the recent years, scientist, researchers and biologist show deep interest in the flows passing through the porous saturated medium due to its vast application in the transportation of toxic fluids industry, in geophysical situations, in transportation of the biological fluids in the human body and plants and in the extraction of oil at onshore and offshore oil rigs. Porous medium consists of small tiny holes spreads in the whole matter for example loaf of bakery bread and beach sand, in human body gallbladder, kidney lungs etc. The flows through a porous medium are of great interest by many researchers in all time in fluid mechanics Ramirez et al. (2014); Basser (2017); Hayat (2017). Darcy investigated unidirectional flow in a uniform medium on steady state into the hydrology of the water supply which gives the direct proportional relation between the rate of flow and pressure difference as mentioned by Neil et al. (2006). When Reynolds number ranges between 1 to 10 inertial term takes additional part in the Darcy's equation due to the presence of significant amount of inertial forces which is known as Forchheimer term and known as Darcy Forchheimer modal. Brinkman also modified Darcy model by just not adding an additional term but he relates the purity and permeability by a self-consistent procedure for large values of porosity. Some of the authors practice to incorporate the Laplacian term to make a "Brinkman-Forchheimer" modal. But this modal gain less confidence by the research as Brinkman model is valid only for high value of porosity but there exist uncertainty about the Forchheimer at high porosity values. Although, by applying formal averaging, one can derive the Brinkman-Forchheimer equation for a closure that involves the material of empirical type which consequently causes loss of facts.

1.7 Magnetohydrodynamics (MHD)

Flows through magnetic fields grabbed considerable attentions of the researchers and scientists due to its diversified applications in geophysics, astrophysics and solar structures etc. Metallurgy and power engineering fields are based on hydromagnetic flows. It is found that magnetic field is capable of controlling the thickening of fluid's viscosity (blood viscosity). The magnetic field also reduces the speed of flow particles and due to this characteristic, fluid velocity can be managed. MHD is also very useful in diagnoses and treatment of hypothermia, intestinal disorders, tumors, MRI and in many other health issues. Many researchers carried out their research work to address in such kind of flow problems like (Sajid et al. (2015); Yaqing and Guo (2017)).

The interaction of magnetic field and fluid flow is dealt in the branch of science known as magnetohydrodynamics. To discourse the properties of applied magnetic field on the fluid flow, the fluid must be electrically conducting. Let $\boldsymbol{E_0}, \boldsymbol{J_0}$ and $\boldsymbol{B_0}$ represents the electric field, current density and magnetic field which would exist in a given situation if $\boldsymbol{V} = 0$. Due to fluid motion, $\boldsymbol{E_0}$, $\boldsymbol{J_0}$ and $\boldsymbol{B_0}$ are influenced and have infinitesimal modifications $\boldsymbol{e}, \boldsymbol{j}$ and $\boldsymbol{b}$ respectively and the resulting electric field becomes $\boldsymbol{E} = \boldsymbol{E_0} + \boldsymbol{e}$, current density becomes $\boldsymbol{J} = \boldsymbol{J_0} + \boldsymbol{j}$ and magnetic field becomes $\boldsymbol{B} = \boldsymbol{B_0} + \boldsymbol{b}$. These quantities are governed by

$$\nabla \times \boldsymbol{E_0} = 0, \tag{1.5}$$

$$\boldsymbol{J_0} = \sigma \boldsymbol{E_0}, \tag{1.6}$$

$$\nabla \times \boldsymbol{e} = -\frac{\partial \boldsymbol{b}}{\partial t}, \tag{1.7}$$

$$\boldsymbol{j} = \sigma(\boldsymbol{e} + \boldsymbol{V} \times \boldsymbol{B_0}), \tag{1.8}$$

where we have neglected the second order term $\boldsymbol{V} \times \boldsymbol{b}$. Now Faraday's equation gives *evub* as given in Davidson (2001) and so perturbation in the electric field and its effects may also be neglected in Eq. (1.7). Therefore

$$\boldsymbol{J} = \boldsymbol{J_0} + \boldsymbol{j} = \sigma(\boldsymbol{E_0} + \boldsymbol{V} \times \boldsymbol{B_0}) \tag{1.9}$$

and leading order term in the Lorentz force (per unit volume) is

$$\boldsymbol{F} = \boldsymbol{J} \times \boldsymbol{B_0} \tag{1.10}$$

Eqs. (1.9) and (1.10) are all that we require evaluating the Lorentz force in low-Re_m MHD. There is no need to calculate $\bar{b}$ as it does not appear in the Lorentz force. Also, electric field is negligible in comparison to the current density.

1.8 Flow Equations

To study the fluid flow one needs the laws of conservation of mass along with conservation of momentum, first law of thermodynamics and second law of thermodynamics. Not all laws are necessary in all situations. However, the continuity and momentum equations of motion are the basic laws which are there always when we study any flow phenomena.

1.8.1 Continuity Equation

In differential form the continuity equation is as follows

$$\nabla.(\rho \boldsymbol{V}) + \frac{\partial \rho}{\partial t} = 0, \tag{1.11}$$

For incompressible assumption, when density of the fluid is kept constant then Eq. (1.11) reduces to

$$\nabla.\boldsymbol{V} = 0. \tag{1.12}$$

1.8.2 Momentum Equation

The general form of equation of fluid motion by dropping the body forces caused by any situation is given by

$$\rho\left(\frac{\partial \boldsymbol{V}}{\partial t} + (\boldsymbol{V}.\nabla)\boldsymbol{V}\right) = \nabla.\boldsymbol{\tau}, \tag{1.13}$$

where $\boldsymbol{\tau}$ is the Cauchy stress tensor.

1.8.3 Energy Equation

The analysis of transfer of heat with in the fluid is completely studied by incorporating energy equation to governing equation which is resultant by using first law of thermodynamics under the statement that energy cannot be destroyed nor created. Energy equation in Newtonian and non-Newtonian fluids can be written in vector form as

$$\rho\left(\frac{\partial T}{\partial t} + (\boldsymbol{V}.\nabla)T\right) = \alpha\, \nabla.\nabla \mathrm{T} + \frac{1}{\rho c_p}\tau : \nabla \boldsymbol{V}, \tag{1.14}$$

where T is the temperature, ρc_p is the heat capacity and α is the thermal diffusivity.

1.8.4 Microrotaion Equation

This equation describes the microrotation of the particles in the flow of micropolar fluid and can be written as

$$\rho J^*(\boldsymbol{V}^*.\nabla \boldsymbol{G}^*) = -2\bar{\kappa}\boldsymbol{G}^* - \bar{\gamma}(\nabla \times \nabla \times \boldsymbol{G}^*) + \bar{\kappa}\nabla \times \boldsymbol{V}^* + \left(\bar{\alpha} + \bar{\beta} + \bar{\gamma}\right)\nabla(\nabla.\boldsymbol{G}^*), \tag{1.15}$$

where G^* is the microrotation vector, J^* symbolizes the microgyration parameter, α, β and γ are the coefficients of spin gradient viscosity and $\bar{\kappa}$ characterizes the coefficient of vortex viscosity. The material constraints $\mu, \bar{\kappa}, \bar{\alpha}, \bar{\beta}$ and $\bar{\gamma}$ must satisfies the following relations defined by Eringen (1966) given by

$$2\mu + \bar{\kappa} \geq 0, \ \bar{\kappa} \geq 0, \ 3\bar{\alpha} + \bar{\beta} + \bar{\gamma} \geq 0, \ \bar{\gamma} \geq |\bar{\beta}|. \tag{1.16}$$

1.9 Method of Solution

Since, the governing equation representing the flow models in the succeeding all chapters are nonlinear with relatively complicated physical domain, it is therefore required to choose the highly accurate numerical scheme. Equations introduced by Navier-Stokes are known to be fundamentals of fluid dynamics. The investigations, discussed above in this dissertation are extensions of Navier-Stokes equations applied to model the heat transfer flows through the peristaltic boundaries of different geometries. Since these equations are highly nonlinear and obtaining analytic solution is very complicated and rarely possible. Therefore, we need to adopt some numerical approach. In most of situations, the governing equations are numerically challenging and must be solved by a stable numerical approach converging to physically significant solution. Hence, numerical solution of these systems is significant feature of modern research.

At present, there are many approaches which are in used by different researchers of this area to solve these modeled equations, such as finite difference, finite volume or by using finite element methods. All these methods have been used for computation of results for linear/nonlinear ordinary/partial differential equations. It is seen that the finite element method is emerged as a valuable and fast convergent tool for the solution of Navier-Stokes equations especially where complex geometry or complex boundary conditions are involved as compare to other analytical and numerical method. So the choice of the numerical technique is very important part in the simulation of peristaltic models. Besides other available techniques, on the basis of more advantages, we will adopt Finite Element Method which is explained in the following subsection.

1.9.1 Finite Element Method (FEM)

FEM is a computational scheme to solve ordinary and partial differential equations for many problems of science and engineering. This numerical approach is more reliable which can be justified. The advantages and disadvantages of this method in contrast of finite difference and with finite volume methods are as: The basic fact of finite

difference method is that it very easy to apply and in programming for the domain which can be divided in number of rectangles of equal dimensions. But, it has major disadvantages as it is difficult where the boundary of the domain is curved. For example, in our thesis where the geometry contains peristaltic walls, secondly it has difficult stability and convergence analysis and lastly, it is very difficult in mesh adaptations, which are required in proposed study. Finite Volume methods are based on the physical conservation laws of the system to be studied. It is problematic on the unstructured meshed and its stability and convergence analysis are difficult as for finite difference scheme. Comparatively, finite element method is high in accuracy and provides easy treatment for the complex geometries and boundary conditions as given in (Reddy (2014): Logan (2002)). So it can handle present model more efficiently and accurately.

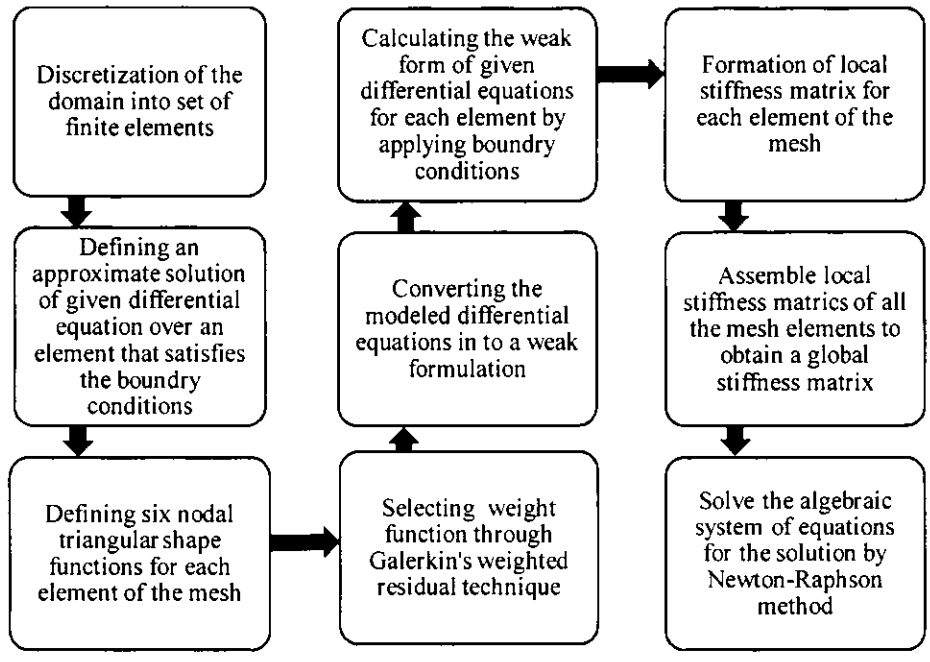

Figure 1.1: Flow chart of the procedure of finite element method

In finite element method, considered domain may be assumed as an assemblage of simple geometrical shapes, known as elements, against these elements we introduce approximation functions also called shape functions or interpolation functions. The finite element method is a piecewise (or element-wise) application of the variational and weighted-residual methods. For a given BVP, it is possible to develop different finite element approximations (or finite element models), depending on the choice of a particular variational and weighted-residual formulation. Galerkin weighted residual

technique of FEM has been extensively used by researchers to solve this type of research problems and we would use this technique to carry out solution.

In general, the following steps offered in the flow chart given in **Figure 1.1** are commonly implemented to get a solution using FEM

To demonstrate the method, we considered the differential equation as

$$Lu - f = 0 \tag{1.17}$$

Domain of above problem is Ω, L is differential operator, f is a given function and u is dependent function. We approximate u as

$$u \approx \tilde{u} = \sum_{i=1}^{n} \psi_i u_i, \tag{1.18}$$

where ψ_i are interpolating function and u_i corresponds to unknown variable for each node. Incorporation of $\tilde{u}$ in (1.17) does not satisfy the equation identically, rather we have the following equation

$$L\tilde{u} - f = \epsilon \tag{1.19}$$

where $\epsilon \neq 0$ shows residue which appears as solution is approximate instead of exact. In weighted residual scheme n unknowns u_i are determined in such a way that residual ϵ is minimized all over the domain. To accomplish this task we introduce weighted average of residual which must become zero all over domain Ω. If we select n weight functions W_i and following equation

$$\int_{\Omega} W_i \, \epsilon d\Omega = 0, \tag{1.20}$$

is essential to hold throughout the domain Ω against every weight function (i.e. ϵ must be perpendicular to span of W_i), then residual ϵ becomes zero in some average sense. After specifying weight functions we are left with a system of n equations to be solved simultaneously against nodal variables.

Various weighted-residual schemes differ mainly by choice of weight function. Generally, derivation of finite-element equations involve Galerkin's scheme. In Galerkin approach, weight functions are identical to that of approximation functions, i.e. $W_i = \psi_i$ for $i = 1,2,\ldots,n$ Therefore following equation holds in Galerkin's approach

$$\int_{\Omega} \psi_i (L\tilde{u} - f) \, d\Omega = 0; i = 1,2,\ldots,n \tag{1.21}$$

The left side of expression (1.21) may be assumed as summation of expressions leading the behavior of Eq. (1.17) against each element. We may approximate u against an individual element as

$$\tilde{u}^{(ele)} = \sum_{i=1}^{n} \psi_i{}^{(ele)} u_i{}^{(ele)}, \tag{1.22}$$

Here index *(ele)* corresponds to a particular element and n is number of nodes on that element. The left side of expression (1.21) may be expressed as summation in following form

$$\int_{\Omega^{(ele)}} \psi_i{}^{(ele)} \left(L\tilde{u}^{(ele)} - f^{(ele)}\right) d\Omega^{(ele)} = 0; \qquad i = 1,2,\ldots,n. \tag{1.23}$$

Similar expression may be obtained for every element of the domain and included to an assembly. This assemblage of local elements results into a global system of nonlinear algebraic equations. Procedure of assembling the local expressions does not involve spurious contributions until the interpolating expressions ψ_i fulfill compatibility condition explained above.

The modeled equations of problems related to peristaltic flow discussed in this thesis consists of nonlinear partial differential equations which are simulated by finite element method. The codes are developed in MATLAB to solve the governing equations subject to some boundary conditions. Algorithm to develop the codes is explained by (Abaid (2016); Bang and Kwon (2000); Jiajan (2010)).

1.10 Literature Review

Peristalsis is a phenomenon in which transportation of the fluid is caused by the progressive transverse waves generated by flexible boundary walls of the channel or tube's. This type of flow occurs in the human body like the motion of chyme through the digestive (gastrointestinal) tract, transportation of urine passing through the ureter and the swallowed food passing through the esophagus, etc. Peristaltic pumping is also very helpful in designing many biomedical devices like a heart-lung machine to maintain the circulation of the blood during critical operations. The mechanism of peristalsis also involves in plant physiology. In spite of the practical significance of peristalsis, the topic has been initially discussed by Latham (1966) in his dissertation. One year later, Burns and Parks (1967) studied the peristaltic motion through axially symmetric pipes and channel with the implementation of the assumption that Reynolds number is small and studied two extreme cases of peristaltic motion in the absence of pressure gradient and flow under the influence of pressure with fixed and sinusoidal moving walls. Shapiro et al. (1969) extended the idea of peristaltic motion by considering different assumptions. The most famous assumptions are long wavelength along with low Reynolds number assumptions and such investigation are limited to

physiological peristaltic flows because in such flows, the value of Reynolds number is engaged with very small values. The flow of chyme in a small intestine is a prominent example of such flows where the wavelength of peristaltic wave is approximately very large (0.125cm) as compared to the radius of the tube (0.008 cm). Fung and Yih (1968) and several other authors investigated the peristaltic motion under various simplifying assumptions. The most common of these are long wavelength along with low Reynolds number assumptions. The applicability of such assumptions is only limited to physiological peristaltic flows. This is because the Reynolds number characterizing such flows is very less in number. Moreover, in such flows, the wavelength of peristaltic waves is quite large in contrast with the radius of the organ. A typical example of such a flow is found in small intestine. Zien and Ostrach (1970) presented the result in a narrow range and in accordance of Reynolds number the reflux phenomenon does not change the whole situation in the flow. It has been reported by Lew et al. (1971) that Reynolds number in such type of flow is small less than unity. Yin and Fung (1971) gives the comparison of the theoretical and available experimental results of peristaltic transport. These result shows good agreement of the theoretical results with the experimental results and includes the influence of peristaltic reflux. Jaffrin (1973) investigated the peristaltic flow in a two-dimensional tube using perturbation method. Manton (1975) studied the peristaltic pumping at low Reynolds number and specific for long wavelength and concluded that reflux arises independent of the shape of the wave in the presence of adverse mean pressure gradient. Two dimensional peristaltic flow with solid particle between two flexible vertical walls that are submerged in a towing tank filled with biological fluid in a laboratory was studied by Hung and Brown (1976) using experimental approach. Later Brown and Hung (1977) gave the comparison of experimental and computational results for two dimensional peristaltic flows. They implemented finite difference method to solve the Navier-Stokes equations for peristaltic motion for finite wall-wave curvature. The finite bending as well as contraction of waves in the peristaltic motion of incompressible waves was investigated by Wilson and Panton (1979). They obtained the results of lateral bending and complex wave motion by using the perturbation method. Shukla et al. (1980) investigated the peristaltic flow by considering the bio-fluid in which characteristics of peripheral viscosity is taken into account. It is shown that fractional force and viscosity caused by the peripheral layer have direct relation and flow flux have inverse relation with the viscosity caused by the peripheral layer. Shukla and Gupta (1982) investigated the

peristaltic transport of non-Newtonian fluid passing through tube by considering peripheral layer, the power-law fluid is assumed consistent to show the results for pseudoplastic nature of the fluid. Srivastava and Srivastava (1982) investigated the peristaltic transport of physiological fluid assuming the two-layered model under long wavelength assumption. In their study, the comparison of the obtained results to the results without peripheral layer is included which exhibits that in case of peripheral layer case, the magnitude of rise in the pressure is low as compare to the case of flow without peripheral layer effects.

The first comprehensive investigation in two-dimensional peristaltic flow in the channel is provided by Takabatake and Ayukawa (1982). They solved the Navier-Stokes equation by using finite difference method that equipped with upwind successive over relaxation famously known as SOR method and presented the obtained results for moderate Reynolds number and compare their results with those of the perturbation analysis of Zein and Ostrach (1971) and Jaffrin (1973). Bohme and Friedrich (1983) investigated the viscoelastic fluid in the peristaltic flow generated by infinite sinusoidal wave train by neglecting the inertia which reflects low Reynolds number and considered constant pressure over the cross-section. Longuet-Higgins (1983) investigated the peristaltic pumping in the water waves and calculated the streaming caused by the gravity waves in which they considered that one side of the fluid is rigid while other is flexible. The study given by Shapiro et al. (1969) was extended by Brasseur et al. (1987) and gave detail investigation of the effects caused by the peripheral layer with diverse viscosity on the mechanism of peristaltic pumping of Newtonian fluid and phenomena of reflux. The boundary integral method is used to investigate the peristaltic flow under the assumption of creeping flow introduced by Pozrikidis (1987). Takabatake et al. (1988) studied peristaltic transpiration in tube numerically by using finite difference method and concluded that the peristaltic mixing is greater in the tube as compared to that of the channel. Finite element analysis of peristaltic transportation was provided by Takabatake et al. (1990) in which they clarified that when wall slope becomes high, it significantly strengthens the rising ability of the pressure at zero time-mean flow rate. Siddiqui and Schwarz (1994) studied the second-order fluid passing through a tube. Peristaltic pumping of the fluid containing solid particles was investigated by Fauci (1992) and concluded the results based on the effects of velocity for a situation in which diameter of the particles becomes equal to the channel width. Kumar and Naidu (1995) studied the two-

dimensional peristaltic flow under the influence of magnetic field by converting governing equations in the stream-vorticity formulation. Unlike earlier studies, they claimed that their solution is well convergent at high values of Reynolds number even up to 100 but they did not give any comparison of their solution with Takabatake et al. (1990). The peripheral layer viscosity and frictional force was investigated by Usha and Rao (1995) for peristaltic transport of bio fluid passing in elliptic cross sectional pipe with the help of elliptic cylindrical coordinate system. Rao and Usha (1995) also provided the study about the peristaltic transport in a circular tube in pumping and co-pumping regions for immiscible viscous fluids. Misra and Pandey (1995) analyzed the peristaltic mechanism of viscous incompressible fluid passing through the tapered tube. The nonlinear convective acceleration is considered to study the problem by using perturbation method.

Hayat et al. (2006) studied the behavior of Jeffery fluid endoscopic effect in peristaltic transport in the section between the two uniform concentric tubes. The analytical results for velocity and axial pressure gradient are provided while numerical integration is incorporated to study the frictional force and pressure on the outer and inner tube. A generalized approach to study the non-Newtonian behavior of power-law fluid in peristaltic transport is presented by Ikbal et al. (2008). The flow is assumed to be two dimensional unsteady which allows both the radial as well as the axial components of the velocity to take part in the motion of the fluid. Hariharan et al. (2008) examined the peristaltic mechanism in a diverging tube through which non-Newtonian fluid is passing. They considered Bingham fluid and power-law fluid passing through a diverging tube where walls of the tube obeys the various wave forms such as sinusoidal, multi-sinusoidal, square and trapezoidal waves. Pandey and Chaube (2010) premeditated the motion of incompressible viscoelastic fluid through a tube generated by peristalsis. Perturbation method is employed to governing equations that are modelled under the assumption of low Reynolds number along with long wavelength. Nadeem and Akram (2010) used the perturbation method to investigate the peristaltic motion of Williamson model passing through the axisymmetric channel and concluded that for small values of Williamson parameter, fluid shows Newtonian fluid nature and for high values of Williamson parameter, pressure curves become nonlinear. Dharmendra (2011) investigated peristaltic motion of Maxwell fluid passing in uniform tube to study the application towards endoscopy. He used homotopy perturbation method and variation iterative scheme by assuming inner tube to be inflexible while

outer tube is flexible. The one of the important outcome form his investigation is that in case of pressure and frictional force, the effects of all the parameters in involved are entirely opposite. Hayat et al. (2011) considered compliant walls to invstigate the peristaltic motion of incompressible viscous fluid under the assumptions of long wavelength along with low Reynolds number. The expression for the velocity, temperature, stream function are also included in their investigation and are analyzed through the graphs with detailed discussion. Gad (2014) also considered complaint walls to investigate the hall current effects on the peristaltic mechanism and found mean flow reversal at the central region and near the wall of the channel. Akbar and Nadeem (2014) gave the exact solution for the study of biviscosity fluid for a peristaltic flow in an endoscope to predict that increasing values of biviscosity coefficient and strengthening magnetic field increase the pressure in all the pumping regions. Abbas et al. (2016) explored the three dimensional peristaltic flow in a non- uniform channel with the flexible walls containing hyperbolic tangent fluid. In their study, the inertial effects are neglected by means of assumption of the lubrication theory. Peristaltic flows for different physical flow situation with different types of fluids were investigated by the researcher in last couple of years Tripathi et al. (2017); Zahir et al. (2017); Longo et al. (2017); Poursharifi and K. Sadeghy (2017); Hayat et al. (2017); Akram et al. (2017) and Fusi and A. Farina (2017). The Galileo transformation is used by Moradi et al. (2017) to convert the unsteady physical form the steady one to investigate the peristaltic annular flow.

Recently scientists, researchers and biologists show deep interest in the study of the problems of fluid flow through the porous medium due to its extensive range of applications in industry including geophysical and biological transportation of fluid in the human body and plants, extraction of oils from underground oil reservoirs discussed in Allen (1984) and Allen et al. (1988). Few examples of porous medium are beach sand and a loaf of bakery bread. This type of flow attains considerable attention in the literature Vafai, and R. Thiyagaraja (1987) and Whitaker (1986). Porous medium basically consists of small tiny holes which are distributed in the whole matter. Examples of the porous medium in the human body are gallbladder, human lung, and kidneys. Darcy's law plays a vital role for the researchers to study the porosity in different flow phenomenon. Hill and Strahgan (2009) studied the Poiseuille flow passing through a highly porous saturated medium by considering the Darcy-Brinkman equations. Ervin et al. (2016) presented the model and numerical solution for

generalized Newtonian fluid flowing through the porous saturated medium. Peristaltic flow of the pulsatile fluid passing through the porous medium was considered and analyzed by Afifi and Gad (2003). The frequency of the traveling wave is assumed equivalent to the pressure gradient to elaborate the solution of the Navier-Stokes equations by using perturbation method. Rao and Mishra (2004) investigated peristaltic transportation by applying Beavers-Joseph slip boundary condition on power-law fluid passing through the axisymmetric porous tube. They concluded that negative time mean flow occurs in free pumping region in both cases of shear thinning and shear thickening fluid for the contraction and as well as expansion of the straight section dominated (SSD) wave. Mishra and Rao (2005) studied the model for a flow passing through the gastrointestinal tract in which peristaltic flow with a porous peripheral layer is investigated in a channel by Darcy and Brinkman equation. It is concluded that for greater pressure in two layered model, peristalsis acts as a pump where as in peripheral layered model peristalsis acts as a pump at low pressure.

Hall effects are studied by Hayat et al. (2007) in the peristaltic transportation of Maxwell fluid through a uniform porous medium. Modified Darcy model is incorporated in governing equation and solve them for the small amplitude ratio. Asymmetric channel was considered by Elshehawey et al (2006) to analyze the peristaltic motion in wave frame of through a porous filled medium. Adomian decomposition method is used to find the stream function explicitly which exhibits that velocity of the fluid is related to permeability parameter by direct relation. Heat transfer mechanism in peristaltic flow passing through a vertical annulus saturated with porous medium by applying the assumptions of long wavelength approximation is studied by Vajarvelu et al. (2007) and found that by increasing the free convection parameter about 1 to 2 percent, the mean flux increases by 10 to 12 percent and heat transfer through the peristaltic wall is highly dependent on the amplitude ratio of the peristaltic wave. Nonlinear peristaltic transport through inclined axisymmetric channel filled with porous medium was investigated by Kothandapani and Srinivas (2008). They studied the flow by considering the Newtonian fluid in wave frame of reference that moves with the similar speed as of the velocity of the wave. The effects of the partial slip condition on the peristaltic motion through a porous saturated medium was investigated by Hayat et al. (2008). Adomian decomposition method is implemented to solve the governing equation to obtain the solution in terms of stream function for axial velocity whereas numerical integration is implemented for pumping and trapping phenomenon.

Heat transfer effects for the peristaltic flow of conducting fluid passing through the porous medium was investigated by Hayat et al. (2009). In their investigation, the magnetohydrodynamic effects were also taken in asymmetrical channel. Heat transfer analysis for peristaltic motion of a Newtonian fluid passing through the asymmetric vertical channel filled with porous medium was presented by Srinivas and Gayathri (2009). The problem is expressed in the wave frame under the assumptions of long wavelength along with low Reynolds number. Abd elmabound and Mekheimer (2011) studied the second order fluid in peristaltic flow thorough a porous filled channel with harmonically undulating extensible walls. Numerical results are formulated to examine the effects of the pressure rise per wavelength and frictional force. Heat transfer effects in the transport of Jeffery fluid passing in the vertical stratum by means of peristalsis was investigated by Vajravelu et al. (2011) by using perturbation technique. They noticed that the strong effects of the wall deformation parameter and Jeffery number appeared on the trapping bolus. In one more study, Vajravelu et al. (2012) extended the model of peristaltic transporation through a symmetric channel for a Williamson fluid. The exact solution for this model becomes singular, hence spate perturbation solution is formulated to bring out qualitative features of the model. Dharmendra (2013) presented the heat flow analysis of the peristalsis through a channel of finite length filled porous medium and deduced that peristaltic heat flow can be enhanced by increaseing the values of Grashof number and thermal conductivity. The peristaltic flows through porous medium gains considerable attention in the last few years by Tripathi and Bég (2014); Tripathi et al. (2015); Sankad and Nagathan (2015); Sankad and Patil (2015); Babu et al. (2015); Sankad and Nagathan (2016); Ramesh and Devakar (2017) and Hayat et al. (2017). The study related to peristaltic transportation of blood passing through the porous filled micro vessels was given by Ranjit et al. (2018). The mathematical model considered in their investigation is suitable to analyze the joule heating and zeta potential is also taken in account in existence of magnetic field. The porous medium is analyzed with the help of Darcy law and Debye-Huckel approximation is used. The finding of this investigations improves the medical therapies to modulate the blood flow and hence casuses to reduce the pain in the human body.

Flows through magnetic fields grabbed considerable attention by the researchers and scientists due to its diversified applications in geophysics, astrophysics and solar structures etc. Metallurgy and power engineering fields based on hydromagnetic flows.

It is found that magnetic field is capable of controlling the thickening of fluid's viscosity (blood viscosity). The magnetic field reduces the speed of flow particles and due to this characteristic, fluid velocity can be managed. MHD is also very useful in diagnosing and treatment of hypothermia, intestinal disorders, tumors, MRI and in many other health issues. El-Shehawey (2002) studied the peristaltic motion propagated by sinusoidal wave in the channel with pours walls in which incompressible viscous fluid is filled under the impact of externally applied magnetic field. Naby et al. (2006) presented the studied phenomena of peristaltic motion of Newtonian and Carreau fluid passing through the channel under uniform magnetic field. It is noted that due to increase in Hartmann number that corresponds to strong magnetic field, the pressure rise and friction force increases for both Newtonian and Carreau fluid for certain rates of the time mean flow. Eldabe et al. (2007) considered biviscosity fluid in the peristaltic motion passing through the non-uniform magnetic field with the effects of induced magnetic field. Ebaid et al. (2008) analytically and numerically investigated the properties of magnetic field along with the condition of wall slip on the peristaltic motion passing through the asymmetric channel. Srinivas and Kothandapani (2009) studied the MHD peristaltic flow for heat and mass transfer in which porous medium with compliant walls are also considered. They provided analytical solution in the form of stream function of modelled governing equation under the assumptions of lubrication theory. Srinivas et al. (2009) extended the work given in (2009) by incorporating the effects of slip conditions on the same flow model with elastic wall properties. It has been found by them that increasing Knudsen number enhances the appearance of the trapped bolus. Yildirim and Sezer (2010) investigated the peristaltic flow under the influence of the magnetic field in an asymmetrical channel with partial slip. Homotopy perturbation method is implemented to sort out the solution of the governing equation that are simplified by applying the assumptions of long wavelength with low Reynolds number. Hayat et al. (2010) examined the peristaltic flow of fourth grade type fluid passing through asymmetrical channel that is inclined a certain angle under the impact of inclined magnetic field. They concluded that the increase in strength of magnetic field enhances the velocity of the fluid. Vajravelu et al. (2013) provided the study about the MHD peristaltic transport of a Carreau fluid passing through channel with velocity slip condition. The effects of temperature and concentration jump conditions are also analyzed in their study.

Ramesh and Devakar (2015) investigated the magnetohydrodynamics peristaltic transport of couple stress fluid for analysis of heat transfer passing through the porous symmetrical inclined channel. The flow model is formulated under the assumptions of long wave length along with low Reynolds number and exact solution is provided for stream function, pressure gradient and heat transfer analysis. Peristaltic motion under the effect of radially varying magnetic field of a Jeffry fluid passing through a tube with an endoscope is provided by Abd-Alla et al. (2015). Zeeshan et al. (2015) explored the two phase unidirectional flow analytical in a symmetric channel under the inducement of magnetic field. The flow model is solved by using homotopy perturbation method and found that due to quasi-statically unstableness void fraction bubbles rapidly approaches to zero and increasing Lorentz force decreases the velocity while weber number and power law index support the velocity. Now a days, due to diverse application in the industry and bio medical science, peristaltic flows under the inducement of the magnetic field gains considerable attention and studied extensively Shit and Roy (2014); Hayat et al. (2018); Kothandapani and Srinivas (2018); Hussain et al. (2018); Khan et al.(2018) and Misra et al. 2016). Kothandapani et al. (2016) inspected the peristaltic flow of fourth grade fluid under the influence of magnetic field in an asymmetrical channel and found that axial velocity decreases with upsurge in Hartmann number and pressure rise in case of fourth grade fluid is higher than that of Newtonian fluid.

Heat transfer analysis on peristaltic motion in different physical situations attains a considerable attention due to its numerous applications on the industrial scale. It includes transportation of different toxic fluids in which temperature of the fluid is vital rule. Researchers and scientists continuously improving the literature to enhance the efficiency of the peristaltic transportation in such type of processes. Radhakrishnamacharya and Srinivasulu (2007) provided the study about peristaltic transport in which heat transfer and effects of wall properties are analyzed. Perturbation method is used to solve the governing equations and predicts that increase in elastic tension as well as participated mass characterizing parameters enhances the heat transfer phenomena. Srinivas and Kothandapani (2008) investigated the heat transfer phenomena of peristaltic flow passing through the asymmetric channel with different amplitudes and phase. The effects of applied magnetic fields are also discussed through the involvement in the governing equation through Lorentz force. Mehkheimer and Abd Elmaboud (2008) considered the peristaltic flow in the vertical annulus to examine the

heat transfer and effects of magnetic field in peristaltic flow of Newtonian fluid to study its application in an endoscope. Kothandapani and Srinivas (2008) considered porous medium in the peristaltic flow to analyze the heat transfer phenomena on under the inducement of applied magnetic field. Assumptions of lubrication theory are implemented to the flow model and concluded that heat transfer can be enhanced by increasing the permeability parameter while strengthening of magnetic field reduces the heat transfer ability. Hayat et al. (2009) studied the heat transfer phenomena for electrically conducting fluid in peristaltic flow through a porous saturated medium. It is noted that behavior of hydromagntic fluid in the vicinity of the peristaltic wall and in the neighbor of center of the channel is entirely different and heat transfer is noted much greater in the case of MHD flow as compared to that of hydrodynamic flow. Curved channel was considered by Ali et al. (2010) to investigate the heat transfer mechanism in peristaltic flow. The flow is numerically stimulated by shooting method equipped with Runge-Kutta algorithm and gave interesting result that heat transferred in curved channel is lesser in magnitude as compared to that of flow in the straight channel. Muthuraj and Srinivas (2010) explored he effects of heat transfer through mixed convective mechanism in a wavy channel oriented vertically in which thermal waves are travelling through the porous medium.

Hayat et al. (2010) provided the effects on the peristalsis due to heat transfer and slip condition on the flow propagated in various wave forms under the assumptions of low Reynolds number along with long wavelength. The effects of inducement of magnetic field on the flow model also included which leads to the finding that the effect of the magnetic field in the augmented and retrograde pumping regions is opposite. Hayat and Hina (2010) considered the Maxwell fluid in the peristaltic flow under the inducement of magnetic field to analyze the transfer of heat and mass along with the wall properties. Fourth grade fluid was considered to discuss the mechanism of heat transmission with induced magnetic field by Hayat et al. (2010). The assumptions of low Reynolds number, long wavelength with low Deborah number are implemented in their investigation to observe the effects of induced magnetic field and current density on the flow. Srinivas et al. (2011) examined the heat transfer mechanism through mixed convection in the peristaltic flow passing through the asymmetric channel. The effects of chemical reaction in mixed convective heat transfer on peristaltic motion through vertical asymmetrical channel filled with porous material was investigated by Srinivas and Muthuraj (2011). Perturbation solution is found to understand the mechanism of

heat transfer in presence of magnetic field on Carreau fluid transported by peristaltic transportation of by Hayat et al. (2011) for small values of Weissenberg number. Hayat et al. (2011) further provided the study considering the curved channel to analyze the heat and mass transfer with wall properties for third grade fluid. They concluded that heat transfer is noticed much faster in planner channel as compared to the curved channel but maximum value of temperature and mass concentration is higher in flow passing through curved channel as equated to that of flow in straight channel. Saleem and Haider (2014) studied the peristaltic transport of creeping flow of non-Newtonian fluid to analyze the mechanism of heat and mass transfer. They claimed that the results are similar to the case of viscous fluid up to first order in creeping flow while afterwards for second order, the results matches with the results for Maxwell fluid and temperature profile can be enhanced by increasing the Weissenberg and Brickman numbers. The Burgers fluid which is non-Newtonian fluid categorized as rate type fluid was considered by Javed et al. (2014) in peristaltic motion to study the heat transfer mechanism in a channel with compliant walls. It was concluded in their study that heat transfer can be enhanced by increasing the elastic parameters involved in the flow model. Abd-Alla et al. (2014) investigated the rotational effect and initial stress effects on the transfer of heat in peristaltic flow of fourth order fluid under the impact of applied magnetic field. Heat transfer mechanism is widely investigated by Mustafa et al (2014); Hameed et al. (2015); Muthuraj et al. (2016); Ramesh (2016); Hayat et al. (2016) and Hayat et al. (2017) in the study of the peristaltic fluid in different flow situations for numerous fluids to utilize the benefits in transporting of fluid on different levels. Mixed convection heat transfer and effects of shear thickening and shear thinning was investigated by Tanveer et al. (2017) in a peristaltic transportation of Sisko fluid passing through a curved channel. They concluded that increase in curvature causes decease in velocity and temperature distribution of the fluid and concentration of homogeneous and heterogeneous reaction are reverse to each other.

The plasma shows the Newtonian fluid behavior while blood shows non-Newtonian behavior is reported by Johnston et al. (2004). At low shear rates, blood shows non-Newtonian behavior in small arteries but in large arteries at high shear rates, it performs as Newtonian is reported by Rathod and Tanveer (2009). When blood flows through narrow arteries at a low shear rate, it behaves like a Casson fluid reported by Srivastava and Srivastava (1984); Sankar (2009) and Nagarani et al. (2006). In narrow arteries with a diameter of $130 - 1000\ \mu m$, Casson fluid is useful to consider it as a blood flow

model Merrill et al. (1965) and Merrill et al. (2013). But on reviewing the literature, it is evident that no hard effort has been made to present the study about the transport of the fluid of non-Newtonian category in case of a small amplitude of wave before Raju and Deventhan (1972). Srivastava and Srivastava (1965) investigated blood transportation by ignoring peripheral layer which allows blood to behave as single layered Casson fluid. Later, Srivastava (1987) presented the study for the axisymmetric flow of Casson fluid passing in a circular tube. Das and Batara (1993) investigated the fully developed model of Casson fluid for steady flow passing through the tube at low Dean Number. Perturbation method is implemented to peristaltic flow model of physiological fluids when Casson fluid is considered in channel by Mernone et al. (2002). Effects of inclined channel and its width size significantly effects the motion of the fluid in peristaltic flow of Casson fluid was concluded by Nagarani (2010). Kumari et al. (2011) extended the work of Nagarani (2010) by incorporating the magnetic field to the flow model to analyze and presened the study about the peristaltic motion of Casson fluid in a channel inclined at some angle. The permeable walls of the channel of different wave forms was considered in the investigation of peristaltic motion of a Casson fluid by Srinivas et al. (2014). It was concluded that increase in yield stress behavior of Casson fluid causes decrease in the flux at a given pressure difference.

The magnetic effects in the study of peristaltic motion of Casson fluid passing through the asymmetrical channel was investigated by Akbar (2015) to enhance the utilization of this type of low model in the refinement of crude oil. It was concluded that dominance of the electromagnetic forces in comparison to viscous forces reduces the size and number of the bolus. Implementation of magnetic field was also considered in metachronal beating of cilia of Casson fluid is presented in literature by Akbar and Khan et al. (2015). Exact solutions of the governing equations that are modelled by applying the assumptions of lubrication theory were calculated to observe the qualitatively same behavior of velocity for Newtonian and Casson fluid but quantitatively velocities are different as velocity of the Casson fluid is lesser than the velocity of the Newtonian fluid. To analyze the magnetic effects on the bio fluids in different flow models and curved channels are also studied by Shit et al. (2016); Ali et al. (2016). Heat transfer analysis in the metachronal wave for beating cilia equipped with thermal diffusivity/conductivity and velocity slip effects for Casson fluid flowing in elliptic trajectories under the impact of magnetic field was investigated by Akbar et al. (2016). It was noticed that raise of temperature can be controlled by both Casson

fluid parameter and applying strength of magnetic field. Casson fluid parameter also enhances the size and number of bolus in trapping phenomenon and decrease in pressure rise per wavelength is noticed for increasing the electromagnetic forces but it enhances by the greater cilia length.

The concept of micropolar fluids was introduced by Eringen (1966) and studied the individual substructure effects on the flow by suspensions of concentrated rigid neutrally buoyant particles in the viscous fluid. However, such type of fluids backing the couple stresses as well as body couples thus exhibits the microinertial and microrotational effects. The microrotation vector in the flow of micropolar fluid model is a basically independent kinematic vector that reveals the microrotation of the particles. However, more detail of the theory of microrotation of the particles in the fluids was discussed in Ariman (1973) and Ariman et al. (1974). The peristaltic transportation of a micropolar fluid transmiting through flexible walls of the tube was provided by Devi and Devanathan (1975) with small amplitude of the sinusoidal wave. Srinivasacharya et al. (2003) examined the behavior of micropolar fluid in a peristaltic flow passing through tube and predict that for micropolar fluid, peristalsis acts as a pump and rise in pressure is noted as compare to that of Newtonian fluid and for free pumping in peristaltic motion of micropolar fluid, pumping flux is very small for both Newtonian and micropolar fluid. Hayat et al. (2003) formulated the exact solution for parasitic motion in different wave form of a channel that contains the micropolar fluid. It is observed that for low adverse pressure gradient, retrograde pumping exists in case of triangular waves and multi sinusoidal waves in comparison to the case of other wave forms such as square wave, sinusoidal wave and trapezoidal wave. The effect of the endoscope through concentric tubes was studied by Hayat and Ali (2008). They considered the peristaltic motion of micropolar fluid caused by moving outer wall while assuming inner wall fixed. Ali and Hayat (2008) modeled the problem in which micropolar fluid is considered in peristaltic motion passing through the tube and exact solution is formulated and expression for shear stress is also provided. It was concluded by them that in symmetric channel, shear stress at both peristaltic walls increase with increase in coupling parameter while in asymmetric channel shear stress increase in the one wavelength and exhibits opposite behavior in other. Muthu et al. (2008) studied the impact of the wall properties for transportation of micropolar fluid in the peristaltic mechansim passing through the concentric circular cylindrical tubes. Finite difference technique is applied to examine the viscoelastic or elastic wall properties to the

governing model under the assumptions of long wavelength and low Reynolds number. Peristaltic motion of micropolar fluid through a tube was also studied by Wang et al. (2011). They compared the peristaltic pumping and free pumping flux for Newtonian and non-Newtonian fluids. It is noticed that the lubrication theory was widely used to study the peristaltic motion of the micropolar fluid. Pandey and Chaube (2011) investigated the peristaltic motion through porous medium in which they assumed micropolar fluid passing through the channel in presence of magnetic field. It is observed through the analysis given by them that magnetic forces enhances the peristaltic pumping while porous medium causes the reduction in peristaltic pumping. This work is extended by Abd-Alla et al. (2013) by investigating rotational effects in the peristaltic transportation of the non-Newtonian micropolar fluid through a channel saturated with porous medium under the influence of externally applied uniform magnetic field. The results shows that rotation, magnetic field and micropolar parameters significantly affects the peristaltic pumping. Abou-zeid (2016) used homotopy perturbation method to study the thermal diffusion and viscous dissipation in peristaltic flow of micropolar nanofluid. Hayat et al. (2016) investigated the peristaltic transportation of micropolar fluid passing through the curved channel equipped with Newtonian heating to study the effects of heat source/sink and homogeneous-heterogeneous reactions. Coupled equation are formulated to present the flow model by applying the assumptions of long wavelength along with low Reynolds number. Abdelsalam and Vafai (2017) provided the study about the peristaltic flow in a microfluidic channel occupied with compressible fluid to investigate the effects of rheological properties and inducement of magnetic field. The key observation of the investigation that arise is that the suppression effect of retardation time significantly reduces the flow and reverse flow is occurred due to acoustic streaming quadratic effects.

It is noted by reviewing the literature that peristaltic motion of Newtonian/non-Newtonian fluids in tube/channel for different physical situation were studied by using the assumptions of lubrication theory which vanishes the contribution of inertial forces and not valid for all wavelengths. But this is not the case in the flows related to engineering field such as transport of blood, slurries and corrosive fluids by means of peristaltic pumps. In such flows, there arise a need to analyze peristaltic flow at moderate Reynolds number The investigation involves the mathematical modeling and numerical solution of peristaltic transportation passing through a channel without

incorporating long wavelength with low Reynolds number are investigated and presented by Hamid et al. (2017) and Javed et al. (2017). Finite element technique based on Galerkin's formulation defined in Kwon and Bang (1991) and Ferreira (2009) is implemented to numerically simulate the governing set of nonlinear partial differential equations that presents the effect of inertial forces in shape of graphs of longitudinal velocity, pressure rise per wavelength and contours of streamlines for moderate Reynolds number and other pertinent parameters along with the detailed discussion is made in every chapter of this thesis.

Chapter 2

Hydromagnetic Peristaltic Flow in a Porous-Saturated Channel

Main goal of this chapter is to provide the mathematical modelling and simulation of the complete set of Navier-Stokes equations that presents the peristaltic transport of Newtonian fluid passing through the channel saturated by the uniformly distributed porous medium that is placed in the influence of externally applied magnetic field by uniform source. The problem is modeled in term of system that contains nonlinear partial differential equations. Equations are modeled without incorporating famous assumptions of lubrication theory which gives the liberty to set nonzero moderate values of Reynolds number. Galerkin's Formulated finite element method is implemented to find out the solution of the governing equations numerically. The obtained numerical results are established in decent agreement with the results available in the literature. The obtained results are presented graphically along with detail discussion is provided.

2.1 Problem Formulation

Consider an electrically conducting fluid in a two dimensional flow of through a channel filled with porous medium of uniformly distributed pores throughout the surface. All the thermo-physical properties own by the fluid are assumed to be constant and flow is considered to be unsteady. A uniform magnetic field of strength B_0 is implemented orthogonally to the flow direction. The properties and effects of induced magnetic field on the flow are neglected by assuming a small magnetic Reynolds number. It is supposed that a continuous wave is travelling periodically on the walls of the peristaltic channel. The flow is assumed in the direction of x −axis and y −axis is taken perpendicular to the direction of the flow. The flow is assumed to be symmetric about x −axis called the axis of symmetry. In the fixed frame, the movement of the boundary obeys the relation given in Eq. (2.1) as follows

$$H(X,t) = a - b\cos\left[\frac{2\pi(X-ct)}{\lambda}\right], \tag{2.1}$$

where c corresponds to the wave speed, a symbolized half width of the channel, b represents amplitude and λ corresponds to the wavelength. The schematic diagram of the considered flow model is presented in **Figure 2.1**.

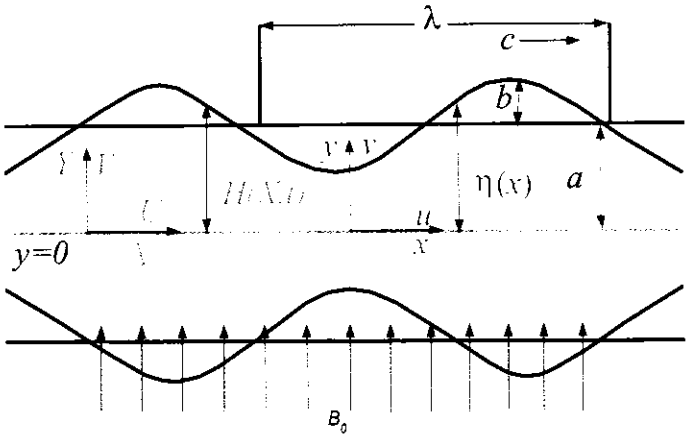

Figure 2.1: Geometry of the peristaltic channel flow

Firstly, we transform the equations that govern the flow model of two-dimensional flow passing through porous medium for a viscous fluid with inducement of a transverse magnetic field along with suitable boundary conditions on the present flow situation under investigation in the wave frame of reference (x^*, y^*) which is connected to fixed frame (X, Y) by the Galileans transformations given as

$$u^* = U - c, \quad x^* = X - ct, \quad v^* = V, \quad y^* = Y. \tag{2.2}$$

The problem in the wave frame takes the form

$$\frac{\partial u^*}{\partial x^*} + \frac{\partial v^*}{\partial y^*} = 0, \tag{2.3}$$

$$\rho\left(u^*\frac{\partial u^*}{\partial x^*} + v^*\frac{\partial u^*}{\partial y^*}\right) = -\frac{\partial p^*}{\partial x^*} + \mu\left(\frac{\partial^2 u^*}{\partial x^{*2}} + \frac{\partial^2 u^*}{\partial y^{*2}}\right) - \left(\sigma B_0^2 + \frac{\mu}{k}\right)(u^* + c), \tag{2.4}$$

$$\rho\left(u^*\frac{\partial v^*}{\partial x^*} + v^*\frac{\partial v^*}{\partial y^*}\right) = -\frac{\partial p^*}{\partial y^*} + \mu\left(\frac{\partial^2 v^*}{\partial x^{*2}} + \frac{\partial^2 v^*}{\partial y^{*2}}\right) - \frac{\mu}{k}v^*, \tag{2.5}$$

$$\eta(x^*) = a - b\cos\left(\frac{2\pi x^*}{\lambda}\right), \tag{2.6}$$

$$\left.\begin{aligned} v^* = 0, \quad \frac{\partial u^*}{\partial y^*} = 0, \quad &\text{at} \quad y^* = 0 \\ u^* = -c, \quad v^* = -\frac{2\pi bc}{\lambda}\sin\left(\frac{2\pi x^*}{\lambda}\right) \quad &\text{at} \quad y^* = \eta(x^*) \end{aligned}\right\}. \tag{2.7}$$

For further analysis, we must make governing equations dimensionless by incorporating dimensionless variables defined as

$$\left.\begin{aligned} \alpha = \frac{a}{\lambda},, \phi = \frac{b}{a}, u = \frac{u^*}{c}, v = \frac{v^*}{c}, x = \frac{x^*}{\lambda}, y = \frac{y^*}{a}, \\ p = \frac{a^2}{\lambda \mu c} p^*(x^*), \eta = \frac{\eta(x^*)}{a}, q = \frac{q^*}{ch}, \psi = \frac{\psi^*}{ca}, \omega = \frac{\omega^*}{c/a} \end{aligned}\right\}. \tag{2.8}$$

Defining the stream function ψ through the usually velocity-stream function relation

$$u = \frac{\partial \psi}{\partial y}, v = -\alpha \frac{\partial \psi}{\partial x}. \tag{2.9}$$

After eliminating the pressure terms, Eqs. (2.3) – (2.7) in terms of vorticity ω and stream function ψ can be written as

$$\alpha^2 \frac{\partial^2 \psi}{\partial x^2} + \frac{\partial^2 \psi}{\partial y^2} = -\omega, \tag{2.10}$$

$$\mathrm{Re}\left(\frac{\partial \psi}{\partial y}\frac{\partial \omega}{\partial x} - \frac{\partial \psi}{\partial x}\frac{\partial \omega}{\partial y}\right) = \nabla^2 \omega + M^2 \frac{\partial^2 \psi}{\partial y^2} - \frac{1}{K}\omega, \tag{2.11}$$

where $\mathrm{Re} = \alpha c a/\nu$ is Reynolds number, $K = k/a^2$ is the permeability allows by the porous medium, $\alpha = a/\lambda$ is wave number and $M = \sqrt{\sigma/\mu} B_o a$ corresponds he magnetic parameter known as Hartmann number. The boundary conditions (2.7) take the form

$$\left.\begin{aligned} \frac{\partial^2 \psi}{\partial y^2} = 0, \quad \frac{\partial \psi}{\partial x} = 0, \quad \text{at} \quad y = 0 \\ \frac{\partial \psi}{\partial y} = -1, \quad \frac{\partial \psi}{\partial x} = 2\pi\phi \sin 2\pi x, \quad \text{at } y = \eta(x) \end{aligned}\right\}. \tag{2.12}$$

$$\text{where } \eta(x) = 1 - \phi\cos(2\pi x)$$

The augmented constraints on introduced stream function ψ defined by $\psi = 0$ at $y = 0$ while at $y = \eta(x)$, $\psi = q$ as given by Lew et al. (1971) which are in consequence of the prescription constant rate of flow $q(= q^*/aC)$ in fixed frame at every cross-section. The dimensionless rate of flow in both frames are related by $Q = q + 1$, where $Q(= Q^*/aC)$ represents the time mean flow rate considered in moving frame. For slow flow rate the equations under the assumption of lubrication theory can be reduced which are presented by Takabatake et al. (1990).

2.2 Numerical Analysis

In order to solve the considered model numerically, the governing equations presented in Eqs. (2.10) and (2.11) with the boundary conditions contained by Eq. (2.12) are

numerically solved by using Galerkin weighted residual finite element method in the limited region of L(say) amount of waves that travels in a moving frame equipped with the two end sections in which we have assumed one is to be fixed while other is considered as moving wall. Continuity of flow allows as to compute the solution of governing system of equations as the approach of wave by wave taking single wave at a time, then interchanges to second and so on in the similar passion. In all such simulation cases, fast, less costly, highly convergent results have been achieved in about $2-4$ number of iterations. For the computation purpose, the domain is discretized into non-uniform mesh of six nodal quadratic triangle elements with the help of built-in pdetool in MATLAB. The stream function and vorticity function given in the governing equations is approximated by

$$\psi = \sum_{k=1}^{n} N_k \psi_k \, , \omega = \sum_{k=1}^{n} N_k \omega_k, \tag{2.13}$$

where ψ_k and ω_k are nodal approximation of ψ and ω at each element. The value of the upper limit in summation is taken $n = 6$ in our case as we incorporated quadratic six nodal triangular elements. The Galerkin weighted residual approach followed by finite element method is applied to the governing Eq. (2.10) and (2.11) given as

$$\int_{\Omega} w_1 \left(\alpha^2 \frac{\partial^2 \psi}{\partial x^2} + \frac{\partial^2 \psi}{\partial y^2} + \omega \right) d\Omega = 0, \tag{2.14}$$

$$\int_{\Omega} w_2 \left(\mathrm{Re} \left(\frac{\partial \psi}{\partial y} \frac{\partial \omega}{\partial x} - \frac{\partial \psi}{\partial x} \frac{\partial \omega}{\partial y} \right) - \left(\alpha^2 \frac{\partial^2 \omega}{\partial x^2} + \frac{\partial^2 \omega}{\partial x^2} \right) - M^2 \frac{\partial^2 \psi}{\partial y^2} + \frac{1}{K} \omega \right) d\Omega = 0, \tag{2.15}$$

in above equations w_1 and w_2 are weight function and Ω is the domain of the problem. After simplifying Eqs. (2.14) and (2.15), we obtain,

$$\int_{\Omega} \left(\alpha^2 \frac{\partial w_1}{\partial x} \frac{\partial \psi}{\partial x} + \frac{\partial w_1}{\partial y} \frac{\partial \psi}{\partial y} \right) d\Omega + \int_{\Omega} w_1 \omega \, d\Omega = \int_{\Gamma} w_1 \frac{\partial \psi}{\partial n} d\Gamma, \tag{2.16}$$

$$\int_{\Omega} \mathrm{Re} w_2 \left(\frac{\partial \psi}{\partial y} \frac{\partial \omega}{\partial x} - \frac{\partial \psi}{\partial x} \frac{\partial \omega}{\partial y} \right) d\Omega - \int_{\Omega} \left(\alpha^2 \frac{\partial w_2}{\partial x} \frac{\partial \omega}{\partial x} + \frac{\partial w_2}{\partial y} \frac{\partial \omega}{\partial y} \right) d\Omega +$$

$$M^2 \int_{\Omega} \frac{\partial w_2}{\partial y} \frac{\partial \psi}{\partial y} d\Omega + \frac{1}{K} \int_{\Omega} w_2 \omega d\Omega = \int_{\Gamma} w_2 \frac{\partial \omega}{\partial n} d\Gamma + M^2 \int_{\Gamma} w_2 \frac{\partial \psi}{\partial n} d\Gamma, \tag{2.17}$$

Upon introducing Eq. (2.13) into Eqs. (2.16) and (2.17) and considering the discretized domain, we have

$$-\sum_i B_{ki}^e \omega_i + \sum_i A_{ki}^e \psi_i = S_n^{k^e}, \tag{2.18}$$

$$\sum_i A_{ki}^e \omega_i + \mathrm{Re} \sum_i C_{kij}^e \psi_i \omega_i + M^2 \sum_i D_{ki}^e \psi_i + \frac{1}{K} \sum_i B_{ki}^e \omega_i = M^2 S_n^{k^e}, \tag{2.19}$$

where

$$\left.\begin{aligned} A_{ki}^{e} &= \int_{\Omega^e}\left(\alpha^2\frac{\partial N_k}{\partial x}\frac{\partial N_i}{\partial x}+\frac{\partial N_k}{\partial y}\frac{\partial N_i}{\partial y}\right)d\Omega \\ B_{ki}^{e} &= \int_{\Omega^e} N_k N_i\, d\Omega \\ C_{kij}^{e} &= \int_{\Omega^e} N_k\left(\frac{\partial N_i}{\partial y}\frac{\partial N_j}{\partial x}-\frac{\partial N_j}{\partial x}\frac{\partial N_i}{\partial y}\right)d\Omega \\ D_{ki}^{e} &= \int_{\Omega^e}\frac{\partial N_k}{\partial y}\frac{\partial N_i}{\partial y}d\psi d\omega \\ S_n^{k^e} &= \int_{\Gamma} N_k\bar{S}_k d\Gamma \end{aligned}\right\}. \tag{2.20}$$

The global system turns in the matrix form can be written as

$$\boldsymbol{KA} = \boldsymbol{F}, \tag{2.21}$$

in which

$$\begin{aligned} K_{ij} &= \begin{bmatrix} -B_{ki}^{e} & A_{ki}^{e} \\ A_{ki}^{e} + 1/K\, B_{ki}^{e} & \mathrm{Re}C_{kij}^{e}\omega_i + M^2 D_{ki}^{e} \end{bmatrix}, A_k = \begin{bmatrix} \omega_k \\ \psi_k \end{bmatrix}, \\ F &= \begin{bmatrix} S_n^{k^e} \\ M^2 S_n^{k^e} \end{bmatrix}. \end{aligned} \tag{2.22}$$

The obtained system of non-linear algebraic residual Eq. (2.21) for final solution is further exposed to Newton-Raphson method. This iterative process is iterated till the convergence criteria is achieved i.e. error between two iteration is 10^{-14}.

2.3 Analysis of the Pressure

Periodicity of the flow yields that the pressure and stress fields are only computed in the central region of the discretized domain that occupies only single wavelength. It is convenient to reduced pressure gradient from governing Navier-Stokes equations in dimensionless form

$$\frac{\partial p}{\partial x} = \mathrm{Re}\left(\frac{\partial^2\psi}{\partial y^2}\frac{\partial\psi}{\partial x}-\frac{\partial^2\psi}{\partial x\,\partial y}\frac{\partial\psi}{\partial y}\right)-\frac{\partial\omega}{\partial y}-M^2\left(\frac{\partial\psi}{\partial y}+1\right)-\frac{1}{K}\left(\frac{\partial\psi}{\partial y}+1\right), \tag{2.23}$$

$$\frac{\partial p}{\partial y} = \mathrm{Re}\alpha^2\left(\frac{\partial^2\psi}{\partial x^2}\frac{\partial\psi}{\partial y}-\frac{\partial^2\psi}{\partial x\,\partial y}\frac{\partial\psi}{\partial x}\right)-\alpha\frac{\partial\omega}{\partial x}-\frac{1}{K}\frac{\partial\psi}{\partial y}. \tag{2.24}$$

In the wave frame at center line $y = 0$, pressure-rise per wavelength is expressed as

$$\Delta p_\lambda = \int_0^\lambda \frac{dp}{dx}dx. \tag{2.25}$$

2.4 Validation

In this section, a comparison of the numerical results based on our code with the results of Jaffrin (1973), Takabatake et al. (1990) and Kumar and Naidu (1995) are sought. To this end, the curves of pressure rise per wavelength based on our solution is compared with the corresponding pressure rise per wavelength curves obtained through the solution of Jaffrin (1973); Takabatake et al. (1990) and Kumar and Naidu (1995) in **Figures 2.2-2.4**. It is observed that our results in the limiting case ($M = 0, 1/K = 0$) are in close agreement with corresponding result of Jaffrin (1973) and Kumar and Naidu (1995). The solution of Jaffrin (1973) is purely analytical and therefore it serves as a benchmark solution in the comparison. The solution of Takabatake et al. (1990) shows large deviation from the solution of Jaffrin (1973) and therefore it also deviates from our solution. With this validation, the confidence is therefore very high on the present FEM computations and therefore our analysis presented here is valid and valuable.

2.5 Results and Discussion

In this division, solution obtained by computations of the developed governing problem are presented through plots of velocity, contours of streamlines, and pressure rise per wavelength against involved parameters including Hartmann number M, Reynolds number Re, wave number α volume flow rate Q and amplitude ratio ϕ.

2.5.1 Velocity field

At a cross-section $x = 0$, the profiles of longitudinal velocity for several values of volume flow rate, Hartmann number, wave number, Reynolds number, permeability parameter and amplitude ratio are shown through **Figures 2.5-2.9**. It is perceived that longitudinal velocity upsurges with increasing the rate of volume flow over the whole cross-section. In contrast, the longitudinal velocity component decreases near the channel center $y = 0$ while it shows converse trend in the vicinity of the channel wall with increasing either of Reynolds number, wave number or permeability parameter. Moreover, the effects of increasing Hartmann number and amplitude ratio is to accelerate the flow near the channel center $y = 0$. It is further noted that for large values of Reynolds number, the longitudinal velocity achieves its maximum before the central plane $y = 0$. This observation is perhaps not reported in earlier studies and it may be attributed to strong inertial effects induced for large values of Reynolds number.

Moreover, long wavelength along with low Reynolds number theory is not able to predict such non-linear effects. The increase in the longitudinal velocity due to upsurge in the strength of the applied magnetic field is attributed to fact that magnetic body force excites the bulk motion due to peristalsis resulting in the flow acceleration near the channel center $y = 0$. This fact can also be verified by the examination of Eq. (2.23) which shows that the magnitude of magnetic force is direct proportional to the flow velocity. It is further noted from Eq. (2.23) that magnitude of resistance to flow offered by porous medium is inversely proportional to the longitudinal flow velocity. It is because of this fact that longitudinal flow velocity decrease with increasing the permeability parameter in vicinity of the channel center $y = 0$. To preserve the assumed flow rate, the flow velocity of the channel will upsurge. The decrease in longitudinal velocity near the channel center $y = 0$ with increasing Reynolds number is justified on the following grounds. Since Reynolds number is defined as the ratio of inertial forces over to the viscous force, higher values of Reynolds number corresponds to the situation of stronger inertial effects or compared to the viscous effects near the channel wall. In such circumstances, the flow accelerates near the solid wall to preserve the given flow rate, the flow velocity decreases, resulting in the flow deceleration near the channel center.

2.5.2 Trapping and vorticity

The contours of streamlines for presentation of the trapping phenomenon are shown in **Figures 2.10-2.14** for various values of time mean flow rate Q, permeability of porous medium K, Hartmann number M, wave number α, Reynolds number Re and amplitude ratio ϕ. **Figure 2.10** Shows that trapped bolus of fluid exists in the central region of the channel for lesser time mean flow rate Q. Moreover, trapped bolus moves toward the boundary wall with increasing time mean flow rate Q. These observations are in accordance with that of previous available studies based on lubrication approximation. The effect of Reynolds number on the trapping phenomenon can be detected through **Figure 2.11**. This figure clearly indicates non-trivial effect of increasing Reynolds number on trapping phenomenon. It is perceived that the circulation of trapped bolus increases with increasing Reynolds number. Again this is because of smaller viscous effect in comparison with the inertial effects. The effect of Hartmann number on trapping are elucidated in **Figure 2.12**. It is seen that the introduction of Lorentz force due to magnetic field causes a rise in the circulation of the trapped bolus of fluid. This

fact is strikingly different from what we observed from previous available studies based on lubrication approximation given in Takabatake et al. (1990); Fauci (1992) and Kumar and Naidu (1995). It is reported that Lorentz force due to magnetic field reduces the circulation of the trapped bolus of field. The effect of permeability parameter on trapped bolus of fluid can be observed through **Figure 2.13**. This figure reveals that peristaltic mixing due to circulation is also extensively dependent on the permeability parameter. In fact, much greater peristaltic mixing is realized in non-porous channel than that of porous-saturated channel. The contours of vorticity in wave frame for various values of permeability parameter are revealed through **Figure 2.14-2.16.** It is observed that vorticity is maximum near the peristaltic wall and it decreases by going towards the central region of the channel. For the lesser values of permeability parameter, the vorticity lines are analogous in form or shape to that of peristaltically moved boundary wall and lines of extreme vorticity are clustered in the vicinity of dilating part of the channel. However, the lines of maximum vorticity penetrate toward the center of the channel due to upsurge in permeability parameter. The effect of Reynolds number on vorticity are analogous to that of effects of permeability parameter. In contrast, the lines of maximum vorticity shifted toward the dilating part of the channel with increasing Hartmann number.

2.5.3 Pressure distribution

Figures 2.17-2.22 are displayed to illustrate the variation in the graphs of pressure rise per wavelength ΔP_λ for numerous values of involved parameters. **Figure 2.17** demonstrates the relationship between pressure rise per wavelength with the flow rate for different range of values of Reynolds number. Here, it is noted that for a fixed value of prescribed rate of flow Q, ΔP_λ increases with aggregated Reynolds number. The effects of electromagnetic forces that represents by Hartmann number on pressure rise per wavelength ΔP_λ in region of peristaltic pumping for a static value of flow rate are similar to the effects of Reynolds number as shown in **Figure 2.18**. On the other side, in the same region for a static value of flow rate, the behavior of pressure rise per wavelength ΔP_λ is decreasing with increasing the permeability of the saturated porous medium as shown in **Figure 2.19**.The influence prescribed by wave number α on ΔP_λ is shown in **Figure 2.20**. This figure indicates that the effect of α on ΔP_λ are analogous to the effect of the parameters Re and M. The plot of ΔP_λ versus $1/K$ for a specific

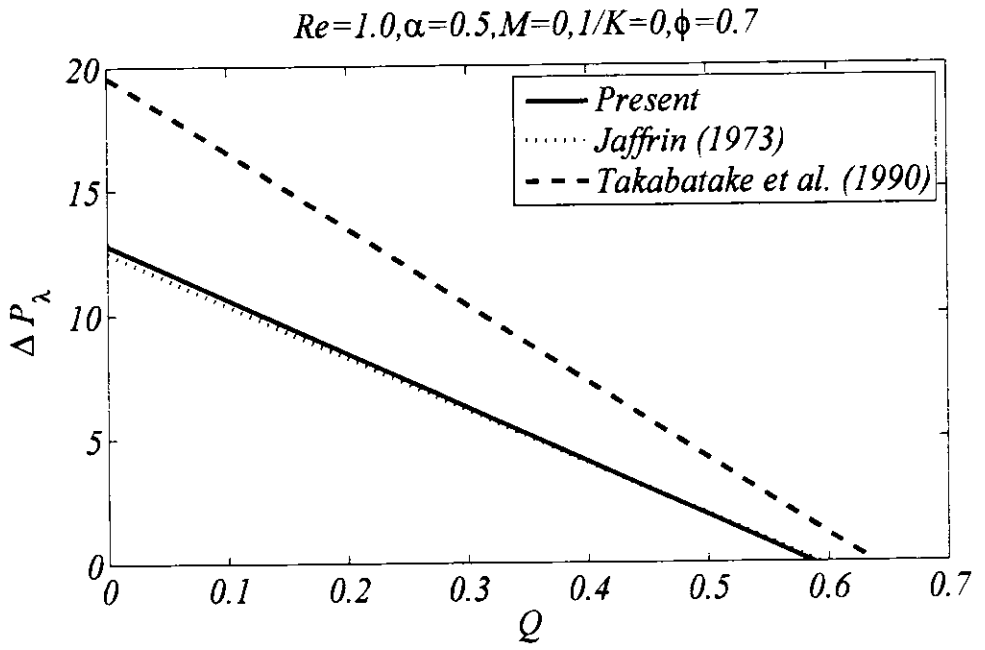

(a)

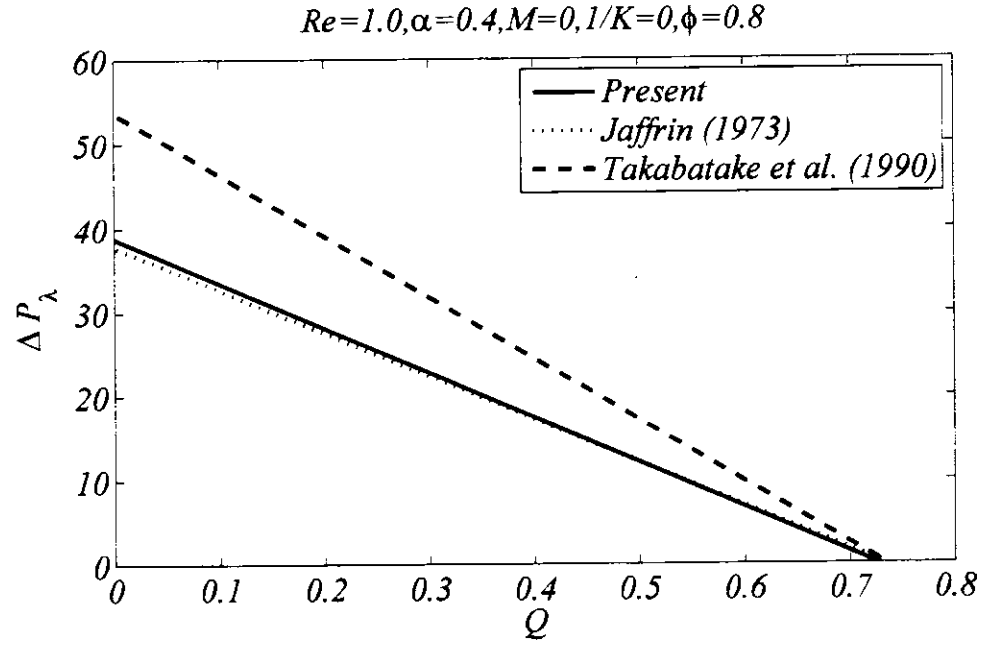

(b)

Figure 2.2: Comparison of pressure rise per wavelength with that of Jaffrin (1973) and Takabatake et al. (1990)

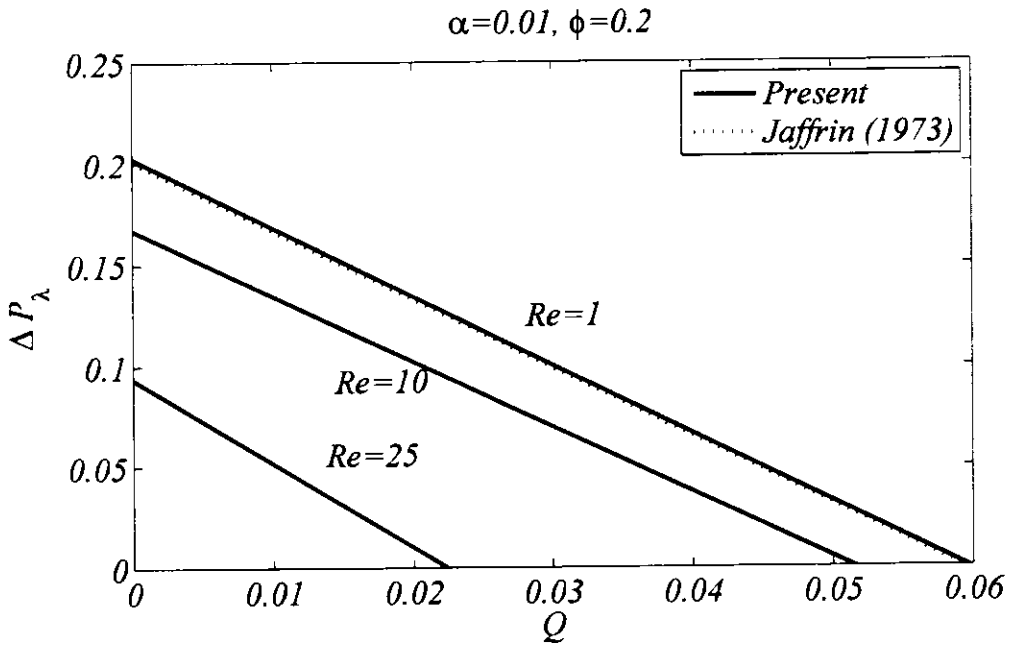

Figure 2.3: Pressure distribution for various values of the parameter *Re* along with the comparison with the available results of Jaffrin (1973)

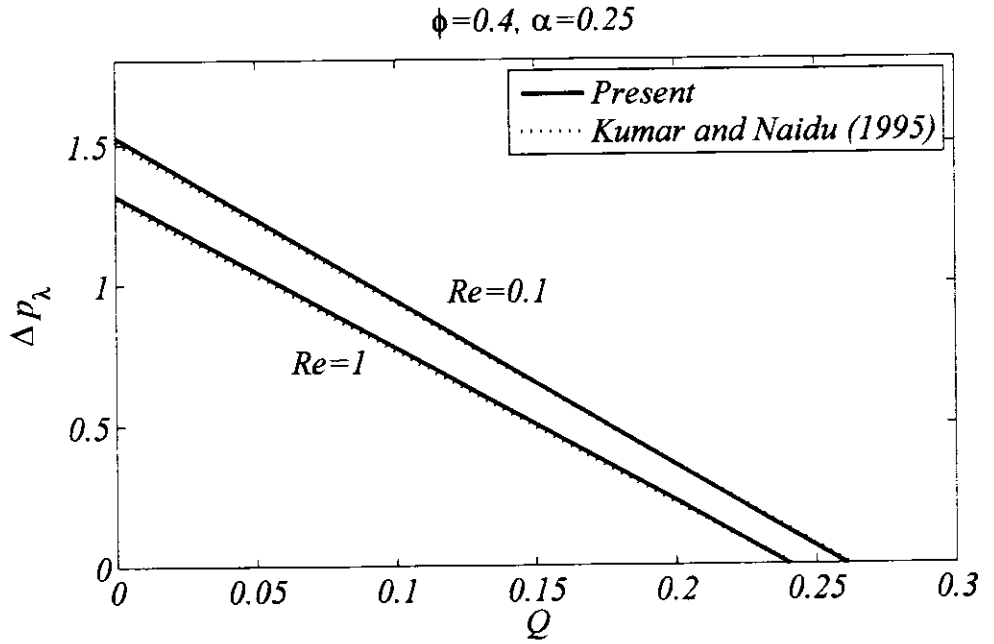

Figure 2.4: Pressure distribution for various values of the parameter Re along with the comparison with the available results of Kumar and Naidu (1995)

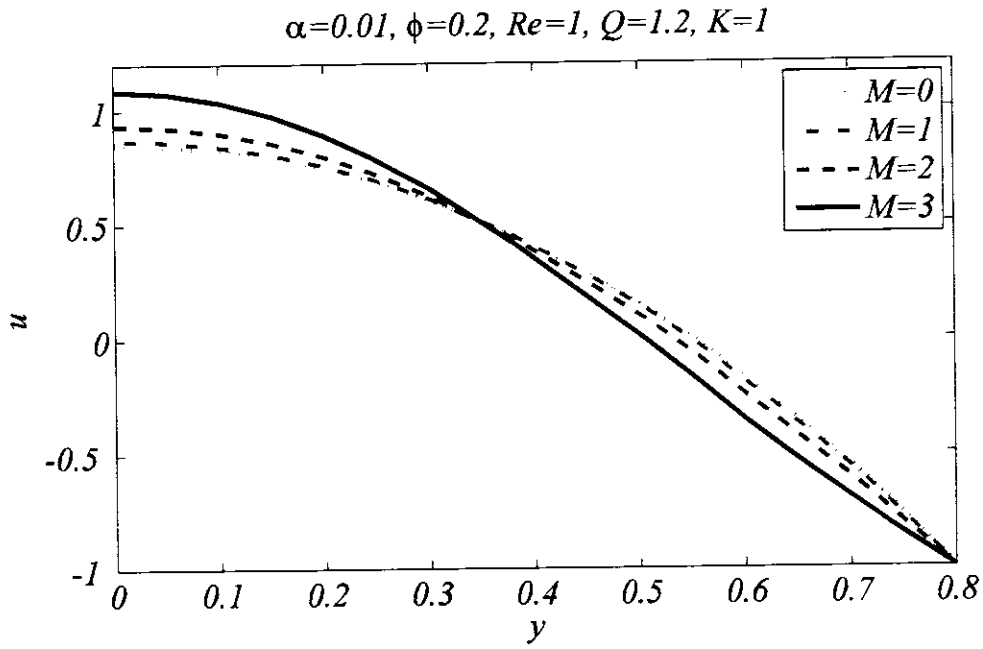

Figure 2.5: Graphs of longitudinal velocity distribution for various values of the parameter M against fixed values of other parameters

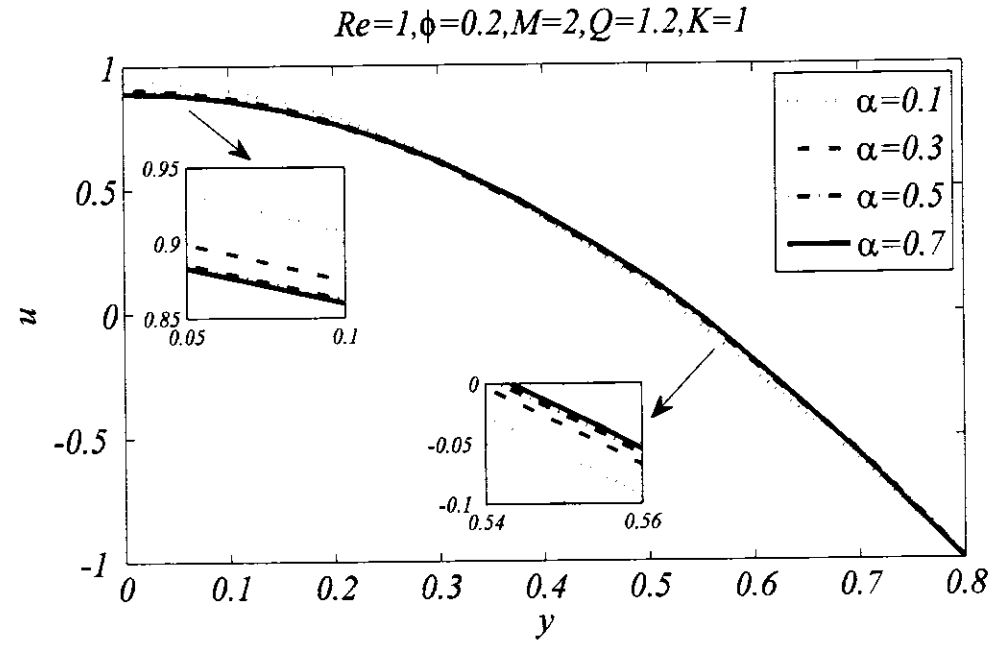

Figure 2.6: Graphs of longitudinal velocity distribution for various values of the parameter α against fixed values of other parameters

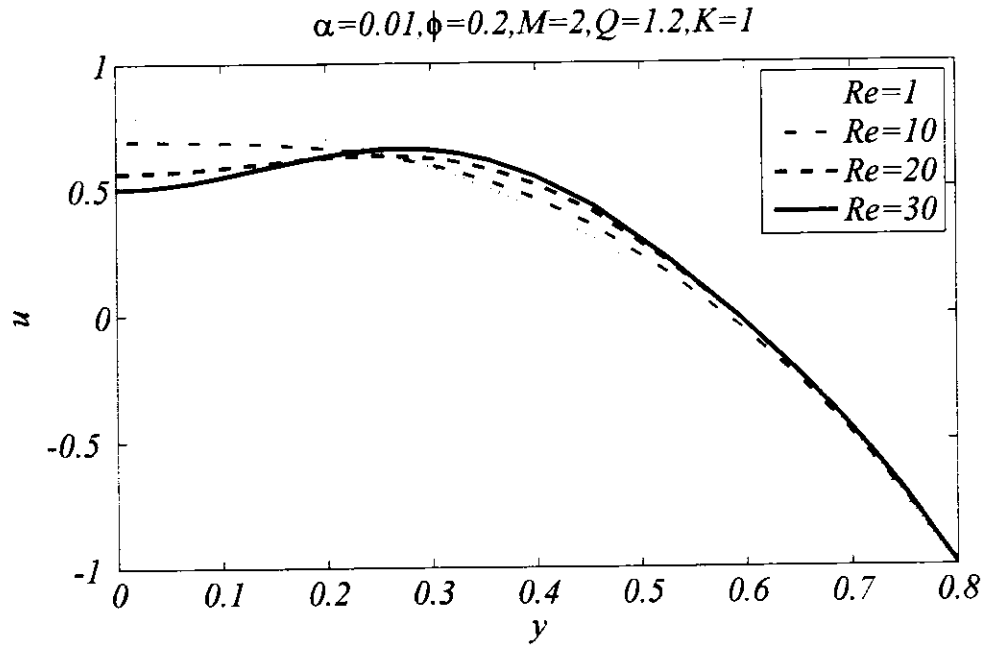

Figure 2.7: Graphs of longitudinal velocity distribution for various values of the parameter *Re* against fixed values of other parameters

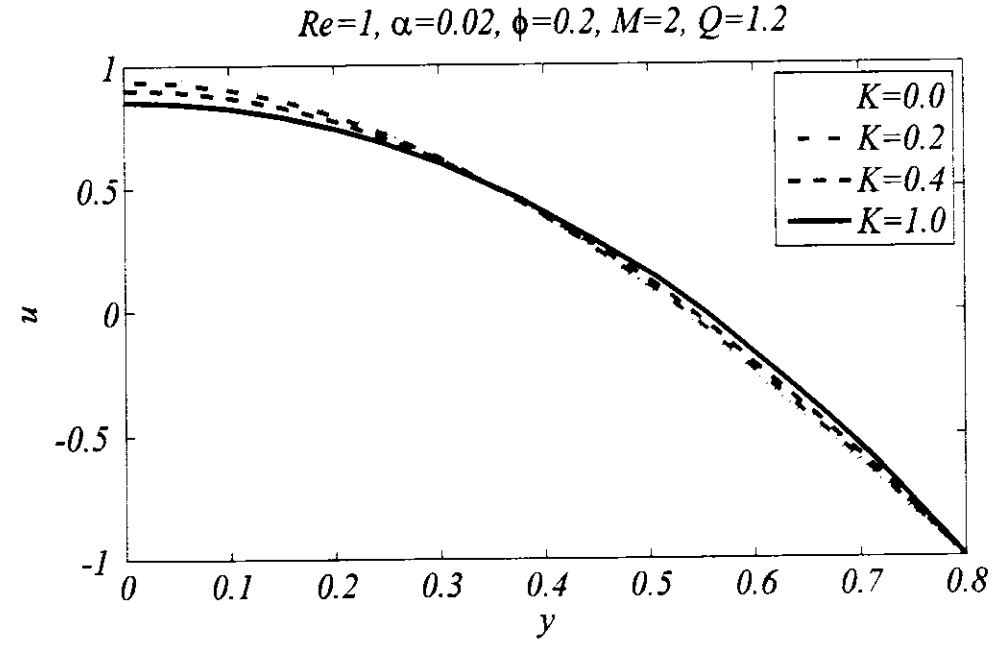

Figure 2.8: Graphs of longitudinal velocity distribution for various values of the parameter *K* against fixed values of other parameters

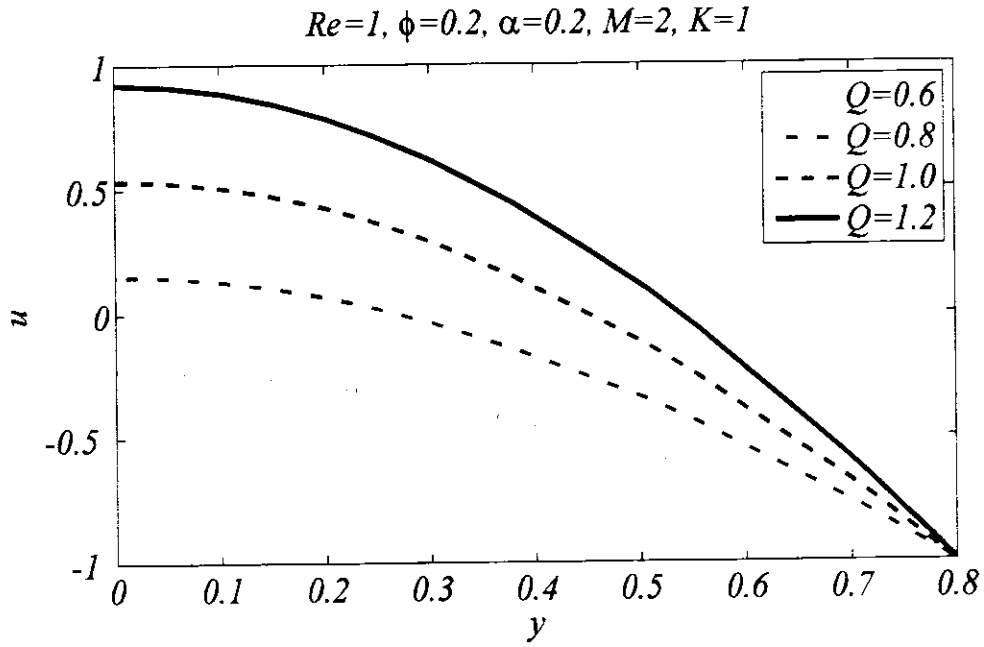

Figure 2.9: Graphs of longitudinal velocity distribution for various values of the parameter Q against fixed values of other parameters

values of flow rate belonging to co-pumping region where $Q > 0$ & $\Delta P_\lambda < 0$) is shown through **Figures 2.21 and 2.22** for different values of Re and M, respectively. It is observed that for this value of flow rate, ΔP_λ is negative against all the considered values of $1/K, M$ and Re which shows that the pressure supports the flow due to peristalsis. Moreover, the magnitude of backing provided by the pressure increases with an increase in both Reynolds number and Hartmann number, while it decreases with increase in the permeability of the porous medium.

(a)

(b)

(c)

(d)

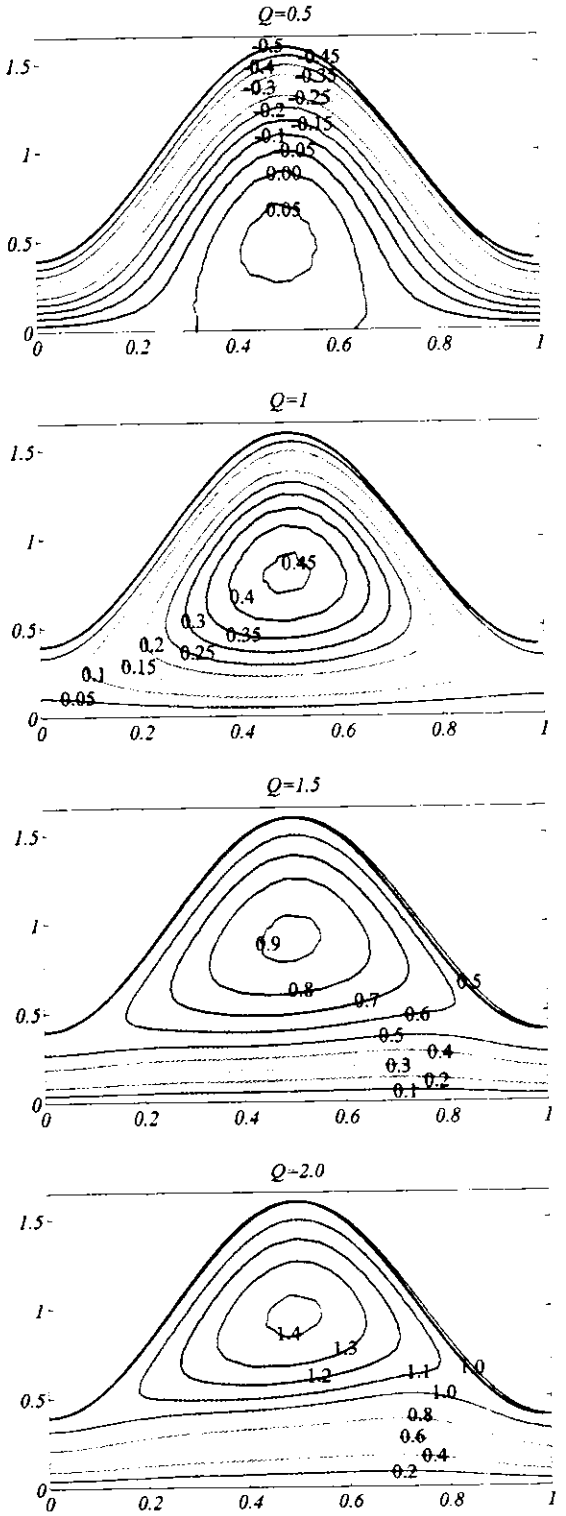

Figure 2.10: Variation of streamlines for various values of Q against $\mathrm{Re} = 1.0, M = 2.0, \alpha = 0.2, \phi = 0.6$ and $K = 1$ in wave frame

(a)

(b)

(c)

(d)

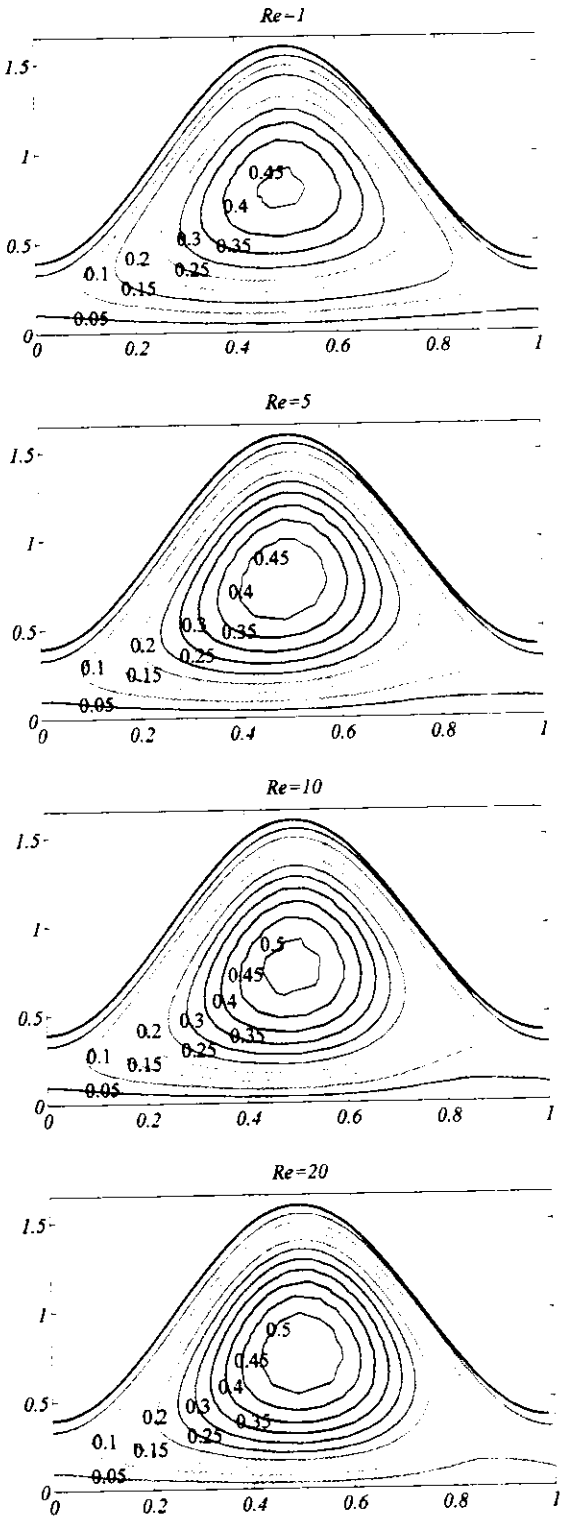

Figure 2.11: Variation of streamlines for various values of Re against $Q = 1.0, M = 2.0, \alpha = 0.2, \phi = 0.6$ and $K = 1$ in wave frame

(a)

(b)

(c)

(d)

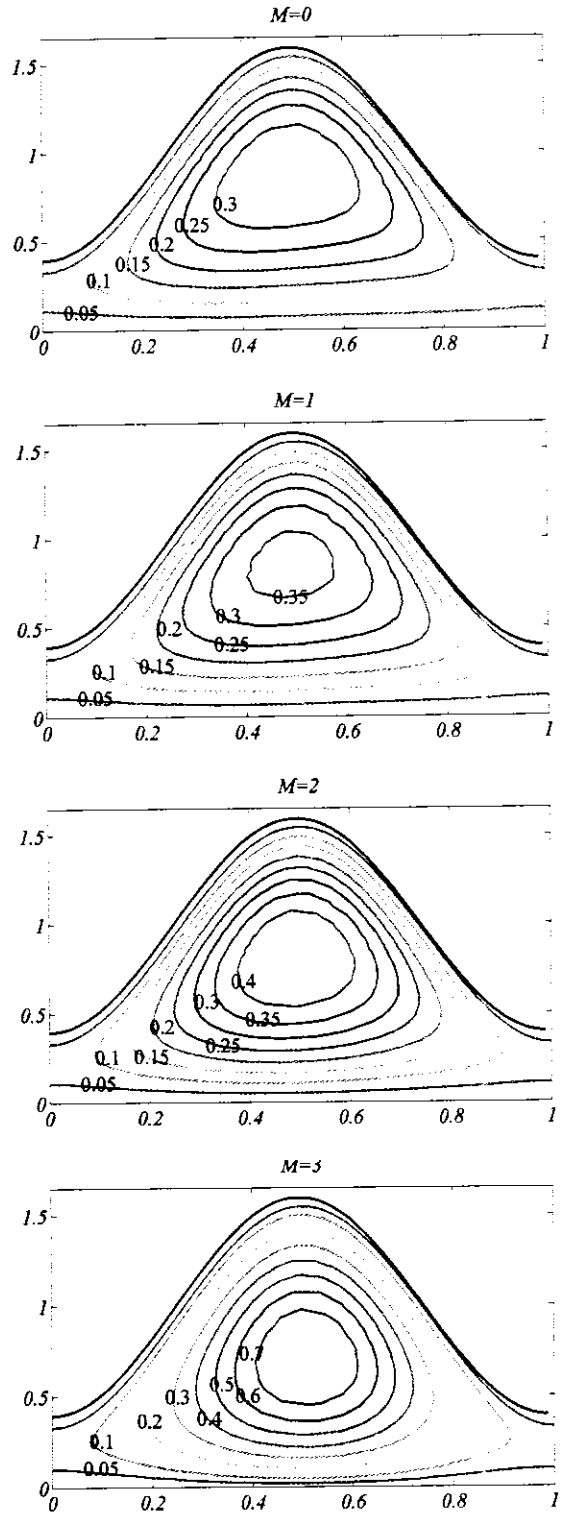

Figure 2.12: Variation of streamlines for various values of M against $Re = 1.0, Q = 1.0, \alpha = 0.2, \phi = 0.6$ and $K = 1$ in wave frame

(a)

(b)

(c)

(d)

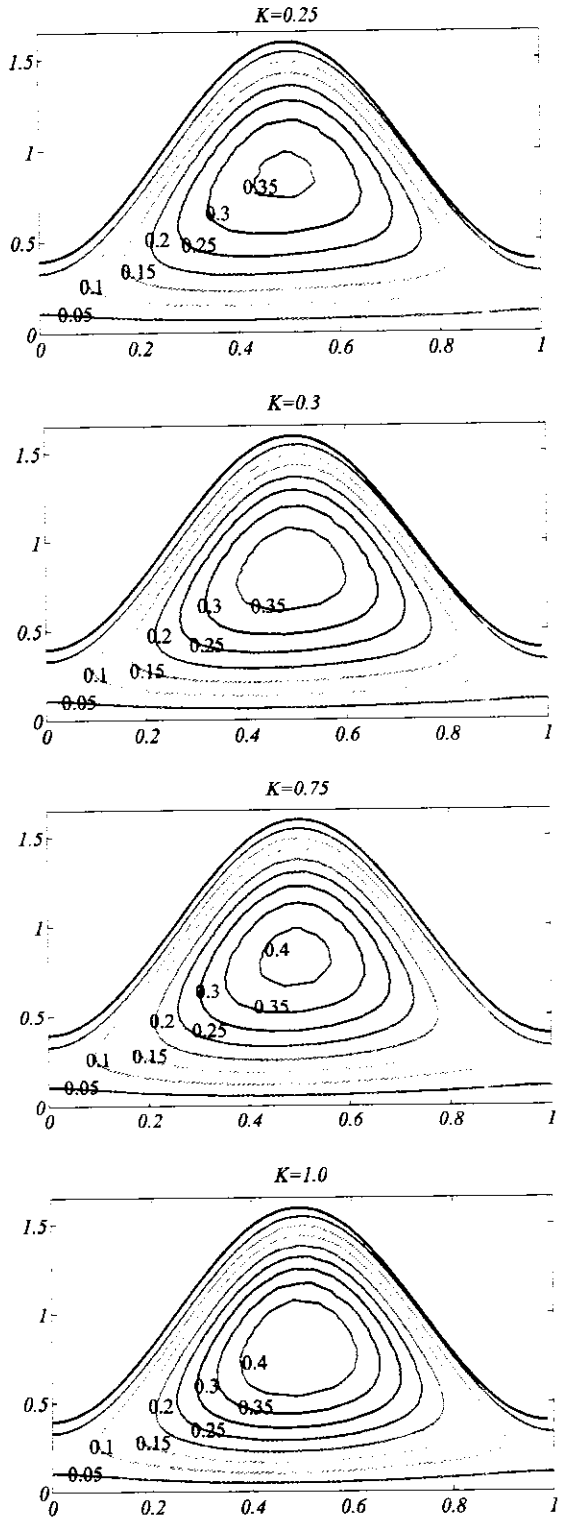

Figure 2.13: Variation of streamlines for various values of K against $\mathrm{Re} = 1.0, Q = 1.0, \alpha = 0.2, \phi = 0.6$ and $M = 2.0$ in wave frame

(a)

(b)

(c)

(d)

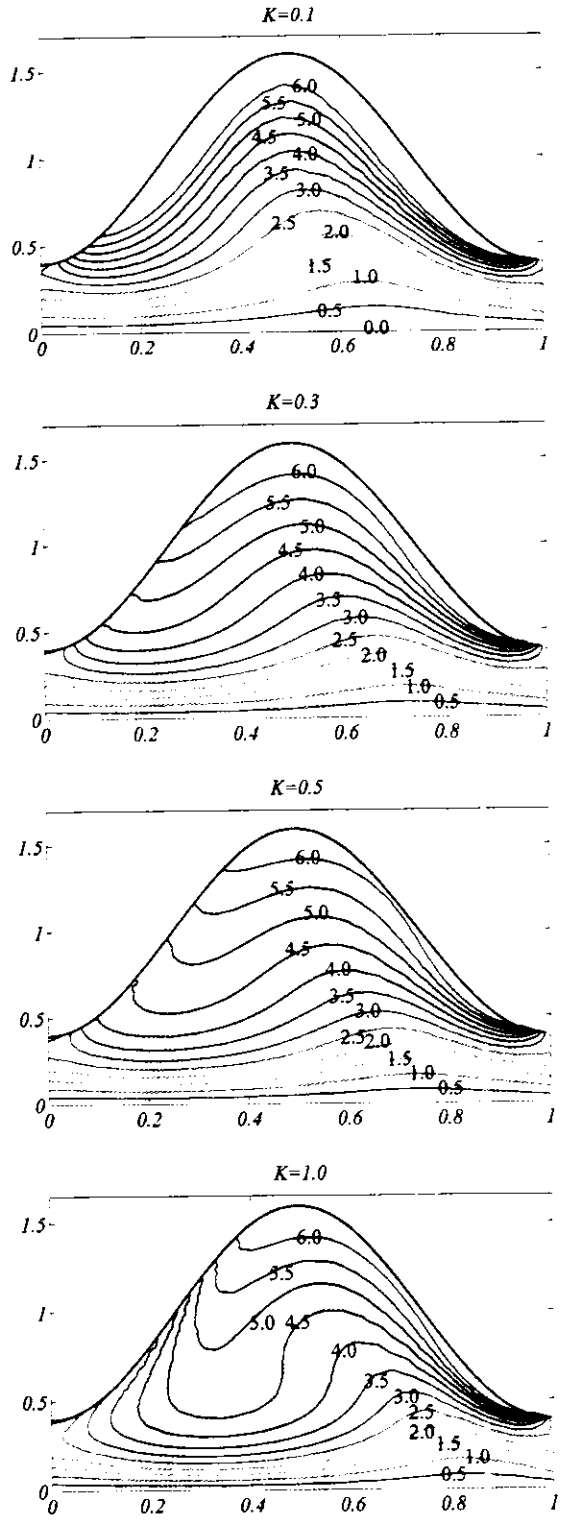

Figure 2.14: Variation of vorticity for various values of K against $\mathrm{Re} = 10, Q = 1.0, M = 2.0, \alpha = 0.5$ and $\phi = 0.6$

(a)

(b)

(c)

(d)

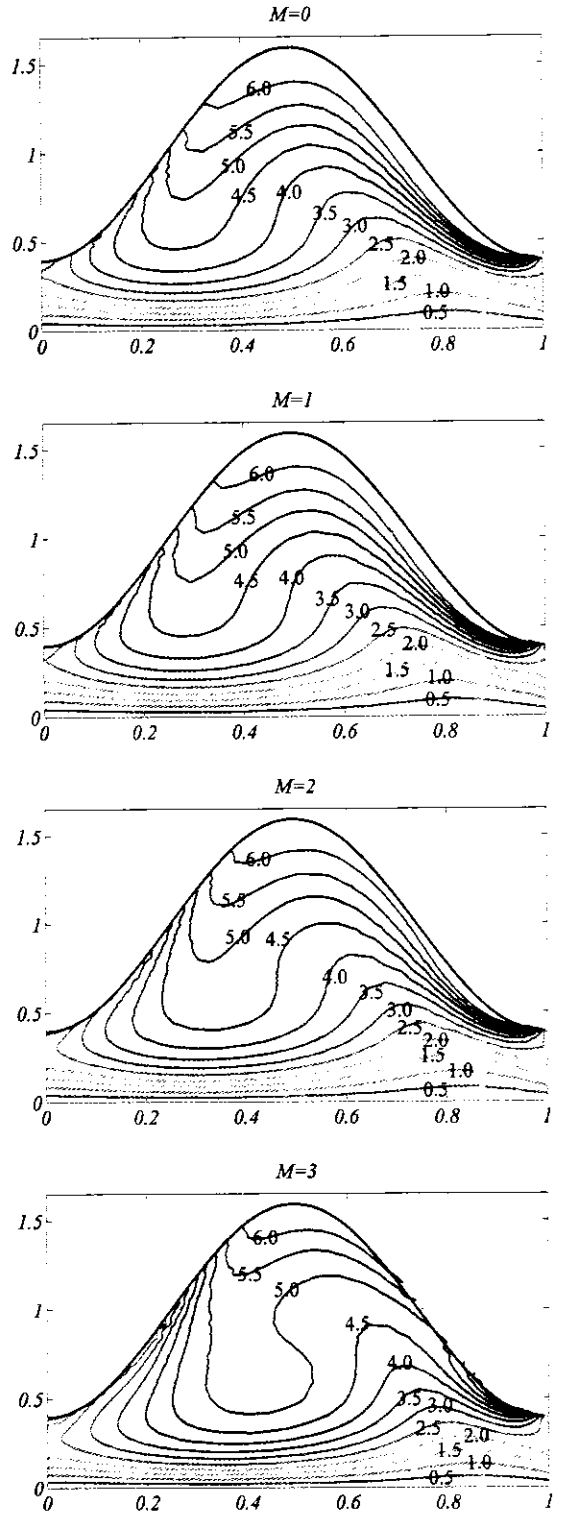

Figure 2.15: Variation of vorticity for various values of M against $Re = 10, Q = 1.0, \alpha = 0.5, \phi = 0.6$ and $K = 1$

(a)

(b)

(c)

(d)

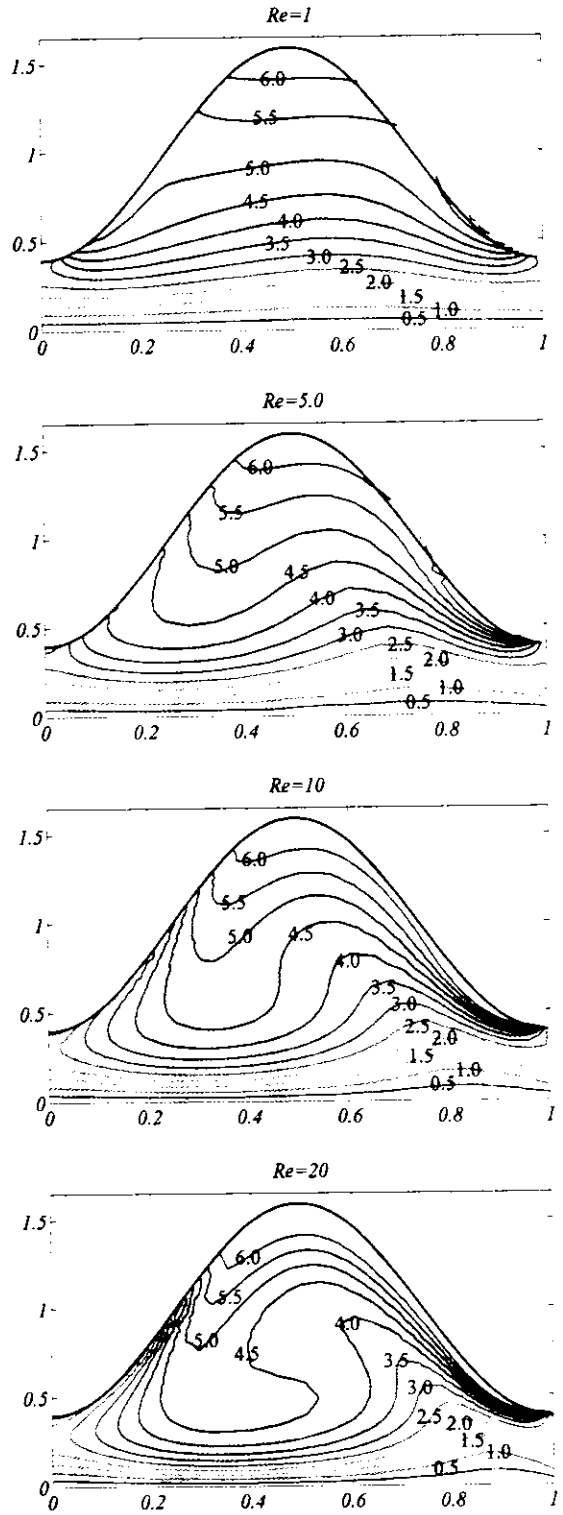

Figure 2.16: Variation of vorticity for various values of Re against $Q = 1.0, \alpha = 0.5, \mathrm{M} = 2.0\ \phi = 0.6$ and $K = 1$

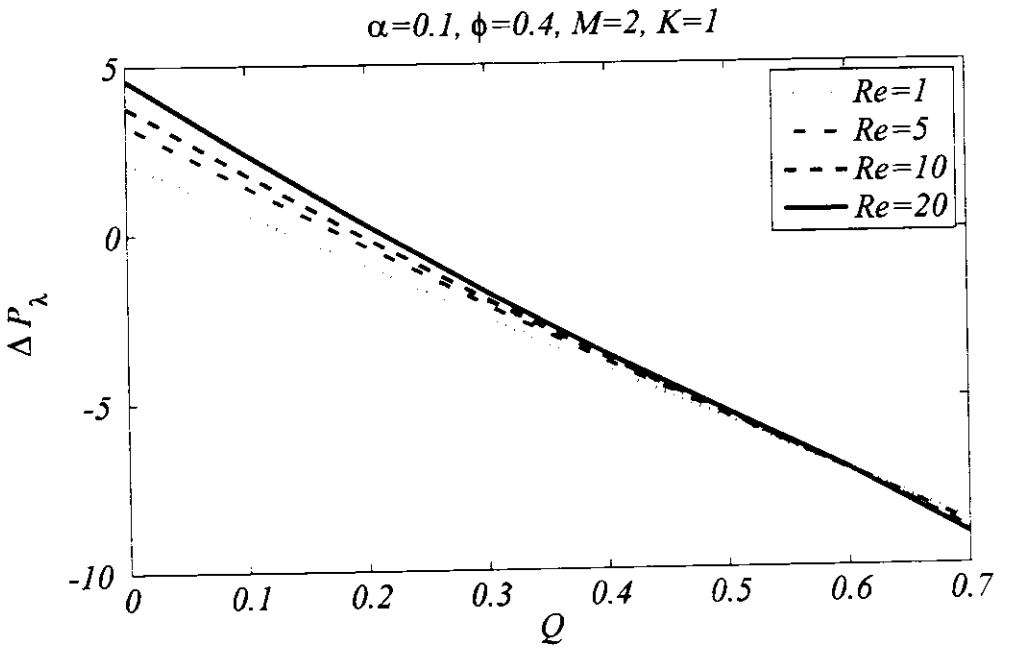

Figure 2.17: Pressure distribution for various values for Re

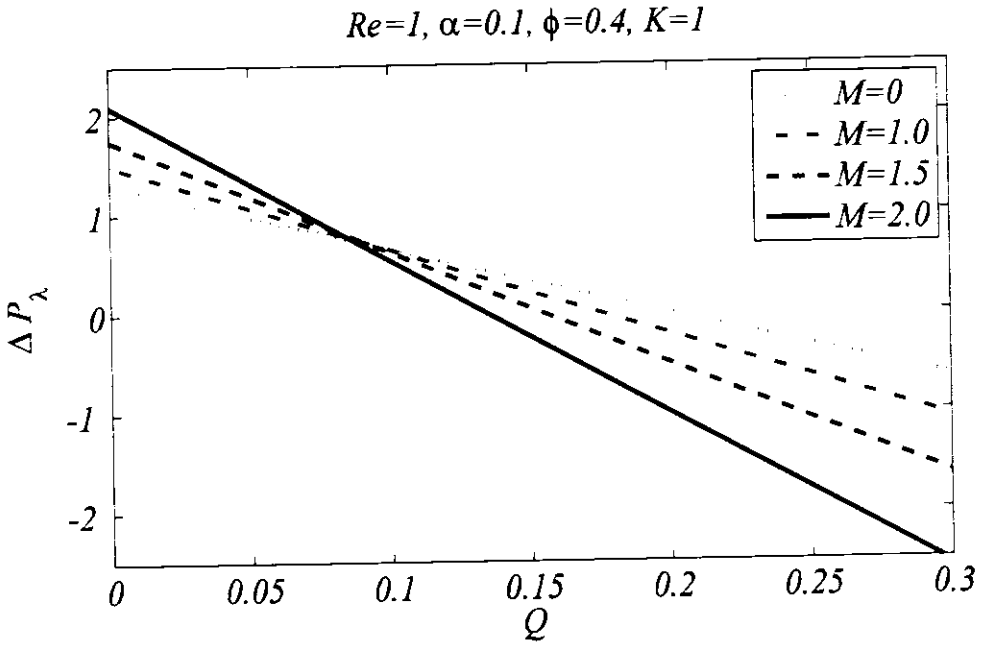

Figure 2.18: Pressure distribution for various values for M

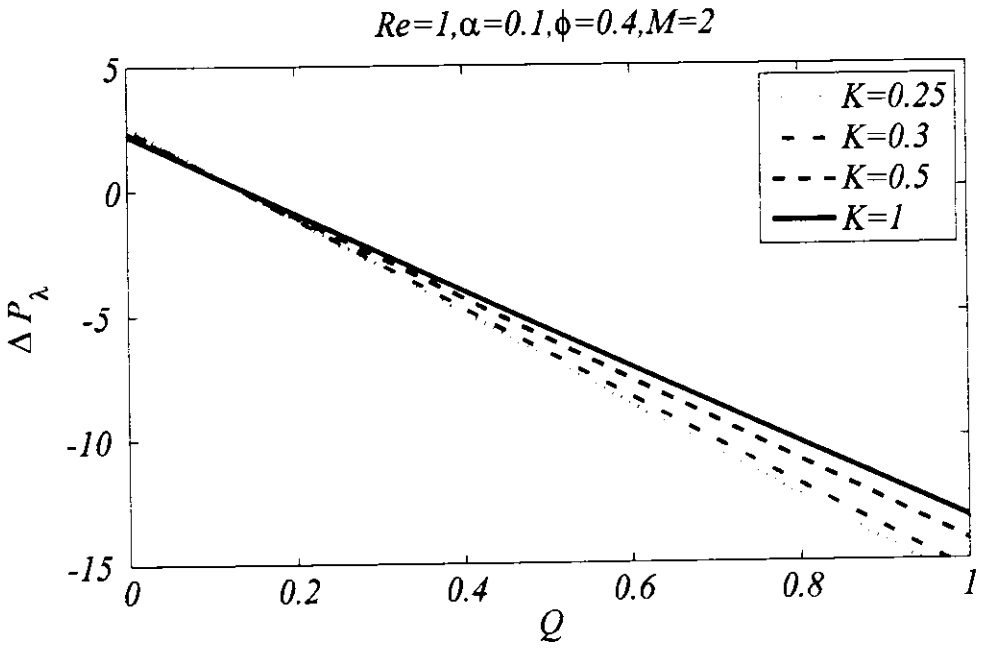

Figure 2.19: Pressure distribution for various values for K

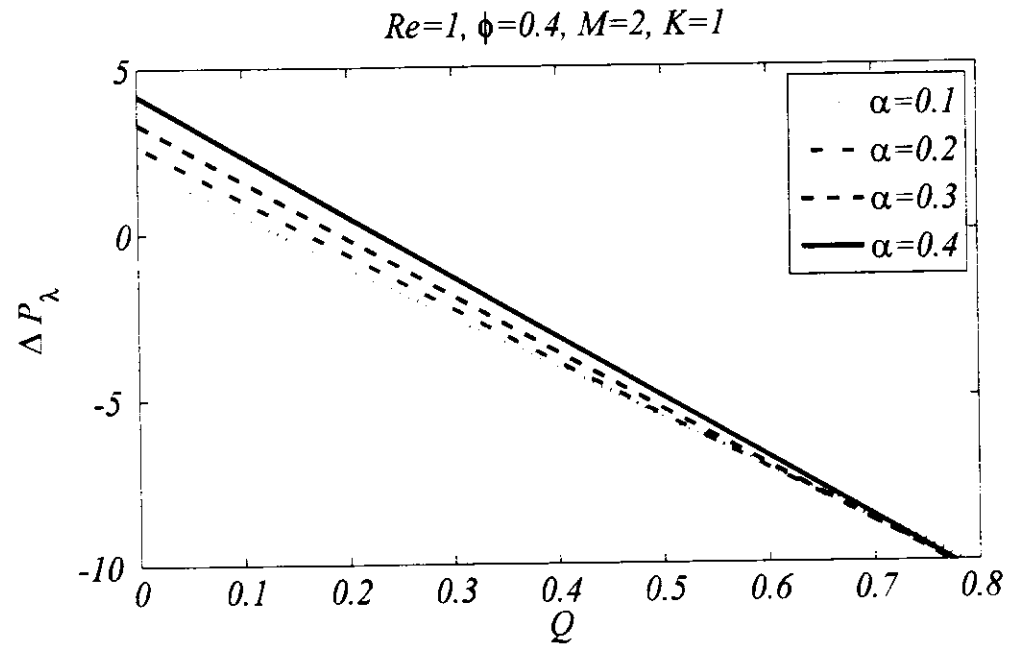

Figure 2.20: Pressure distribution for various values for α

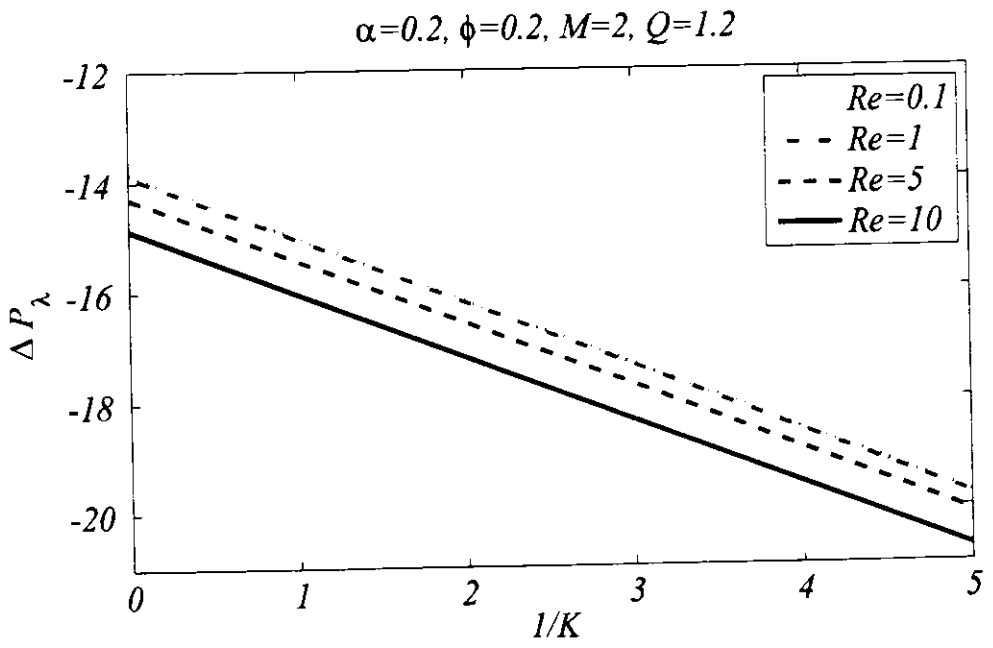

Figure 2.21: Pressure distribution for various values against $1/K$ at different Re

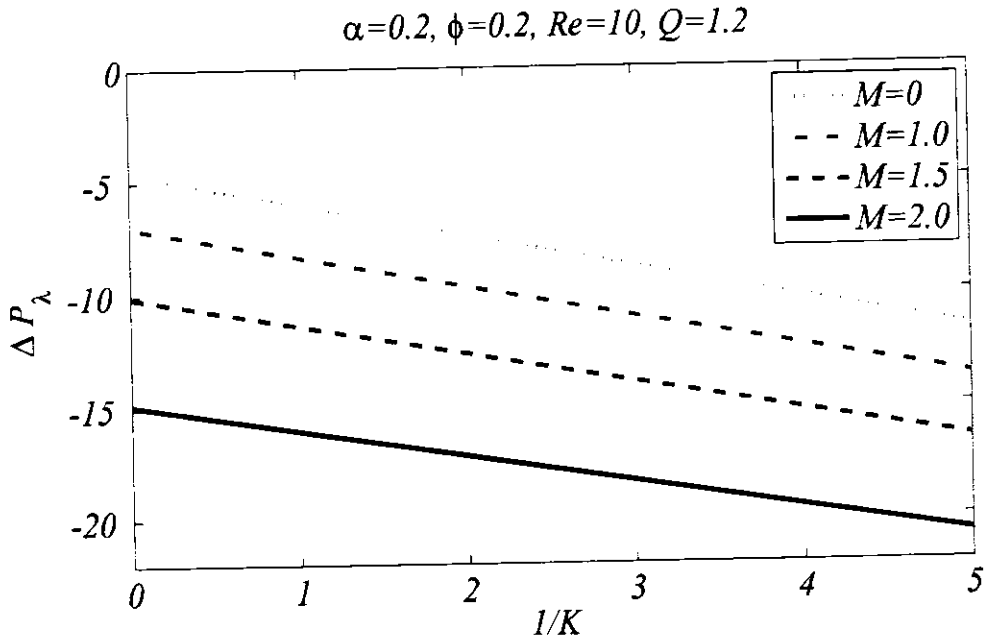

Figure 2.22: Pressure distribution for various values against $1/K$ at different M

2.6 Conclusions

The numerical study about the flow of Newtonian fluid passing through the channel under the inducement of applied magnetic field induced by progressive movement of the peristaltic waves is presented using finite element method. The obtained numerical results are compared with previous available results and an excellent correlation is achieved. The computations are carried out to obtain stream function and vorticity for arbitrary finite values of Reynolds number and wave number. The calculations of longitudinal velocity as well as pressure rise per wavelength are based on the post-processing of the results. It is found that the results obtained without employing long wavelength along with low Reynolds number assumptions are significantly different from that of based on long wavelength along with low Reynolds number assumptions. The obtained numerical results indicate that longitudinal velocity in vicinity of the central part of the channel $y = 0$ falls with increasing both Reynolds number and wave number. Moreover, for greater values of Reynolds number it achieves maximum value before the $y = 0$. The circulation of trapped bolus increases with increasing the Reynolds number. Most importantly, it is found different to that of previous results based on long wavelength along with low Reynolds numbers. The diffusion of vorticity from the boundaries to the channel center increases with increasing the permeability of the porous medium against the permeability parameter and Reynolds number while an opposite trend is noted with increasing Hartmann number. The inclusion of inertial in the force balance results in the reduction of pressure rise per wavelength in the pumping region.

Chapter 3

Mixed Convective Peristaltic Flow in a Vertical Channel

In this chapter, mixed convective heat transfer analysis is presented in the study of peristaltic flow passing through the vertical channel. Mathematical modeling of governing equations are presented in which heat generation term is introduced in the energy equation. The set of nonlinear partial differential equations are exposed to Galerkin's formulated finite element method to obtain the numerical results. The assumptions of long wavelength and low Reynolds number are neglected to present the role of inertial forces in the heat transfer analysis of peristaltic flow. The results obtained are validated with available results in literature and presented through graphs with different suitable ranges of the parameters involved in the modelled equations.

3.1 Problem Formulation

Consider the motion of Newtonian fluid through a vertical channel having inner width size $2d$. The flow is assumed in such a way that the propagation of waves is along the x −axis with velocity c and y −axis is taken normal to the channel. The peristaltic wall of channel is assumed to have some temperature T_1 and follows the sinusoidal wave shape represented by Eq. (2.1). The coordinates of velocity, pressure and temperature in fixed and moving frame of reference are related by set of expression given in Eq. (2.2) and Eq. (3.1)

$$p = p^*, \quad T^* = T_1, \tag{3.1}$$

In fixed frame of reference, the continuity, momentum and energy equations for the assumed problem are

$$\frac{\partial U}{\partial X} + \frac{\partial V}{\partial Y} = 0, \tag{3.2}$$

$$\rho\left(\frac{\partial U}{\partial t} + U\frac{\partial U}{\partial X} + V\frac{\partial U}{\partial Y}\right) = -\frac{\partial p}{\partial X} + \mu\left(\frac{\partial^2 U}{\partial X^2} + \frac{\partial^2 U}{\partial Y^2}\right) + \rho g\beta_T(T - T_0), \tag{3.3}$$

$$\rho\left(\frac{\partial V}{\partial t} + U\frac{\partial V}{\partial X} + V\frac{\partial V}{\partial Y}\right) = -\frac{\partial p}{\partial Y} + \mu\left(\frac{\partial^2 V}{\partial X^2} + \frac{\partial^2 V}{\partial Y^2}\right), \tag{3.4}$$

$$\rho c_p \left(\frac{\partial U}{\partial t} + U\frac{\partial T}{\partial X} + V\frac{\partial T}{\partial Y}\right) = \kappa^* \left(\frac{\partial^2 T}{\partial X^2} + \frac{\partial^2 T}{\partial Y^2}\right) + Q_0, \tag{3.5}$$

in which μ is the viscosity ρ is the density, g is the acceleration caused by gravity, β_T is thermal expansion coefficient, c_p is specific heat at constant pressure, κ^* is the thermal conductivity and Q_0 represents constant heat generation within the flow domain.

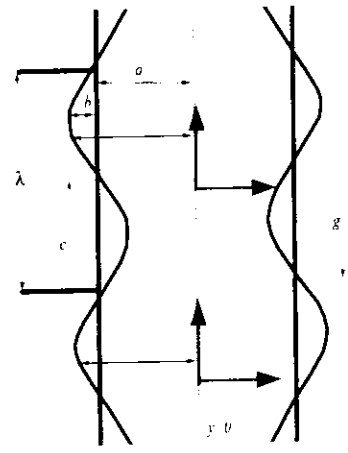

Figure 3.1: The geometry of considered two-dimensional peristaltic channel.

The boundary conditions that are imposes on the problem are

$$V = 0, \quad \frac{\partial U}{\partial Y} = 0, \quad \frac{\partial T}{\partial Y} = 0 \quad \text{at} \quad Y = 0, \tag{3.6}$$

$$U = 0 \quad V = \frac{\partial H}{\partial T}, \quad T = T_1 \quad \text{at} \quad Y = H. \tag{3.7}$$

Equations that govern the flow in wave frame are as follows

$$\frac{\partial u^*}{\partial x^*} + \frac{\partial v^*}{\partial y^*} = 0, \tag{3.8}$$

$$\rho\left(u^*\frac{\partial u^*}{\partial x^*} + v^*\frac{\partial u^*}{\partial y^*}\right) = -\frac{\partial p^*}{\partial x^*} + \mu\left(\frac{\partial^2 u^*}{\partial x^{*2}} + \frac{\partial^2 u^*}{\partial y^{*2}}\right) + \rho g \beta_T (T^* - T_0), \tag{3.9}$$

$$\rho\left(u^*\frac{\partial v^*}{\partial x^*} + v^*\frac{\partial v^*}{\partial y^*}\right) = -\frac{\partial p^*}{\partial y^*} + \mu\left(\frac{\partial^2 v^*}{\partial x^{*2}} + \frac{\partial^2 v^*}{\partial y^{*2}}\right), \tag{3.10}$$

$$\rho c_p \left(u^*\frac{\partial T^*}{\partial x^*} + v^*\frac{\partial T^*}{\partial y^*}\right) = \kappa^* \left(\frac{\partial^2 T^*}{\partial x^{*2}} + \frac{\partial^2 T^*}{\partial y^{*2}}\right) + Q_0. \tag{3.11}$$

The configuration of the considered peristaltic wall can be written as given in Eq. (2.6) and the condition of no slip and the symmetry condition on $y^* = 0$ & $y^* = \eta(x^*)$ respectively can be specified by

$$v^* = 0, \quad \frac{\partial u^*}{\partial y^*} = 0, \qquad \frac{\partial T^*}{\partial y^*} = 0 \quad \text{at} \quad y^* = 0, \tag{3.12}$$

$$u^* = -c, \quad v^* = -\frac{2\pi bc}{\lambda}\sin\left(\frac{2\pi x^*}{\lambda}\right), \quad T^* = T_1 \quad \text{at} \quad y^* = \eta(x^*). \tag{3.13}$$

Defining new variables along with defined in Eq. (2.8)

$$\mathrm{Re} = \frac{ca}{\nu}\alpha, \beta = \frac{Q_0 a^2}{\kappa^*(T_1 - T_0)}, \theta = \frac{T^* - T_0}{T_1 - T_0}, Gr = \frac{\rho g a \beta (T_1 - T_0)}{\mu c}, \mathrm{Pr} = \frac{\mu c}{k^*}. \tag{3.14}$$

in Eqs. (3.8) – (3.11), we get the new form

$$\alpha^2 \frac{\partial^2 \psi}{\partial x^2} + \frac{\partial^2 \psi}{\partial y^2} = -\omega, \tag{3.15}$$

$$\mathrm{Re}\left(\frac{\partial \psi}{\partial y}\frac{\partial \omega}{\partial x} - \frac{\partial \psi}{\partial x}\frac{\partial \omega}{\partial y}\right) = \nabla^2 \omega - Gr\frac{\partial \theta}{\partial y}, \tag{3.16}$$

$$\mathrm{RePr}\left(\frac{\partial \psi}{\partial y}\frac{\partial \theta}{\partial x} - \frac{\partial \psi}{\partial x}\frac{\partial \theta}{\partial y}\right) = \nabla^2 \theta + \beta, \tag{3.17}$$

where Gr symbolized Grashof number, β symbolized heat generation parameter and Pr symbolized Prandtl number. The boundary conditions defines in the form of $\psi(x, y)$ are as follows

$$\begin{aligned} &\psi = 0, \quad \frac{\partial^2 \psi}{\partial y^2} = 0, \quad \frac{\partial \psi}{\partial x} = 0, \qquad \frac{\partial \theta}{\partial y} = 0 \quad \text{at} \quad y = 0, \\ &\psi = q, \quad \frac{\partial \psi}{\partial y} = -1, \quad \frac{\partial \psi}{\partial x} = 2\pi\phi \sin 2\pi x, \quad \theta = 1 \quad \text{at} \quad y = \eta(x) \end{aligned} \tag{3.18}$$

where

$$u = \frac{\partial \psi}{\partial y}, v = -\alpha\frac{\partial \psi}{\partial x}, \omega = \alpha\frac{\partial v}{\partial x} - \frac{\partial u}{\partial y} \text{ and } \nabla^2 = \alpha^2\frac{\partial^2}{\partial x^2} + \frac{\partial^2}{\partial y^2}. \tag{3.19}$$

3.2 Numerical Analysis

In the previous sections we have modeled the governing equations which are valid for non-zero Reynolds and wave numbers and cannot be transformed to ordinary differential equations. Finite element method has been preferred to other methods due to its several advantages to obtain the solution of nonlinear system of partial differential equations. The foremost advantage of finite element method is that it works with non-uniform mesh which results in more accurate numerical approximations in particular when you are dealing with complex geometries and irregular boundary conditions. It provides the user liberty to choose the shape functions and types of elements according to the problem. This approach returns more accurate solutions with less computational cost. To deal with the partial differential equations, finite element method of Gelerkin's

approach is applied to solve Eqs. (3.15)-(3.17) subject to the boundary conditions (3.18) in any finite region of L(say) number of waves in a refrernce of wave frame having two end sections with one fixed while the other one is moving boundary. In all the cases, the computed results are highly convergent and satisfy the tolerance of $\varepsilon_\psi = \varepsilon_\omega = 10^{-14}$and $\varepsilon_\theta = 10^{-13}$. The numerical computations are made by using non-uniform meshing of quadratic elements with the help of pdetool available in MATLAB. The stream function, vorticity and temperature functions are approximated by function given in Eq. (2.13) and Eq. (3.20)

$$\theta = \sum_{k=1}^{n} N_k \theta_k, \tag{3.20}$$

in which θ_k are element nodal approximation of θ. The Galerkin finite element is endorsed to governing Eqs. (3.15) - (3.17) as follows

$$\int_\Omega w_1 \left(\alpha^2 \frac{\partial^2 \psi}{\partial x^2} + \frac{\partial^2 \psi}{\partial y^2} + \omega\right) d\Omega = 0, \tag{3.21}$$

$$\int_\Omega w_2 \left(\mathrm{Re}\left(\frac{\partial \psi}{\partial y}\frac{\partial \omega}{\partial x} - \frac{\partial \psi}{\partial x}\frac{\partial \omega}{\partial y}\right) - \left(\alpha^2 \frac{\partial^2 \omega}{\partial x^2} + \frac{\partial^2 \omega}{\partial y^2}\right) + Gr\frac{\partial \theta}{\partial y}\right) d\Omega = 0, \tag{3.22}$$

$$\int_\Omega w_3 \left(\mathrm{RePr}\left(\frac{\partial \psi}{\partial y}\frac{\partial \theta}{\partial x} - \frac{\partial \psi}{\partial x}\frac{\partial \theta}{\partial y}\right) - \left(\alpha^2 \frac{\partial^2 \theta}{\partial x^2} + \frac{\partial^2 \theta}{\partial y^2}\right) - \beta\right) d\Omega = 0, \tag{3.23}$$

in equations w_1, w_2 and w_3 are symbolized the weight functions and Ω is the integral domain. After simplifying Eqs. (3.21) to (3.23), we obtain

$$\int_\Omega \left(\alpha^2 \frac{\partial w_1}{\partial x}\frac{\partial \psi}{\partial x} + \frac{\partial w_1}{\partial y}\frac{\partial \psi}{\partial y}\right) d\Omega - \int_\Omega w_1 \omega \, d\Omega = \int_\Gamma w_1 \frac{\partial \psi}{\partial n} d\Gamma, \tag{3.24}$$

$$\int_\Omega \mathrm{Re} w_2 \left(\frac{\partial \psi}{\partial y}\frac{\partial \omega}{\partial x} - \frac{\partial \psi}{\partial x}\frac{\partial \omega}{\partial y}\right) d\Omega + \int_\Omega \left(\alpha^2 \frac{\partial w_2}{\partial x}\frac{\partial \omega}{\partial x} + \frac{\partial w_2}{\partial y}\frac{\partial \omega}{\partial y}\right) d\Omega + Gr \int_\Omega w_2 \frac{\partial \theta}{\partial y} d\Omega = \int_\Gamma w_2 \frac{\partial \omega}{\partial n} d\Gamma, \tag{3.25}$$

$$\int_\Omega \mathrm{RePr}\, w_3 \left(\frac{\partial \psi}{\partial y}\frac{\partial \theta}{\partial x} - \frac{\partial \psi}{\partial x}\frac{\partial \theta}{\partial y}\right) d\Omega + \int_\Omega \left(\alpha^2 \frac{\partial w_3}{\partial x}\frac{\partial \theta}{\partial x} + \frac{\partial w_3}{\partial y}\frac{\partial \theta}{\partial y}\right) d\Omega - \int_\Omega w_3 \beta d\Omega = \int_\Gamma w_3 \frac{\partial \theta}{\partial n} d\Gamma. \tag{3.26}$$

By considering the discretized domain, we put Eqs. (2.13) and (3.20) in (3.24)-(3.26) to get

$$-\sum_i B_{ki}^e \omega_i + \sum_i A_{ki}^e \psi_i = S_n^{k^e}, \tag{3.27}$$

$$\sum_i A_{ki}^e \omega_i + \mathrm{Re} \sum_i C_{kij}^e \psi_i \omega_i + Gr \sum_i B1_{ki}^e \theta_i = S_n^{k^e}, \tag{3.28}$$

$$\sum_i A^e_{ki}\theta_i + \mathrm{RePr}\sum_i C^e_{kij}\psi_i\theta_i = S^{k^e}_n + \beta S^{k^e}, \tag{3.29}$$

where

$$\left.\begin{aligned} A^e_{ki} &= \int_{\Omega^e}\left(\alpha^2\frac{\partial N_k}{\partial x}\frac{\partial N_i}{\partial x}+\frac{\partial N_k}{\partial y}\frac{\partial N_i}{\partial y}\right)d\Omega \\ B^e_{ki} &= \int_{\Omega^e} N_k N_i\, d\Omega \\ B1^e_{ki} &= \int_{\Omega^e} N_k\frac{\partial N_i}{\partial y}\,d\Omega \\ C^e_{kij} &= \int_{\Omega^e} N_k\left(\frac{\partial N_i}{\partial y}\frac{\partial N_j}{\partial x}-\frac{\partial N_j}{\partial x}\frac{\partial N_i}{\partial y}\right)d\Omega \\ D^e_{ki} &= \int_{\Omega^e}\frac{\partial N_k}{\partial y}\frac{\partial N_i}{\partial y}\,d\psi d\omega, \\ S^{k^e}_n &= \int_\Gamma N_k\bar{S}_k d\Gamma \\ S^{k^e} &= \int_\Gamma N_k d\Gamma \end{aligned}\right\}. \tag{3.30}$$

The global system takes the following form of matrix

$$\boldsymbol{KA} = \boldsymbol{F}, \tag{3.31}$$

where

$$K_{ij} = \begin{bmatrix} -B^e_{ki} & A^e_{ki} & 0 \\ A^e_{ki} & \mathrm{Re}C^e_{kij}\omega_i & GrB1^e_{ki} \\ 0 & \mathrm{RePr}C^e_{kij}\theta_i & A^e_{ki} \end{bmatrix}, A_k = \begin{bmatrix}\omega_k \\ \psi_k \\ \theta_k\end{bmatrix}, F = \begin{bmatrix} S^{k^e}_n \\ 0 \\ S^{k^e}_n + \beta S^{k^e}\end{bmatrix}. \tag{3.32}$$

The obtained system of non-linear algebraic residual Eq. (3.31) are solved using Newton-Raphson method. The process is iterated until the convergence condition is achieved i.e. error between two iteration is 10^{-14}.

3.3 Analysis of the Pressure

Periodicity of the flow yields that the pressure and stress fields are only computed in the central region of the domain that occupies only one wavelength. It is convenient to reduced pressure gradient from governing Navier-Stokes equations in dimensionless form

$$\frac{\partial P}{\partial x} = \mathrm{Re}\left(\frac{\partial^2\psi}{\partial y^2}\frac{\partial\psi}{\partial x}-\frac{\partial^2\psi}{\partial x\,\partial y}\frac{\partial\psi}{\partial y}\right)-\frac{\partial\omega}{\partial y}+Gr\theta. \tag{3.33}$$

$$\frac{\partial P}{\partial y} = \mathrm{Re}\alpha^2\left(\frac{\partial^2\psi}{\partial x^2}\frac{\partial\psi}{\partial y}-\frac{\partial^2\psi}{\partial x\,\partial y}\frac{\partial\psi}{\partial x}\right)-\alpha\frac{\partial\omega}{\partial x}. \tag{3.34}$$

3.4 Validation

A comparison for validation of the obtained numerical results with the analytical results of Srinivas et al. (2011) in the special case are presented in **Figure 3.2**. It is observed that our results in the limiting case ($Re = 0, \alpha = 0$) are in close agreement with corresponding result of Srinivas et al. (2011). The solution given in the Srinivas et al. (2011) is analytical approximation computed by perturbation method.

3.5 Results and Discussion

This section presents to analyze the results of the modeled problem in terms of velocity distribution, heat characteristics, trapping phenomenon and rise in pressure against different involved flow parameters.

3.5.1 Velocity field and temperature characteristics

The graphs of longitudinal velocity u and the temperature profile θ are presented in the **Figures 3.3 – 3.6** to see the effects of Reynolds number Re, time mean flow rate Q, Grashof number Gr and heat generation parameter β. From these figures, it is detected that both longitudinal velocity and temperature profile achieve maximum in the vicinity of the center of the channel. Moreover, parabolic behavior by velocity and temperature graphs is observed in all the cases. In **Figure 3.3(a)**, we observe the effect of Reynolds number Re on velocity distribution. We see that near the center of the channel, increase in Re causes decrease in velocity while an opposite attitude is perceived at the wall. So, it predicts the dominance of inertial effects to viscous forces in the center of the channel causes decrease in velocity of the fluid while in the region of the wall dominance of inertial forces enhances the velocity. **Figure 3.3(b)** illustrates that an increase in Re rises the temperature over the whole cross-section. This observation is not reported in earlier studies and it is indorsed to strong inertial effects induced for non-zero large values of Reynolds number. Moreover, assumptions of long wavelength along with the low Reynolds number theory is not able to predict such non-linear effect. **Figures 3.4(a)** and **3.4(b)** show the outcome of time mean flow rate Q on velocity distribution and temperature profile, respectively. Both figures show that the rise in volume flow rate Q enhances longitudinal velocity and temperature profile. **Figure 3.5(a)** presents the outcome of Grashof number Gr on longnitudanl velocity profile. We see that the behavior of velocity due to Grashof number Gr at the wall and near the center is

different. In the region $0 \leq y \leq 0.2$, we observe that dominance of buoyancy forces reduces the velocity but after this region $y \geq 0.2$, increase in velocity is observed at the same Gr. **Figure 3.5(b)** exhibits the decreasing behavior in temperature distribution by enhancing Gr in the whole domain. As increase in Grashof number corresponds to enhance the buoyancy forces caused by temperature difference, due to which its effect appear at the center of the channel and so causes the decrease in temperature rise. In **Figure 3.6(a)**, we observe that for the velocity distribution, heat generation parameter β exhibits same behavior as that of Grashof number but in **Figure 3.6(b)** temperature increases due to increase in the heat generation parameter β, which is quite natural. Hence, Grashof number Gr also helps to control the heat in the fluid flow with heat generation parameter and its effects are opposite to the effect of heat generation parameter β.

3.5.2 Trapping and vorticity

The behavior of streamlines in wave frame for stationary wall is mostly similar as that of wall but sometime situation arises that pattern of streamlines get split and encloses a bolus of fluid particles in circular closed streamlines formed so that circular region is created. On the other hand, in the fixed frame, the waves trapped the fluid bolus with speed of wave. To examine the variation of streamlines, we plotted contours of streamlines for different values of the parameter involved as shown in **Figures 3.7 – 3.11**. **Figure 3.7** shows the behavior of streamlines with variation of Reynolds number Re. It is observed that size of bolus magnifies with the increase in Reynolds number and as far as the number of bolus are concern, we observe that number of boluses also increases with increase in Re. It is owing to the fact that increase in inertial effects causes rise in velocity profile of the fluid, so the solution surface attains more height. **Figure 3.8** shows the variation of streamlines for diverse values of Grashof number Gr. It is noticed that the trapped bolus exists near the central region of the channel for smaller values of Grashof number. Moreover, it moves in lower region of the boundary wall with increase in Grashof number as shown in **Figure 3.8**. **Figure 3.9** provides the behavior of heat generation parameter β on streamlines. From this figure, we observe the increase in the size of bolus due to increase in heat generation parameter β. **Figure 3.10** shows increase in the size of trapped bolus with increase in wave number α. It is also observed that for small α, the boluses are trapped near the wall but when we increase the wave number α, the bolus moves towards the central

part of the region. **Figure 3.11** illustrates the consequence of time mean flow rate Q on the streamlines. We observed a rapid upsurge in the number and size of bolus with small increase in the flow rate Q.

In **Figures 3.12 – 3.17**, we plotted the isothermal lines for different flow parameters. In **Figure 3.12**, we observed that by increasing Reynolds number, isothermal lines shows enhanced curvature effects and formation of bolus appears where complete bolus is developed in the central region for $Re = 12$. **Figure 3.13** shows that increase in Grashof number increases curvature effects near central wall and observed same smoothness of curvature near the peristaltic wall in all cases. **Figure 3.14** exhibits the effect of increasing heat generation parameter β on isothermal lines. It is observed that isothermal lines congregated at central wall and move towards the wall channel. Variation in isothermal lines for different values of Prandtl number Pr may be seen in **Figure 3.15**. We can see that more curvature effect in central region with more number of bolus due to increase in the value of Pr. **Figure 3.16** shows decrease in curvature of isothermal lines with increase in the wave number α. In **Figure 3.17**, we see the effect of time mean flow rate Q on isothermal lines which displays that upsurge in this factor causes the bending of the isothermal lines in the vicinity of central part of the channel towards upper region. The effects of different values of the Reynolds number Re on graphs of vorticity are displayed in **Figure 3.18**. It can be distinguished from the figure that vorticity is created at the peristaltic wall then it disperses towards the central region of the channel with increase in the values of Reynolds number.

3.5.3 Pressure distribution

The pressure rise per wave length has been plotted through **Figures 3.19 – 3.24** against time mean flow rate for different range of values of involved parameters. There are following four types of flow region. When the flow is in regions $\Delta P_\lambda > 0$ and $Q > 0$ which represents the quadrant I then it corresponds to Peristaltic/Positive pumping. When the flow is in regions $\Delta P_\lambda > 0$ and $Q < 0$ which represents quadrant II then it corresponds to Retrograde/Backward pumping. When the flow is in regions $\Delta P_\lambda < 0$ and $Q < 0$ which represents quadrant III then it corresponds to co-pumping. When the flow is in regions $\Delta P_\lambda < 0$ and $Q < 0$ which represents quadrant IV then it corresponds to augmented pumping region. Also when the flow is in regions $\Delta P_\lambda = 0$ and $Q > 0$ which means, in quadrant IV then it is free pumping region. Pressure gradient is known

as adverse pressure if $\Delta P_\lambda > 0$ and favorable pressure if $\Delta P_\lambda < 0$. In **Figure 3.19**, the influence of Reynolds number Re on pressure rise per wave length has been shown. We noticed that the increase in Re causes increase in the pressure due to the dominance of inertial forces over viscous forces. It is owing to the fact that when we rise the strength of Re, it enhances the inertial effects as compared to viscous effects, hence more pressure is required to maintain the flow in the channel. We further observed that when time mean flow rate approaches to 1, all the lines coincide which reflects the same amount of pressure at that point. It is observed through **Figures 3.20–3.22** that increase in Prandtl number Pr, Grashof number Gr and heat generation parameter β drops pressure rise per wave length but in the case of amplitude ratio ϕ and wave number α, opposite behavior is seen in **Figure 3.23** and **3.24** respectively.

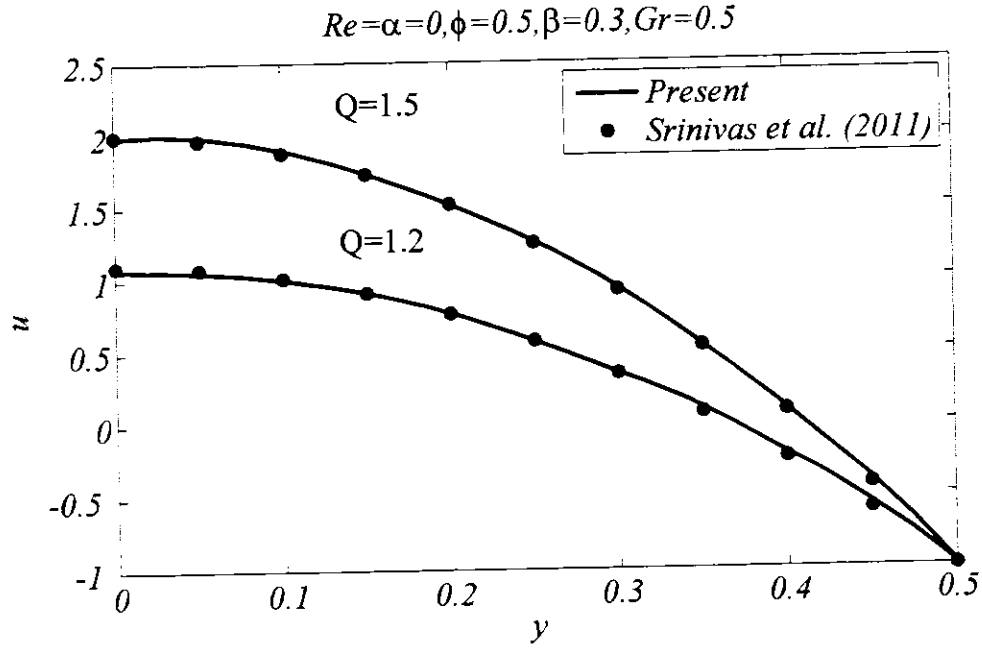

Figure 3.2: Comparison of computed velocity profile with that of Srinivas et al. (2011).

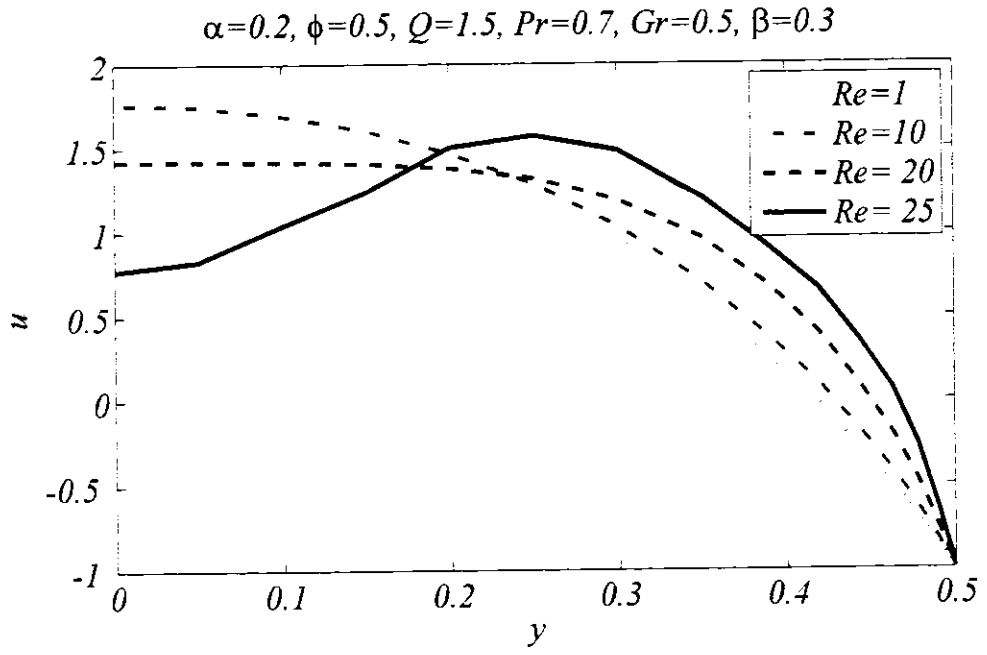

(a)

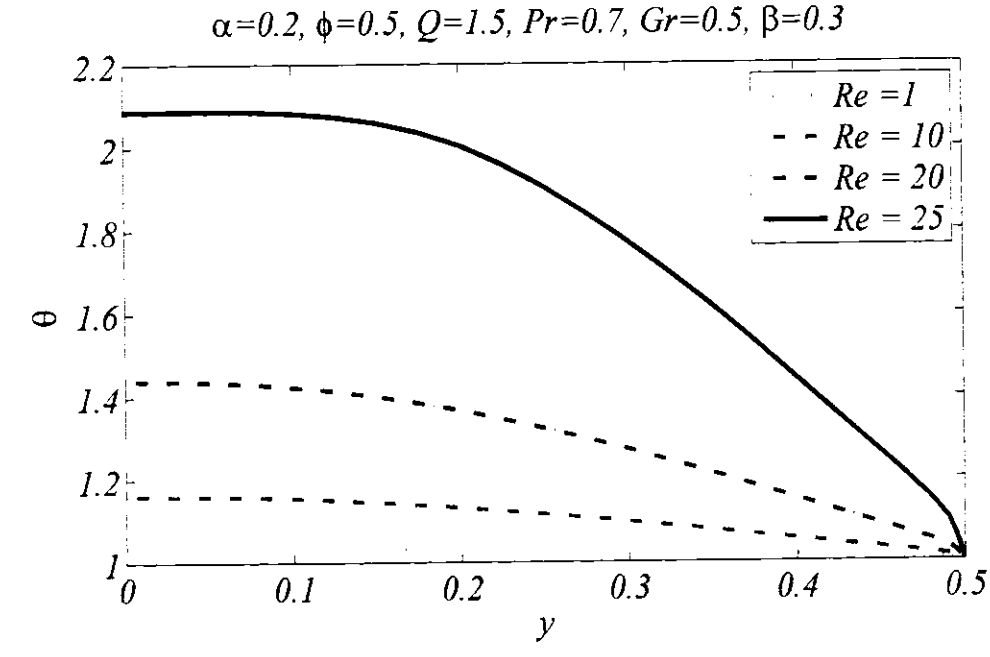

(b)

Figure 3.3: Graphs of longitudinal velocity **(a)** and temperature distribution **(b)** for various values of *Re* when other parameters are fixed

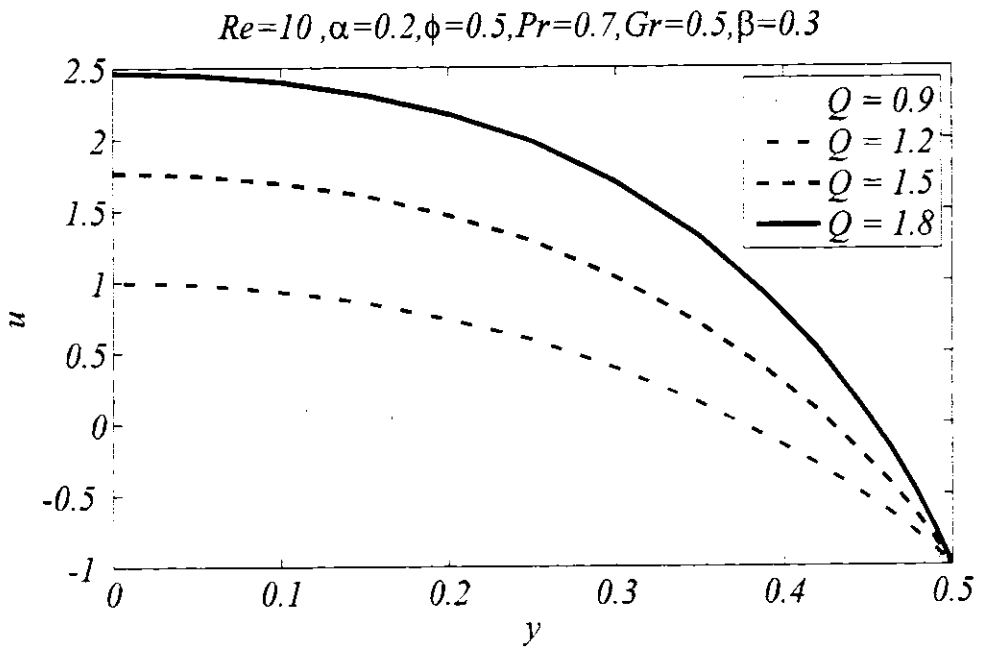

(a)

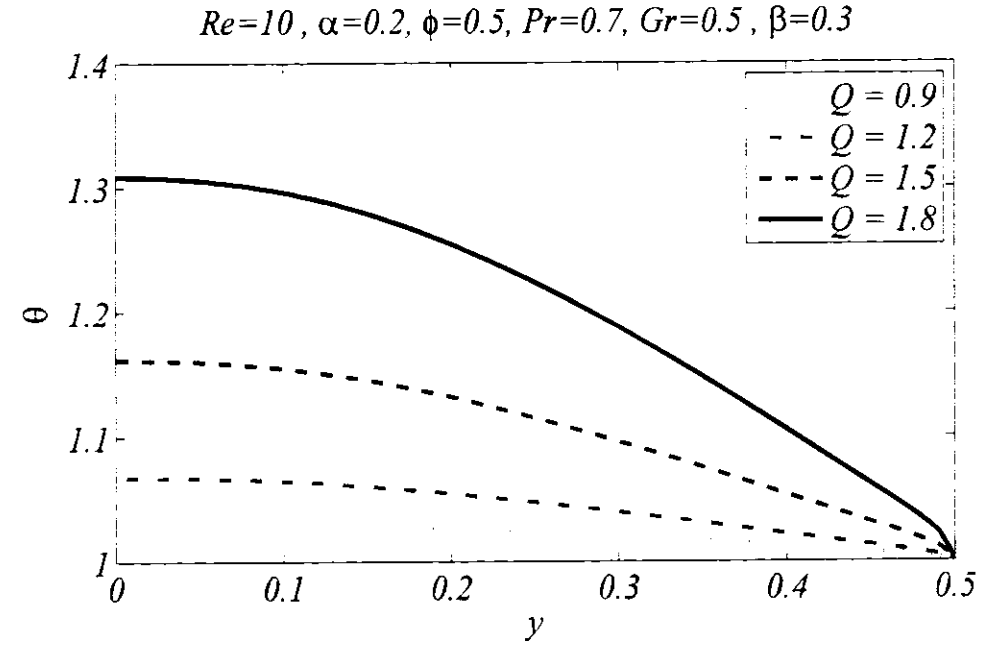

(b)

Figure 3.4: Graphs of longitudinal velocity **(a)** and temperature distribution **(b)** for various values of Q when other parameters are fixed

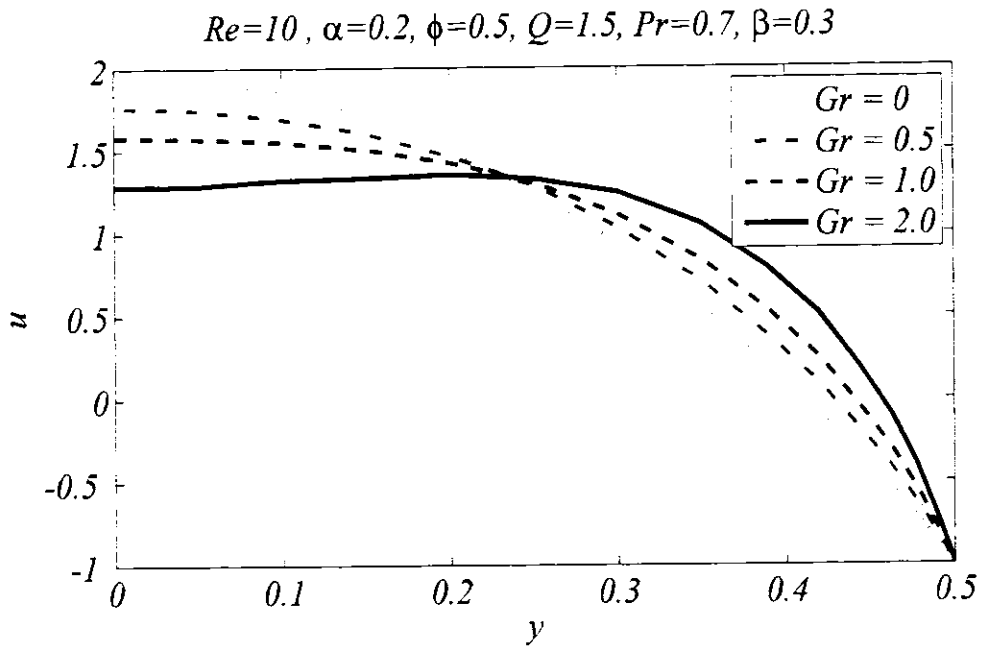

(a)

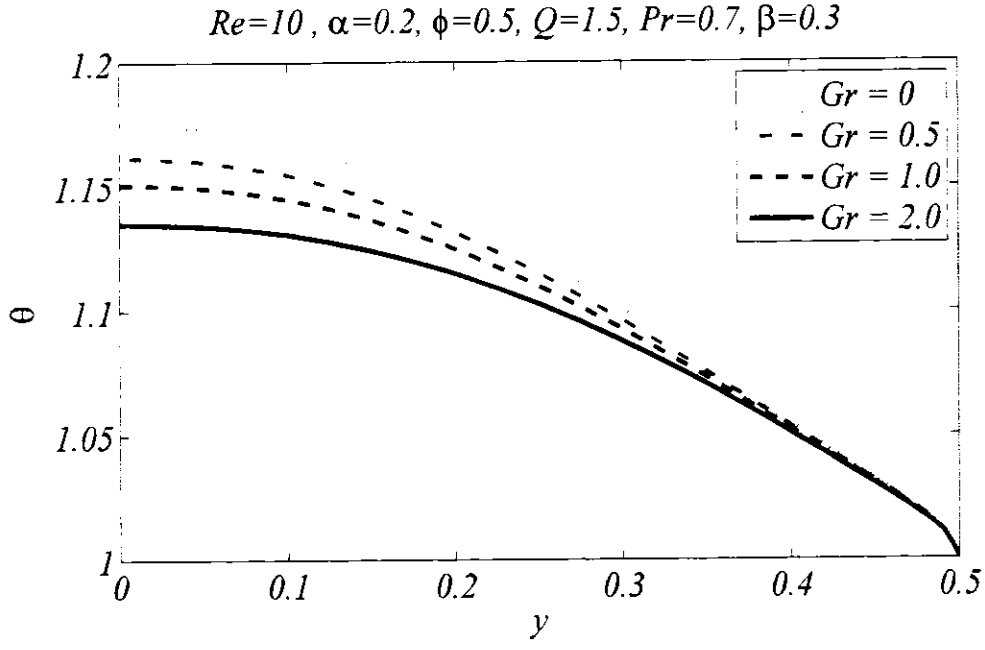

(b)

Figure 3.5: Graphs of longitudinal velocity distribution **(a)** and temperature profile **(b)** for various values of Gr when other parameters are fixed

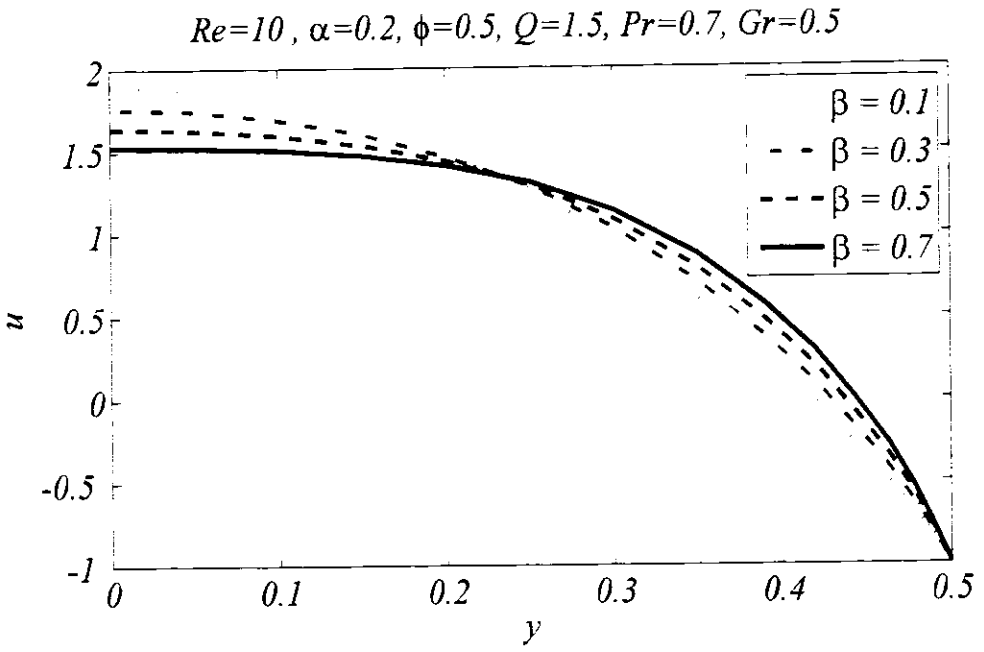

(a)

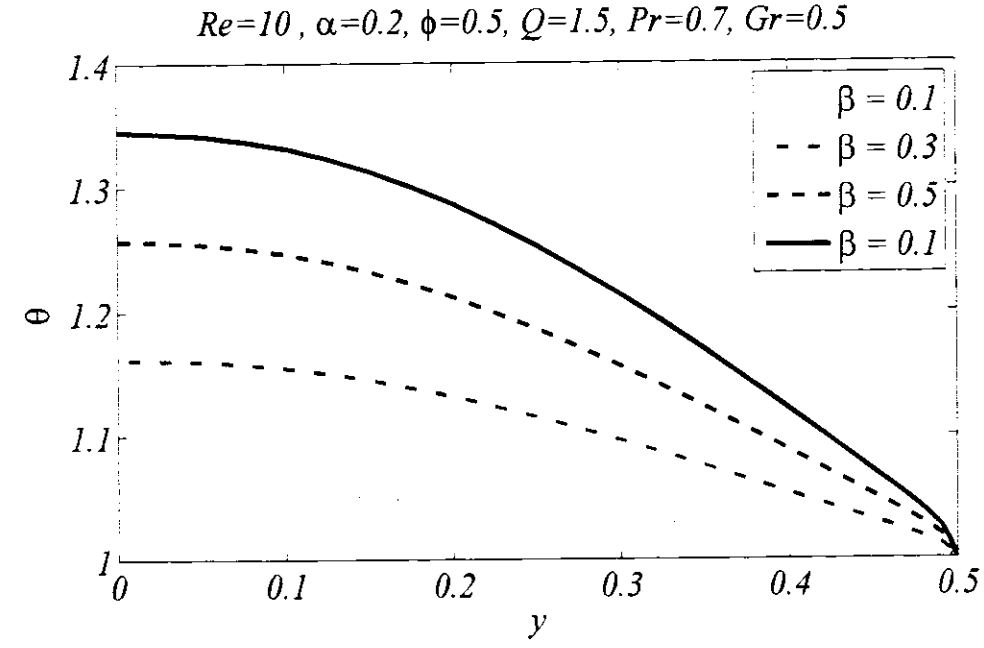

(b)

Figure 3.6: Graphs of longitudinal velocity distribution **(a)** and temperature profile **(b)** for various values of β when other parameters are fixed

(a)

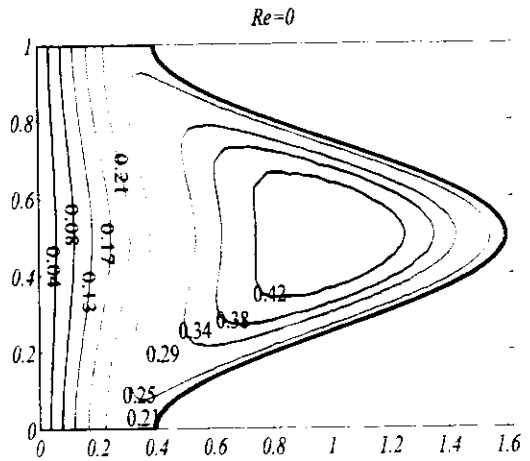

(b)

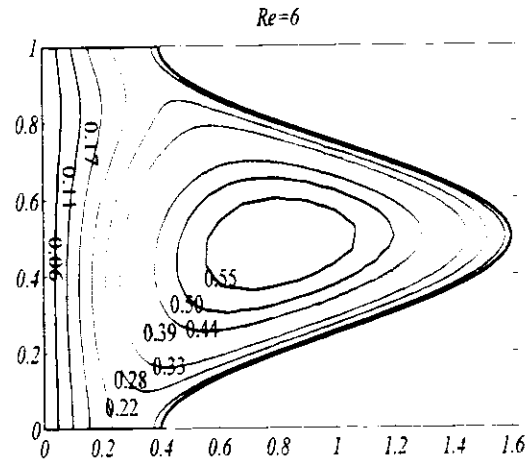

(c)

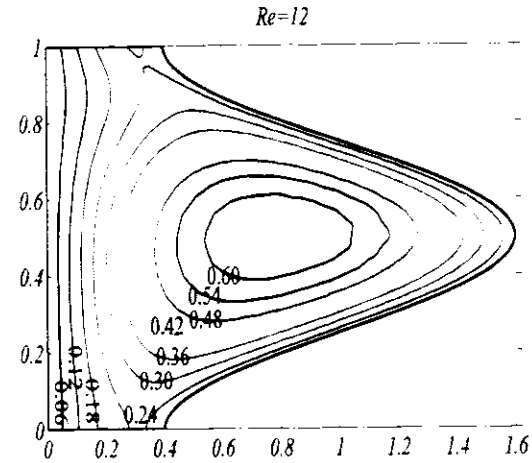

Figure 3.7: Variation of the streamlines for various values of Re against fixed values of $\alpha = 0.3, \phi = 0.6, Q = 1.2, Gr = 0.5, Pr = 0.7$ and $\beta = 0.3$ in wave frame of reference

(a)

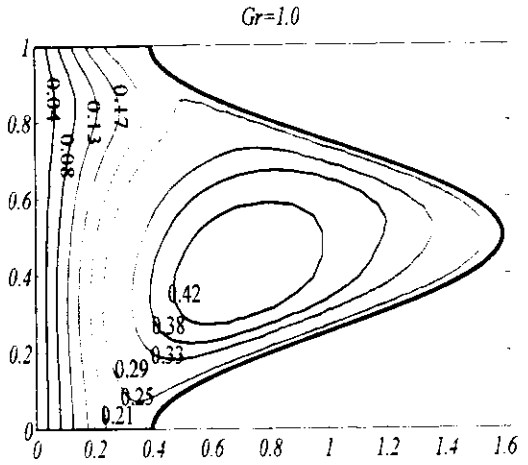

(b)

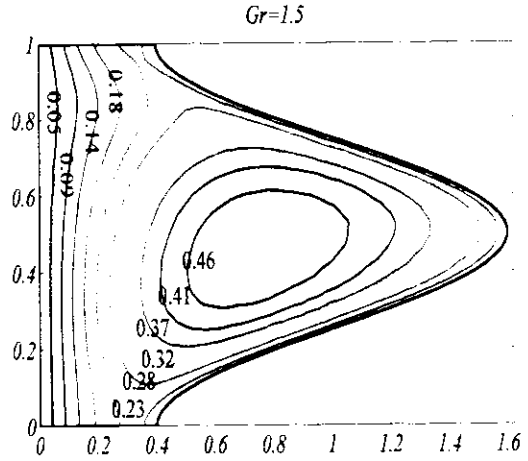

(c)

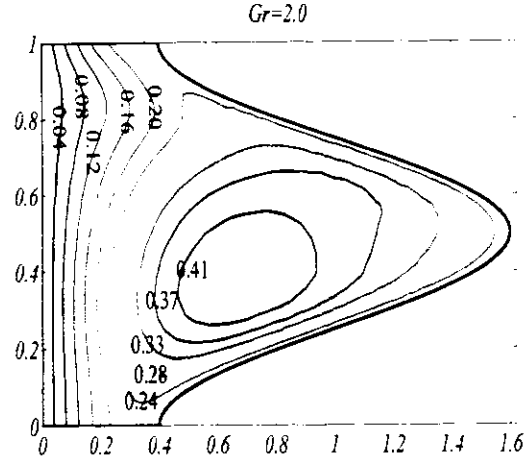

Figure 3.8: Variation of the streamlines for various values of Gr against fixed values of $Re = 6, \alpha = 0.3, \phi = 0.6, Q = 1.2, Pr = 0.7$ and $\beta = 0.3$ in wave frame of reference

(a)

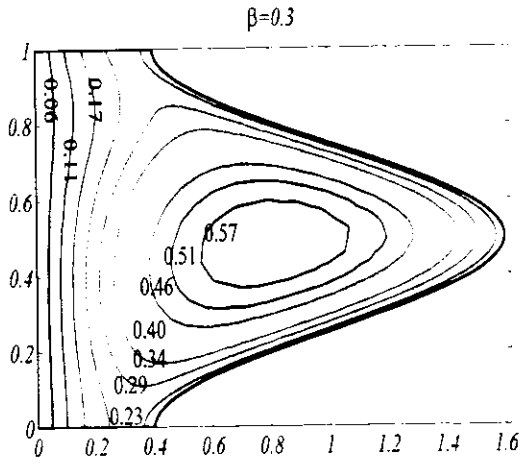

(b)

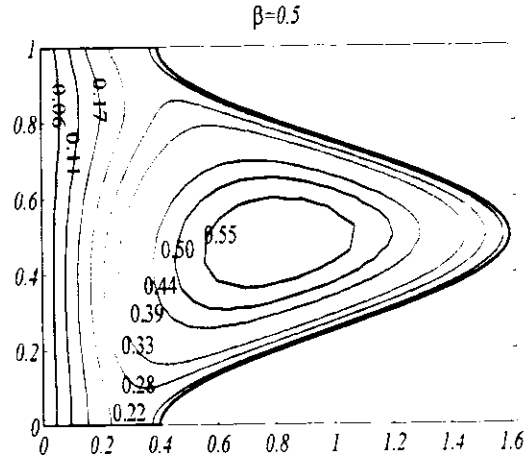

(c)

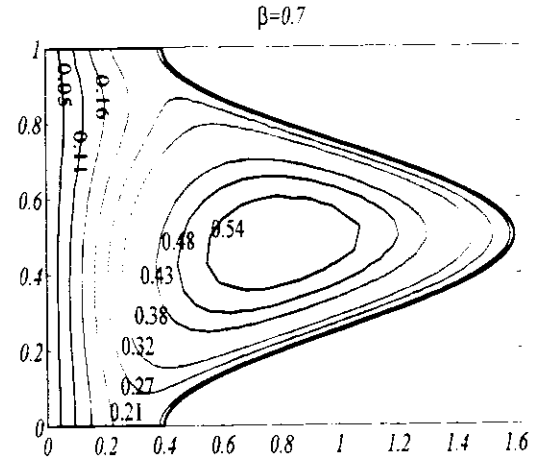

Figure 3.9: Variation of the streamlines for various values of β against fixed values of $Re = 6, \alpha = 0.3, \phi = 0.6, Q = 1.2, Gr = 0.5$ and $Pr = 0.7$ in wave frame of reference

(a)

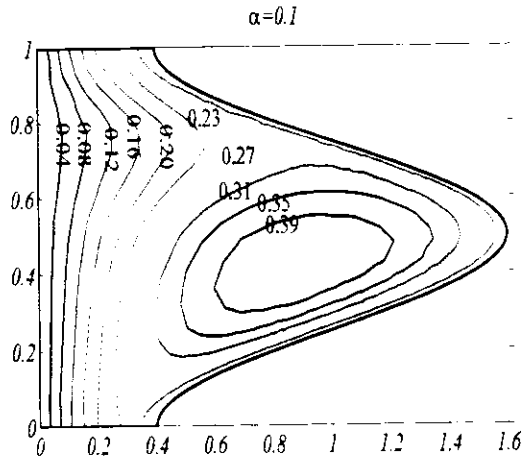

(b)

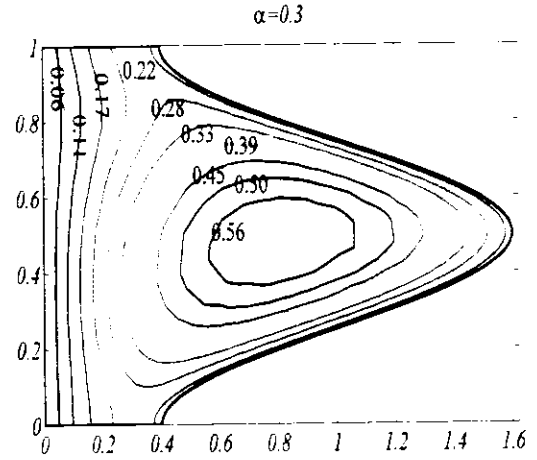

(c)

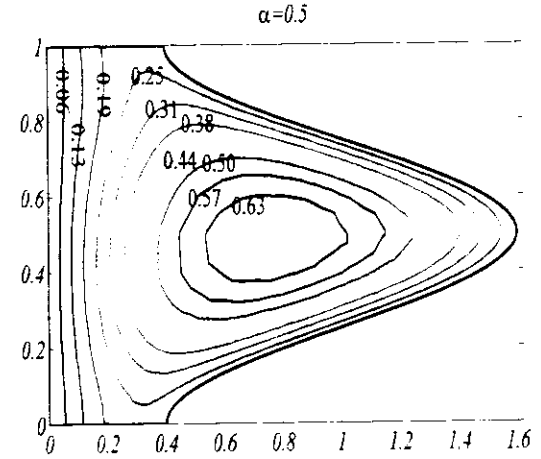

Figure 3.10: Variation of the streamlines for various values of α against fixed values of $Re = 6, \phi = 0.6, Q = 1.2, Gr = 0.5, Pr = 0.7$ and $\beta = 0.3$ in wave frame of reference

(a)

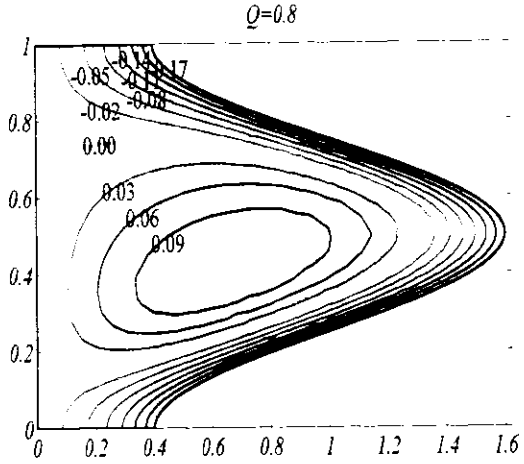

(b)

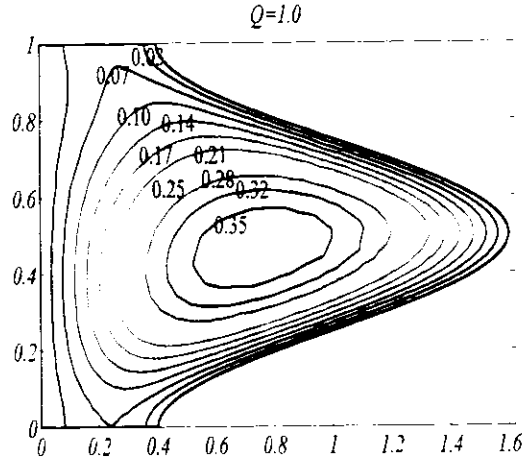

(c)

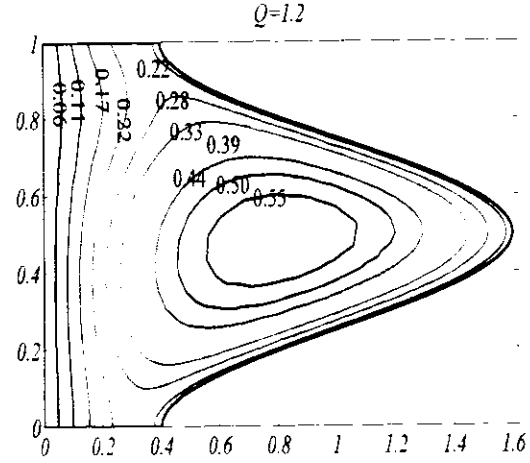

Figure 3.11: Variation of the streamlines for various values of Q with fixed values of $Re = 6, \alpha = 0.3, \phi = 0.6, Gr = 0.5, Pr = 0.7$ and $\beta = 0.3$ in wave frame of refrence

(a)

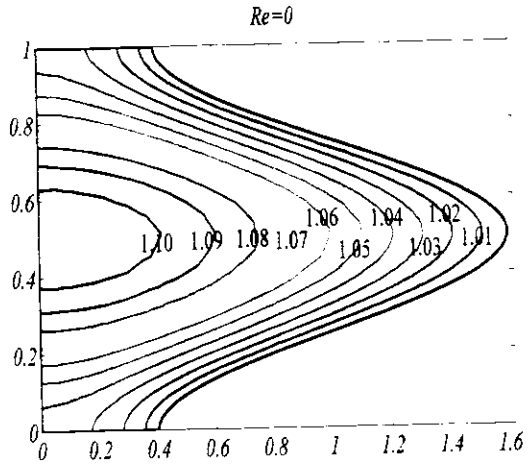

(b)

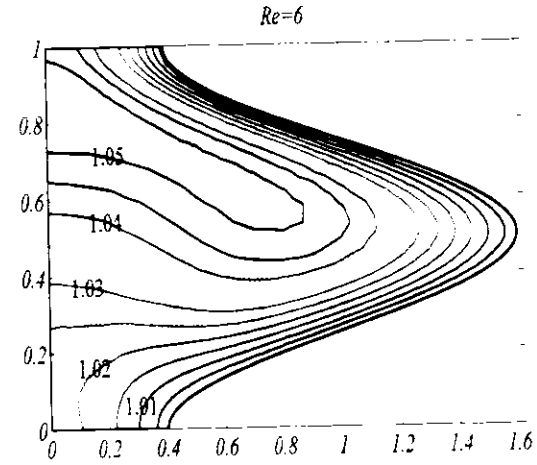

(c)

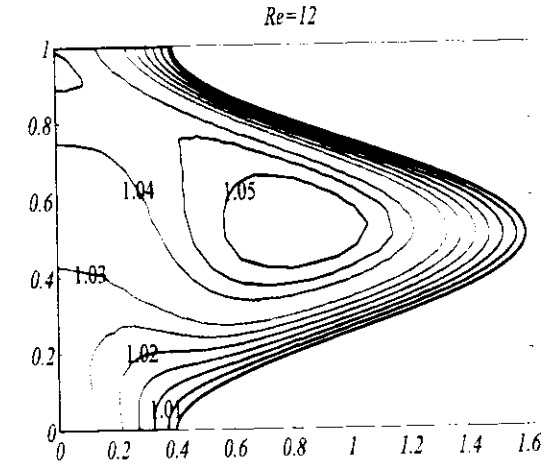

Figure 3.12: Variation of the isothermal lines for various values of Re against fixed values of $\alpha = 0.3, \phi = 0.6, Q = 1.2, Gr = 0.5, Pr = 0.7$ and $\beta = 0.3$ in wave frame of reference

(a)

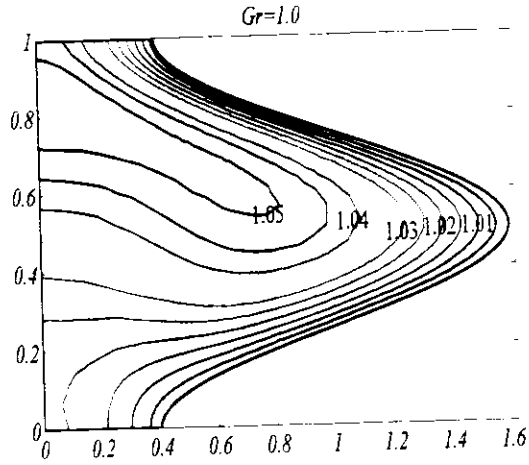

(b)

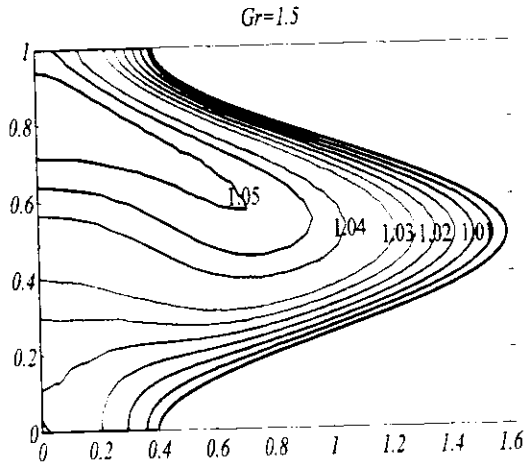

(c)

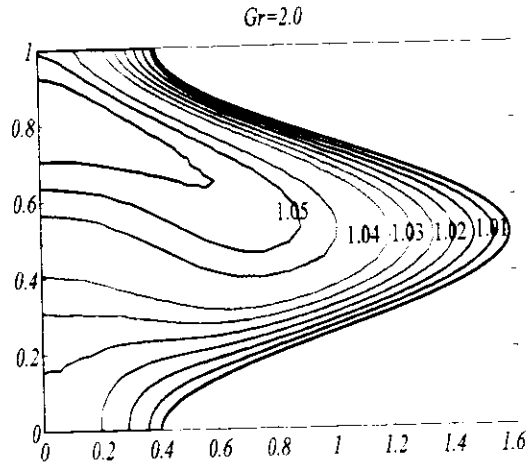

Figure 3.13: Variation of the isothermal lines for various values of Gr against fixed values of $Re = 6, \alpha = 0.3, \phi = 0.6, Q = 1.2, Pr = 0.7$ and $\beta = 0.3$ in wave frame of reference

(a)

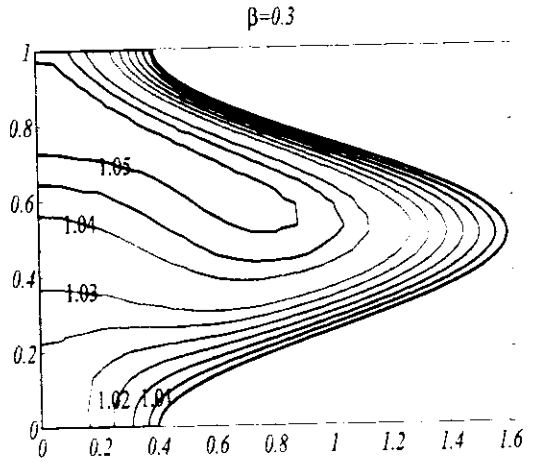

(b)

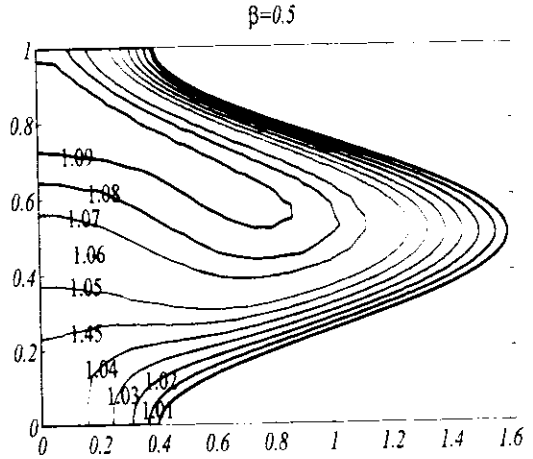

(c)

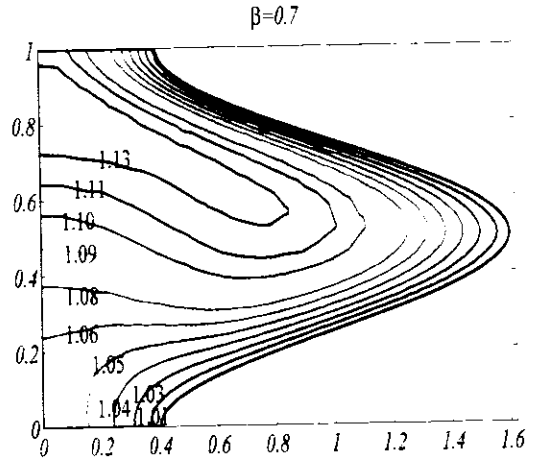

Figure 3.14: Variation of the isothermal lines for various values of β against fixed values of $Re = 6, \alpha = 0.3, \phi = 0.6, Q = 1.2, Gr = 0.5$ and $Pr = 0.7$ in wave frame of reference

(a)

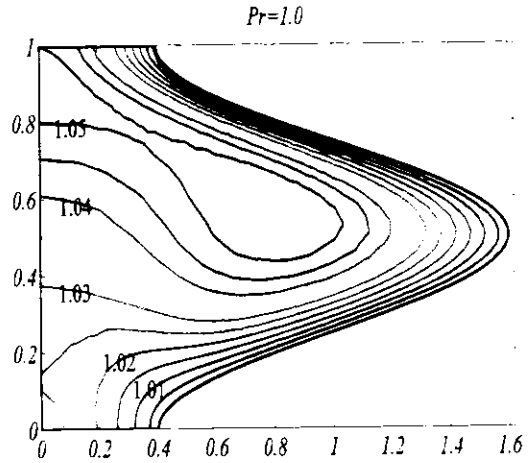

(b)

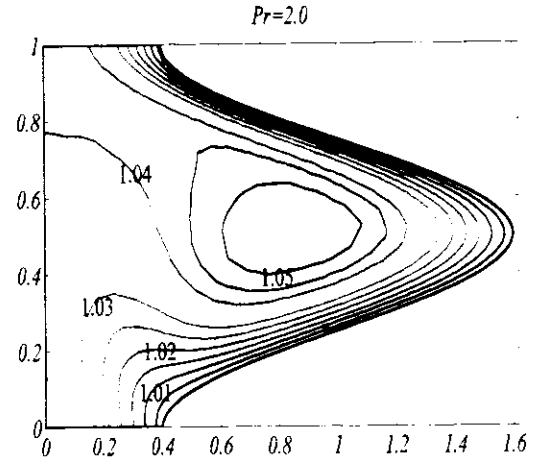

(c)

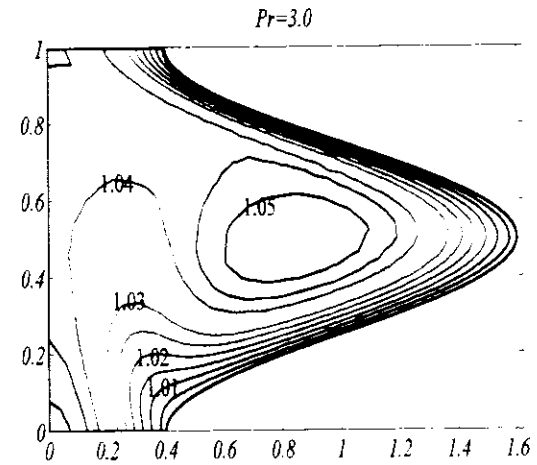

Figure 3.15: Variation of the isothermal lines for various values of Pr against fixed values of $Re = 6, \alpha = 0.3, \phi = 0.6, Q = 1.2, Pr = 0.7$ and $\beta = 0.3$ in wave frame of reference

(a)

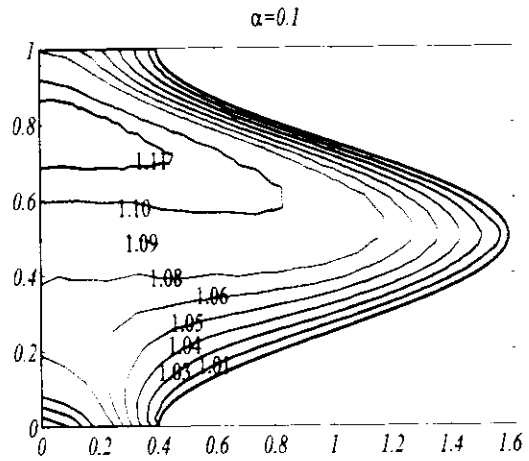

(b)

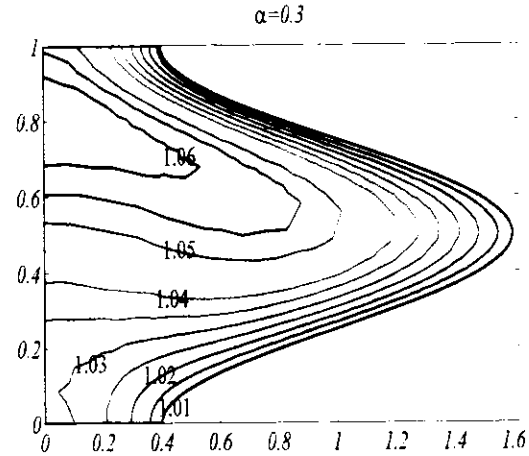

(c)

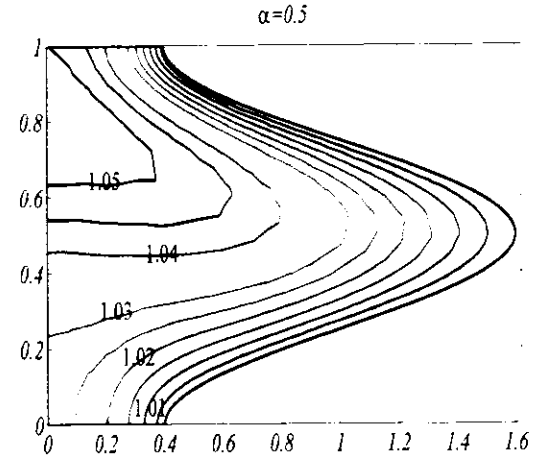

Figure 3.16: Variation of the isothermal lines for various values of α against fixed values of $Re = 6, \phi = 0.6, Q = 1.2, Gr = 0.5, Pr = 0.7$ and $\beta = 0.3$ in wave frame of reference

(a)

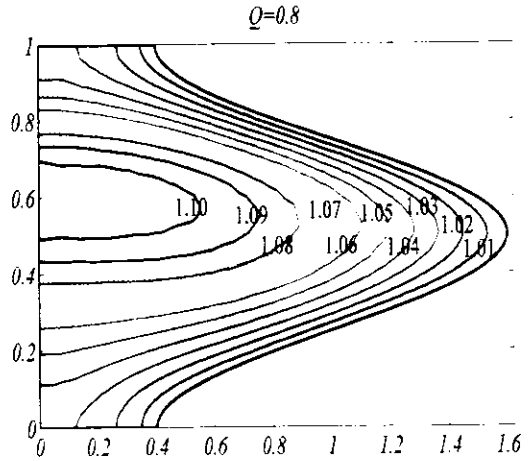

(b)

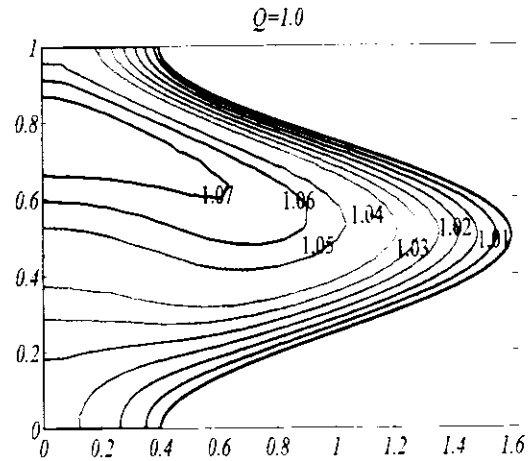

(c)

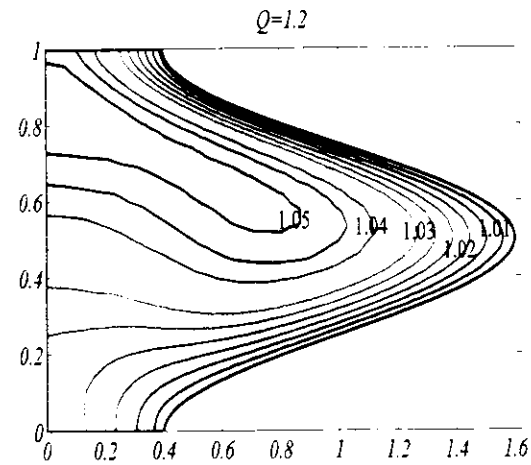

Figure 3.17: Variation of the isothermal lines for various values of Q against fixed values of $Re = 6, \alpha = 0.3, \phi = 0.6, Gr = 0.5, Pr = 0.7$ and $\beta = 0.3$ in wave frame of reference

(a)

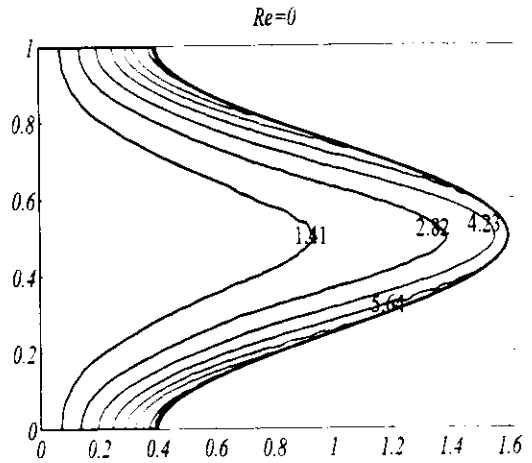

(b)

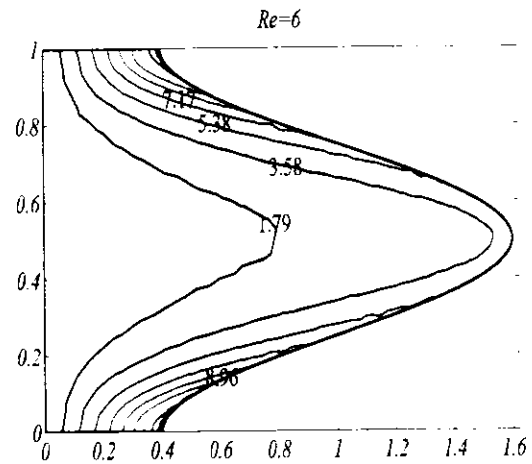

(c)

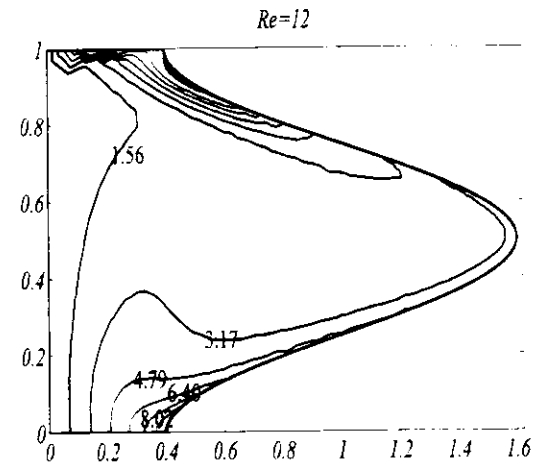

Figure 3.18: Vorticity for various values of Re against fixed values of $\alpha = 0.3, \phi = 0.6, Q = 1.2, Gr = 0.5, Pr = 0.7$ and $\beta = 0.3$ in wave frame of reference

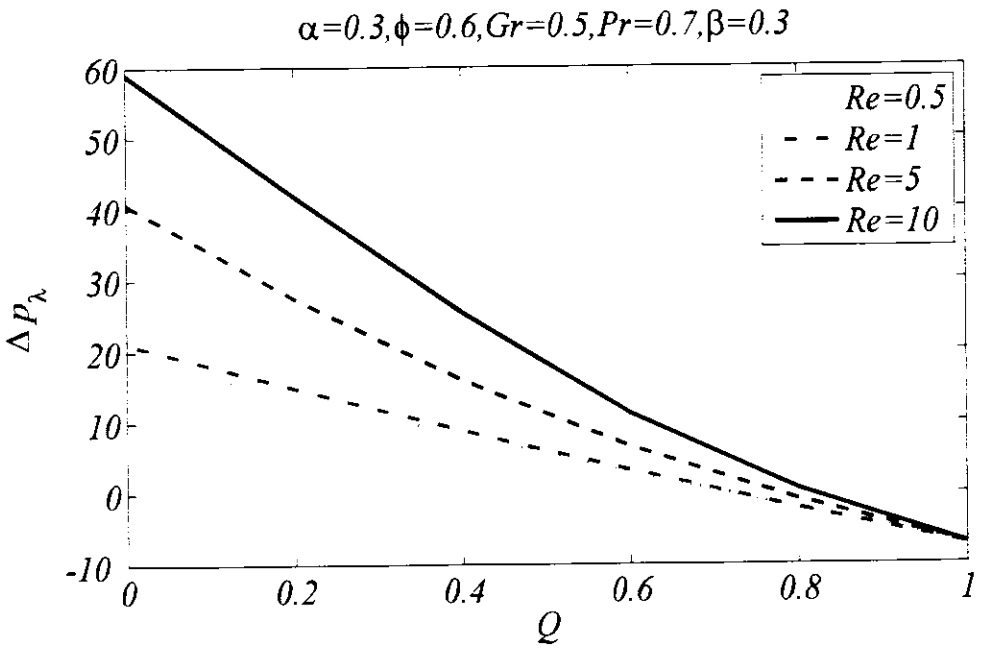

Figure 3.19: Pressure rise per wave length for various values of *Re* against fixed values of the other parameters

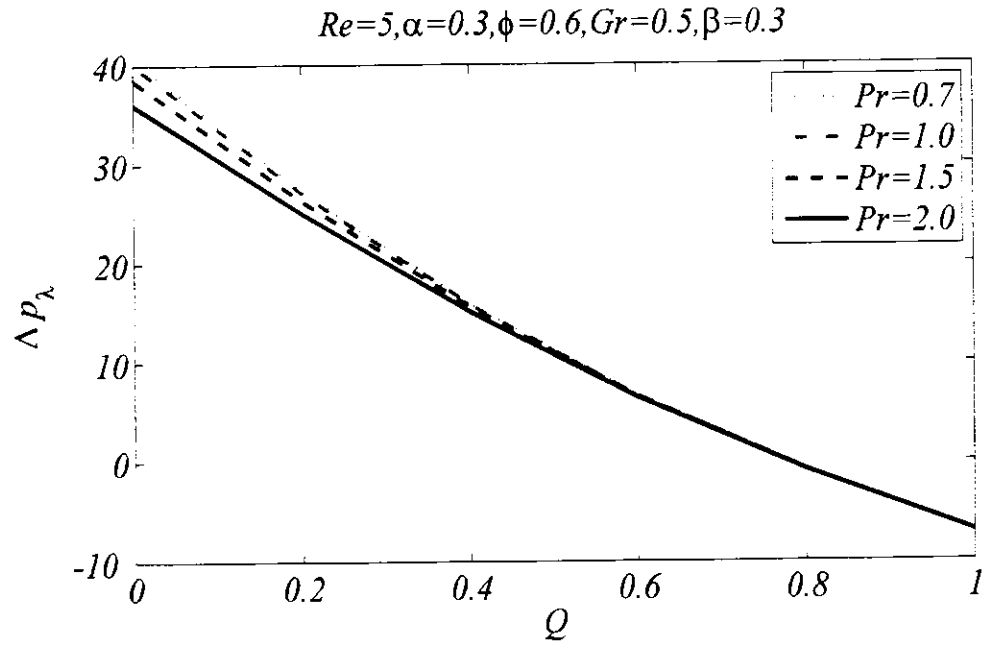

Figure 3.20: Pressure rise per wave length for various values of *Pr* against fixed values of the other parameters

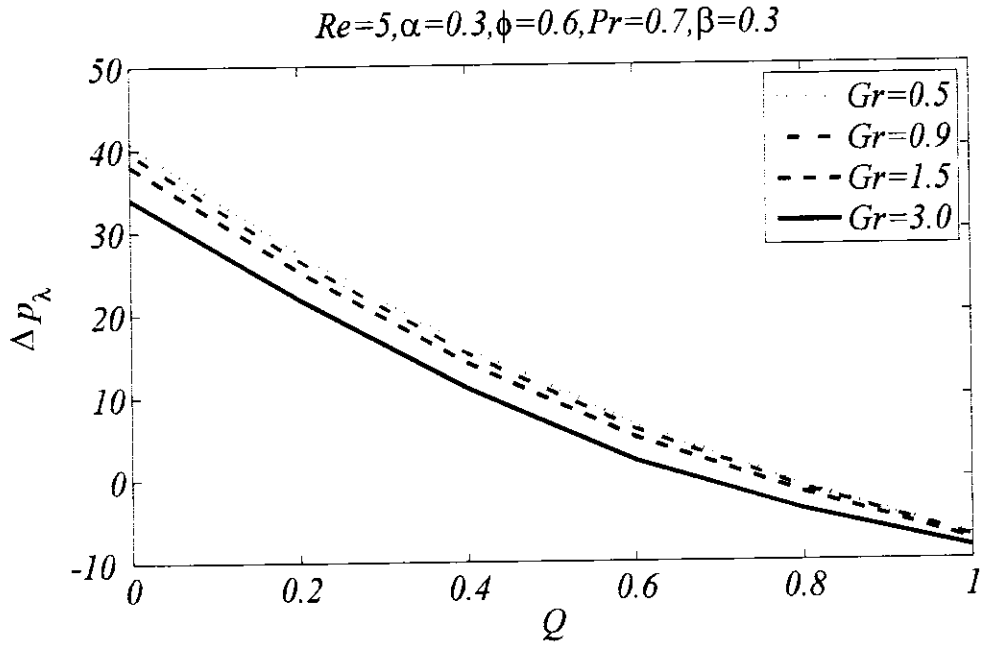

Figure 3.21: Pressure rise per wave length for various values of Gr against fixed values of the other parameters

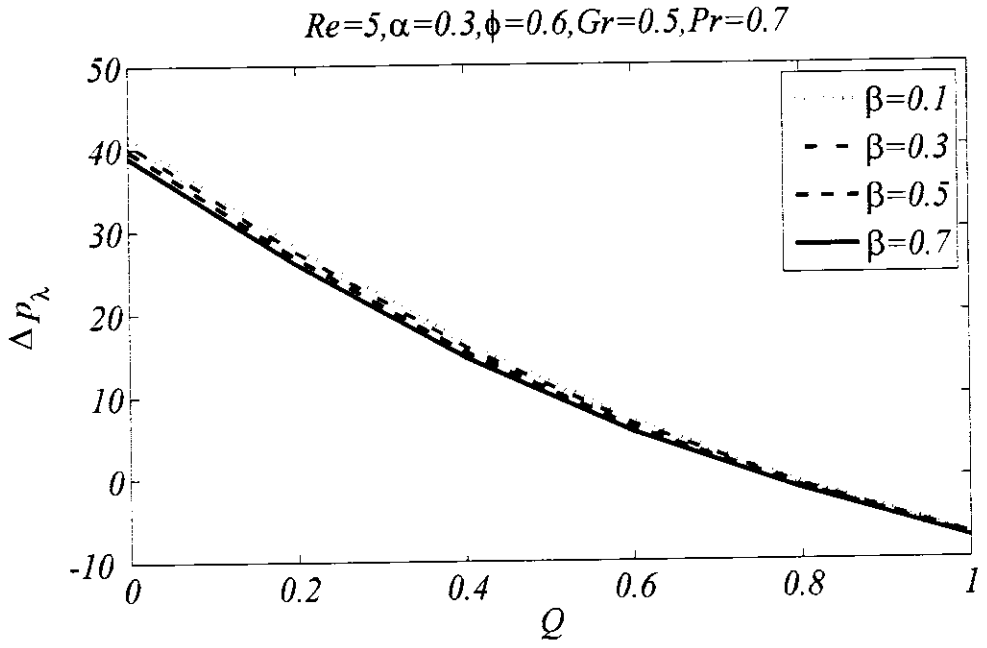

Figure 3.22: Pressure rise per wave length for various values of β with fixed values of other parameters

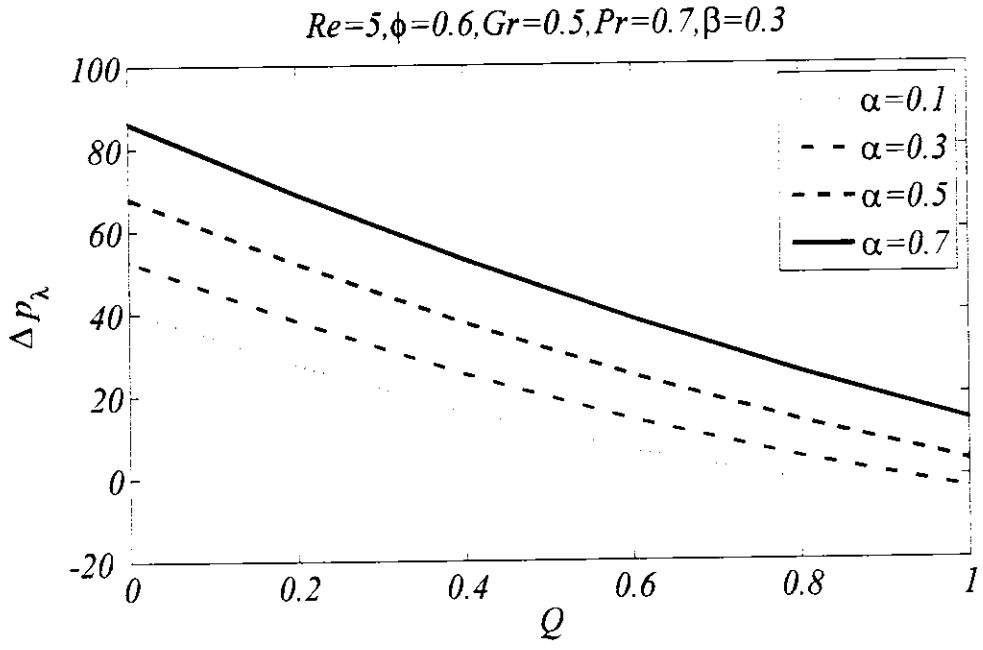

Figure 3.23: Pressure rise per wave length for various values of α against fixed values of the other parameters

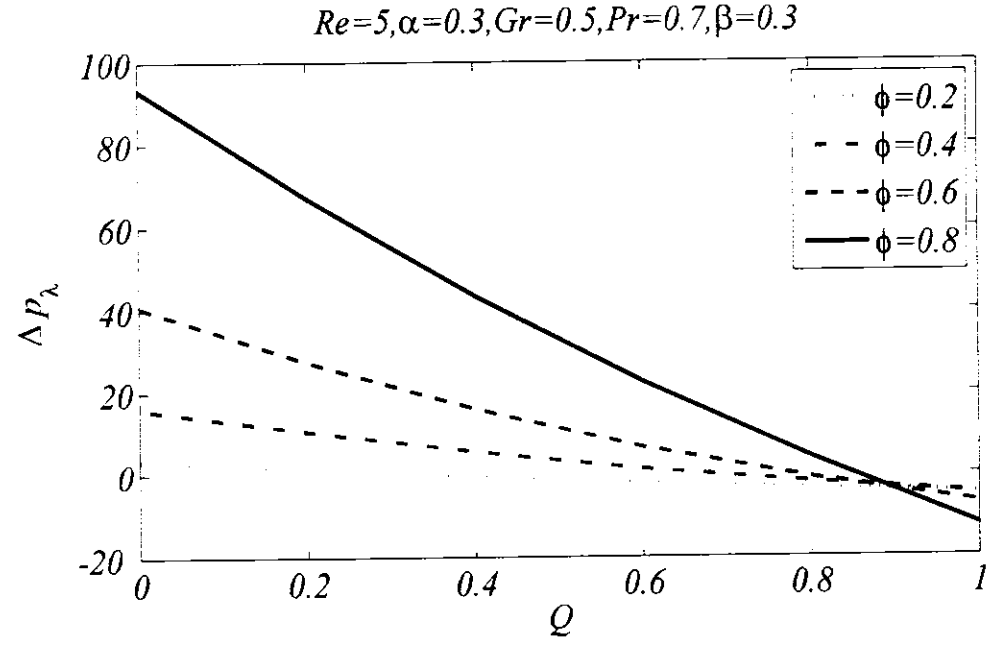

Figure 3.24: Pressure rise per wave length for various values of ϕ against fixed values of the other parameters

3.6 Conclusions

The heat transfer analysis in the mechanism of peristaltic flow through the vertical channel has been presented numerically. The governing equations are modeled in the absence of long wave length approximation which allows us to observe the effects of all the parameters with moderate values. The numerical solutions for stream function, pressure rise per length as well as temperature profile are found. The effects of involved parameters on the velocity, heat transfer, and the trapping due to the peristaltic wall are discussed in detail. From the analysis, the main outcomes for different flow characteristics are summarized. Increase in heat generation reduces the velocity near the central region and improves the velocity in neighbor of peristaltic wall. It also enhances the size of bolus and curvature effect on isothermal lines and drops the pressure. Increase in the Grashof number causes fall in velocity near the central region and rises the velocity neighbor of peristaltic wall and consequently pressure drops appeared. Increase in time mean flow rate supports the enhancement of velocity, temperature and size of bolus. Escalation in wave number enhances the volume of the bolus, reduces curvature effect of isotherms and rises the pressure.

Chapter 4

Hydromagnetic Peristaltic Transport of Casson Fluid through a Channel

The modeling and simulation presented in this chapter is about the peristaltic flow of a Casson fluid passing through a channel with the inducement of applied magnetic field in the moving frame of reference by constant velocity along with the wave. The developed mathematical model is presented by a set of partial differential equations. A numerical algorithm based on finite element method with Galerkin weighted residual technique is implemented to evaluate the numerical solution of the modeled governing partial differential equations in the stream-vorticity formulation. The obtained results are independent of low Reynolds number and long wavelength assumptions, so the effects of non-zero moderate Reynolds number are presented. Comparison of the obtained results in present analysis with the available results in limiting case in the literature is included as well and good agreement is found. The expression for the pressure is also calculated implicitly and discussed through graphs. Computed solutions are presented by the contours of streamlines and graphs of vorticity. Longitudinal velocity profile and pressure distribution against variation of various involved parameters are also presented through graphs. The results obtained illustrates that the strength of circular movement for stream function enhances by magnifying the values of the parameters Reynolds and Hartmann numbers. Enhancement in longitudinal velocity is noted by increasing the Reynolds number and Casson parameter while increasing Hartmann number reduces the longitudinal velocity.

4.1 Problem Formulation

The unsteady two-dimensional incompressible peristaltic flow of Casson fluid is considered passing through the channel of infinite length and of width $2a$. The fluid is assumed electrically conducting under the influence of applied uniform magnetic field with strength $\boldsymbol{B_0}$ perpendicular to the flow. We have considered the problem in which $\boldsymbol{B}$ influences $\boldsymbol{V}$ via the Lorentz force. To ensure that $\boldsymbol{B}$ remains unaffected by $\boldsymbol{V}$, we must restrict ourselves to low magnetic Reynolds numbers. The flow is along horizontal x-axis where y-axis is considered perpendicular to the flow where it is further assumed

that x-axis is along the central line of the channel as shown in **Figure 2.1**. It is assumed that a wave with speed c propagates in the x −direction such that the wall of the channel obeys the relation defined in Eq. (2.1). The equations that governs the motion of unsteady peristaltic flow of Casson fluid in the inducement of applied uniform magnetic fields in component form in fixed frame can be written as

$$\frac{\partial U}{\partial X}+\frac{\partial V}{\partial Y}=0, \tag{4.1}$$

$$\rho\left(\frac{\partial U}{\partial t}+U\frac{\partial U}{\partial X}+V\frac{\partial U}{\partial Y}\right)=-\frac{\partial P}{\partial X}+\mu\left(\frac{1}{\zeta}+1\right)\left(\frac{\partial^2 U}{\partial X^2}+\frac{\partial^2 U}{\partial Y^2}\right)-\sigma B_0^2 U, \tag{4.2}$$

$$\rho\left(\frac{\partial V}{\partial t}+U\frac{\partial V}{\partial X}+V\frac{\partial V}{\partial Y}\right)=-\frac{\partial P}{\partial Y}+\mu\left(\frac{1}{\zeta}+1\right)\left(\frac{\partial^2 V}{\partial X^2}+\frac{\partial^2 V}{\partial Y^2}\right). \tag{4.3}$$

Introducing the well-known transformations given in Eq. (2.2) and (3.1). The equations that describe the flow in the moving frame are

$$\frac{\partial u^*}{\partial x^*}+\frac{\partial v^*}{\partial y^*}=0, \tag{4.4}$$

$$\rho\left(u^*\frac{\partial u^*}{\partial x^*}+v^*\frac{\partial u^*}{\partial y^*}\right)=-\frac{\partial p^*}{\partial x^*}+\mu\left(\frac{1}{\zeta}+1\right)\left(\frac{\partial^2 u^*}{\partial x^{*2}}+\frac{\partial^2 u^*}{\partial y^{*2}}\right)-\sigma B_0^2(u^*+c), \tag{4.5}$$

$$\rho\left(u^*\frac{\partial v^*}{\partial x^*}+v^*\frac{\partial v^*}{\partial y^*}\right)=-\frac{\partial p^*}{\partial y^*}+\mu\left(\frac{1}{\zeta}+1\right)\left(\frac{\partial^2 v^*}{\partial x^{*2}}+\frac{\partial^2 v^*}{\partial y^{*2}}\right), \tag{4.6}$$

where ρ, ζ, σ, p^*, μ and B_0 represents density, material parameter, electrical conductivity, pressure, the coefficient of viscosity and strength of the applied magnetic field respectively. The wall movement in transformed variables is represented in Eq. (2.6). The appropriate boundary conditions are

$$\left.\begin{aligned}&\frac{\partial u^*}{\partial y^*}=0, \quad v^*=0, && \text{at} \quad y^*=0,\\ &u^*=-c, \quad v^*=-\frac{2\pi bc}{\lambda}\sin\left(\frac{2\pi x^*}{\lambda}\right) && \text{at} \quad y^*=\eta(x^*)\end{aligned}\right\} \tag{4.7}$$

To present the theoretical analysis in terms of normalized quantities, dimensionless variables involved are given in Eq. (2.8). In terms of those normalized variables, after eliminating pressure gradient term by cross differentiation, the boundary value problem takes the following form

$$\alpha^2\frac{\partial^2\psi}{\partial x^2}+\frac{\partial^2\psi}{\partial y^2}=-\omega, \tag{4.8}$$

$$\mathrm{Re}\left(\frac{\partial\psi}{\partial y}\frac{\partial\omega}{\partial x}-\frac{\partial\psi}{\partial x}\frac{\partial\omega}{\partial y}\right)=\left(\frac{1}{\zeta}+1\right)\nabla^2\omega+M^2\frac{\partial^2\psi}{\partial y^2}, \tag{4.9}$$

$$\left.\begin{aligned}&\frac{\partial^2\psi}{\partial y^2}=0, \quad \frac{\partial\psi}{\partial x}=0, && \text{at} \quad y=0,\\ &\frac{\partial\psi}{\partial y}=-1, \quad \frac{\partial\psi}{\partial x}=2\pi\phi\sin 2\pi x, && \text{at} \quad y=\eta(x)\end{aligned}\right\}. \tag{4.10}$$

where

$$u = \frac{\partial \psi}{\partial y}, v = -\alpha \frac{\partial \psi}{\partial x}, \omega = \alpha \frac{\partial v}{\partial x} - \frac{\partial u}{\partial y}, \tag{4.11}$$

$$\nabla^2 = \alpha^2 \frac{\partial^2}{\partial x^2} + \frac{\partial^2}{\partial y^2}, \phi = \frac{b}{\lambda}, \mathrm{Re} = \frac{ca}{\nu}\alpha, M = \sqrt{\frac{\sigma}{\mu}} B_0 a. \tag{4.12}$$

4.2 Numerical Analysis

The flow problem defined in Eqs. (4.8) and (4.9) subject to the boundary conditions given in (4.10) is solved numerically. Galerkin's variational finite element method based on technique is implemented to one part of moving wave which is considered to be our domain. Highly convergent results with tolerance $\varepsilon_\psi = \varepsilon_\omega = 10^{-14}$, have been obtained in $2-4$ number of iterations in all cases considering non-uniform mesh of quadratic triangular elements with six nodes using pedtool in MATLAB. The approximation of stream function and vorticity is given in Eq. (2.13). The weak form of the governing equation gives

$$\int_\Omega w_1 \left(\alpha^2 \frac{\partial^2 \psi}{\partial x^2} + \frac{\partial^2 \psi}{\partial y^2} + \omega\right) d\psi d\omega = 0, \tag{4.13}$$

$$\int_\Omega w_2 \left(\mathrm{Re}\left(\frac{\partial \psi}{\partial y}\frac{\partial \omega}{\partial x} - \frac{\partial \psi}{\partial x}\frac{\partial \omega}{\partial y}\right) - \left(\frac{1}{\zeta} + 1\right)\left(\alpha^2 \frac{\partial^2 \omega}{\partial x^2} + \frac{\partial^2 \omega}{\partial x^2}\right) - M^2 \frac{\partial^2 \psi}{\partial y^2}\right) d\psi d\omega = 0, \tag{4.14}$$

where w_1 and w_2 are the weight functions. After simplification of Eq. (4.13) and (4.14), we obtain,

$$\int_\Omega \left(\alpha^2 \frac{\partial w_1}{\partial x}\frac{\partial \psi}{\partial x} + \frac{\partial w_1}{\partial y}\frac{\partial \psi}{\partial y}\right) d\Omega + \int_\Omega w_1 \omega \, d\Omega = \int_\Gamma w_1 \frac{\partial \psi}{\partial n} d\Gamma, \tag{4.15}$$

$$\int_\Omega \mathrm{Re} w_2 \left(\frac{\partial \psi}{\partial y}\frac{\partial \omega}{\partial x} - \frac{\partial \psi}{\partial x}\frac{\partial \omega}{\partial y}\right) d\Omega + \left(\frac{1}{\zeta} + 1\right) \int_\Omega \left(\alpha^2 \frac{\partial w_2}{\partial x}\frac{\partial \omega}{\partial x} + \frac{\partial w_2}{\partial y}\frac{\partial \omega}{\partial y}\right) d\Omega + M^2 \int_\Omega \frac{\partial w_2}{\partial y}\frac{\partial \psi}{\partial y} d\Omega = \left(\frac{1}{\zeta} + 1\right) \int_\Gamma w_2 \frac{\partial \omega}{\partial n} d\Gamma + M^2 \int_\Gamma w_2 \frac{\partial \psi}{\partial n} d\Gamma. \tag{4.16}$$

Introducing Eq. (2.13) into Eqs. (4.15) and (4.16) and considering the discretized domain, simplified form of the governing equations in terms of system of algebraic equations is given by

$$-\sum_i B_{ki}^e \omega_i + \sum_i A_{ki}^e \psi_i = S_n^{k^e}, \tag{4.17}$$

$$\left(\frac{1}{\zeta} + 1\right) \sum_i A_{ki}^e \omega_i + \mathrm{Re} \sum_i C_{kij}^e \psi_i \omega_i + M^2 \sum_i D_{ki}^e \psi_i = M^2 S_n^{k^e}, \tag{4.18}$$

where

$$\left.\begin{aligned} A^e_{ki} &= \int_{\Omega^e}\left(\alpha^2\frac{\partial N_k}{\partial x}\frac{\partial N_i}{\partial x}+\frac{\partial N_k}{\partial y}\frac{\partial N_i}{\partial y}\right)d\Omega \\ B^e_{ki} &= \int_{\Omega^e} N_k N_i\, d\Omega \\ C^e_{kij} &= \int_{\Omega^e} N_k\left(\frac{\partial N_i}{\partial y}\frac{\partial N_j}{\partial x}-\frac{\partial N_j}{\partial x}\frac{\partial N_i}{\partial y}\right)d\Omega \\ D^e_{ki} &= \int_{\Omega^e}\frac{\partial N_k}{\partial y}\frac{\partial N_i}{\partial y}d\psi d\omega \\ S^{k^e}_n &= \int_{\Gamma} N_k\bar{S}_k d\Gamma \end{aligned}\right\}. \tag{4.19}$$

The global system is formulated and presented in matrix form defined as

$$\boldsymbol{KA} = \boldsymbol{F}, \tag{4.20}$$

where

$$K_{ij} = \begin{bmatrix} -B^e_{ki} & A^e_{ki} \\ \left(\frac{1}{\zeta}+1\right)A^e_{ki} & \mathrm{Re}C^e_{kij}\omega_i + M^2 D^e_{ki} \end{bmatrix}, A_k = \begin{bmatrix}\omega_k \\ \psi_k\end{bmatrix}, F = \begin{bmatrix} S^{k^e}_n \\ M^2 S^{k^e}_n\end{bmatrix}. \tag{4.21}$$

The non-linear algebraic system given in Eq. (4.20) is solved by using Newton's Raphson method iteratively to obtained desired accuracy.

4.3 Analysis of the Pressure

As Periodicity of the flow yields that the pressure and stress fields are only computed in the central region of the domain that occupies only one wavelength. It is convenient to reduced pressure gradient from governing Navier-Stokes equations in dimensionless form

$$\frac{\partial P}{\partial x} = \mathrm{Re}\left(\frac{\partial^2\psi}{\partial y^2}\frac{\partial\psi}{\partial x}-\frac{\partial^2\psi}{\partial x\partial y}\frac{\partial\psi}{\partial y}\right) - M^2\left(\frac{\partial\psi}{\partial y}+1\right) - \left(1+\frac{1}{\zeta}\right)\frac{\partial\omega}{\partial y}, \tag{4.22}$$

$$\frac{\partial P}{\partial y} = \mathrm{Re}\alpha^2\left(\frac{\partial^2\psi}{\partial x^2}\frac{\partial\psi}{\partial y}-\frac{\partial^2\psi}{\partial x\partial y}\frac{\partial\psi}{\partial x}\right) - \alpha\left(1+\frac{1}{\zeta}\right)\frac{\partial\omega}{\partial x}. \tag{4.23}$$

4.4 Validation

The numerical results obtained through present computations are validated against the results of Mehkeimer (2003), Jaffrin (1973) and Takabatake and Ayukawa (1982). The solution of Jaffrin (1973) is approximate and only valid for small values of wave number and Reynolds number. The comparison of the obtained velocity with the results of Mehkeimer (2003) is shown in **Figure 4.1**. It shows that our result is good agreement with that of Mekheimer's (2003). The comparison of pressure rise per wavelength based on the present FEM solution with results of Jaffrin (1973) and Takabatake and Ayukawa (1982) is plotted against flow rate in the fixed frame in **Figure 4.2**. It can be observed that our results are in excellent agreement with the Jaffrin (1973) results. The pressure-flow rate curves predicted by the FEM solution of Takabatake and Ayukawa

(1982) shows a significant deviation from the corresponding curve based on Jaffrin (1973) solution.

4.5 Result and Discussion

The numerical scheme discussed in the section 4.2 is implemented to obtain contours of streamlines, vorticity, graphs of longitudinal velocity and pressure distribution. Influence of amplitude ratio ϕ, Reynolds number Re, volume flow rate Q, Cason fluid parameter ζ, the Hartmann number M and the wave number α on the quantities of the interest are presented graphically and discussed in detail.

4.5.1 Velocity field

Figures 4.3- 4.6 are presented to analyze the influence of the involved parameters in the modeled equation on the velocity field at cross-section $x = 0$ for the case of Newtonian and non-Newtonian fluid. **Figure 4.3** shows that the upsurge in time mean flow rate Q enhances the velocity of the fluid in the whole region of the channel. The effects of Casson fluid parameter ζ on the velocity field are presented in **Figure 4.4**. It is observed that velocity field increases in the central part of the channel by enhancing the casson fluid parameter while decrease is noted in the region near the walls of the channel. The comparison of the velocity profile of Newtonian and non-Newtonian Casson fluid for diverse values of Hartmann number M and Reynolds number Re are presented in **Figures 4.5** and **4.6**. These figures show that the behavior of velocity for Newtonian and non-Newtonian Casson fluids in the central part of the channel and near in the peristaltic walls of the channel are entirely different. The increase in Hartmann number reflects the dominance of electromagnetic forces on viscous forces causing decrease in the velocity field in central region of the channel and increases the longitudinal velocity in region near the wall of the channel for both Newtonian and non-Newtonian fluid case. It can also be seen from **Figure 4.5(a)** that the flow becomes reversed near the wall for $M > 5$ but for Casson fluid, no such flow reversal is observed up to $M = 7$. Moreover, the flow is slower for Non-Newtonian Casson fluid because of stronger viscous effect in comparison to Newtonian fluid. The opposite behavior is reported by increasing the Reynolds number in **Figure 4.6**. Here flow is positive near the wall up to Re =15 but for the greater value of Reynolds number flow reversal is again observed near the wall. On contrary, for Casson fluid, no such flow reversal is observed up to $Re = 20$.

4.5.2 Trapping and vorticity

The formulation of a circulating bolus of fluid in the closed streamlines in the wave frame of the reference is known as trapping. The viscosity of the Casson fluid depends on the Casson fluid parameter and fluid becomes more viscous and becomes thicker as we increase the value of the Casson fluid parameter. The behavior of streamlines against Casson fluid parameter ζ is observed in **Figure 4.7**. The figure indicates that the volume of the trapping bolus increases by increasing the value of Casson fluid parameter. Furthermore, with the increasing values of Casson fluid parameters, the bolus marginally move towards center of the channel and the interface streamlines appear below the wall. The influence of Reynolds number on the behavior of streamlines are shown in **Figure 4.8**. Since Reynolds number corresponds to the ratio of the inertial forces over the forces caused by viscosity of the fluid, so the non-zero Reynolds number provided the effect of inertial forces on the considered flow model. For the larger value of Reynolds number which indicated the dominance of the inertial forces over viscous forces, the volume of bolus increase and bolus moves to the left side of the channel and more curvature effects of streamlines are noticed on the right side of the center of the channel. **Figure 4.9** shows the effects of Hartmann number on streamlines which shows opposite behavior as in the case of Reynolds number. Hartmann number shows the influence of the applied magnetic field on the flow modeled. As Hartmann number is representative of electromagnetic force cause by the applied magnetic field defined as the ratio of the electromagnetic force caused by the magnetic field to the viscous force, so by enhancing the values of Hartmann number reflected to the strong magnetic field which causes the resistance in the flow of the fluid so the trapped bolus formed shrinks which can be observed from **Figure 4.9**. **Figure 4.10** exhibits the effects of different values of wave number on the behavior of the streamlines. These effects are presented first time for the study of peristaltic flow of Casson fluid, as in earlier studies the use of lubrication theory is widely used which was not able to predict such effects. Since wave number corresponds to the ratio between the half width of the channel and the length of the wave in motion, so by enhancing values of the wave number considerably effects the flow of Casson fluid in Peristaltic motion which can be noticed by magnifying the volume of the trapped bolus through **Figure 4.10**. The vorticity field for various values of Casson fluid parameter γ is presented in **Figure 4.11**. For small value of ζ the curvature effects is dominant in middle part of the channel as the fluid is less viscous

and it penetrates to right side for large value for γ when the fluid is comparatively thicker. Moreover, the curvature effect is also dominant near the crest regions which means that the rotation of the fluid particles near the wall compared to the center of the channel is fast for large value of Casson fluid in comparison with that of Newtonian fluid.

4.5.2 Pressure distribution

The purpose of this subsection is to examine the important phenomena of pressure rise per wavelength in peristaltic transportation. Usually, three ranges of pumping in peristalsis are possible, for $\Delta P > 0$ corresponds to augmented pumping region while $\Delta P = 0$ is the free pumping region and $\Delta P < 0$ is the co-pumping region. The pressure rise is plotted against time mean flow rate to see the effects of change in values of different involved parameters in **Figure 4.12**. **Figure 4.12** reveals the effect of Reynolds number Re on pressure rise per wavelength. It is observed that for large values of Reynolds number which enhances the dominance of the inertial forces gives rise in pressure. Furthermore, pressure rise per wavelength shows non-linear behavior which is mainly caused by strong inertial forces. It is also noted that dominance of inertial forces to viscous forces causes augmentation in a rise in pressure and this fact is not yet reported. On the other hand, the increase in pressure rise is noticed with growing values of the Hartmann number M as shown in **Figure 4.13.** So, one way to control the pressure rise of peristaltic motion of Casson fluid in terms of blood flow model is by enhancing the strength of applied magnetic field, this fact is widely used in MRI and other bio medical treatments. Furthermore, increasing wave number α shows analogous behavior as of Reynolds number presented in **Figure 4.14**. The free pumping in this case is reported at $Q = 0.4$. The decrease in pressure rise in the pumping region is noticed through **Figure 4.15** due to increase in Casson fluid parameter γ, because of rise in viscosity, flow becomes slow and the pressure rise decreases. **Figure 4.15** also shows that in the augmented region $-1 < Q < 0.3$ pressure rise gives opposite result as compared to that of pumping region $0.3 < Q < 1$. Free pumping corresponds to $\Delta P = 0$ at $Q = 0.3$.

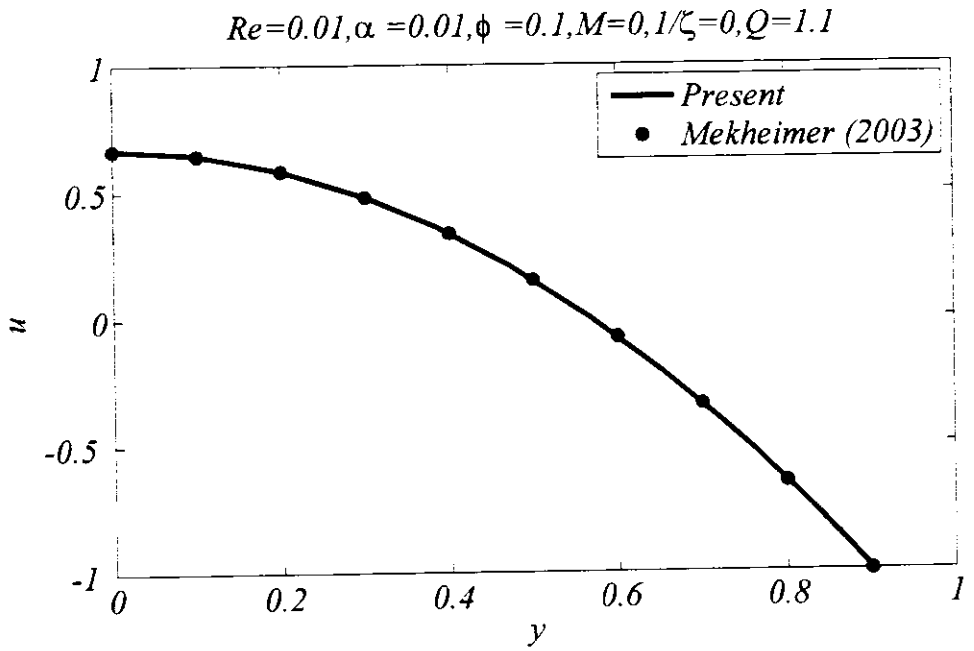

Figure 4.1: Comparison of computed velocity profile (solid line) of a sinusoidal wave with that of Mekheimer (2003)

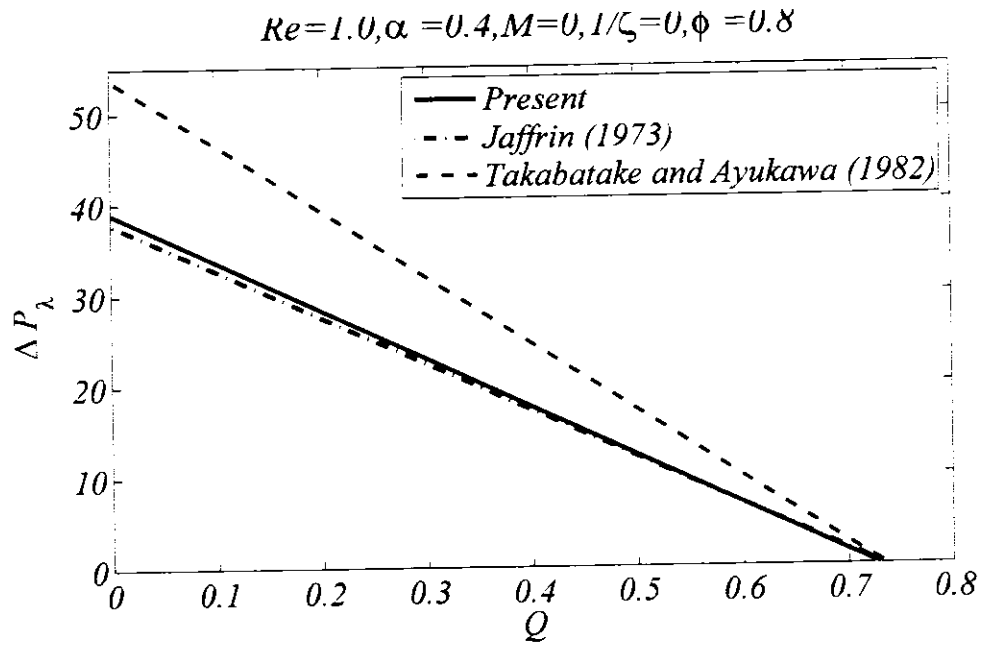

Figure 4.2: Comparison of computed pressure profile of the sinusoidal waveform with that of Jaffrin (1973) and Takabatake and Ayukawa (1982)

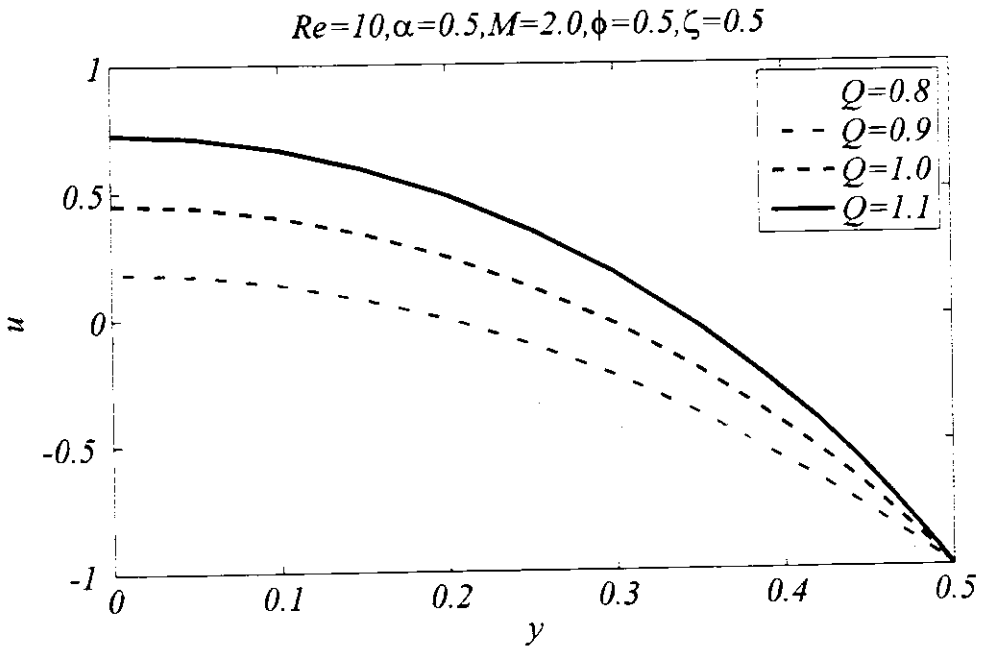

Figure 4.3: Graphs of longitudinal velocity for various values of Q against fixed values of other parameters

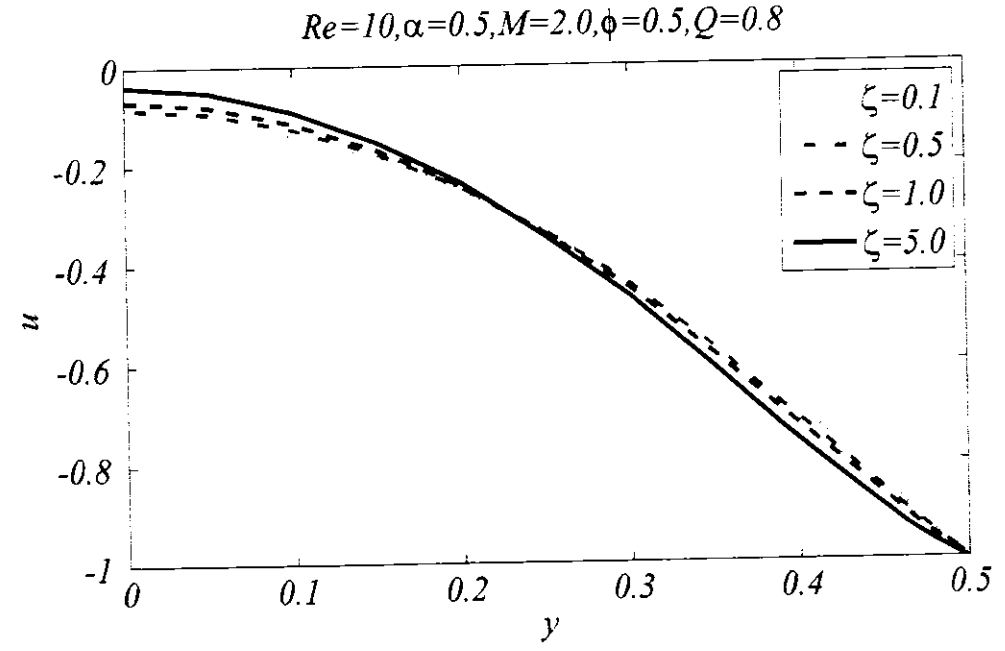

Figure 4.4: Graphs of longitudinal velocity for various values of ζ against fixed values of other parameters

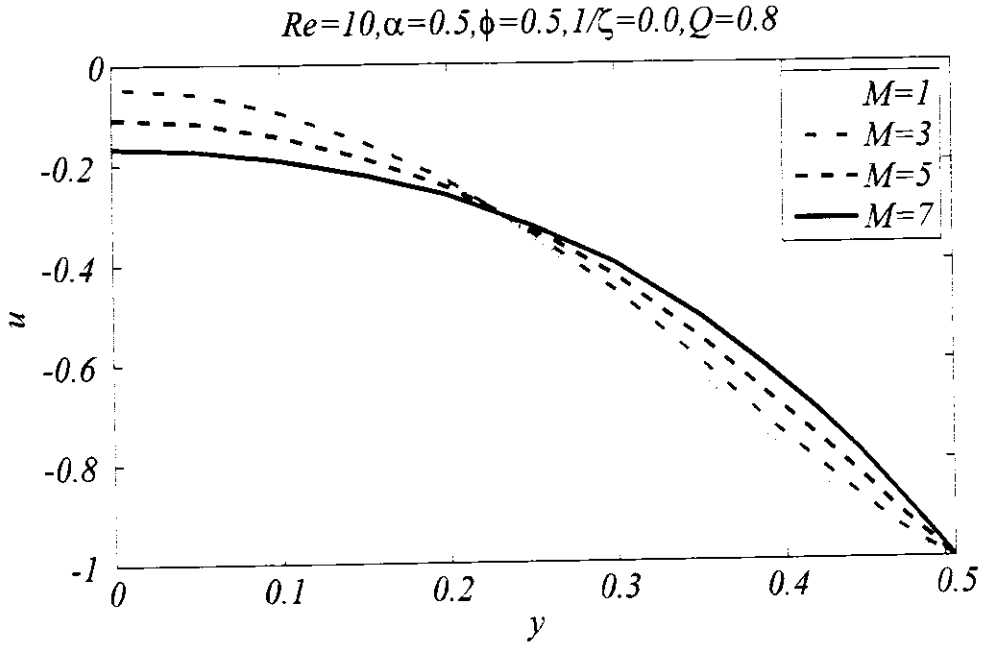

(a)

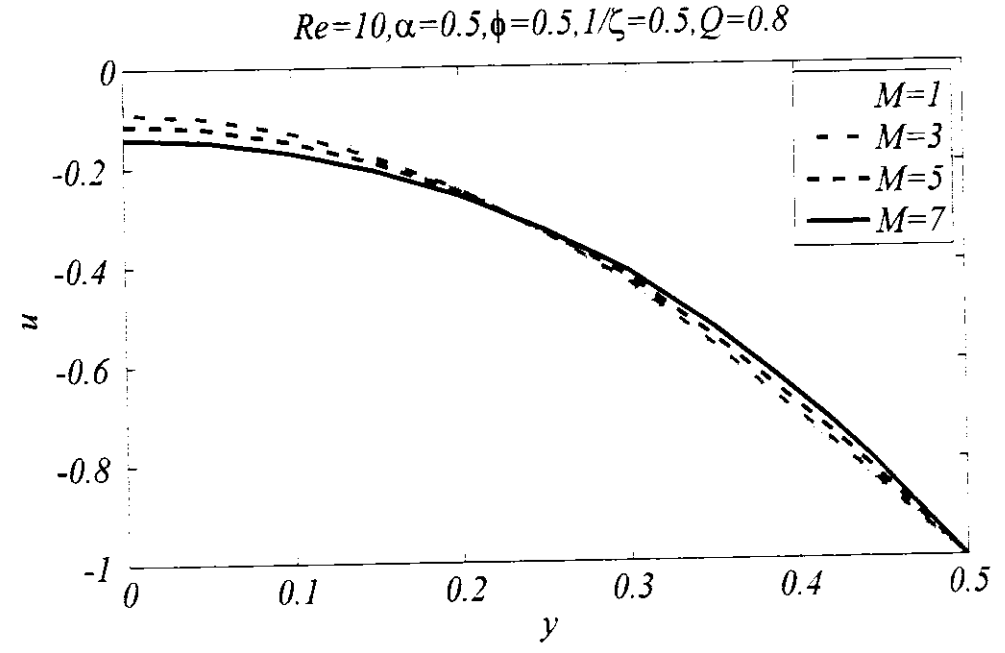

(b)

Figure 4.5: Comparison of longitudinal velocity for various values of M for Newtonian **(a)** Non-Newtonian fluid **(b)** with other parameters are fixed

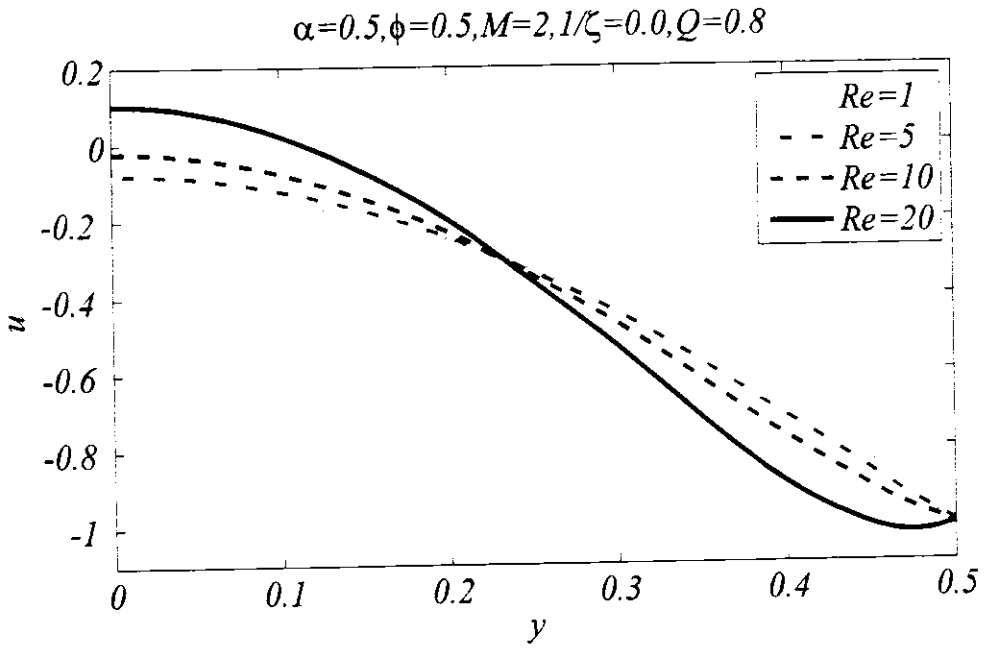

(a)

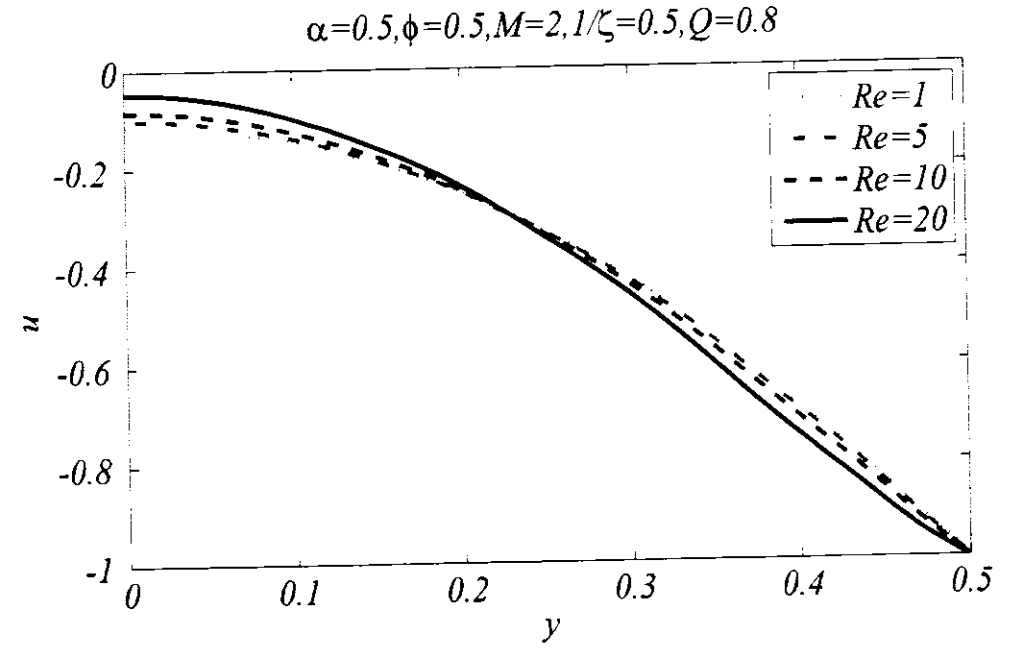

(b)

Figure 4.6: Comparison of longitudinal velocity for various values of *Re* for Newtonian **(a)** Non-Newtonian fluid **(b)** with other parameters are fixed

(a)

(b)

(c)

(d)

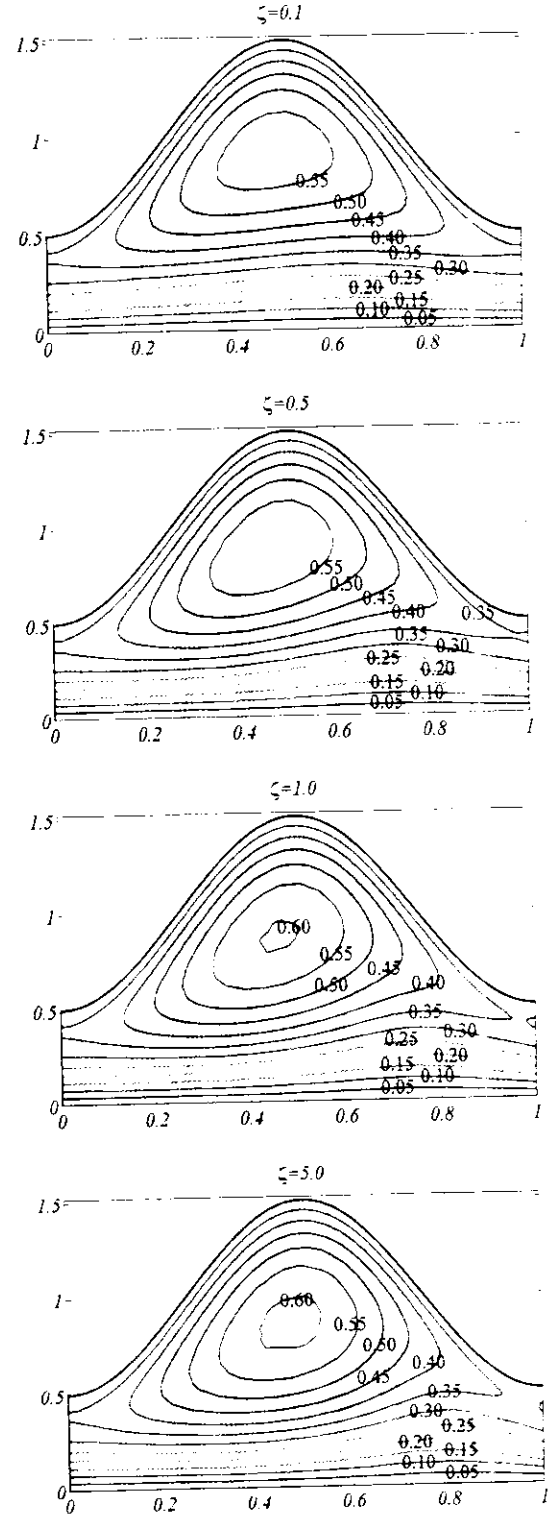

Figure 4.7: Variation of streamlines against different values of ζ in wave frame at $Re = 10, \alpha = 0.2,, M = 2\phi = 0.5$ and $Q = 1.3$

(a)

(b)

(c)

(d)

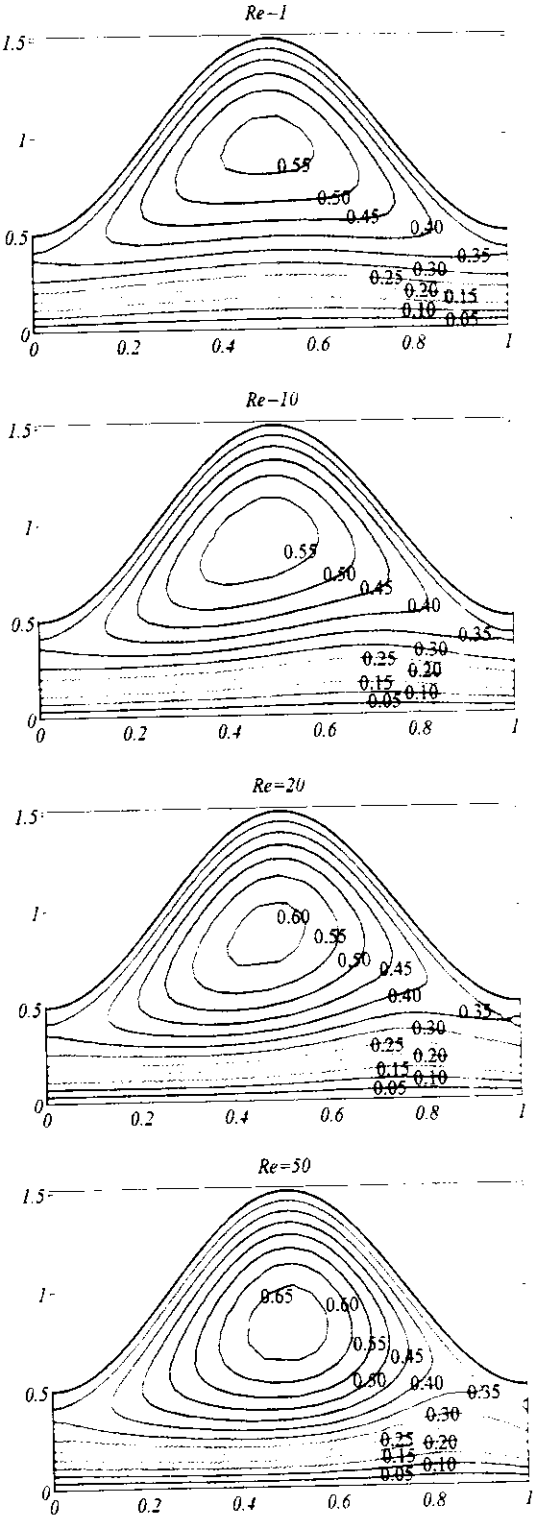

Figure 4.8: Variation of streamlines against different values of Re in wave frame at $\zeta = 0.3, M = 2, \alpha = 0.2, \phi = 0.5$ and $Q = 1.3$

(a)

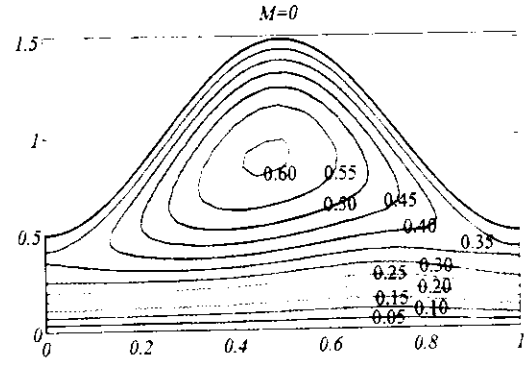

(b)

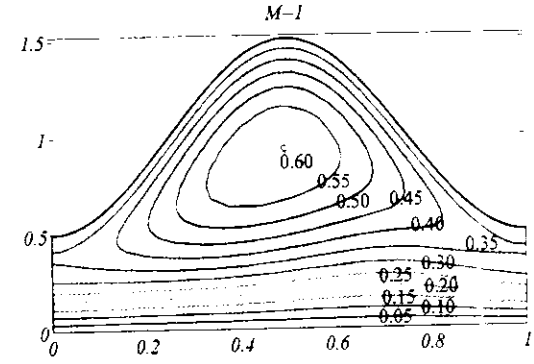

(c)

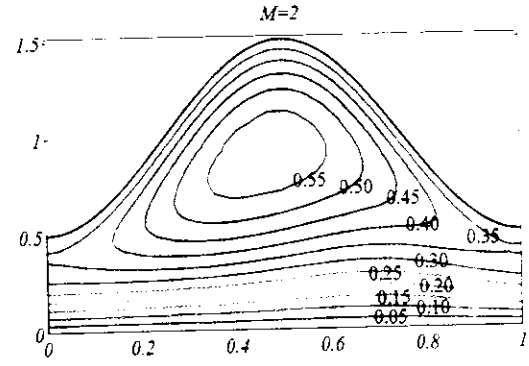

(d)

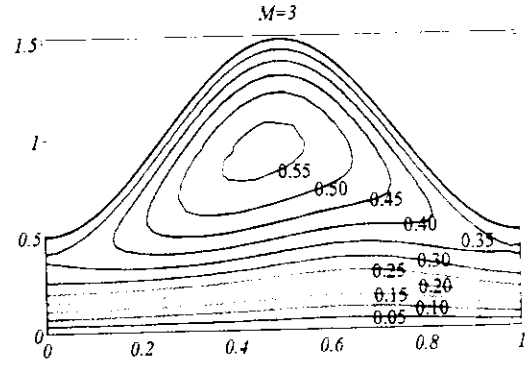

Figure 4.9: Variation of streamlines against different values of M in wave frame at $Re = 10, \zeta = 0.3, \alpha = 0.2, \phi = 0.5$ and $Q = 1.3$

(a)

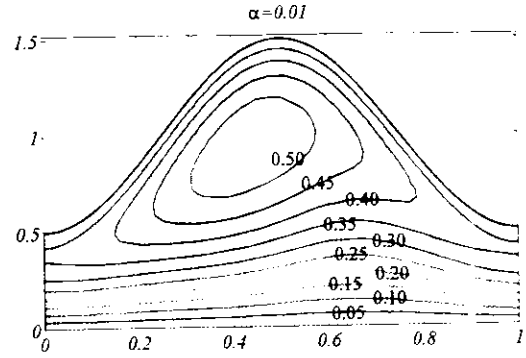

(b)

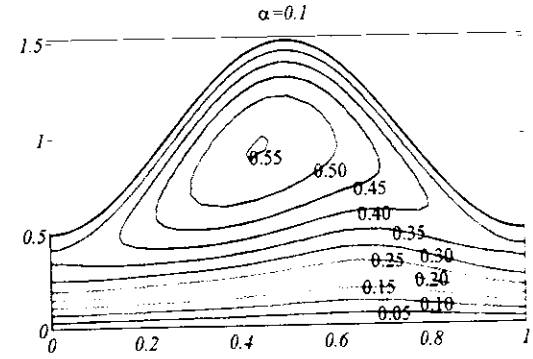

(c)

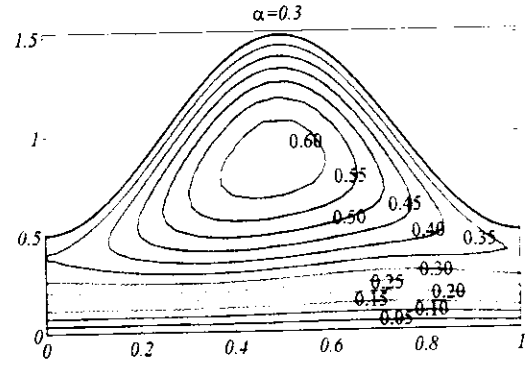

(d)

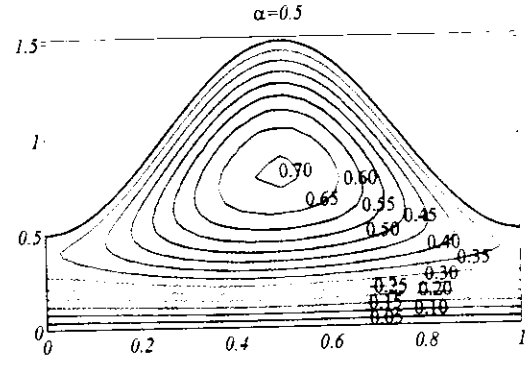

Figure 4.10: Variation of streamlines against different values of α in wave frame at $Re = 10, M = 2, \zeta = 0.3, \phi = 0.5$ and $Q = 1.3$

(a)

(b)

(c)

(d)

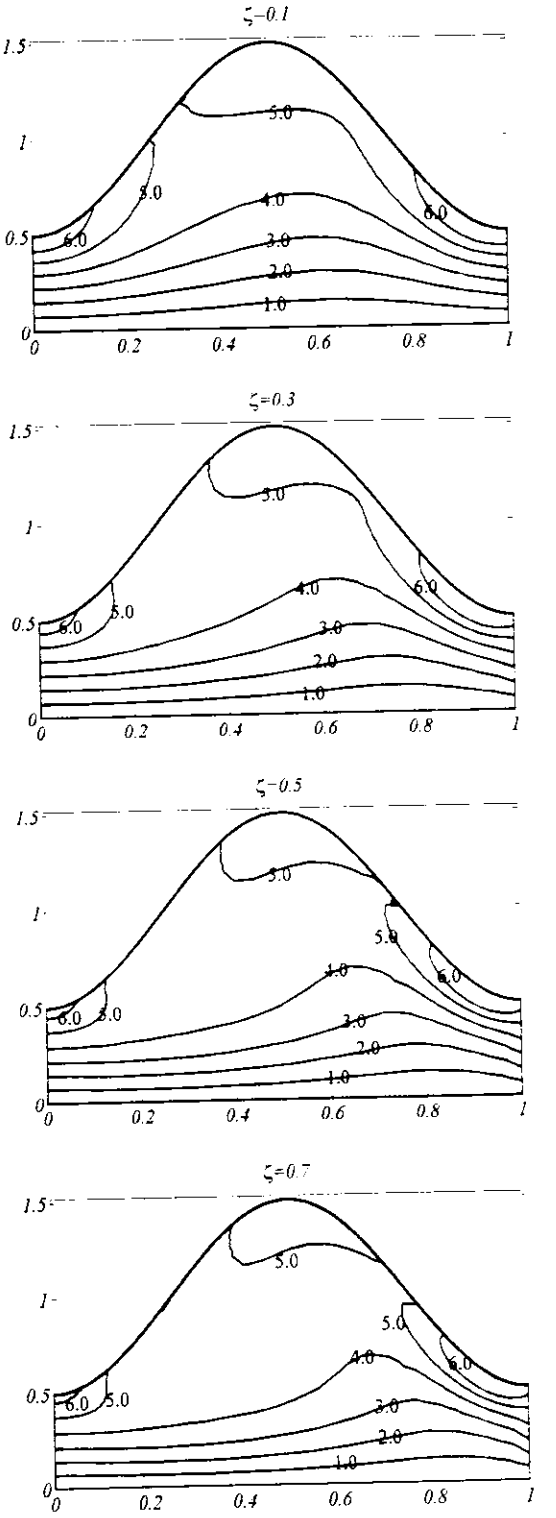

Figure 4.11: Variation of vorticity for different values of ζ at $Re = 10.0, M = 2, \alpha = 0.2$, $\phi = 0.5$ and $Q = 1.3$

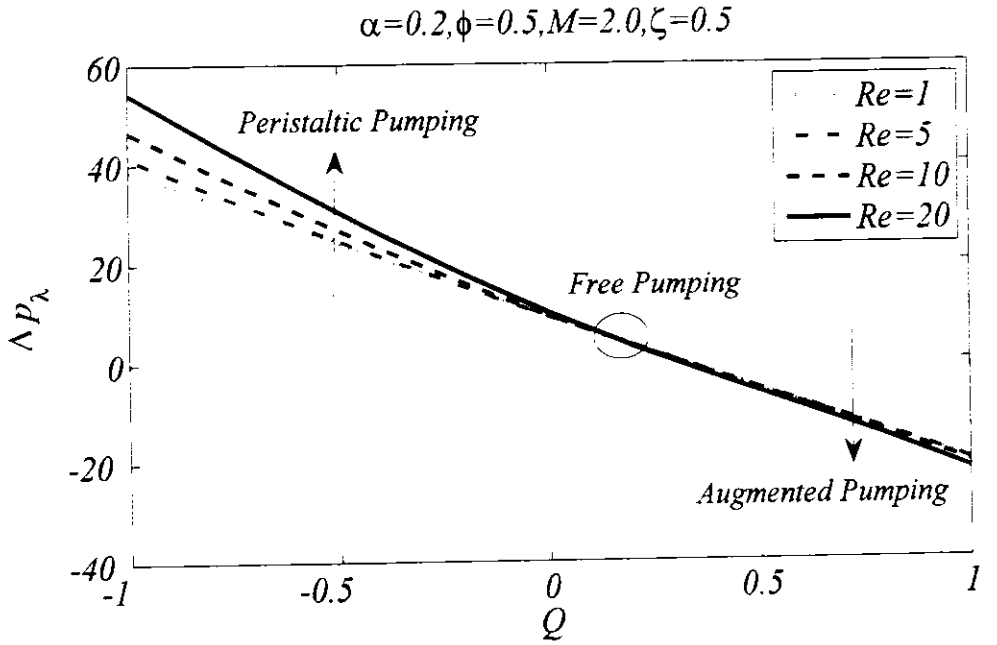

Figure 4.12: Pressure distribution for various values of Re against fixed values of other parameters

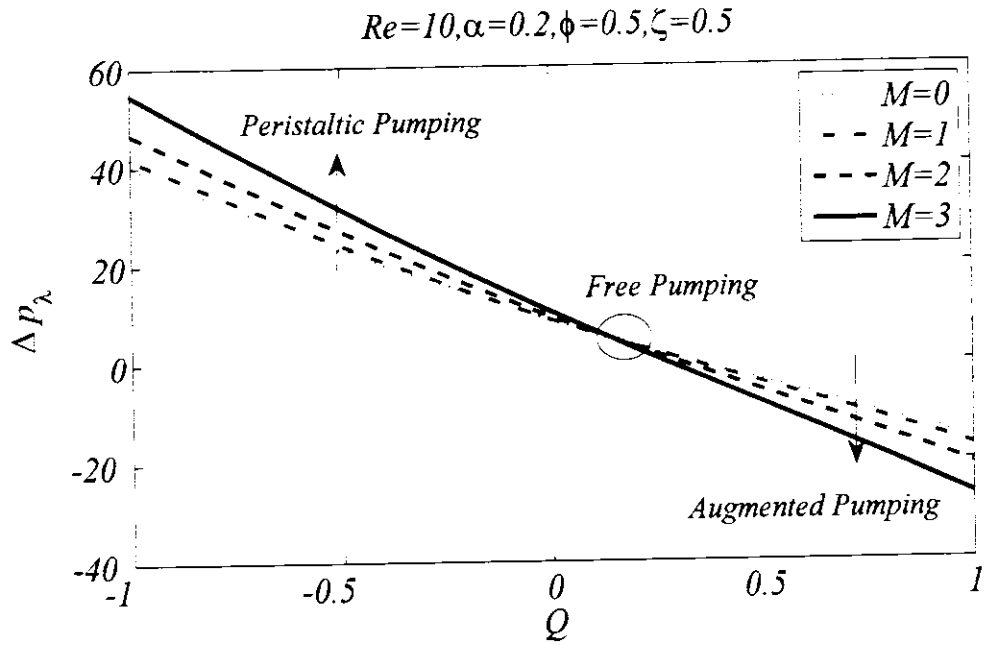

Figure 4.13: Pressure distribution for various values of M against fixed values of other parameters

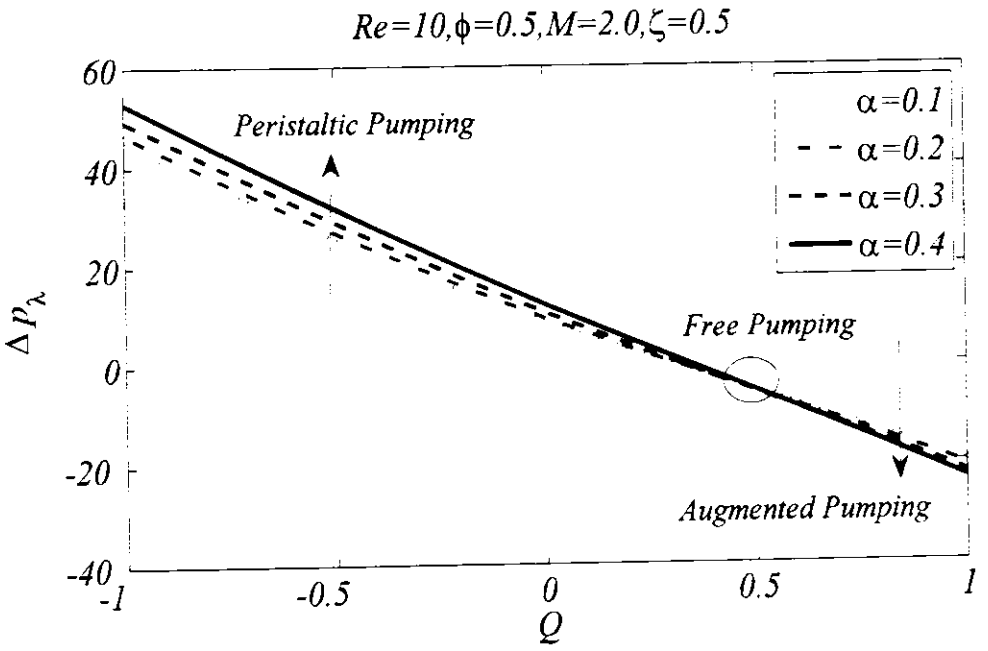

Figure 4.14: Pressure distribution for various values of α against fixed values of other parameters

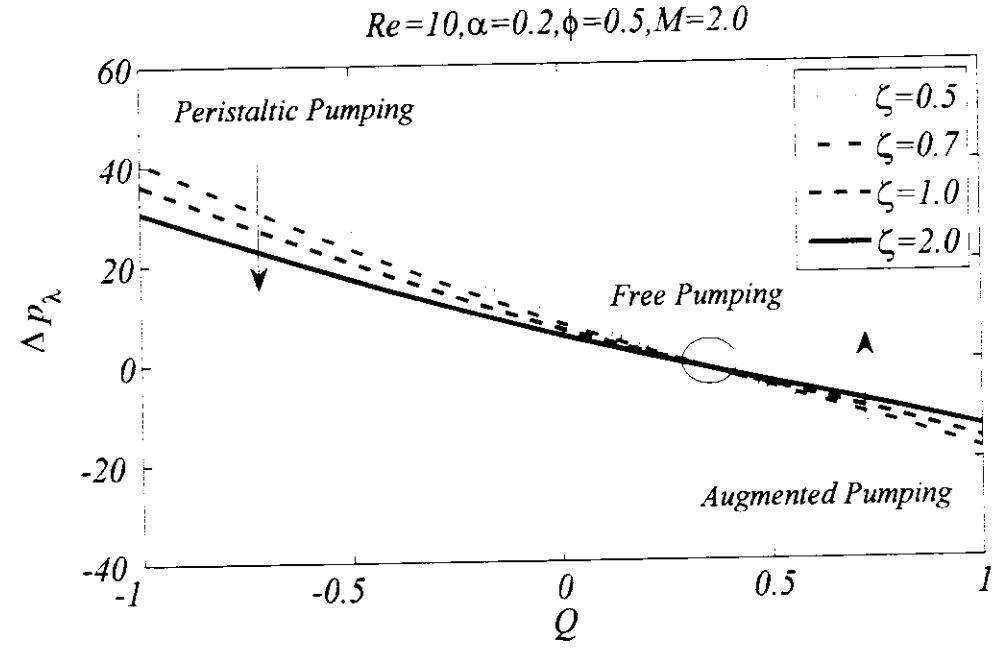

Figure 4.15: Pressure distribution for various values of ζ against fixed values of other parameters

4.6 Conclusions

The numerical simulation of hydromagnetic peristaltic flow of a Casson fluid through a channel is studied without employing the famous hypothesis of lubrication theory which gives us the chance to present the effects of all the involved parameters including Reynolds number at moderate values. The numerical results are presented through graphs and detailed discussion of the velocity profile, the contours of streamlines, vorticity and pressure rise per wavelength. It is observed that increase in Casson fluid parameter causes increase the volume of the bolus and slight movement towards center of the channel, increases in the velocity near the central region of the channel and decreases in the region of peristaltic wall. As far as the effect of Casson fluid parameter on vorticity is concern, more curvature effects are noted in central part for small values of Casson fluid parameter, and for large values of Casson fluid parameter more curvature effects in crest region are noted. The increasing values of Hartmann and Reynolds numbers causes increase in volume of the bolus while increase in velocity is noted near the center of the channel and opposite behavior is observed near the peristaltic wall. Comparison of Newtonian with the non-Newtonian Casson fluid is offered by plotting different graphs and found that the flow is comparatively slower in the case of the non-Newtonian Casson fluid with that of Newtonian fluid.

Unlike the earlier studies, the effects of dominant inertial forces in the study of the peristaltic flow of Casson fluid are discussed by setting moderate values of Reynolds number in the presence of non-zero wave number, which was neglected yet due to imposition of the long wavelength and low Reynolds approximations in most studies. First time in literature, the solution of the full form Navier-Stokes equations for the peristaltic motion of Casson fluid is provided. Hence, it is hoped that present study will serve as a benchmark for further research on peristaltic flows of non-Newtonian fluids without applying assumption of lubrication theory.

Chapter 5

Hydromagnetic Peristaltic Flow of Micropolar Fluid through a Channel

The analysis given in the current chapter is about the MHD flow of micropolar fluid induced by peristaltic waves passing through the porous saturated channel at large Reynolds number. The flow model is formulated without considering the assumptions of lubrication theory which yields the governing equations into a non-linear set of coupled partial differential equations which allows studying the peristaltic mechanism at non-zero Reynolds and wave numbers. To certify the correctness of the developed code, obtained outcomes are compared with the results presented in the literature and found in excellent covenant. The influence of other involved parameters on velocity, stream function and microrotation are discussed through graphs plotted by using Galerkin's finite element method. Besides that, the phenomena of pumping and trapping are also analyzed in the later part of the chapter. It is found that the peristalsis mixing can be enhanced by increasing Hartmann number while it reduces by increasing permeability of the porous medium.

5.1 Problem Formulation

Consider an unsteady two-dimensional peristaltic flow of micropolar fluid passing through a channel of width $2a$ with speed c occupied with porous-saturated medium. The fluid is assumed to be electrically conducting and uniform magnetic field is applied normal to the direction of the flow with strength B_0. The flow is assumed along x-axis while the y-axis is considered orthogonal to the flow. Here, due to small conductivity of fluid, the low R_m-approximation is assumed which allows to neglect induced magnetic field in comparison of applied magnetic field. The symmetry of the flow is about x-axis which is shown in **Figure 2.1**.Movement of the flexible boundary walls in the fixed frame of reference (X, Y) obeys the relation given in Eq. (2.1). For peristaltic flow of electrically conducting micropolar fluid under the inducement of the magnetic field passing through the porous saturated channel, the laws that conserved the mass, linear momentum and angular momentum are expressed as

$$\nabla . \boldsymbol{V}^* = 0, \tag{5.1}$$

$$\rho(\boldsymbol{V}^* . \nabla \boldsymbol{V}^*) = -\nabla P + (\mu + \bar{\kappa})\nabla^2 \boldsymbol{V}^* + \bar{\kappa}\nabla \times \boldsymbol{G}^* + \boldsymbol{J} \times \boldsymbol{B} - \frac{\mu}{k}\boldsymbol{V}^*, \tag{5.2}$$

$$\rho J^*(\boldsymbol{V}^* . \nabla \boldsymbol{G}^*) = -2\bar{\kappa}\boldsymbol{G}^* - \bar{\gamma}(\nabla \times \nabla \times \boldsymbol{G}^*) + \bar{\kappa}\nabla \times \boldsymbol{V}^* + (\bar{\alpha} + \bar{\beta} + \bar{\gamma})\nabla(\nabla . \boldsymbol{G}^*), \tag{5.3}$$

where $\boldsymbol{V}^*$is the velocity vector define as $\boldsymbol{V}^* = (u^*, v^*, 0)$, $\boldsymbol{G}^*$ is the microrotation vector defined as $\boldsymbol{G}^* = (0, 0, g^*)$, $\boldsymbol{J}$ corresponds to the current density, $\boldsymbol{B}$ is the applied magnetic field defined as $\boldsymbol{B} = (0, B_0, 0)$, ρ corresponds to the fluid density, p^* symbolized the pressure of the fluid, J^* symbolized the microgyration parameter, μ represents classical viscosity coefficient, k represents the permeability of porous medium, $\bar{\alpha}, \bar{\beta}$ and $\bar{\gamma}$ are the coefficients of spin gradient viscosity and $\bar{\kappa}$ characterizes the coefficient of vortex viscosity. The material constraints $\mu, \bar{\kappa}, \bar{\alpha}, \bar{\beta}$ and $\bar{\gamma}$ must satisfies the following relations Eringen (1966) given in Eq. (1.16). Here, it is required to solve the considered problem in wave frame of reference (x^*, y^*). The wave frame and fixed frame (X, Y) are connected by the relations given in Eqs. (2.2) and (3.1), the Eqs. (5.1) to (5.3) govern the two-dimensional micropolar fluid flow through a uniform porous saturated medium subject to transverse uniform magnetic field in the wave frame that yields following simplified equations

$$\frac{\partial u^*}{\partial x^*} + \frac{\partial v^*}{\partial y^*} = 0, \tag{5.4}$$

$$\rho\left(u^*\frac{\partial u^*}{\partial x^*} + v^*\frac{\partial u^*}{\partial y^*}\right) = -\frac{\partial p^*}{\partial x^*} + (\mu + \kappa)\left(\frac{\partial^2 u^*}{\partial x^{*2}} + \frac{\partial^2 u^*}{\partial y^{*2}}\right) + \kappa\frac{\partial g^*}{\partial y^*} - \left(\sigma B_0^2 + \frac{\mu}{k}\right)(u^* + c) \tag{5.5}$$

$$\rho\left(u^*\frac{\partial v^*}{\partial x^*} + v^*\frac{\partial v^*}{\partial y^*}\right) = -\frac{\partial p^*}{\partial y^*} + (\mu + \kappa)\left(\frac{\partial^2 v^*}{\partial x^{*2}} + \frac{\partial^2 v^*}{\partial y^{*2}}\right) - \kappa\frac{\partial g^*}{\partial x^*} - \frac{\mu}{k}(v^* + c), \tag{5.6}$$

$$\sigma J^*\left(u^*\frac{\partial g^*}{\partial x^*} + v^*\frac{\partial g^*}{\partial y^*}\right) = -2\kappa g^* + \gamma\left(\frac{\partial^2 g^*}{\partial x^{*2}} + \frac{\partial^2 g^*}{\partial y^{*2}}\right) + \kappa\left(\frac{\partial v^*}{\partial x^*} - \frac{\partial u^*}{\partial y^*}\right), \tag{5.7}$$

with appropriate boundary conditions

$$\left.\begin{aligned} &\frac{\partial u^*}{\partial y^*} = 0, \quad v^* = 0, && g^* = 0 \ \text{ at } y^* = 0, \\ &u^* = c, \quad v^* = -\frac{2\pi bc}{\lambda}\sin\left(\frac{2\pi x^*}{\lambda}\right), && g^* = 0 \ \text{ at } y^* = \eta(x^*) \end{aligned}\right\}, \tag{5.8}$$

where $\eta(x^*)$ represents the restriction in the wave frame of the moveable boundary wall, which takes the form given in Eq. (2.6). To make the above model dimensionless, dimensionless variables given in Eq. (2.8), (3.14) and (5.9) are incorporated into each equation

$$g = \frac{g^*}{c}, J = \frac{J^*}{a^2}, K = \frac{k^*}{a^2}, Re = \frac{ca}{\nu}\alpha, M = \sqrt{\frac{\sigma}{\mu}}B_0 a. \tag{5.9}$$

where K symobolized the permeability of the porous medium. Eliminating pressure gradient terms by cross differentiation, and by inserting the stream function along with vorticity defined by the relations given in Eq. (4.11), governing equations for the considered flow in $\psi - \omega$ formulation takes the form

$$\alpha^2 \frac{\partial^2 \psi}{\partial x^2} + \frac{\partial^2 \psi}{\partial y^2} = -\omega, \tag{5.10}$$

$$Re\left(\frac{\partial \psi}{\partial y}\frac{\partial \omega}{\partial x} - \frac{\partial \psi}{\partial x}\frac{\partial \omega}{\partial y}\right) = \frac{1}{1-N}(\nabla^2 \omega - N\nabla^2 g) + M^2 \frac{\partial^2 \psi}{\partial y^2} - \frac{1}{k}\omega, \tag{5.11}$$

$$ReJ\left(\frac{1-N}{N}\right)\left(\frac{\partial \psi}{\partial y}\frac{\partial g}{\partial x} - \frac{\partial \psi}{\partial x}\frac{\partial g}{\partial y}\right) = \omega - 2g + \frac{2-N}{m^2}\nabla^2 g, \tag{5.12}$$

The boundary conditions take the form given as

$$\left.\begin{array}{lll} \frac{\partial \psi}{\partial x} = 0, & \frac{\partial^2 \psi}{\partial y^2} = 0, & g = 0, \quad \text{at } y = 0, \\ \frac{\partial \psi}{\partial x} = 2\pi\phi \sin 2\pi x, & \frac{\partial \psi}{\partial y} = -1, & g = 0, \quad \text{at } y = \eta(x) \end{array}\right\}. \tag{5.13}$$

where $N = \kappa/(\mu + \kappa)$ is the coupling number ranges from 0 to 1, $m^2 = \alpha^2\kappa(2\mu + \kappa)/(\gamma(\mu + \kappa))$ symbolizes the micropolar parameter and $\nabla^2 = \frac{\partial^2}{\partial x^2} + \frac{\partial^2}{\partial y^2}$.

5.2 Numerical Analysis

To get the numerical solution, governing Eqs. (5.10) - (5.12) subject to boundary conditions (5.13) are exposed to finite element method expressed by Kwon and Bang (1991) and Ferreira (2009). It is a very effective technique used to solve nonlinear equations by involving relatively low investment and rapid convergence. The quality of approximation of finite element method is also very high as compared to other methods. The most attractive and reasonable advantage to use this method is the ability to handle the complex geometries by discretizing the domain into a mesh of triangular/rectangular shape by which solution of the system can be simulated at any point or region of the domain. So, the domain is discretized into a non-uniform mesh of six nodal quadratic triangular elements with the help of pdetool in MATLAB. Once solution matrix on each triangular mesh is obtained, they are assembled into a global system of matrices. First, finite element method is exposed to governing equations to

transform them into a system contains the set of nonlinear algebraic equations which is then cracked by Newton-Raphson method. The technique of the method implemented to the problem is as follows:

The dependent variables involved in governing Eqs. (5.10) - (5.12) are approximated by the function given in Eqs. (2.13) and (5.14)

$$g = \sum_{k=1}^{n} N_k w g_k, \tag{5.14}$$

where ψ_k, ω_k and w_k are nodal element approximation of stream function ψ, vorticity ω and microrotation w respectively. In our situation, we considered quadratic triangular elements which corresponds to $n = 6$. After applying Galerkin's finite element method to Eqs. (5.10) to (5.12), we get

$$\int_{\Omega} w_1 \left(\alpha^2 \frac{\partial^2 \psi}{\partial x^2} + \frac{\partial^2 \psi}{\partial y^2} + \omega\right) d\Omega = 0, \tag{5.15}$$

$$\int_{\Omega} w_2 \left(Re\left(\frac{\partial \psi}{\partial y}\frac{\partial \omega}{\partial x} - \frac{\partial \psi}{\partial x}\frac{\partial \omega}{\partial y}\right) - \frac{1}{1-N}\left(\alpha^2 \frac{\partial^2 \omega}{\partial x^2} + \frac{\partial^2 \omega}{\partial y^2}\right) + \frac{N}{1-N}\left(\alpha^2 \frac{\partial^2 g}{\partial x^2} + \frac{\partial^2 g}{\partial y^2}\right) - M^2 \frac{\partial^2 \psi}{\partial y^2} + \frac{1}{k}\omega\right) d\Omega = 0, \tag{5.16}$$

$$\int_{\Omega} w_3 \left(ReJ\left(\frac{1-N}{N}\right)\left(\frac{\partial \psi}{\partial y}\frac{\partial g}{\partial x} - \frac{\partial \psi}{\partial x}\frac{\partial g}{\partial y}\right) - \omega + 2g - \frac{2-N}{m^2}\left(\alpha^2 \frac{\partial^2 g}{\partial x^2} + \frac{\partial^2 g}{\partial y^2}\right)\right) d\Omega = 0, \tag{5.17}$$

where w_1, w_2 and w_3 represents the weight functions and $d\Omega = 2\pi r dr dz$. Upon simplification of Eqs. (5.15) to (5.17), we get

$$\int_{\Omega} \left(\alpha^2 \frac{\partial w_1}{\partial x}\frac{\partial \psi}{\partial x} + \frac{\partial w_1}{\partial y}\frac{\partial \psi}{\partial y}\right) d\Omega - \int_{\Omega} w_1 \omega \, d\Omega = \int_{\Gamma} w_1 \frac{\partial \psi}{\partial n} d\Gamma, \tag{5.18}$$

$$Re \int_{\Omega} w_2 \left(\frac{\partial \psi}{\partial y}\frac{\partial \omega}{\partial x} - \frac{\partial \psi}{\partial x}\frac{\partial \omega}{\partial y}\right) d\Omega + \frac{1}{1-N}\int_{\Omega} \left(\alpha^2 \frac{\partial w_2}{\partial x}\frac{\partial \omega}{\partial x} + \frac{\partial w_2}{\partial y}\frac{\partial \omega}{\partial y}\right) d\Omega - \frac{N}{1-N}\int_{\Omega} \left(\alpha^2 \frac{\partial w_2}{\partial x}\frac{\partial g}{\partial x} + \frac{\partial w_2}{\partial y}\frac{\partial g}{\partial y}\right) d\Omega + M^2 \int_{\Omega} \left(\frac{\partial w_2}{\partial y}\frac{\partial \psi}{\partial y}\right) d\Omega + \frac{1}{K}\int_{\Omega} w_2 \omega d\Omega = \frac{1}{1-N}\int_{\Gamma} w_2 \frac{\partial \omega}{\partial n} d\Gamma - \frac{N}{1-N}\int_{\Gamma} w_2 \frac{\partial g}{\partial n} d\Gamma + M^2 \int_{\Gamma} w_2 \frac{\partial \psi}{\partial n} d\Gamma, \tag{5.19}$$

$$ReJ\left(\frac{1-N}{N}\right)\int_{\Omega} w_3 \left(\frac{\partial \psi}{\partial y}\frac{\partial g}{\partial x} - \frac{\partial \psi}{\partial x}\frac{\partial g}{\partial y}\right) d\Omega + \frac{2-N}{m^2}\int_{\Omega} \left(\alpha^2 \frac{\partial w_3}{\partial x}\frac{\partial g}{\partial x} + \frac{\partial w_3}{\partial y}\frac{\partial g}{\partial y}\right) d\Omega + 2\int_{\Omega} w_3 g d\Omega - \int_{\Omega} w_3 \omega d\Omega = \frac{2-N}{m^2}\int_{\Gamma} w_3 \frac{\partial g}{\partial n} d\Gamma, \tag{5.20}$$

where Ω is the area integral for each six nodal element and Γ represents the line integral on each six nodal element. After putting Eqs. (2.13) and (5.14)) into Eqs. (5.23) - (5.25) with assuming the discretized domain, one can get

$$\sum_i A_{ki}^e \psi_i - \sum_i B_{ki}^e \omega_i = S_n^{k^e}, \tag{5.21}$$

$$Re\sum_i C^e_{kij}\psi_i\omega_i + \frac{1}{1-N}\sum_i A^e_{ki}\omega_i + M^2\sum_i D^e_{ki}\psi_i - \frac{N}{1-N}\sum_i A^e_{ki}g_i +$$
$$\frac{1}{K}\sum_i B^e_{ki}\psi_i = \frac{1}{1-N}S^{k^e}_{n_1} + \frac{N}{1-N}S^{k^e}_{n_2} + M^2 S^{k^e}_{n}, \quad (5.22)$$

$$\frac{2-N}{m^2}\sum_i A^e_{ki}g_i + ReJ\left(\frac{1-N}{N}\right)\sum_i C^e_{kij}\psi_i g_i + 2\sum_i B^e_{ki}g_i - \sum_i B^e_{ki}\omega_i = \frac{2-N}{m^2}S^{k^e}_{n_2}, \quad (5.23)$$

where

$$\left.\begin{aligned} A^e_{ki} &= \int_{\Omega^e}\left(\alpha^2\frac{\partial N_k}{\partial x}\frac{\partial N_i}{\partial x} + \frac{\partial N_k}{\partial y}\frac{\partial N_i}{\partial y}\right)d\Omega, \\ B^e_{ki} &= \int_{\Omega^e} N_k N_i d\Omega, \\ C^e_{kij} &= \int_{\Omega} N_k\left(\frac{\partial N_i}{\partial y}\frac{\partial N_j}{\partial x} - \frac{\partial N_j}{\partial y}\frac{\partial N_i}{\partial x}\right)d\Omega, \\ D^e_{ki} &= \int_{\Omega}\left(\frac{\partial N_k}{\partial y}\frac{\partial N_k}{\partial y}\right)d\Omega \\ S^{k^e} &= \int_{\Gamma} N_k d\Gamma \\ S^{k^e}_{n_z} &= \int_{\Gamma} N_k\bar{S}_k d\Gamma, \text{ where } z = 1,2 \end{aligned}\right\}. \quad (5.24)$$

After assembly procedure, obtained resulting system (global) in the matrix arrangement is expressed as follows

$$\boldsymbol{KA = F}, \quad (5.25)$$

where the individual matrices are as follows

$$K_{ij} = \begin{bmatrix} -B^e_{ki} & A^e_{ki} & 0 \\ \frac{1}{1-N}A^e_{ki} & Re\, C^e_{kij}\omega_i + M^2 D^e_{ki} + \frac{1}{K}B^e_{ki} & -\frac{N}{1-N}A^e_{ki} \\ -B^e_{ki} & ReJ\, C^e_{kij}w_i & \frac{2-N}{m^2}A^e_{ki} + 2B^e_{ki} \end{bmatrix},$$
$$A_k = \begin{bmatrix}\omega_k \\ \psi_k \\ w_k\end{bmatrix}, F_k = \begin{bmatrix} S^{k^e}_{n} \\ \frac{1}{1-N}S^{k^e}_{n_1} + \frac{N}{1-N}S^{k^e}_{n_2} + M^2 S^{k^e}_{n} \\ \frac{2-N}{m^2}S^{k^e}_{n_2} \end{bmatrix}. \quad (5.26)$$

Eq. (5.25) represents the system of nonlinear algebraic equations which are solved by Newton-Raphson method. The procedure is iterated until the convergence condition described in previous chapter is achieved.

5.3 Analysis of the Pressure

As Periodicity of the flow yields that the pressure and stress fields are only computed in the central region of the domain that occupies only one wavelength. It is convenient to reduced pressure gradient from governing Navier-Stokes equations in dimensionless form

$$\frac{\partial p}{\partial x} = Re\left(\frac{\partial^2\psi}{\partial y^2}\frac{\partial\psi}{\partial x} - \frac{\partial^2\psi}{\partial x\partial y}\frac{\partial\psi}{\partial y}\right) - \frac{1}{1-N}\frac{\partial\omega}{\partial y} + \frac{N}{1-N}\frac{\partial g}{\partial y} - M^2\left(\frac{\partial\psi}{\partial y}+1\right) - \frac{1}{K}\left(\frac{\partial\psi}{\partial y}+1\right), \tag{5.27}$$

$$\frac{\partial p}{\partial y} = \alpha^3 Re\left(\frac{\partial^2\psi}{\partial x^2}\frac{\partial\psi}{\partial y} - \frac{\partial^2\psi}{\partial x\partial y}\frac{\partial\psi}{\partial x}\right) + \alpha^3\frac{1}{1-N}\frac{\partial\omega}{\partial y} - \alpha^2\frac{N}{1-N}\frac{\partial g}{\partial x} - \frac{1}{K}\left(\frac{\partial\psi}{\partial x}+1\right). \tag{5.28}$$

In the wave frame of reference at the center of the channel ($y = 0$), the computation of the pressure rise per wavelength is given in Eq. (2.25) and friction factor takes place by the relation

$$F_\lambda = \int_0^\lambda -h\frac{dp}{dx}dx. \tag{5.29}$$

5.4 Validation

In this section, we validated the computed numerical results by comparing it graphically with the results of Hayat et al. (2007) in limiting case after applying assumptions of lubrication theory in our model at the cross-section $x = 0$ of the channel and setting other values of time-mean flow rate $Q = 1.0$ and $Q = 1.4$. The solution of Hayat et al. (2007) is purely analytical and therefore it serves as a benchmark solution in this comparison. To this end, the curves of velocity based on computed solution are compared with the corresponding velocity curves obtained through the solution of Hayat et al. (2007) as shown in **Figure 5.1**. It is observed that the computed results for the limiting case ($M = 0, 1/K = 0$) are in close agreement with corresponding result of Hayat et al. (2007) and hence the solution computed is correct and the analysis presented is valid.

5.5 Results and Discussion

In this segment, we presented the obtained results through graphs of longitudinal velocity, pressure distribution, contours of streamlines, vorticity and microrotation for the peristaltic flow of micropolar fluid. First time in the literature, the influences of magnetic field and porosity parameter on the peristaltic flow of micropolar fluid at non-zero moderate Reynolds number are discussed by setting suitable values of the participating parameters through the plotted graph.

5.5.1 Velocity profile

The longitudinal velocity profile is plotted at the $x = 0$ cross-section of the channel with variations of participating parameters i.e. Reynolds number Re, wave number α, Hartmann number M, porosity parameter K, micropolar parameter m and coupling parameter N through **Figures 5.2 – 5.7**. It is noted form the figures of longitudinal

velocity that the behavior of velocity in the central part of the channel and in vicinity of the peristaltic walls entirely opposite. The longitudinal velocity for variation of Reynolds number i.e. $Re = 1, 5, 10$ and 20 is plotted with fixed values of $\alpha = 0.1, \phi = 0.5, N = 0.2, m = 2, J = 0.1, M = 2.0, Q = 1.4$ and $K = 0.5$ in **Figure 5.2**. The decrease in velocity is noticed with increase in Reynolds number in vicinity of the center of the channel while reverse behavior is observed in the neighbor of peristaltic wall. It predicts that the dominance of inertial forces to the viscous forces accelerates the velocity of the fluid near the walls of the channel, however, enhancement of inertial forces causes resistance to the flow in central part of the channel. These observations are attributed to strong inertial forces that perhaps is not predicted in earlier studies available in literature. Wave number α is basically the ratio of the half of the width of the channel to the wavelength. As mention above that in the present study, we are dropping the assumptions of low Reynolds number along with long wavelength, so it allows us to study the effects of wave number on the velocity of the fluid. Thus, the current study is valid for both long and short wavelength. To observe the variation of wave number $\alpha = 0.1, 0.3, 0.7$ and 0.9 the longitudinal velocity is plotted in **Figure 5.3** at stable values of other parameters $Re = 0.5, \phi = 0.5, N = 0.2, m = 2, J = 0.1, M = 2.0, Q = 1.4$ and $K = 0.5$. It exhibits the same behavior as that of the Reynolds number on the longitudinal velocity. The effects offered by the porous medium on the velocity profile are presented in **Figure 5.4** by plotting longitudinal velocity for numerous values of the parameter representing permeability of porous medium $K = 0.01, 0.05, 0.1$ and 0.5 with fixed values of $Re = 0.5, \alpha = 0.1, \phi = 0.5, N = 0.2, m = 2, J = 0.1, M = 2.0$ and $Q = 1.4$. It is noted that at the center of the channel, longitudinal flow velocity is in the direct proportional relation to the permeability of porous medium and inverse proportional relation to it near the walls of the channel. The resistance to flow provided by the magnetic field is presented in the **Figure 5.5** by plotting the longitudinal velocity for numerous values of Hartmann number $M = 1, 3, 5$ and 7 at fixed values of $Re = 0.5, \alpha = 0.1, \phi = 0.5, N = 0.2, m = 2, J = 0.1, Q = 1.4$ and $K = 0.5$. The increase in the strength of the magnetic field is attributed to the fact that magnetic body force retard the bulk motion of micropolar fluid due to peristalsis, resulting resistance in the flow near the central region of the channel. **Figures 5.6** and **5.7** are plotted to examine and analyzed the effects of the micropolar and coupling parameters respectively. In both figures, small effects are noticed for the variation of

both parameters. **Figure 5.6** is plotted for variation of micropolar parameter at $m = 1, 3, 5$ and 7 with fixed values of $Re = 0.5, \alpha = 0.01, \phi = 0.5, N = 0.2, J = 0.1, M = 2.0, Q = 1.4$ and $K = 0.5$. The slight decrease in velocity is noted by increasing micropolar parameter at the center of the channel, while in region of the peristaltic wall, enhancing the values of the micropolar parameter accelerates the velocity. The effects of coupling number are opposite to that of effects of micropolar parameter. In the **Figure 5.7**, the variation of the coupling number is presented by plotting longitudinal velocity for $N = 0.2, 0.4, 0.6$ and 0.8 with fixed values of $Re = 0.5, \alpha = 0.01, \phi = 0.5, m = 2, J = 0.1, M = 2.0, Q = 1.4$ and $K = 0.5$ which revels the fact that by escalation of the coupling number, the longitudinal velocity rises near the center of channel, but declines in the vicinity of the moving wall due to the static value of the flux rate is noted.

5.5.2 Trapping phenomena, vorticity and microrotation

Trapping is one of the important physical phenomenon in peristalsis. It depends on the formation of contours of streamlines. Sometimes, streamlines are not moving on the same path similar to that of the peristaltic wall rather splits and encloses a bolus of fluid in closed streamlines and thus circulating region arises. These trapped bolus and their movement along with the wave in the flow exhibit the trapping phenomenon for the peristaltic flow. The trapping phenomenon, vorticity along with microrotation for peristaltic transportation of non-Newtonian micropolar fluid beneath the influence of applied uniform magnetic field in the porous saturated channel for variation of participating parameters are presented in **Figures 5.8 – 5.10**. The effects of moderate Reynolds number on trapping phenomena, vorticity and microrotation of the flow is presented in **Figure 5.8**. The slight increase in the size of the bolus is noted by increasing Reynolds number with the tendency to move towards the central region of the channel. The vorticity generated at the peristaltic wall and disturbed in the central part of the crest region of the peristaltic wave due to increase in the Reynolds number. The microrotation of the micropolar particles is observed almost symmetric for low Reynolds number while the increase in Reynolds number declines the microrotation of the particles. **Figure 5.9** contains graphs of streamlines, vorticity and microrotation under the influence of applied magnetic field. Increase in the Hartmann number M reflects effects of enhancement in the strength of the magnetic field on peristaltic motion which increases the body force in the shape of the Lorentz force. It is noted

from the figure that peristaltic flow of the micropolar fluid is much affected by increasing the strength of magnetic field. The circulation of streamlines is weaken by increasing Hartmann number as the volume of trapping bolus shrinks and decreases in a number of boluses is noted, is consequent bolus formation can be controlled by regulating the strength of externally applied magnetic field. More vorticity lines generate at the peristaltic wall by enhancing the magnetic field with the tendency to cluster in the region of the peristaltic wall is observed. The strength of micro- rotations is noticed to decline with an escalation in the strength of magnetic field. The effects of the permeability of porous medium K on the fluid flow are presented in **Figure 5.10**. The permeability parameter K is not dependent on the nature of the fluid but only depends on the nature of the porous medium. It has been observed that amplification of permeability of porous medium augmented the strength of streamlines circulation that increases the number of the trapped boluses and magnified the size of the bolus. The circulation of the micropolar fluid has been noted in the vicinity of the peristaltic wall, but as we increase the permeability of porous medium, the fewer vorticity lines are noted moving towards the center of the channel which is also evident from the enhancement in the flow of the fluid. The strength of microrotation of the fluid particles escalates with an increase in the permeability allows by the uniform porous medium.

5.5.3 Pressure distribution and friction force

The pressure rise per wavelength on central line $y = 0$ is plotted against time-mean flow rate through **Figures 5.11 – 5.16** to examine the effects of participating parameters in suitable ranges which involves the numerical integration of pressure gradient and **Figures 5.17** and **5.18** presents the effects of friction force. Usually, the flow is discretized into four types of flow regions/quadrants and is known as adverse pressure if $\Delta P_\lambda > 0$ while $\Delta P_\lambda < 0$ is for favorable pressure gradient. The quadrant I corresponds to the flow in which time mean flow is positive with adverse pressure is known as peristaltic/positive pumping quadrant. The quadrant II corresponds to the flow in which time mean flow is negative with adverse pressure is known as retrograde/backward pumping quadrant. The quadrant III corresponds to the flow in which time mean flow is positive with $\Delta P_\lambda < 0$, and is known as co- pumping. The quadrant IV corresponds to the flow in which time mean flow is negative with $\Delta P_\lambda < 0$, and known as augmented pumping quadrant. Furthermore, in quadrant IV, the free pumping region exist when $\Delta P_\lambda = 0$ with $Q > 0$. Here, we discuss the pressure rise per

wavelength for peristaltic in augmented region which are of most interest in engineering and has vast applications including biomedical sciences. The pressure rise per wavelength for numerous values of Reynolds number is plotted in **Figure 5.11**. It reveals that pressure rise is increasing function of the dominant inertial forces induced by enhancing the Reynolds number in the region of peristaltic pumping while it is decreasing function of Re in the augmented region. Furthermore, it is noted that the behavior in the graph of pressure rise per wavelength is linear for small values of Reynolds number and nonlinear concave shape is observed for large values of Reynolds number. The wave number exhibits the same behavior as that of Reynolds number in both peristaltic pumping and augmented region as shown in **Figure 5.12**. **Figure 5.13** displays the characteristics of porous medium on the pressure rise per wavelength. In contrast to the effects of Hartmann number, the increasing values of permeability parameter diminishes the pressure rise in the peristaltic pumping region which can be interpreted in such a way that if the medium becomes more porous that enhances the flow rate by which it can be desisted by low pressure applied against it. The pressure rise per wavelength for different values of Hartmann number is plotted in **Figure 5.14**.

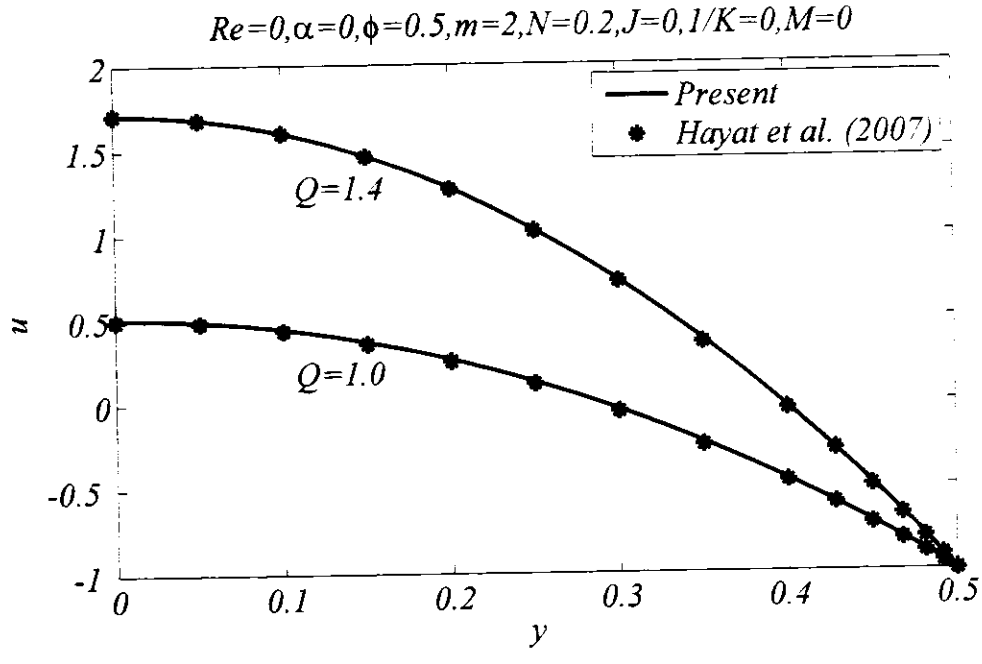

Figure 5.1: Comparison of computed results with that of Hayat et al. (2007) for longitudinal velocity.

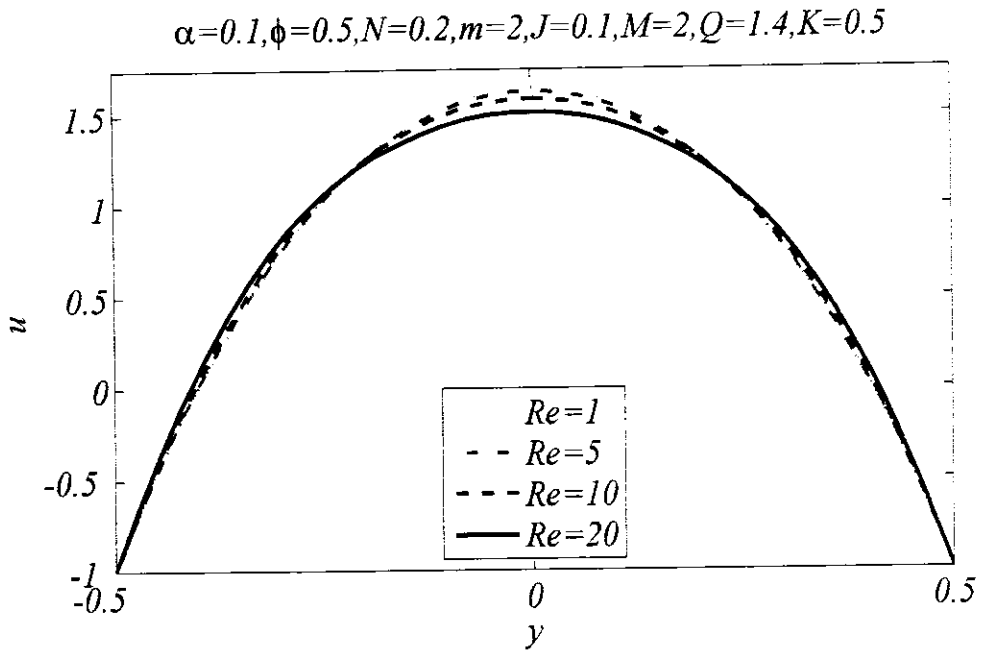

Figure 5.2: Velocity profile for variation of Reynolds number *Re* and values of other parameters are fixed

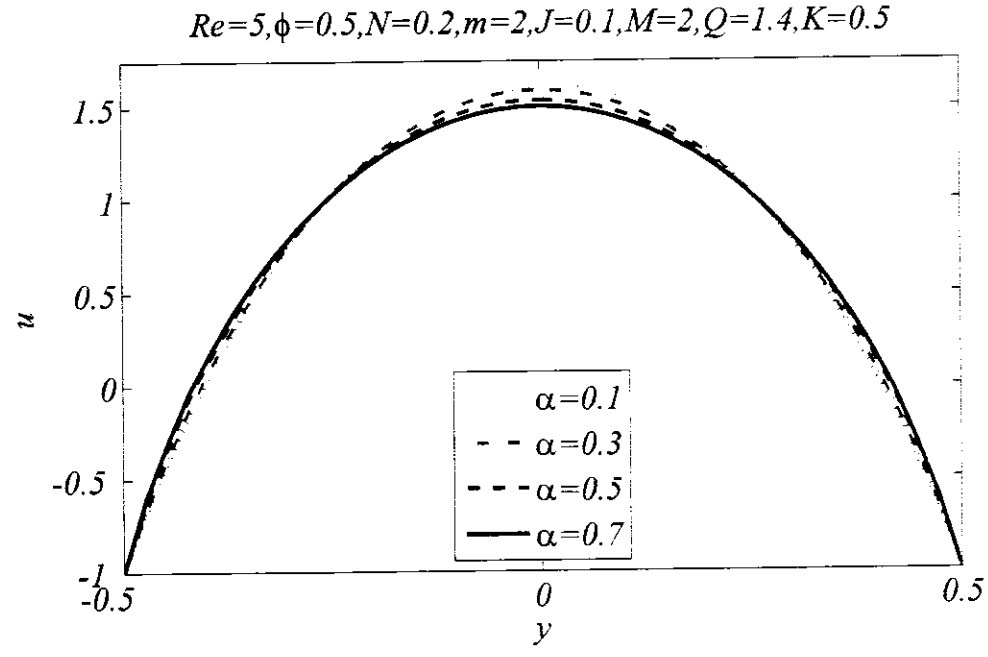

Figure 5.3: Velocity profile for variation of wave number α and values of other parameters are fixed

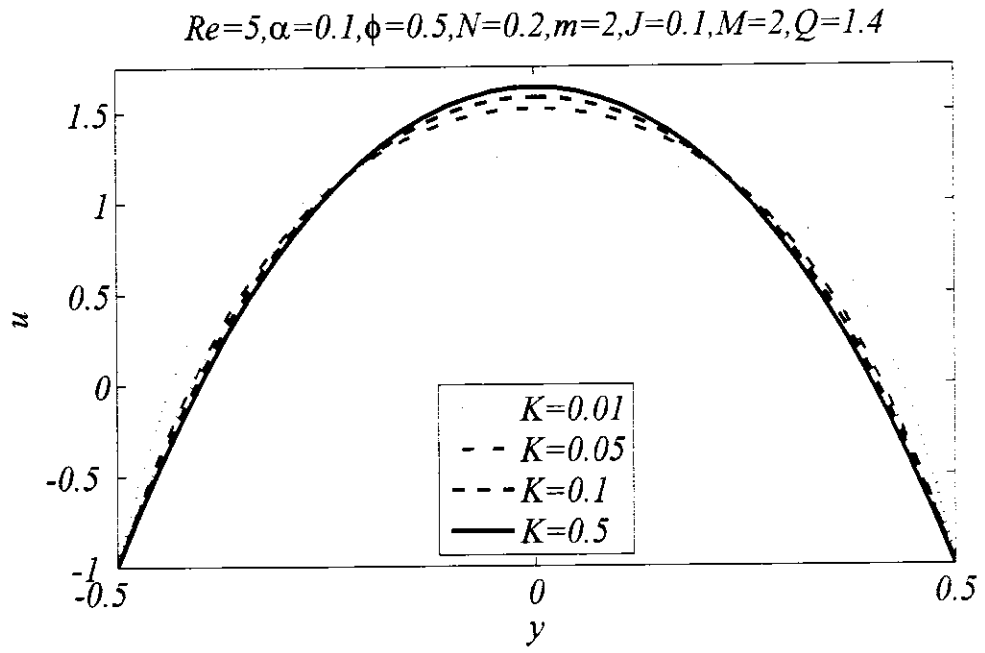

Figure 5.4: Velocity profile for variation of permeability of porous medium K and values of other parameters are fixed

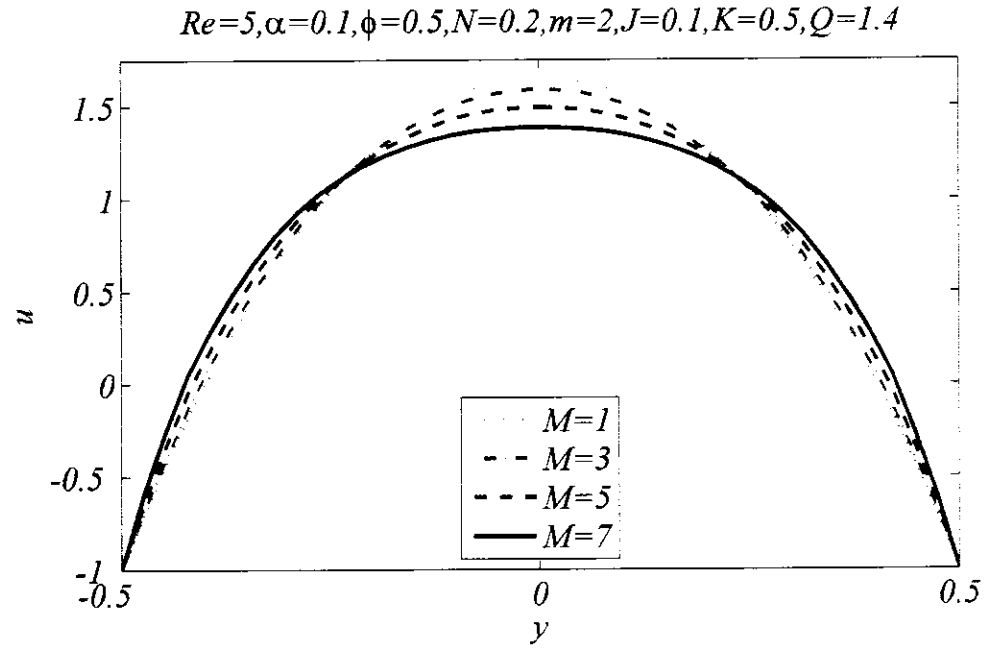

Figure 5.5: Velocity profile for variation of Hartmann number M and values of other parameters are fixed

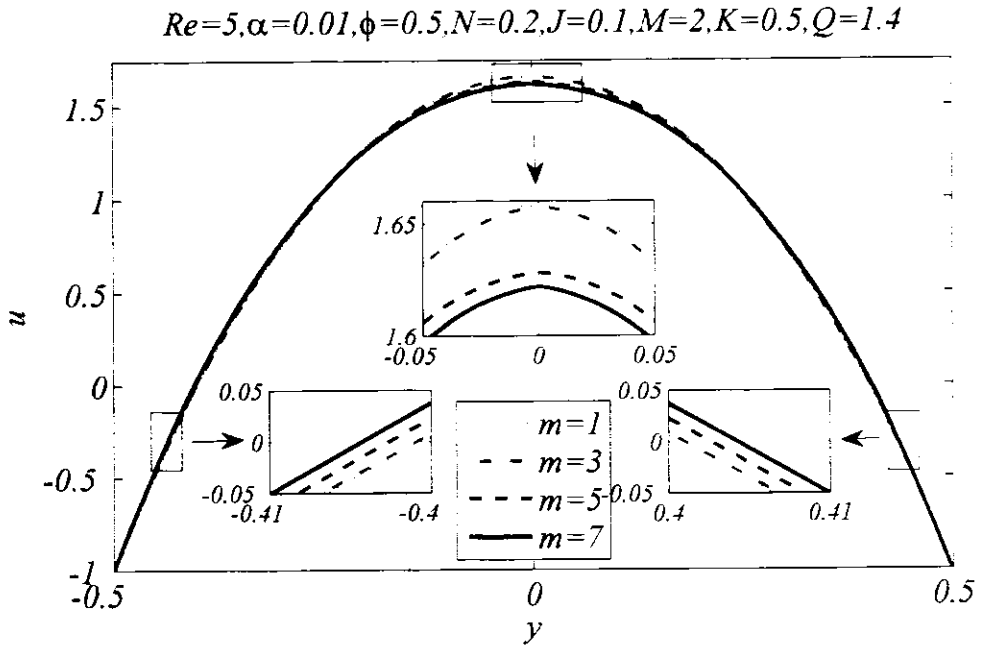

Figure 5.6: Velocity profile for variation of micropolar parameter m and values of other parameters are fixed

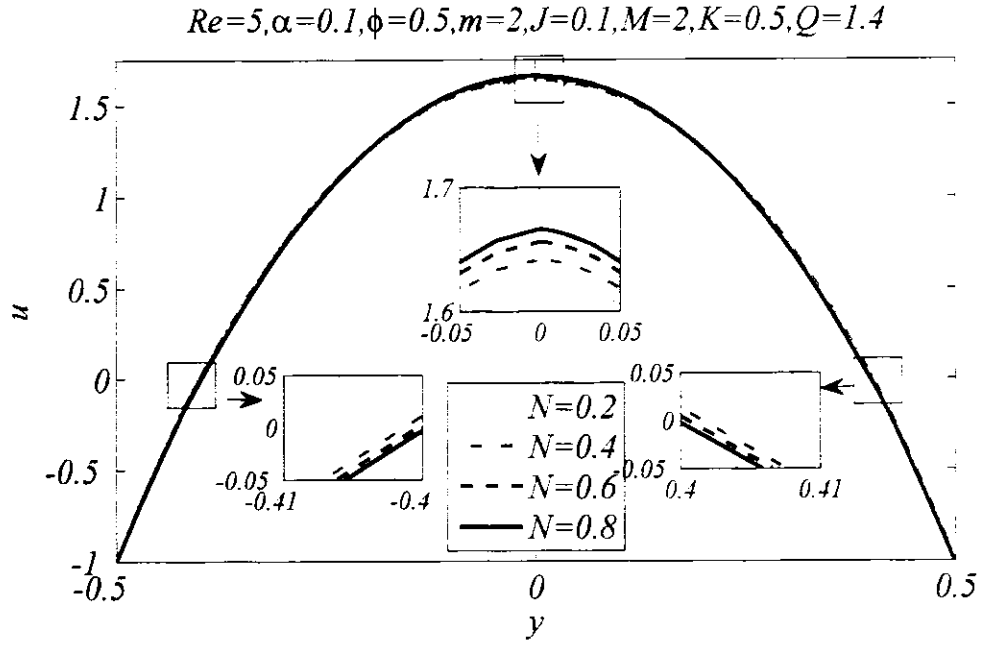

Figure 5.7: Velocity profile for variation of coupling number N and values of other parameters are fixed

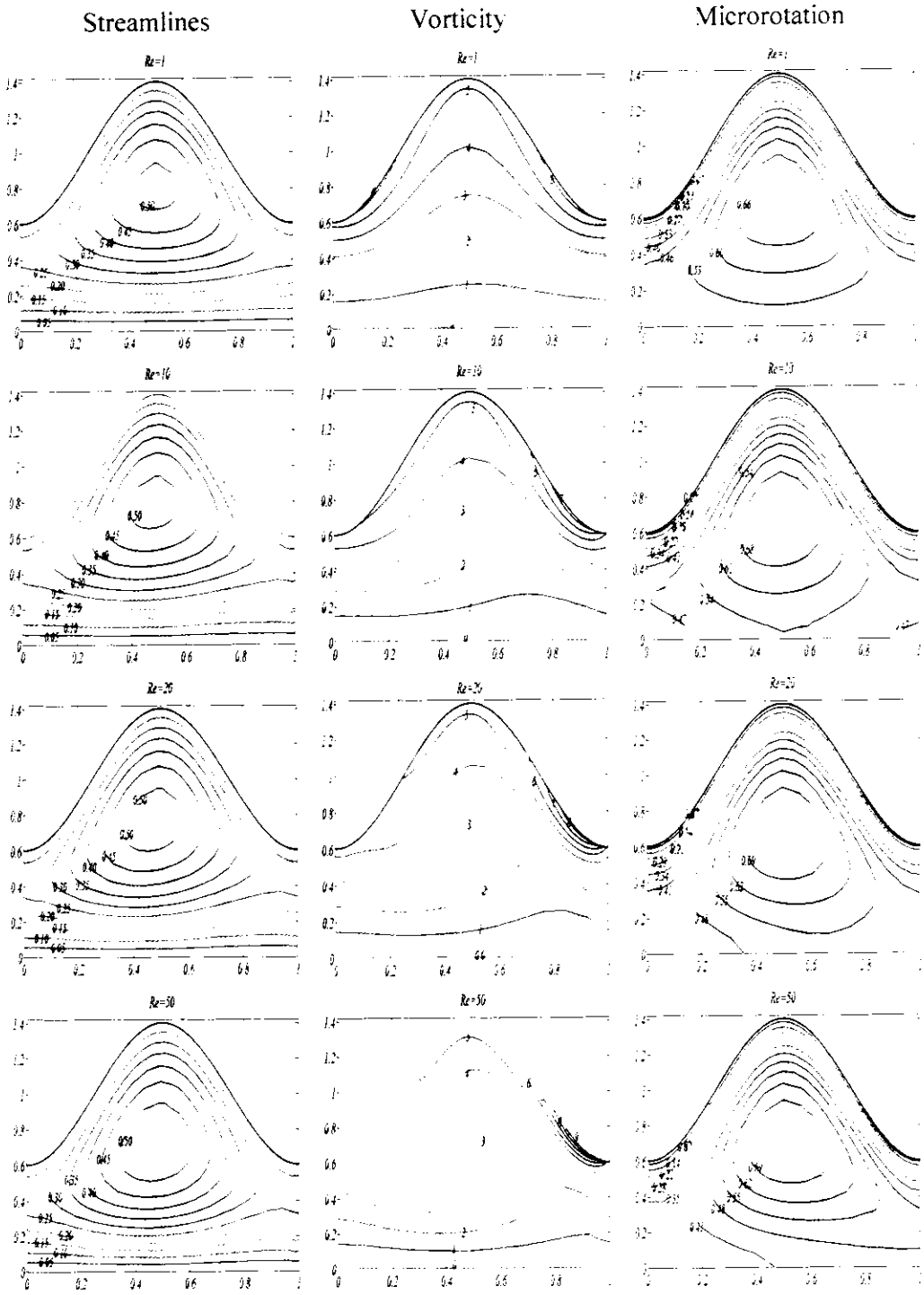

Figure 5.8: Streamlines, vorticity and microrotation for various values of Reynolds number Re and values of other parameters are fixed at $\alpha = 0.5, \phi = 0.4, m = 2, N = 0.5, M = 2, K = 0.5$ and $Q = 1.2$

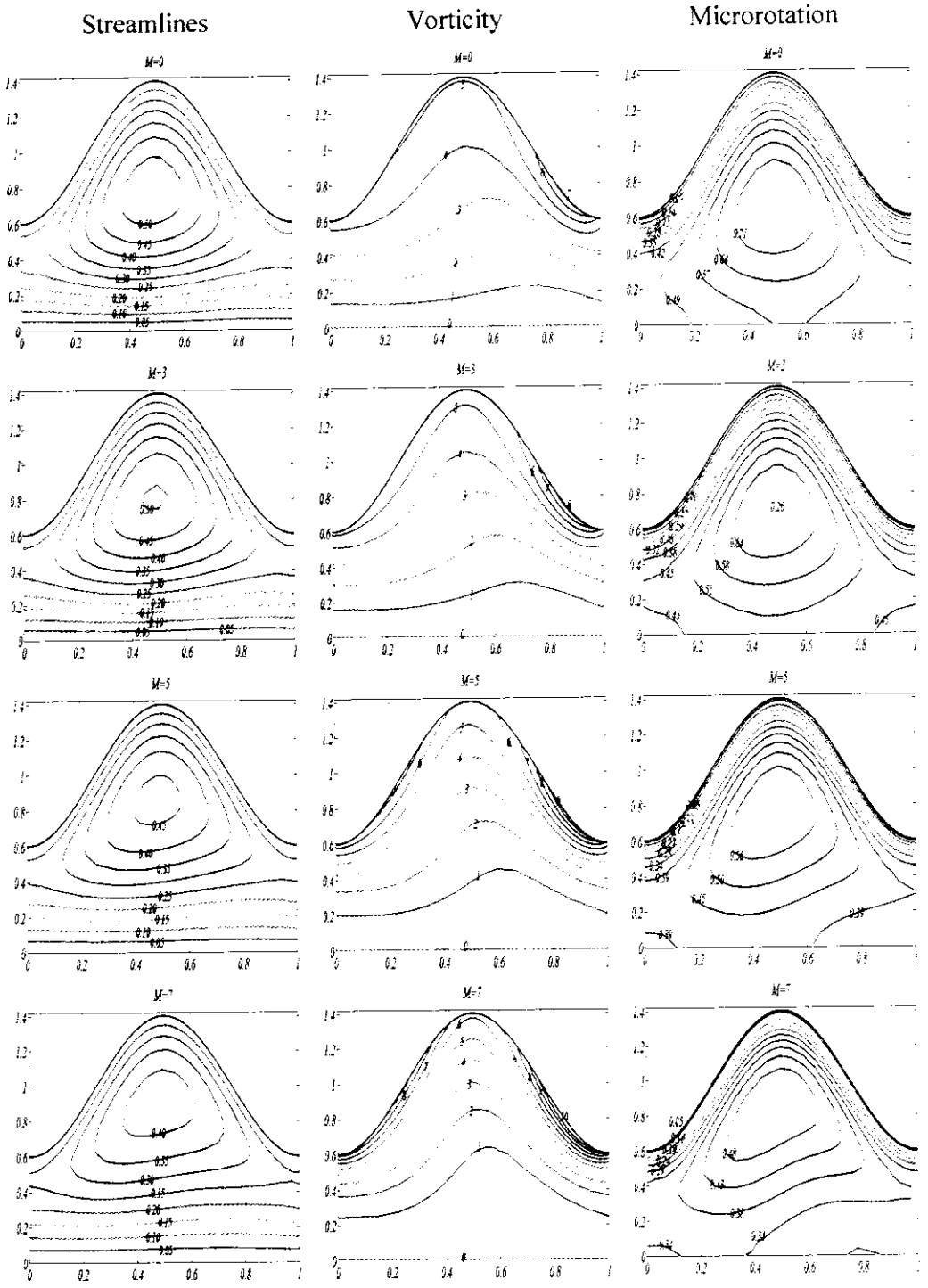

Figure 5.9 Streamlines, vorticity and microrotation for various values of Hartmann number M and values of other parameters are fixed at $Re = 10, \alpha = 0.5, \phi = 0.4, m = 2, N = 0.5, K = 0.5$ and $Q = 1.2$

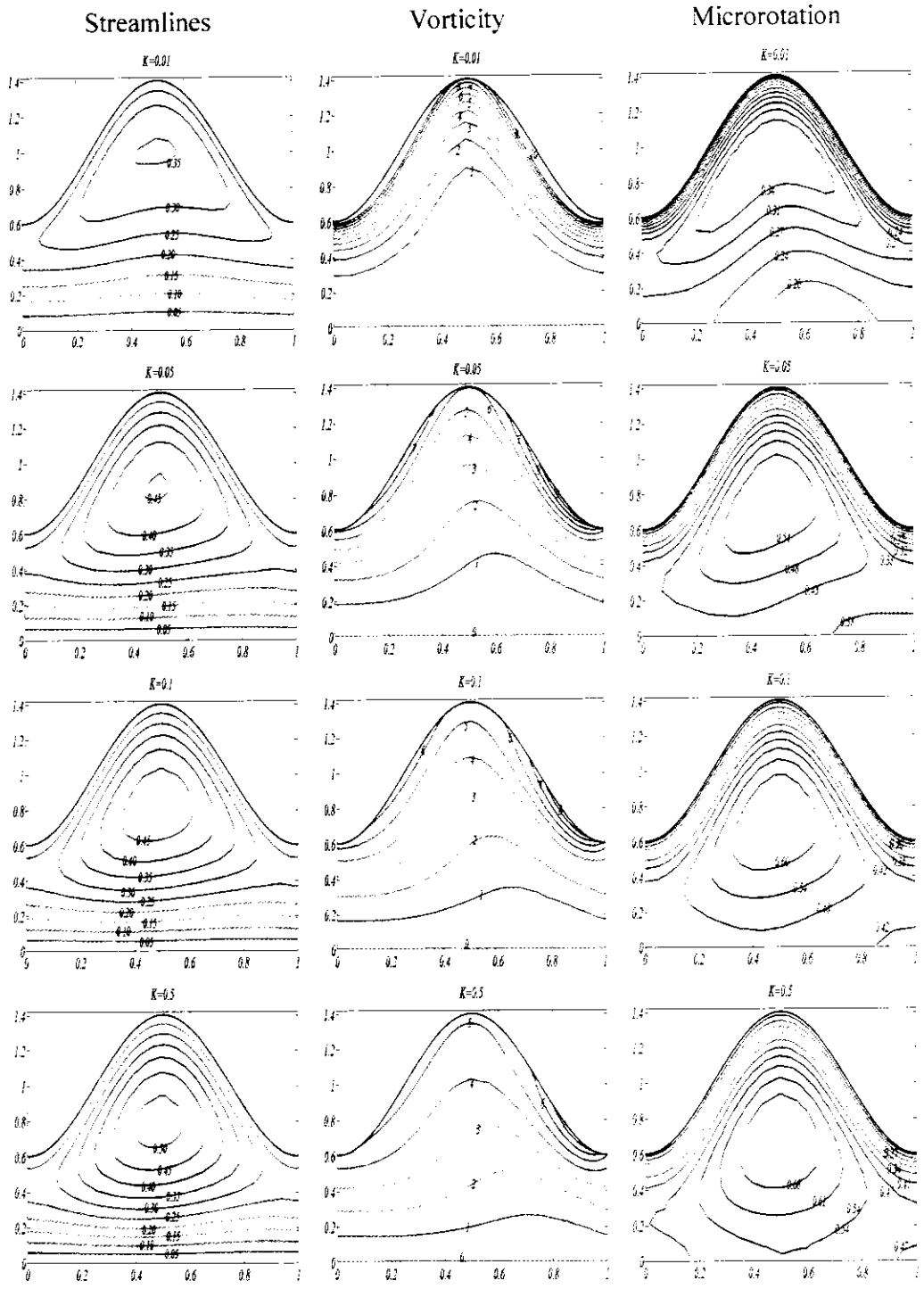

Figure 5.10: Streamlines, vorticity and microrotation for various values of porosity parameter K and values of other parameters are fixed at $Re = 10, \alpha = 0.5, \phi = 0.4, m = 2, N = 0.5, M = 2$ and $Q = 1.2$

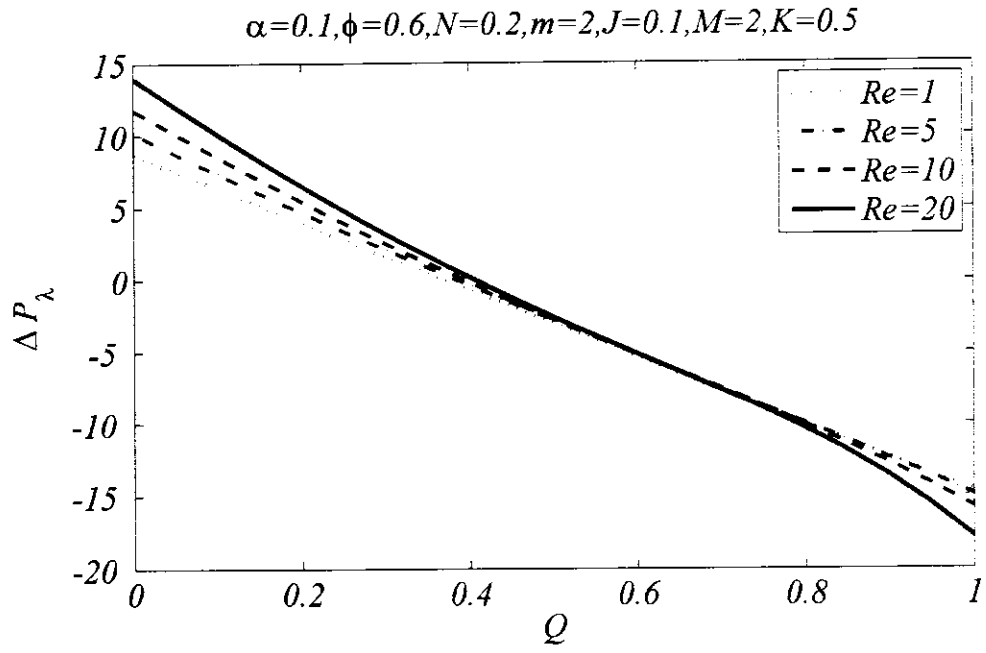

Figure 5.11: Pressure rise per wavelength for variation of Reynolds number *Re* and values of other parameters are fixed

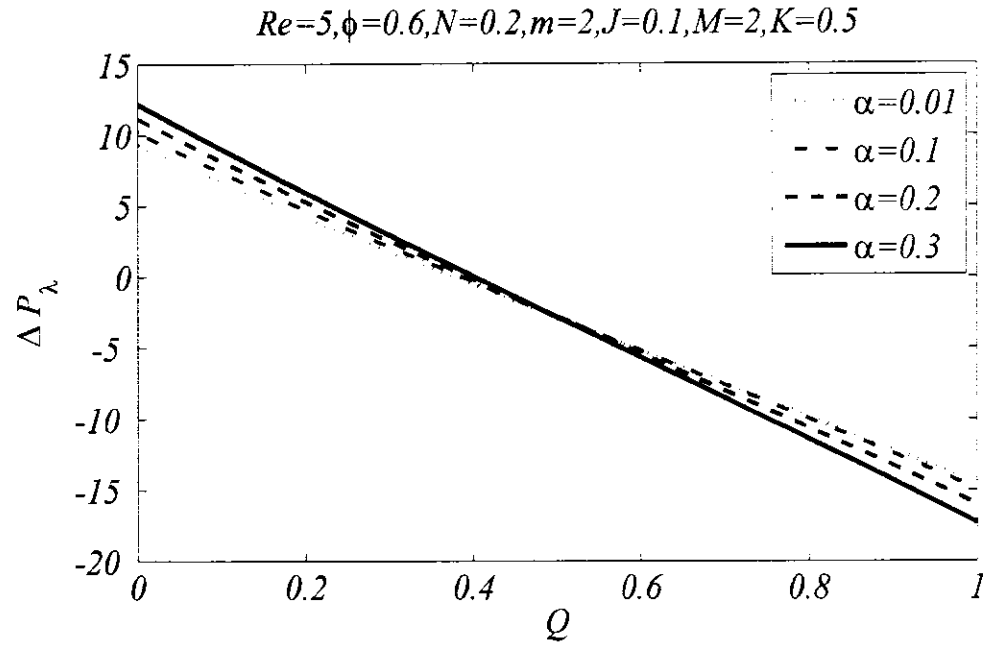

Figure 5.12: Pressure rise per wavelength for variation of wave number α and values of other parameters are fixed

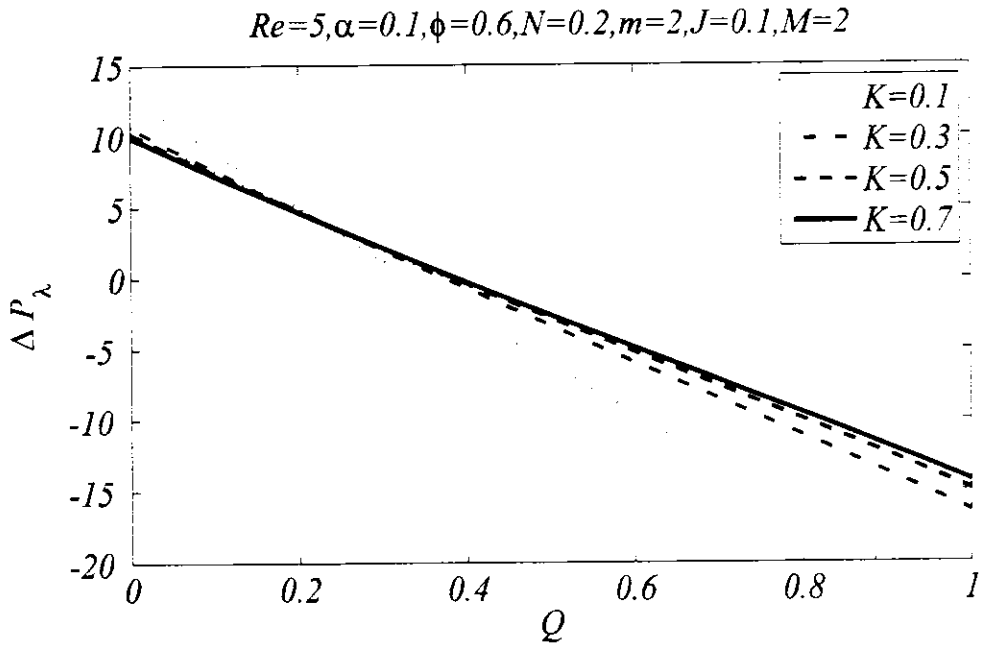

Figure 5.13: Pressure rise per wavelength for variation of permeability parameter K and values of other parameters are fixed

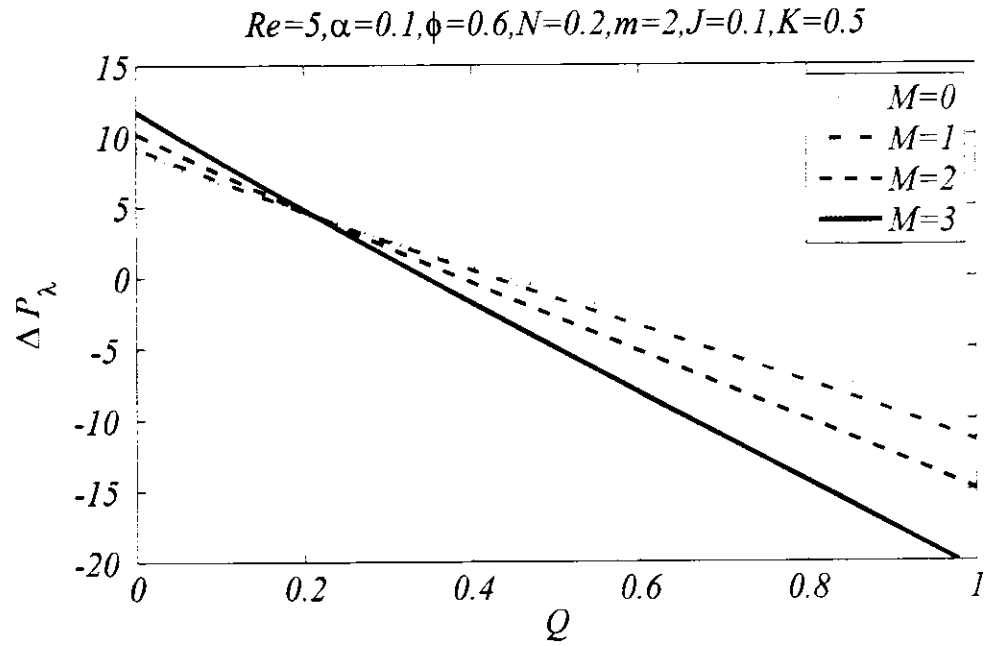

Figure 5.14: Pressure rise per wavelength for variation of Hartmann number and values of other parameters are fixed

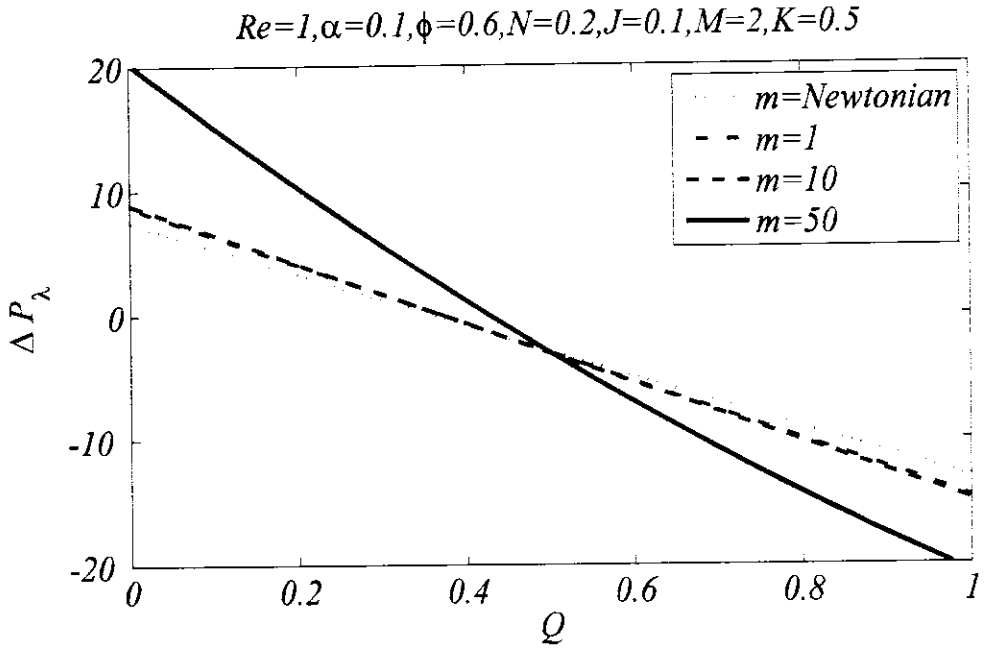

Figure 5.15: Pressure rise per wavelength for variation of micropolar parameter m and values of other parameters are fixed

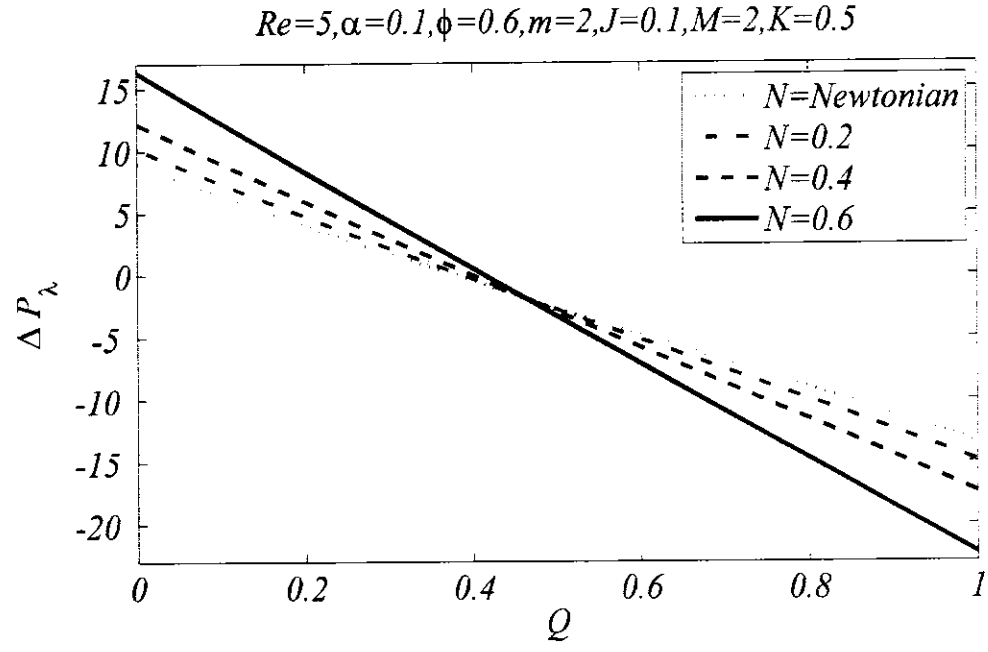

Figure 5.16: Pressure rise per wavelength for variation of coupling number N and values of other parameters are fixed

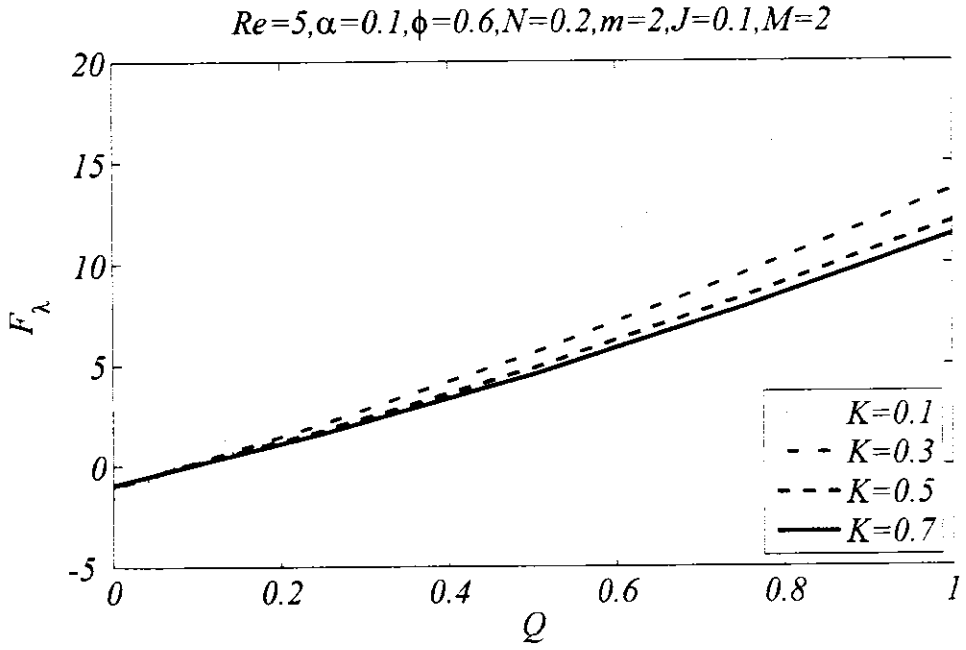

Figure 5.17: Friction force for variation of permeability parameter K and values of other parameters are fixed

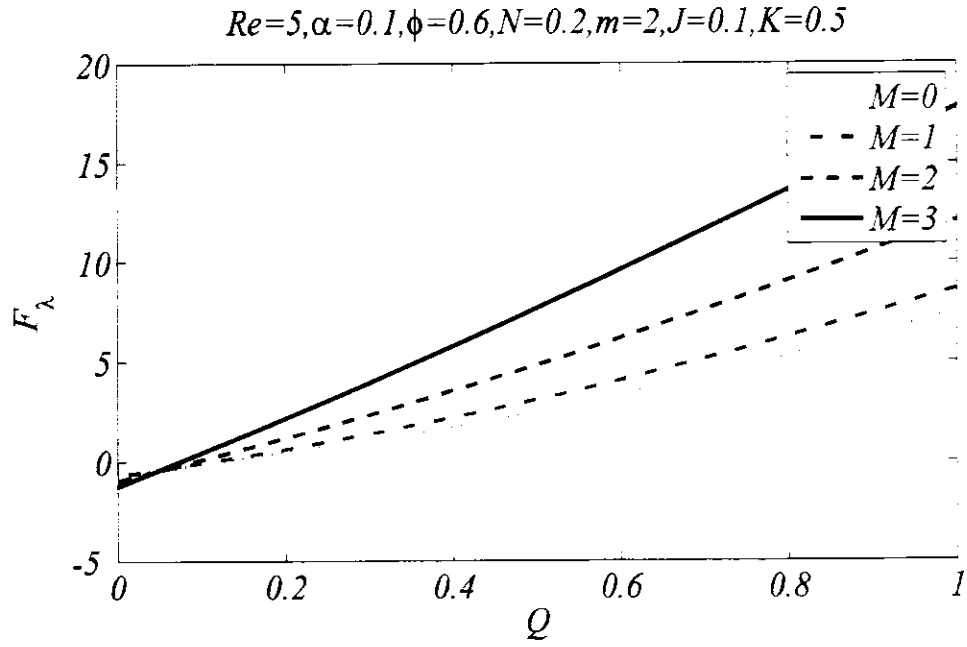

Figure 5.18: Friction force for variation of Hartmann number M and values of other parameters are fixed

It exhibits that in the region of peristaltic pumping, increase in magnetic body force enhances the pressure rise per wavelength and reduces pressure rise in the augmented region. So the strength of the magnetic force is one way to control the pressure rise in both regions. In **Figure 5.15**, the pressure rise per wavelength is plotted to examine the attitudes of micropolar parameter m. It is noted that increasing m causes increase in pressure rise per wave length which is greater as compared to that of Newtonian case in pumping region while its behavior is opposite in augmented region. **Figure 5.16** is constructed to see the effects of coupling number N on pressure rise per wavelength. It is noted that pressure upsurges with accumulating coupling number N and curve representing the trades of Newtonian fluid lies lower the curves corresponds to micropolar fluid in the peristaltic pumping region which reveals that enhancing the coupling parameter gives improved pumping performance. Moreover, increase in coupling parameter decreases the pressure rise in the augmented region. **Figures 5.17** and **5.18** are plotted to examine the characteristics of the friction force in a porous medium and magnetic field. **Figure 5.17** shows that increase in the values of permeability of porous medium decreases the friction force for large values of time mean flow. It is also noted that for large values of time mean flow, friction force increases rapidly. However, it is noted from **Figure 5.18** that the behavior of Hartmann number is opposite as compared to that of permeability parameter.

5.6 Conclusions

In this chapter, the peristaltic transportation of micropolar fluid is carried out for non-zero moderate Reynolds number to examine the effects of the flow in the porous saturated channel beneath the impact of transverse uniform magnetic field applied perpendicular to the flow. In the present study, the assumptions of long wavelength along with low Reynolds number is not considered due to which the effect of inertial forces on the peristaltic mechanism for the motion of non-Newtonian in a porous uniformly saturated medium is presented for the first time in literature. By neglecting above assumptions, the governing equations for the flow model are presented by the set of coupled nonlinear partial differential equations. Modelled equations are exposed to Galerkin weighted residual finite element technique. Comparison of obtained numerical outcomes with the available literature results in limiting case by plotting graph of velocity for altered values of time-mean flow and found in excellent agreement. Computed results are presented through the graphs of velocity, streamlines circulation,

vorticity, microrotations and pressure rise per wavelength. It is concluded that at low Reynolds number, the trapped bolus are symmetrical while increasing Reynolds number magnifying the size of the boluses, increases the pressure rise per wavelength and reduces the velocity. Increasing values of wave number exhibit the same behavior as that of Reynolds number for velocity and pressure profile of the fluid. The rise in strength of magnetic field reduces velocity, the volume and number of trapped bolus. The increase in permeability allows by the porous medium give rise the velocity of the fluid and reduces the pressure in the peristaltic pumping region while increases pressure in augmenting region. Furthermore, the size as well as number of bolus increases by increasing the permeability of porous medium.

Unlike the earlier studies, the effects of dominant inertial forces in the study of the peristaltic flow of micropolar fluid are discussed by setting non-zero moderate values of Reynolds number in the presence of non-zero wave number, which is neglected yet by imposing the long wavelength along with low Reynolds approximations. First time in literature, the solution of the full form of Navier-Stokes equations for the peristaltic motion of non-Newtonian fluid (micropolar fluid) under the influence of magnetic field in a porous medium is provided. Hence, it is hoped that present study serves as a benchmark for further research on peristaltic flows of non-Newtonian fluids without applying assumption of lubrication theory.

Chapter 6

Hydromagnetic Peristaltic Flow through a Porous-Saturated Tube

The main objective of the current chapter is to investigate nonlinear peristaltic flow passing through the tube filled with homogeneous porous medium under the inducment of the externally applied uniform magnetic field numerically without applying assumptions of lubrication theory. The Galerkin's variational approach is used to apply the finite element method to find numerical solution of the modeled governing system of nonlinear partial differential equations. The results are obtained without imposing the assumptions of long wavelength along with the low Reynolds number on modeled equations. Consequently, we obtained the results which are valid for moderate values of wave and Reynolds numbers. The effects of these parameters including Hartmann number, time mean flow rate parameter on longitudinal velocity profile as well as on pressure distribution are presented through graphs. The contours of streamlines are also included and discussed in detail. Linear behavior of pressure is observed for small Reynolds number while for large values of Reynolds number pressure rise per wavelength is observed as nonlinear. It is observed through analysis that peristaltic mixing due to circulation is highly dependent on permeability parameter. Greater peristaltic mixing is noticed in the non-porous tube as compared to that of porous-saturated tube. The obtained numerical outcomes are compared with available analytical results in the literature which establish an excellent agreement.

6.1 Problem Formulation

Let us consider a two dimensional electrically conducting peristaltic flow of Newtonian fluid passing through a tube of width $2a$ saturated with a porous medium with speed c. The magnetic field $\boldsymbol{B}$ having uniform magnitude B_0 is applied orthogonal to the orientation of the flow. Here, due to small conductivity of fluid and to ensure that $\boldsymbol{B}$ is unaffected by the velocity of the fluid, we must restrict ourselves to low magnetic Reynolds numbers R_m and low R_m-approximation allows to neglect induced magnetic field caused by an applied magnetic field. We consider constant thermo-physical properties of the fluid of unsteady peristaltic flow. The flow caused by peristaltic walls

of the tube is considered along the z −direction and r −coordinate assumed in the radial direction. The symmetry of the flow is about z − axis and schematic diagram that explains the geometry of the considered problem is displayed in **Figure 6.1**.

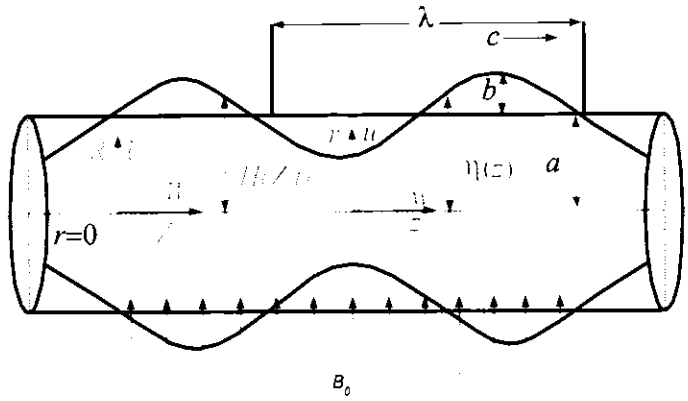

Figure 6.1: Geometrical flow diagram

In fixed frame geometry of peristaltic boundary/wall of the tube obeys Eq. (6.1).

$$H(Z,t) = a - b\cos\left[\frac{2\pi(Z-ct)}{\lambda}\right], \tag{6.1}$$

where λ, b and h are the representatives of wave length, wave amplitude and mean distance from the central axis to the peristaltic wall respectively. Darcy law relates the pressure drop and velocity of Newtonian fluid. Darcy law hold at low speed in an unbounded porous saturated medium states that the induced pressure drop is due to the frictional drag have direct relation to the fluid velocity. The inducement of applied magnetic field in terms of the Lorentz force are discussed and presented in governing equations. In the fixed frame, the governing equation that describes the flow are as follows

$$\frac{\partial W}{\partial Z} + \frac{1}{R}\frac{\partial (RU)}{\partial R} = 0, \tag{6.2}$$

$$\rho\left(\frac{\partial W}{\partial t} + W\frac{\partial W}{\partial Z} + U\frac{\partial W}{\partial R}\right) = -\frac{\partial P}{\partial Z} + \frac{1}{R}\frac{\partial}{\partial R}\left(R\frac{\partial W}{\partial R}\right) + \frac{\partial^2 W}{\partial Z^2} - \frac{1}{k}W - \sigma B_0^2 W, \tag{6.3}$$

$$\rho\left(\frac{\partial U}{\partial t} + W\frac{\partial U}{\partial Z} + U\frac{\partial U}{\partial R}\right) = -\frac{\partial P}{\partial R} + \frac{\partial}{\partial R}\left(\frac{1}{R}\frac{\partial (RU)}{\partial R}\right) + \frac{\partial^2 U}{\partial Z^2} - \frac{1}{k}U. \tag{6.4}$$

The suitable boundary conditions applied on for the considered flow are given as

$$U = 0, \quad \frac{\partial W}{\partial R} = 0 \quad \text{at} \quad R = 0, \tag{6.5}$$

$$W = 0, \quad U = \frac{\partial H}{\partial t} \quad \text{at} \quad R = H. \tag{6.6}$$

The symmetry of the flow is along the no-slip wall corresponds the boundary conditions defined in Eqs. (6.5) and (6.6) imposed on U at $R = 0$ and $R = H$, whereas, the equality of normal velocity of fluid at the wall to normal velocity of wall refers to boundary

condition defined in Eqs. (6.5) and (6.6) on W as $W = \partial H/\partial t$ at $R = H$. The zero transvers velocity at the center corresponds the boundary condition $W = 0$ at $R = 0$. The set of transformation that relates two frames, the lab and wave frame is

$$r^* = R, \quad w^* = W - c, \quad z^* = Z - ct, \quad u^* = U, \tag{6.7}$$

where Z, R and z^*, r^* represents the velocity coordinates in the fixed frame of reference and moving frame of reference respectively and $p^* = P$. The associated boundary conditions for the flow at center and wall of the tube are given by

$$\psi^* = 0 \text{ at } r^* = 0, \quad \psi^* = q^* \text{ at } r = \eta(z^*), \tag{6.8}$$

in which ψ^* and q^* are representatives of the stream function and flow rate in the wave frame of reerfernce respectively where the relation by which q^* can be connected with the time mean flow in lab frame Q^* given by the expression $q^* = Q^* - cH^2(1 + \phi^2/2)$. Implanting the following dimensionless variables to the system of equations

$$\begin{gathered} z = \frac{z^*}{\lambda}, u = \frac{u^*}{c}, r = \frac{r^*}{a}, w = \frac{w^*}{c}, p = \frac{a^2}{\lambda\mu c}p^*(z), \alpha = \frac{a}{\lambda}, \phi = \frac{b}{a}, q = \frac{q^*}{ca}, \\ \psi = \frac{\psi^*}{ca}, \omega = \frac{a\omega^*}{c}, \ \eta = \frac{\eta^*}{a}, h = \frac{h(z^*)}{a}, K = \frac{k^*}{a^2}, Re = \frac{ca}{\nu}\alpha, M = \sqrt{\sigma/\mu}\, B_0 a. \end{gathered} \tag{6.9}$$

And eliminating the pressure gradient term by performing cross differentiation and then using the relations

$$u = -\frac{\alpha}{r}\partial\psi/\partial z \text{ and } w = \frac{1}{r}\partial\psi/\partial r \tag{6.10}$$

in the governing equations, we get stream-vorticity form of equations as follows

$$\frac{\alpha^2}{r}\frac{\partial^2\psi}{\partial z^2} + \frac{\partial}{\partial r}\left(\frac{1}{r}\frac{\partial\psi}{\partial r}\right) = -\omega, \tag{6.11}$$

$$Re\left(\frac{\partial\psi}{\partial r}\frac{\partial}{\partial z}\left(\frac{\omega}{r}\right) - \frac{\partial\psi}{\partial z}\frac{\partial}{\partial r}\left(\frac{\omega}{r}\right)\right) = \frac{1}{r}\mathrm{D}^2(r\omega) + M^2\frac{\partial}{\partial r}\left(\frac{1}{r}\frac{\partial\psi}{\partial r}\right) - \frac{1}{K}\omega, \tag{6.12}$$

where a modified form of Laplacian (D^2) is defined as $\mathrm{D}^2 = \alpha^2\frac{\partial^2}{\partial z^2} + \frac{\partial^2}{\partial r^2} - \frac{1}{r}\frac{\partial}{\partial r}$.

Simplified form of the boundary conditions is given as

$$\left.\begin{array}{llll} \psi = 0, & \frac{\partial}{\partial r}\left(\frac{1}{r}\frac{\partial\psi}{\partial r}\right) = 0, & \frac{1}{r}\frac{\partial\psi}{\partial z} = 0 & \text{at} \quad r = 0 \\ \psi = q, & \frac{1}{r}\frac{\partial\psi}{\partial r} = -1, & \frac{1}{r}\frac{\partial\psi}{\partial z} = 2\pi\phi\sin 2\pi z & \text{at} \quad r = \eta(z) \end{array}\right\}. \tag{6.13}$$

$$\text{where } \eta(z) = 1 - \phi\cos(2\pi z)$$

At the central line of the tube $z = 0$, pressure rise per wavelength in wave frame is given by

$$\Delta p_\lambda = \int_0^\lambda \frac{\partial p}{\partial z}\, dz. \tag{6.14}$$

where $\frac{dP}{dz}$ is directly determined through non-dimensional Navier-Stokes equation.

6.2 Numerical Analysis

In this analysis, the modeled equations are not exposed to assumptions of long wavelength along with low Reynolds number due to which nonlinearity retained in the governing set of partial differential equations. To handle such type of high nonlinear system of partial differential equation, we required highly accurate and robust technique. For this purpose, the modeled Eqs. (6.11) and (6.12) along with the boundary conditions given in Eq. (6.13) are exposed to Galerkin's finite element technique. In this technique, the whole domain is discretized into a mesh of non-uniform quadratic triangular elements by using the pdetool. First, we discretize the problem on each triangular element and then assemble it to the global system and solve by the Newton-Raphson method by using MATLAB 2010a. In all the formulation, tolerance rate of 10^{-14} has been achieved in 3 to 5 number of iteration steps. The approximation of stream function and vorticity is given by

$$\psi = \sum_{k=1}^{n} N_k \psi_k, \quad \omega = \sum_{k=1}^{n} N_k \omega_k, \tag{6.15}$$

where ψ_k and ω_k are the nodal element approximation of ψ and ω respectively. After applying Galerkin's finite element approach to Eqs. (6.11) and (6.12), we get

$$\int_{\Omega} w_1 \left(\frac{\alpha^2}{r} \frac{\partial^2 \psi}{\partial z^2} + \frac{\partial}{\partial r}\left(\frac{1}{r}\frac{\partial \psi}{\partial r}\right) + \omega \right) d\Omega = 0, \tag{6.16}$$

$$\int_{\Omega} w_2 \left(Re \left(\frac{\partial \psi}{\partial r}\frac{\partial}{\partial z}\left(\frac{\omega}{r}\right) - \frac{\partial \psi}{\partial z}\frac{\partial}{\partial r}\left(\frac{\omega}{r}\right)\right) - M^2 \frac{\partial}{\partial r}\left(\frac{1}{r}\frac{\partial \psi}{\partial r}\right) + \frac{1}{K}\omega - \frac{1}{r} D^2(r\omega) \right) d\Omega = 0, \tag{6.17}$$

where w_1 and w_2 represents the weight functions and $d\Omega = 2\pi r dr dz$. Upon simplification of Eqs. (6.16) and (6.17), we get

$$\int_{\Omega} \left(\frac{\alpha^2}{r}\frac{\partial w_1}{\partial z}\frac{\partial \psi}{\partial z} + \frac{\partial w_1}{\partial r}\left(\frac{1}{r}\frac{\partial \psi}{\partial r}\right) - w_1 \omega \right) d\Omega = \int_{\Gamma} w_1 \frac{\partial \psi}{\partial n} d\Gamma, \tag{6.18}$$

$$\int_{\Omega} w_2 Re \left(\frac{\partial \psi}{\partial r}\frac{\partial}{\partial z}\left(\frac{\omega}{r}\right) - \frac{\partial \psi}{\partial z}\frac{\partial}{\partial r}\left(\frac{\omega}{r}\right)\right) d\Omega + \int_{\Omega} \left(\frac{\partial w_2}{\partial r}\frac{1}{r}\frac{\partial (r\omega)}{\partial r} + \frac{\alpha^2}{r}\frac{\partial w_2}{\partial z}\frac{\partial (r\omega)}{\partial z} \right) d\Omega + M^2 \int_{\Omega} \left(\frac{\partial w_2}{\partial r}\frac{1}{r}\frac{\partial \psi}{\partial r} \right) d\Omega + \frac{1}{K}\int_{\Omega} w_2 \omega d\Omega = \int_{\Gamma} w_2 \frac{\partial \psi}{\partial n} d\Gamma + M^2 \int_{\Gamma} w_2 \frac{\partial \psi}{\partial n} d\Gamma, \tag{6.19}$$

where $d\Gamma = \pi r dr dz$. After discretizing the domain and introduction the approximation (6.15) in Eqs. (6.18) and (6.19), we get

$$-\sum_i B_{ki}^e \omega_i + \sum_i A_{ki}^e \psi_i = S_n^{k^e}, \tag{6.20}$$

$$Re \sum_i C_{kij}^e \psi_i \omega_i + \sum_i A_{ki}^e \omega_i + M^2 \sum_i D_{ki}^e \psi_i + \frac{1}{K} \sum_i B_{ki}^e \omega_i = M^2 S_n^{k^e}, \tag{6.21}$$

where

$$\left.\begin{aligned} S_n^{k^e} &= \int_\Gamma N_k \bar{S}_k d\Gamma \\ A_{ki}^e &= \int_{\Omega^e} \left(\frac{\alpha^2}{r} \frac{\partial N_k}{\partial z} \frac{\partial N_i}{\partial z} + \frac{\partial N_k}{\partial r} \left(\frac{1}{r} \frac{\partial N_i}{\partial r} \right) \right) d\Omega \\ B_{ki}^e &= \int_{\Omega^e} N_k N_i d\Omega \\ C_{kij}^e &= \int_\Omega N_k \left(\frac{\partial N_i}{\partial r} \frac{\partial}{\partial z} \left(\frac{N_j}{r} \right) - \frac{\partial N_j}{\partial z} \frac{\partial}{\partial r} \left(\frac{N_i}{r} \right) \right) d\Omega \\ D_{ki}^e &= \int_\Omega \left(\frac{\partial N_k}{\partial r} \frac{1}{r} \frac{\partial N_k}{\partial r} \right) d\Omega \end{aligned}\right\}. \tag{6.22}$$

The obtained global system of matrices is defined as

$$\boldsymbol{KA} = \boldsymbol{F}, \tag{6.23}$$

where

$$K_{ij} = \begin{bmatrix} -B_{ki}^e & A_{ki}^e \\ A_{ki}^e + 1/K\, B_{ki}^e & Re\, C_{kij}^e \omega_i + M^2 D_{ki}^e \end{bmatrix}, A_k = \begin{bmatrix} \omega_k \\ \psi_k \end{bmatrix}, F_k = \begin{bmatrix} S_n^{k^e} \\ M^2 S_n^{k^e} \end{bmatrix}. \tag{6.24}$$

6.3 Validation

In this section, comparison of the obtained numerical results is made graphically with the finding of Shapiro et al. (1969) and Manton (1975) for limiting case. The solution of Shapiro et al. (1969) is purely analytical and therefore it serves as a benchmark solution in this comparison. To this end, the curves of pressure rise per wavelength based on our solution are compared with the corresponding pressure rise per wavelength curves obtained through the solution of Shapiro et al. (1969) as shown in **Figure 6.2**. It is observed that our results for the limiting case ($M = 0, 1/K = 0$) are in close agreement with corresponding result of Shapiro et al. (1969) by considering long wavelength along with low Reynolds number assumptions also. The presented graphs of longitudinal velocity are drawn for non-zero/moderate Reynolds number along with wave number to compare the results with the existing results of Manton (1975) as shown in **Figure 6.3**.

6.4 Results and Discussion

The above discussed numerical scheme is implemented to obtain the solution which is represented by contours of streamlines, curves of the velocity profile and pressure distribution. The effects of involved parameters such as porosity parameter K, volume mean flow rate Q, Reynolds number Re, wave number α and Hartmann number M are discussed through graphs.

6.4.1 Velocity profile

This section is dedicated to detail discussion on the velocity profile of the flow for a variation of different parameter in cross section $z = 0$ of the tube. **Figure 6.4** reveals that at the center of the tube velocity increases by increasing the permeability parameter representing porous medium, but opposite behavior is noted in the region near the peristaltic wall. **Figure 6.5** displays the impact of Hartmann numbers on velocity profile and it is noticed that the velocity decreases near central region and increases in the vicinity of the peristaltic wall due to increase in Hartmann number. In **Figures 6.6** and **6.7** longitudinal velocities are presented for a variation of Reynolds number Re and wave number α respectively at two different values of permeable parameter symbolized by K. It is observed that at both values of permeable parameter K the graph of longitudinal velocity is concave down and decreasing function of y. **Figure 6.6** shows that at the center of the tube, velocity is increasing function of Reynolds number and in the region near the wall of tube, velocity decreases by enhancing the Reynolds number. The opposite behavior is noticed for wave number as shown in **Figure 6.7**. This observation is perhaps not reported in earlier studies, and it may be attributed to strong inertial effects induced due to large values of the Reynolds number. Since, long wavelength along with low Reynolds number theory is not able to predict such non-linear effects. In the case of volume flow rate, velocity upsurges with the increase in the volume flow rate in entire region of the peristlatic tube as shown in **Figure 6.8**.

6.4.2 Trapping phenomenon

To examine the trajectory of the flow field, trapping is very important and informative phenomenon based on the formation of bolus by internal circulation of streamlines. **Figure 6.9** exhibits the variation of pattern of streamlines for different values of Hartmann number. At low Hartmann number, it is noted that trapped boluses are formed at crest portion in the central region. Accumulating Hartmann number enforced the development of the bolus immediate to the wall along with decreased the number of

boluses and condensed size of the bolus. **Figure 6.10** shows the streamlines for variation in permeability of porous medium. This figure reveals that peristaltic mixing due to circulation is also largely dependent on the permeability parameter. In fact, much greater peristaltic mixing is realized in the non-porous tube as compared to that of porous-saturated tube. The behavior of Reynolds number on trapping phenomenon can be observed in **Figure 6.11**. This figure clearly indicates the non-trivial effect of increasing Reynolds number on trapping. It reveals that circulation of trapped bolus magnifies with increasing values of Reynolds number. It is noticed that for small Reynolds number such that $Re = 1$ trapped bolus appears very close to peristaltic wall and moves towards central region for higher values of Re. Streamlines near the central part of tube show more concavity for small Reynolds number as compared to that of large Reynolds number. It also shows that size and number of bolus increases by enhancing the Reynolds number. **Figure 6.12** shows the effects of variation of volume mean flow rate Q, which exhibits that for small values of Q, the trapped bolus formed in the whole region while increasing its value cause smooth streamlines and becomes parallel to central line in the central region of the tube, so increasing volume flow rate assist the velocity of the fluid and corresponds to improve stability.

6.4.3 Pressure distribution

In this section, a detailed discussion is made regarding the behavior of pressure in peristaltic motion for different values of parameters through graphs plotted against volume flow rate Q. **Figure 6.13** shows the pressure rise per wavelength for numerous numerical values of permeability of porous medium. It is noted that pressure rise shows linear behavior against Q and for all values of permeability parameter attributes increasing pressure in positive pumping region while decreasing in augmented region. **Figure 6.14** shows opposite behavior in case of Hartmann number. In other words, by increasing the Lorentz force enforced by increasing magnetic field, pressure rise per wavelength shrinkages in the region of positive pumping region and increases in augmented pumping region. **Figure 6.15** exhibits the effects of Reynolds number on pressure rise per wavelength. This observation is not yet been discussed with non-zero values of Reynolds number, the linear behavior is observed for $Re = 1$ and for greater values, pressure attributes nonlinear concave up and increasing attitude against Q. **Figure 6.16** is plotted to examine the influence of wave number on pressure rise per wavelength which is offered first time in literature for peristaltic flow. It reveals that

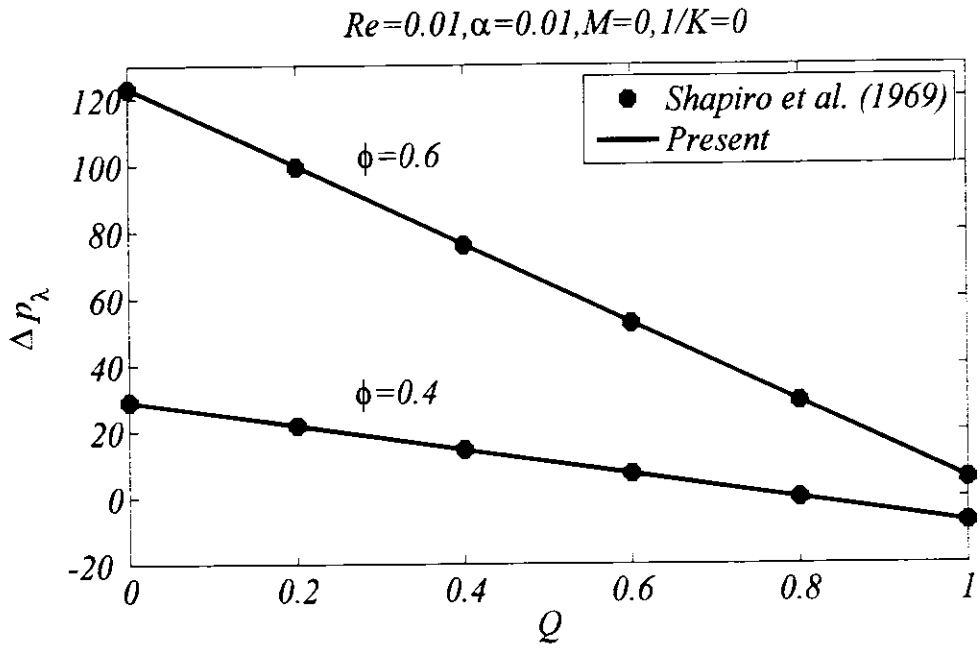

Figure 6.2: Results of Shapiro et al. (1969) in comparison with present results for pressure distribution

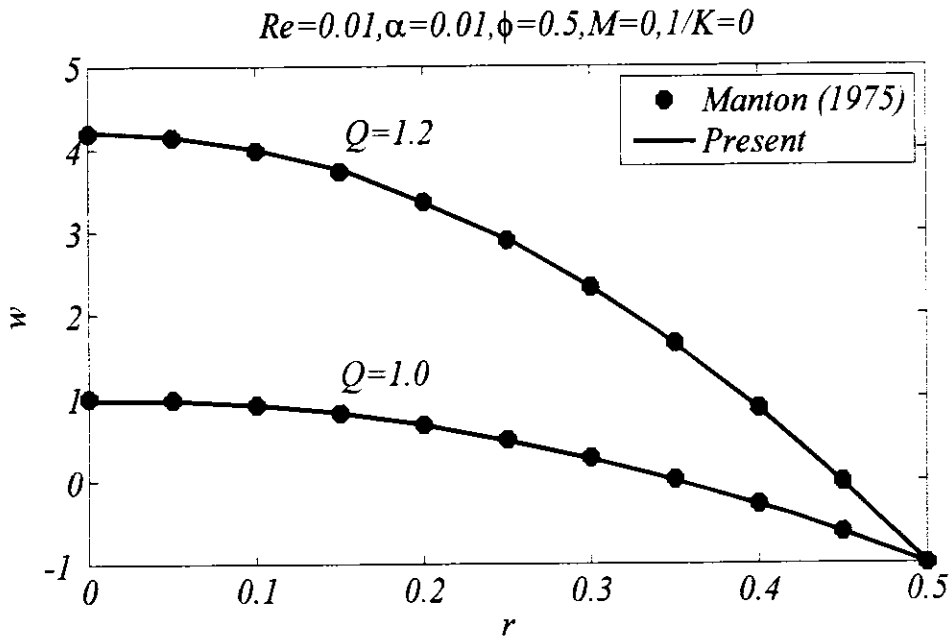

Figure 6.3: Results of Manton (1975) in comparison with present results for longitudinal velocity

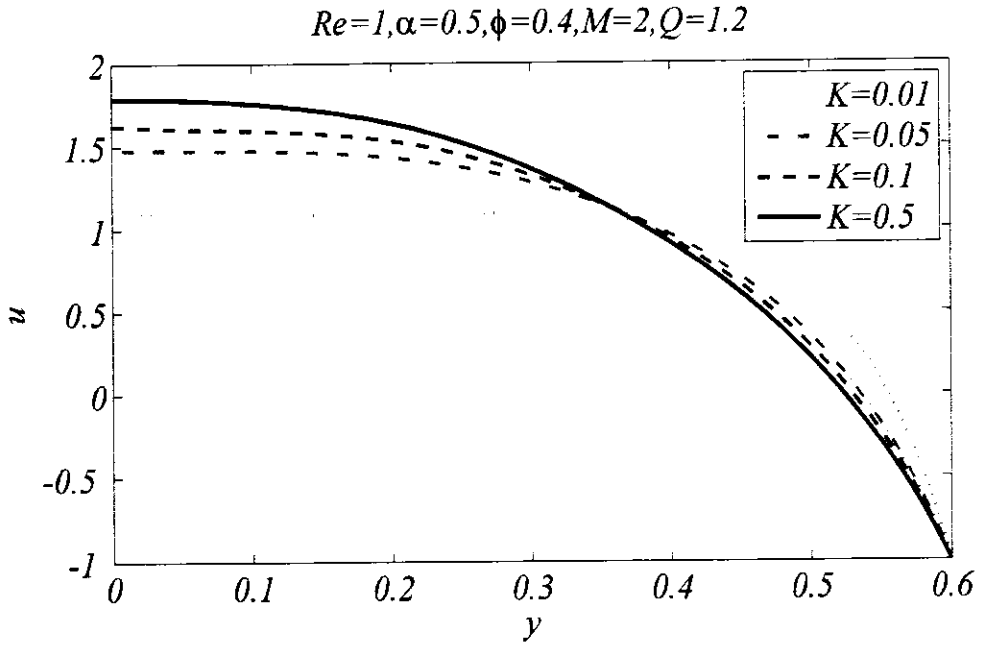

Figure 6.4: Graphs of longitudinal velocity distribution for various values of the parameter K against fixed values of other parameters

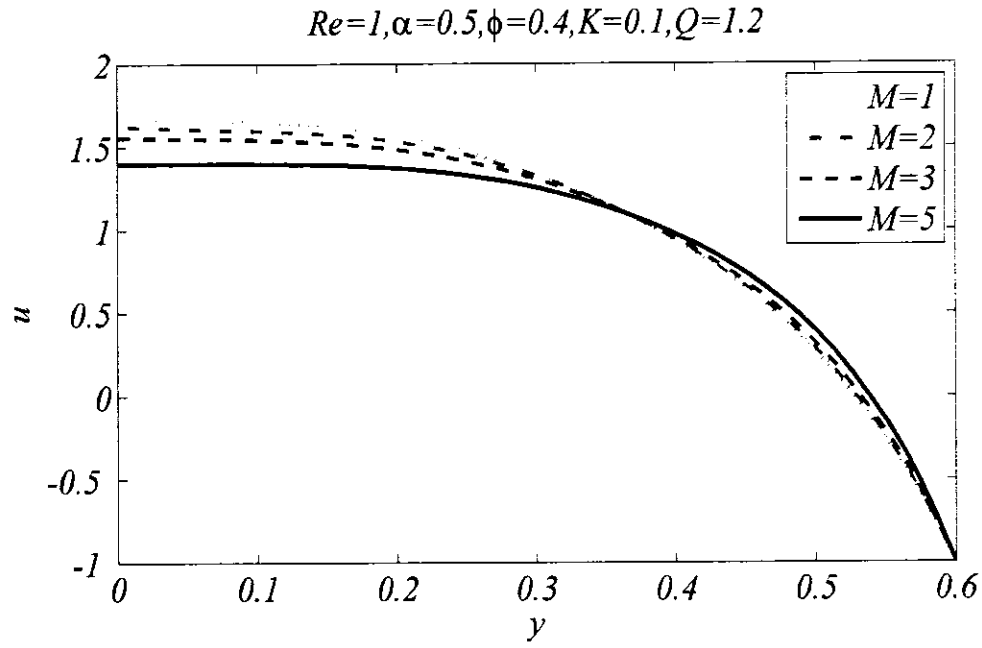

Figure 6.5: Graphs of longitudinal velocity distribution for various values of the parameter M against fixed values of other parameters

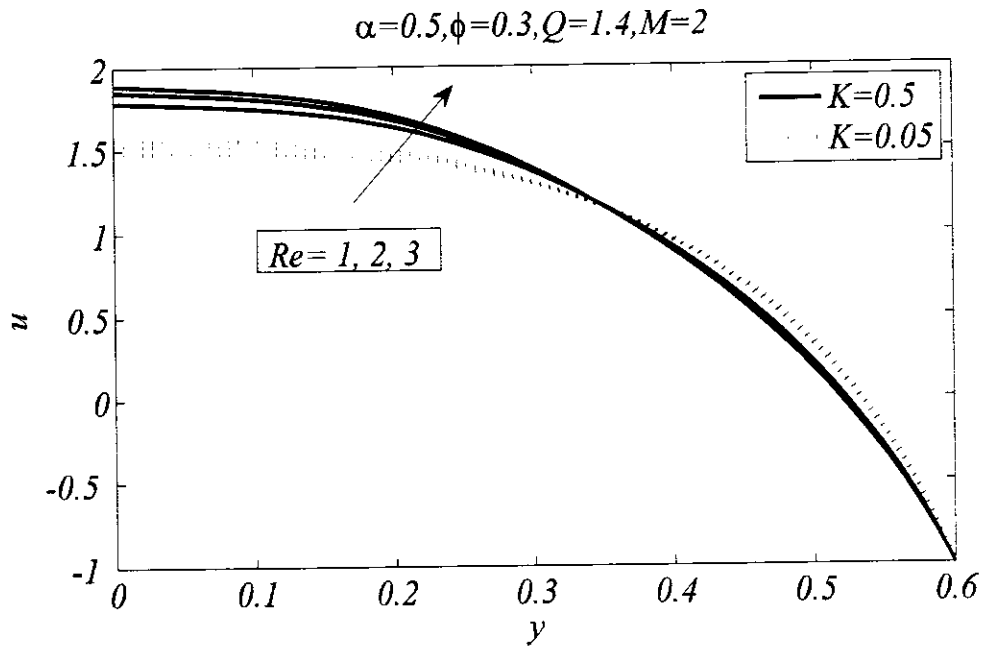

Figure 6.6: Graphs of longitudinal velocity distribution for various values of the parameter Re for $K = 0.5$ (solid line) and $K = 0.05$ (dotted line) against fixed values of other parameters

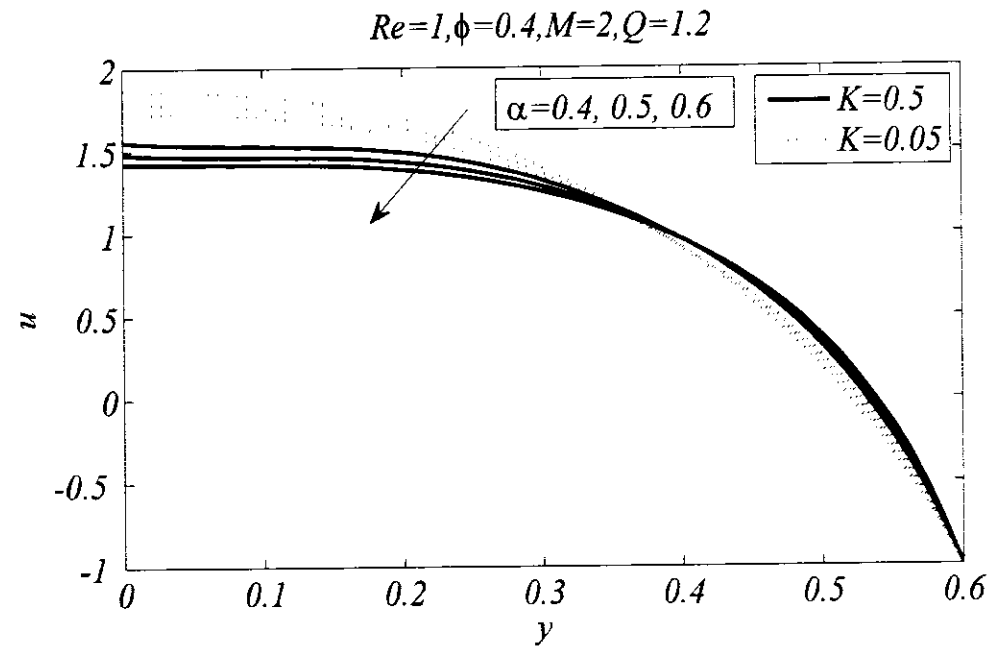

Figure 6.7: Graphs of longitudinal velocity distribution for various values of the parameter α for $K = 0.5$ (solid line) and $K = 0.05$ (dotted line) against fixed values of other parameters

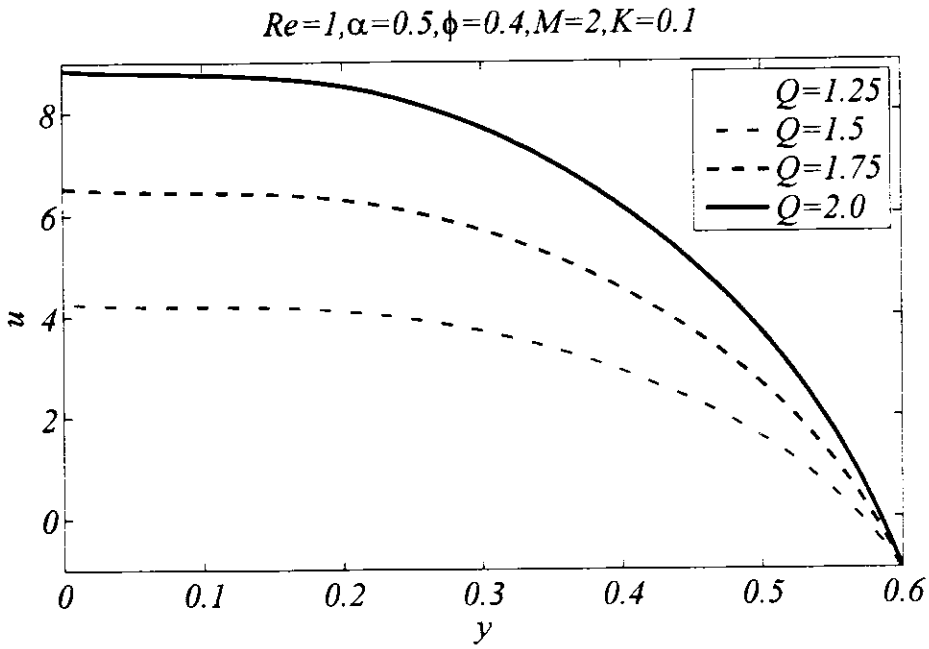

Figure 6.8: Graphs of longitudinal velocity distribution for various values of the parameter Q against fixed values of other parameters

pressure is decreasing for Q in the interval $[0, 1.1]$ and increasing for Q in the interval $[1.1, 1.5]$. The pressure rise per wavelength is also plotted against $1/K$ in **Figures 6.17** and **6.18** for several values of Reynolds and Hartmann numbers respectively. The graphs for behavior of pressure rise per wavelength versus $1/K$ for fixed value of flow rate corresponds to co-pumping region i.e. $Q > 0$ and $\Delta P_\lambda < 0$ as show in **Figures 6.17** and **6.18** for numerous values of the involved paramters Re and M respectively. It reveals that for this value of flow rate, ΔP_λ is negative for all the considered values of $1/K, M$ and Re. Moreover, the magnitude of assistance provided by the pressure increases by decreasing Reynolds number and opposite behavior is observed for Hartmann number while it enhances with increases in the permeability of the porous medium.

(a)

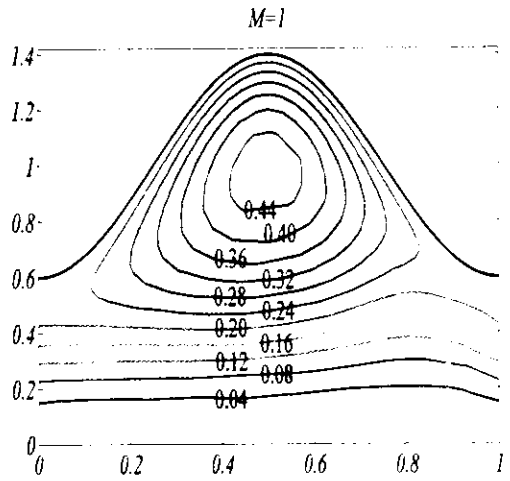

(b)

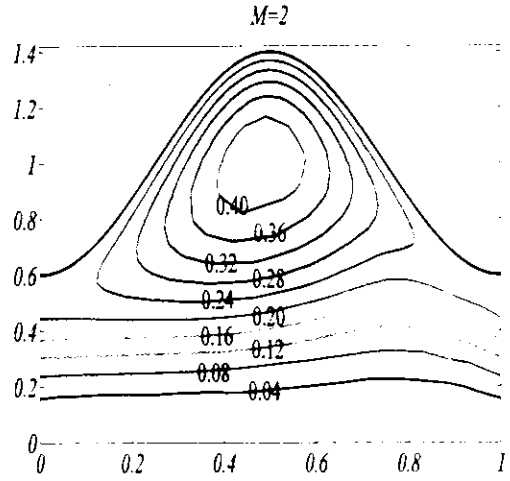

(c)

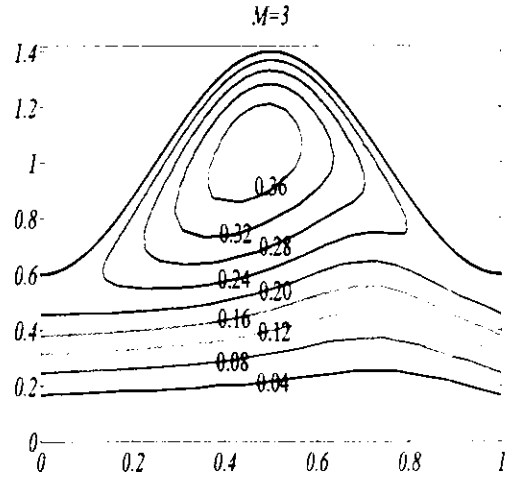

Figure 6.9: Contours of streamlines for $M = 1.0, 2.0$ and 3.0 at fixed values of other parameters as $Re = 5$, $\alpha = 0.2$, $\phi = 0.4$, $K = 0.1$ and $Q = 1.2$ in wave frame.

(a)

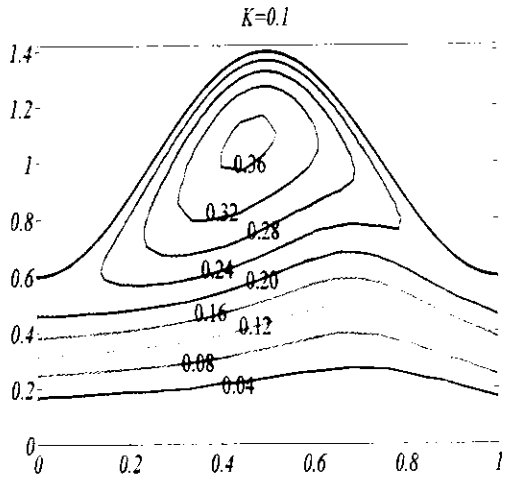

(b)

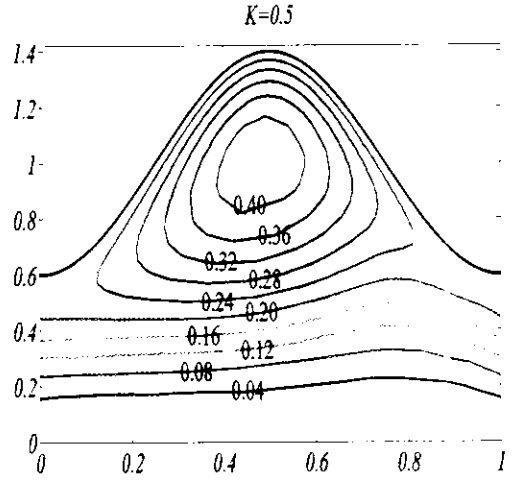

(c)

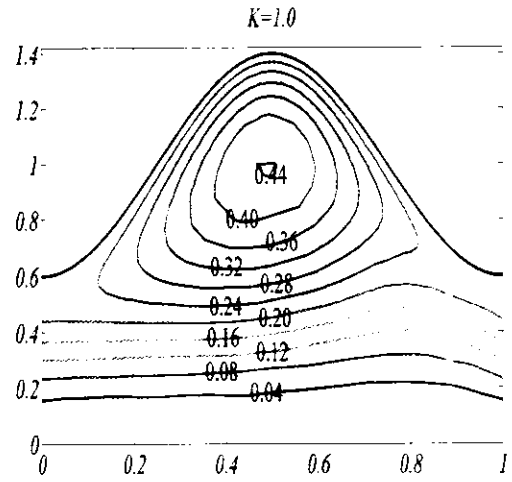

Figure 6.10: Contours of streamlines for $K = 0.1, 0.5$ and 1.0 at fixed values of other parameters as $Re = 5, \alpha = 0.2, \phi = 0.4, M = 2.0, Q = 1.2$ in wave frame

(a)

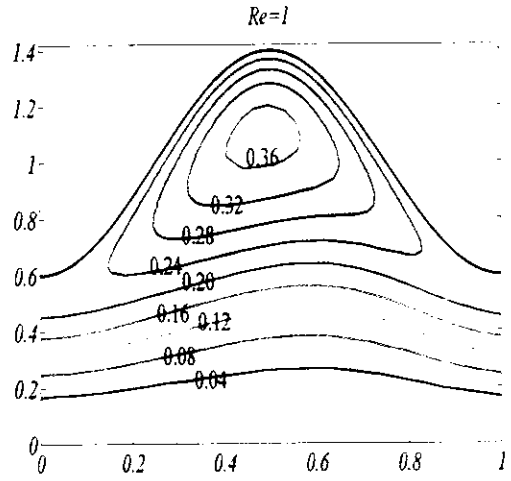

(b)

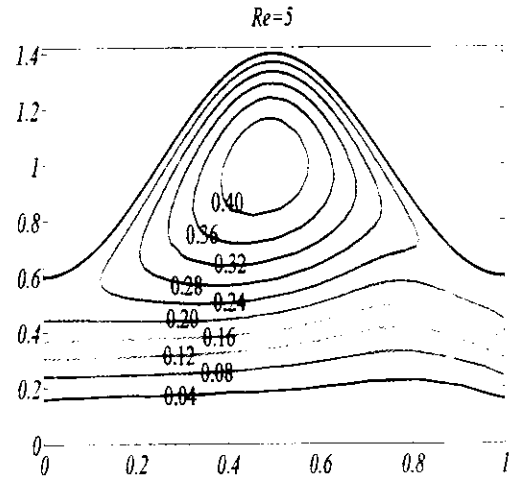

(c)

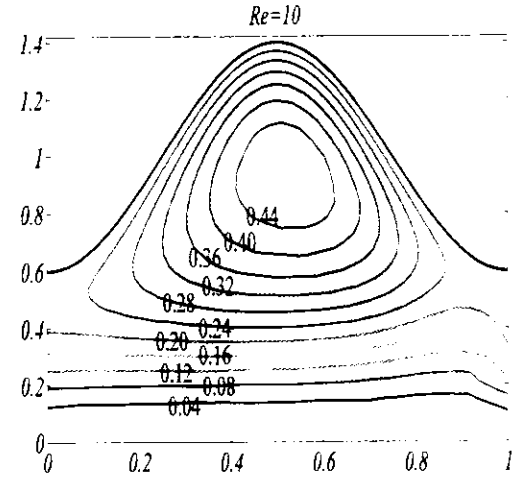

Figure 6.11: Contours of streamlines for $Re = 1,\ 5$ and 10 at fixed values of other parameters as $\alpha = 0.2, \phi = 0.4, K = 0.1, M = 2.0, Q = 1.2$ in wave frame

(a)

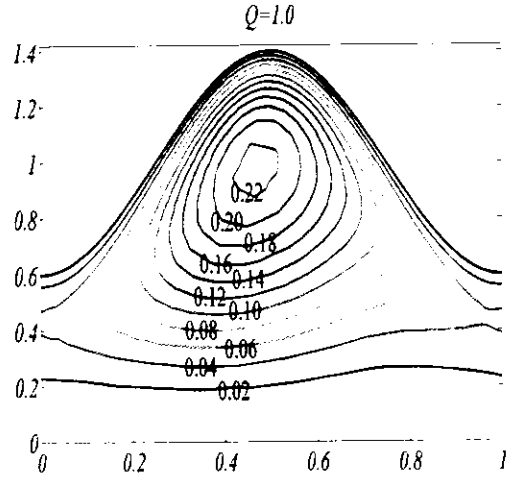

(b)

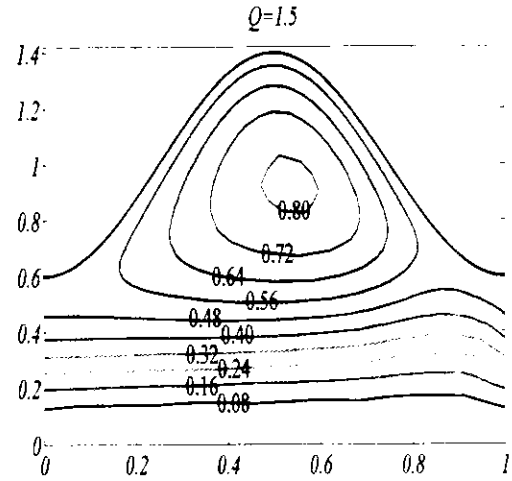

(c)

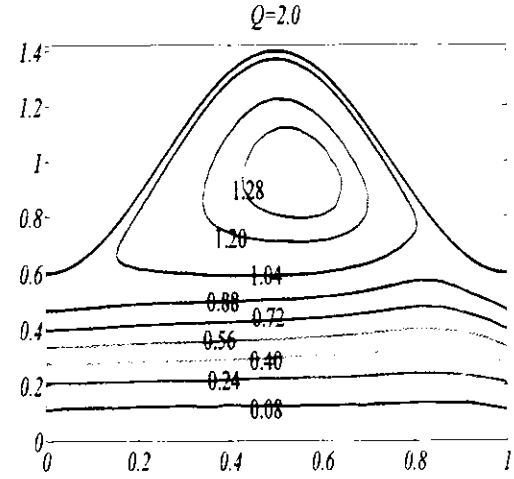

Figure 6.12: Contours of streamlines for $Q = 1.0, 1.5$ and 2.0 at fixed values of other parameters as $Re = 5, \alpha = 0.2, \phi = 0.4, K = 0.1, M = 2.0$ in wave frame

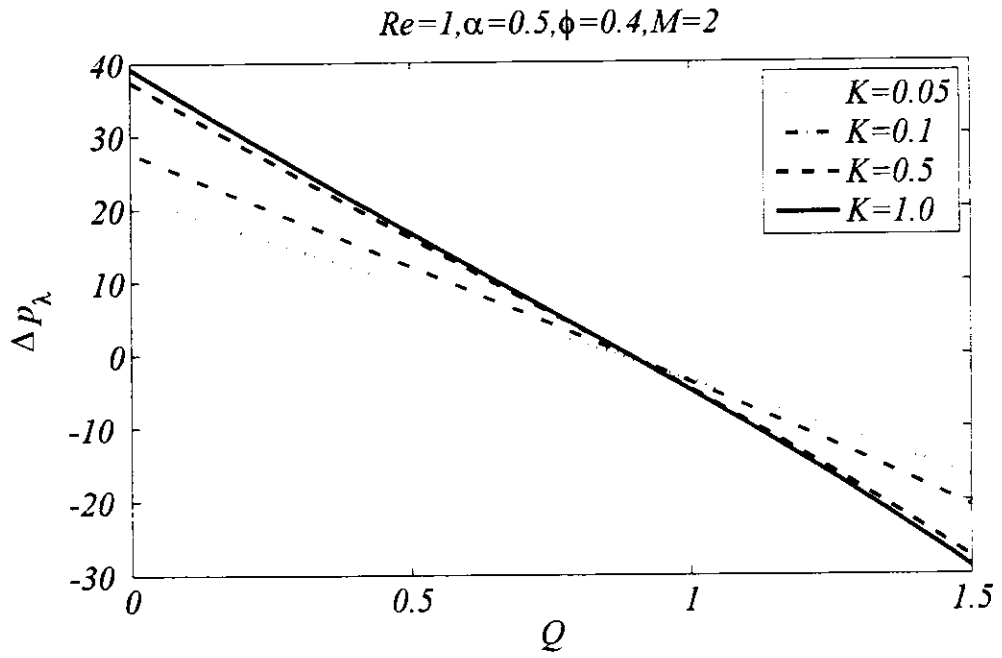

Figure 6.13: Graphs of pressure distribution for several values of K at fixed values of other parameters

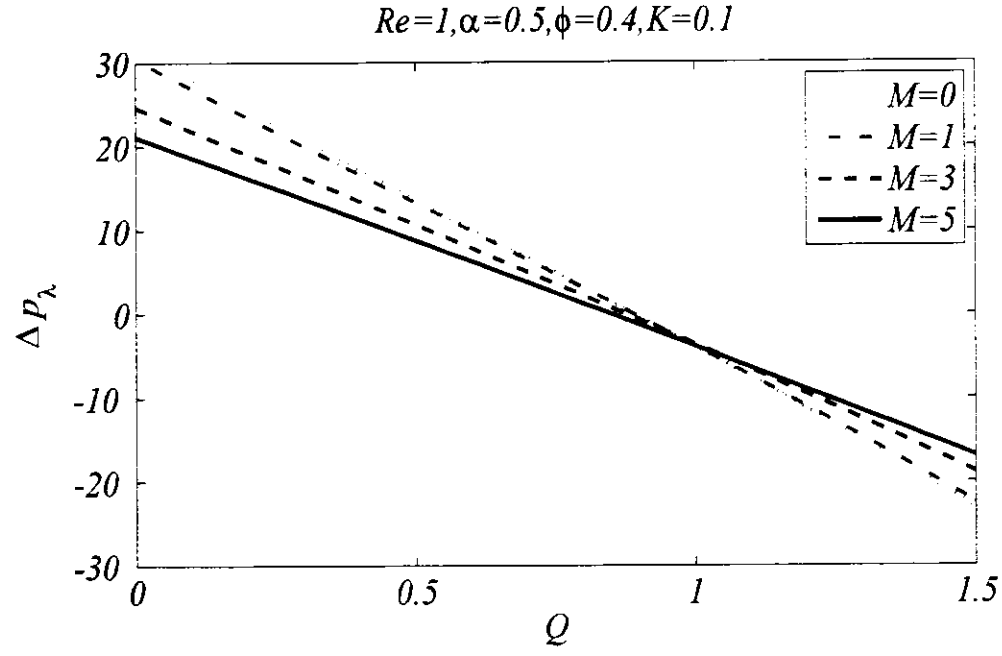

Figure 6.14: Graphs of pressure distribution at several values of M and fixed values of other parameter

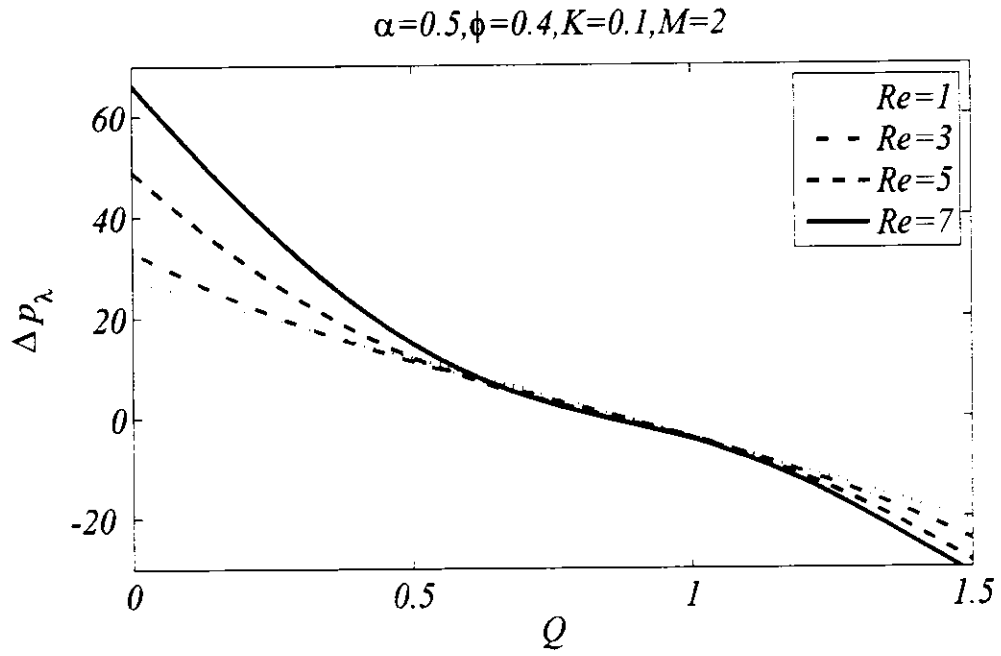

Figure 6.15: Graphs of pressure distribution for several values of *Re* at fixed values of other parameters

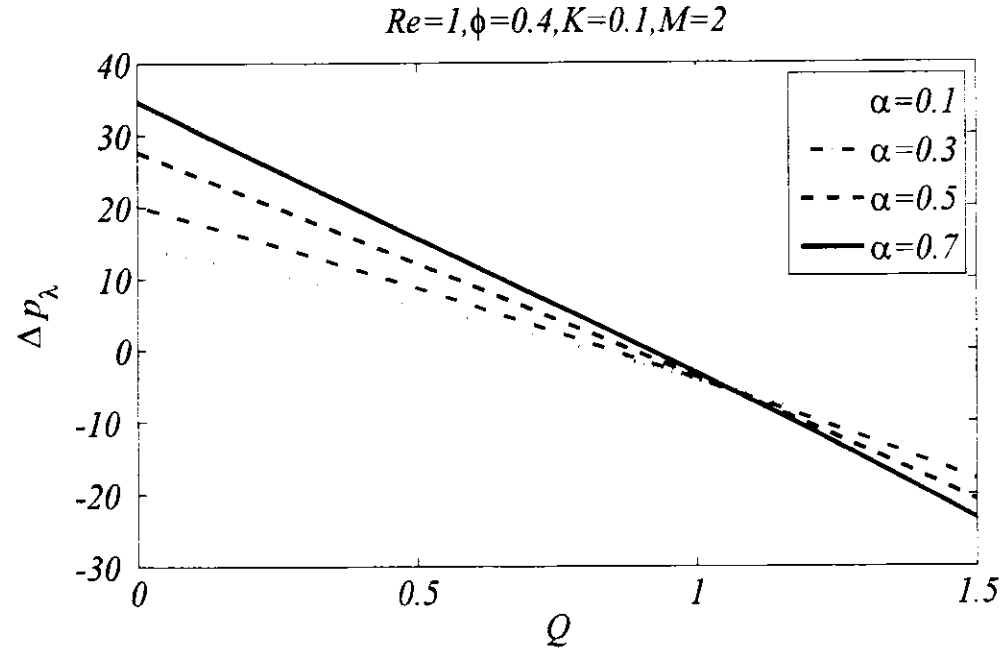

Figure 6.16: Graph of pressure distribution for several values of α at fixed values of other parameters

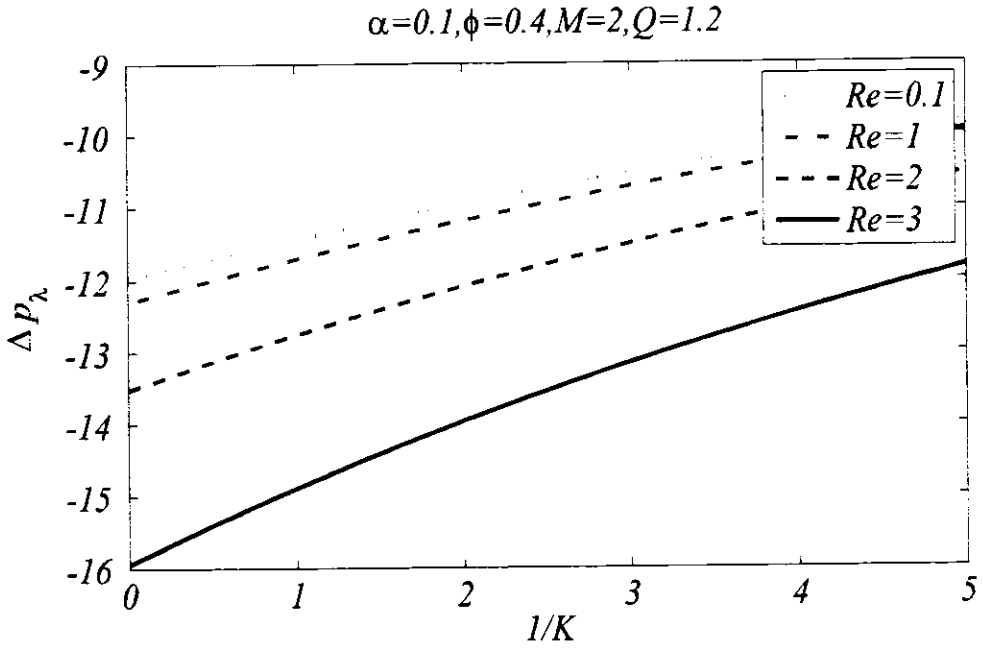

Figure 6.17: Graphs of pressure distribution against $1/K$ for several values of Re at fixed values of other parameters

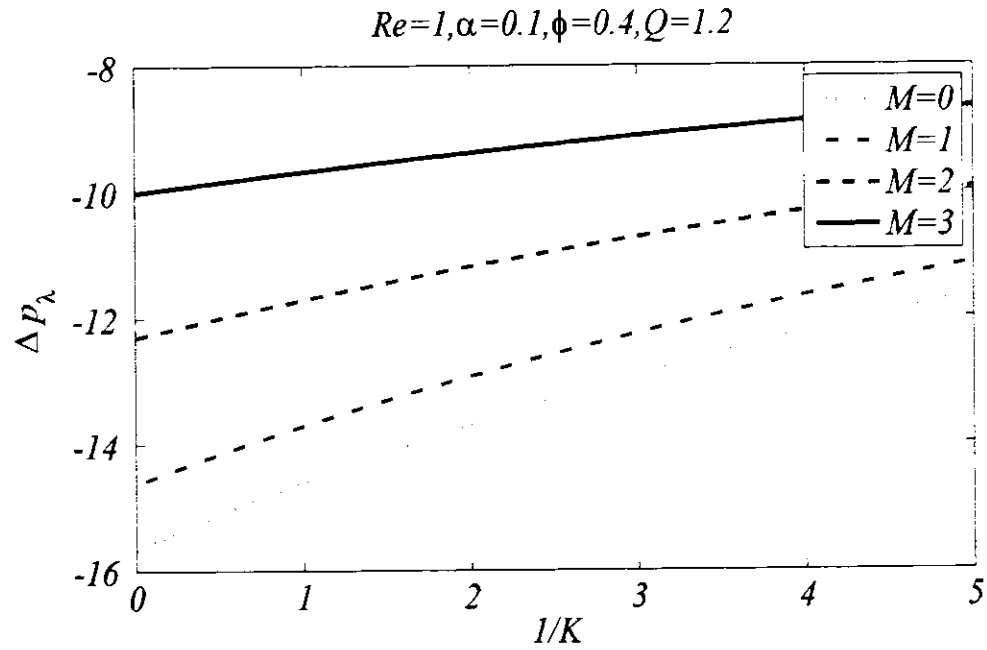

Figure 6.18: Graph of pressure distribution for against $1/K$ for several values of M at fixed values of other parameters

6.5 Conclusions

The numerical analysis of the flow brought by peristaltic waves of a Newtonian fluid passes through the porous medium is presented by using finite element method. The computations are carried out without considering the lubrication theory which allows us to present the stream function and vorticity for arbitrary non-zero values of wave number and Reynolds number which have not been reported yet. The calculations of longitudinal velocity or pressure rise per wavelength are based on the post-processing of the results. The results indicate that the longitudinal velocity at center of the tube increases with increasing both Reynolds number and Hartmann number. Circulation of trapped bolus increases with magnification in the Reynolds and Hartmann numbers. The increase in velocity and consequently decrease in pressure in the central part of the tube is predicted by increasing the the permeability of the porous medium. The numerical results obtained here are also compared with available results and an excellent correlation is achieved. It is hoped that the present study will stimulate further research on peristaltic flows of non-Newtonian fluid without using lubrication approximations and serve as a benchmark for future communications.

Chapter 7

Mixed Convective Peristaltic Flow through a Vertical Tube

This chapter contains comprehensive study of peristaltic flow passing through vertical channel to incorporate the buoyancy forces to analyze the heat transfer analysis through mixed convection in presence of heat generation parameter. The governing equations contains energy equation which includes heat generation parameter. The assumptions of lubrication theory are dropped in mathematical modelling the constitutive equations which arrives the model to set of nonlinear partial differential equations. The present model can be deduce to creeping flow to get the result of long wavelength. Galerkin's formulated finite element method is incorporated to solve the modeled equations and obtain numerical results which are presented through the graphs of different quantities for various values of he participated parameters. It is observed that circulation of bolus increases by increasing the values of the wave and Reynolds numbers. Furthermore, Isothermal lines are symmetric at low time mean flow rates and saturation is observed in the lower part is reported by increasing rate of time mean flow. The decrease in velocity is noted at center due to increasing values of Grashof number, Prandtl number and heat generation parameter, while the slight increase is also observed far away from the center. The decrease in temperature is noted for increasing values of Grashof number while, Prandtl number, heat generation and time-mean flow rate supported the enhancement in temperature.

7.1 Problem Formulation

The motion of the Newtonian fluid is consider through a vertical tube having inner width of size $2a$. The flow is assumed in such a way that the propagation of waves is along the z −axis with velocity c and r is normal to the tube. The temperature of the peristaltic wall of the channel is assumed at some temperature T_1 which follows or obeys sinusoidal wave shape given in Eq. (6.1). The schematic flow diagram is presented in **Figure 7.1**. The partial differential equations correspond to considered model of peristaltic flow in a fixed frame are

$$\frac{1}{R}\frac{\partial(RU)}{\partial R}+\frac{\partial W}{\partial Z}=0, \tag{7.1}$$

$$\rho\left(\frac{\partial U}{\partial t}+U\frac{\partial U}{\partial R}+W\frac{\partial U}{\partial Z}\right)=-\frac{\partial P}{\partial R}+\mu\left(\frac{\partial}{\partial R}\left(\frac{1}{R}\frac{\partial(RU)}{\partial R}\right)+\frac{\partial^2 U}{\partial Z^2}\right), \tag{7.2}$$

$$\rho\left(\frac{\partial W}{\partial t}+U\frac{\partial W}{\partial R}+W\frac{\partial W}{\partial Z}\right)=-\frac{\partial P}{\partial Z}+\mu\left(\frac{1}{R}\frac{\partial}{\partial R}\left(R\frac{\partial W}{\partial R}\right)+\frac{\partial^2 W}{\partial Z^2}\right)+\rho g\beta_T(T-T_0), \tag{7.3}$$

$$\rho\left(\frac{\partial T}{\partial t}+U\frac{\partial T}{\partial R}+W\frac{\partial T}{\partial Z}\right)=\kappa^*\left(\frac{\partial^2 T}{\partial R^2}+\frac{1}{R}\frac{\partial T}{\partial R}+\frac{\partial^2 T}{\partial Z^2}\right)+Q_0, \tag{7.4}$$

in which μ is viscosity, ρ is density, g is acceleration due to gravity, β_T symbolized coefficient of thermal expansion, κ^* corresponds thermal conductivity and Q_0 represents the constant heat generation within the flow domain.

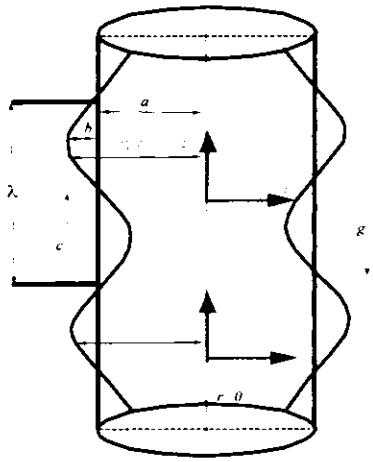

Figure 7.1: Geometry of the peristaltic flow in the tube

The boundary conditions that imposes on the flow problem are

$$U=0,\ \frac{\partial W}{\partial R}=0,\ \frac{\partial T}{\partial Z}=0\ \text{ at }\ R=0, \tag{7.5}$$

$$W=0,\ U=\frac{\partial H}{\partial t},\ T=T_1\ \text{ at }\ R=H. \tag{7.6}$$

The conversion between lab frame and wave frame may be made through following relations given in Eqs. (6.7) and (7.7)

$$p^*=P,\ \ T^*=T, \tag{7.7}$$

The following boundary condition are suitable for moving frame

$$\psi^*=0\ \text{ at }\ r^*=0\ \text{and}\ \psi^*=q^*\ \text{ at }\ r=\eta(z^*) \tag{7.8}$$

Here, stream function is represented by ψ^* in the dimensionless form. Inserting dimensionless variables defined in Eqs. (6.9) and (7.9) to the system,

$$\theta=\frac{T^*-T_0}{T_1-T_0},\beta=\frac{Q_0a^2}{\kappa^*(T_1-T_0)},Gr=\frac{\rho ga\beta(T_1-T_0)}{\mu c},\ \text{Pr}=\frac{\mu c}{\kappa^*}. \tag{7.9}$$

And after eliminating the terms representing pressure gradient from governing equations the combined equation of momentum and temperature equation in the form of stream function ψ and vorticity ω by introducing Eq. (6.10) becomes

$$\frac{\alpha^2}{r}\frac{\partial^2\psi}{\partial z^2}+\frac{\partial}{\partial r}\left(\frac{1}{r}\frac{\partial\psi}{\partial r}\right)=-\omega, \tag{7.10}$$

$$Re\left(\frac{\partial\psi}{\partial r}\frac{\partial}{\partial z}\left(\frac{\omega}{r}\right)-\frac{\partial\psi}{\partial z}\frac{\partial}{\partial r}\left(\frac{\omega}{r}\right)\right)=\frac{1}{r}\mathrm{D}^2(r\omega)-Gr\frac{\partial\theta}{\partial r}, \tag{7.11}$$

$$Re\,Pr\frac{1}{r}\left(\frac{\partial\psi}{\partial r}\frac{\partial\theta}{\partial z}-\frac{\partial\psi}{\partial z}\frac{\partial\theta}{\partial r}\right)=\nabla^2\theta+\beta, \tag{7.12}$$

where $\nabla^2=\alpha^2\frac{\partial^2}{\partial z^2}+\frac{1}{r}\frac{\partial}{\partial r}\left(r\frac{\partial}{\partial r}\right)$ and modified Laplacian operator(D^2) is define as $\mathrm{D}^2=\alpha^2\frac{\partial^2}{\partial z^2}+\frac{\partial^2}{\partial r^2}-\frac{1}{r}\frac{\partial}{\partial r}$. The boundary conditions for considered flow problem become

$$\left.\begin{array}{llll}\psi=0, & \frac{\partial}{\partial r}\left(\frac{1}{r}\frac{\partial\psi}{\partial r}\right)=0, & \frac{1}{r}\frac{\partial\psi}{\partial z}=0, & \frac{\partial\theta}{\partial r}=0 \quad \text{at} \quad r=0\\ \psi=q, & \frac{1}{r}\frac{\partial\psi}{\partial r}=-1, & \frac{1}{r}\frac{\partial\psi}{\partial z}=2\pi\phi\sin 2\pi z, & \theta=1 \quad \text{at} \quad r=\eta(z)\end{array}\right\}. \tag{7.13}$$

7.2 Numerical Analysis

In this section, we presented the numerical solution of Eqs. (7.10) to (7.12) under the constraints of boundary conditions given in (7.13). By neglecting the assumption of long wavelength along with the low Reynolds number, we arrive to a system of the nonlinear partial differential equations equipped along with the complex geometry of peristaltic tube. Thus, we need an efficient and rapid convergent technique to control such type of complicated problem. So the method based on Galerkin's weighted residual technique used in finite element method is implemented by discretizing the domain in a subdomain of six nodal quadratic triangular elements to get the highly convergent results with a tolerance of 10^{-14} which is achieved in a maximum $4-6$ number of iterations. The stream function, vorticity and temperature are approximated by using Eq. (6.15) and following equation

$$\theta=\sum_{k=1}^{n}N_k\theta_k, \tag{7.14}$$

where θ_k are nodal approximation of θ. The Galerkin based finite element method is applied to Eqs. (7.10) to (7.12) gives as

$$\int_\Omega w_1\left(\frac{\alpha^2}{r}\frac{\partial^2\psi}{\partial z^2}+\frac{\partial}{\partial r}\left(\frac{1}{r}\frac{\partial\psi}{\partial r}\right)+\omega\right)d\Omega=0, \tag{7.15}$$

$$\int_\Omega w_2 Re\left(\frac{\partial\psi}{\partial r}\frac{\partial}{\partial z}\left(\frac{\omega}{r}\right)-\frac{\partial\psi}{\partial z}\frac{\partial}{\partial r}\left(\frac{\omega}{r}\right)-\frac{1}{r}\mathrm{D}^2(r\omega)+Gr\frac{\partial\theta}{\partial r}\right)d\Omega=0, \tag{7.16}$$

$$\int_\Omega w_3 Re\,Pr\frac{1}{r}\left(\frac{\partial\psi}{\partial r}\frac{\partial\theta}{\partial r}-\frac{\partial\psi}{\partial z}\frac{\partial\theta}{\partial z}\right)d\Omega-\int_\Omega w_3\left(\frac{\partial^2\theta}{\partial r^2}+\frac{1}{r}\frac{\partial\theta}{\partial r}+\frac{\alpha^2}{r}\frac{\partial^2\theta}{\partial z^2}+\beta\right)d\Omega=0, \tag{7.17}$$

where w_1, w_2 and w_3 corresponds weight functions and $d\Omega = 2\pi r dr dz$. Simplifying the Eqs. (7.15) to (7.17), we get

$$\int_\Omega\left(\frac{\alpha^2}{r}\frac{\partial w_1}{\partial z}\frac{\partial\psi}{\partial z}+\frac{\partial w_1}{\partial r}\left(\frac{1}{r}\frac{\partial\psi}{\partial r}\right)-w_1\omega\right)d\Omega=\int_\Gamma w_1\frac{\partial\psi}{\partial n}d\Gamma, \tag{7.18}$$

$$\int_\Omega w_2 Re\left(\frac{\partial\psi}{\partial r}\frac{\partial}{\partial z}\left(\frac{\omega}{r}\right)-\frac{\partial\psi}{\partial z}\frac{\partial}{\partial r}\left(\frac{\omega}{r}\right)\right)d\Omega+\int_\Omega\left(\frac{\partial w_2}{\partial r}\frac{1}{r}\frac{\partial(r\omega)}{\partial r}+\frac{\alpha^2}{r}\frac{\partial w_2}{\partial z}\frac{\partial(r\omega)}{\partial z}\right)d\Omega+\mathrm{Gr}\int_\Gamma w_2\frac{\partial\theta}{\partial r}d\Omega=\int_\Gamma w_2\frac{\partial(r\omega)}{\partial n}d\Gamma, \tag{7.19}$$

$$Re\,Pr\int_\Omega w_3\frac{1}{r}\left(\frac{\partial\psi}{\partial r}\frac{\partial\theta}{\partial r}-\frac{\partial\psi}{\partial z}\frac{\partial\theta}{\partial z}\right)d\Omega+\int_\Omega\left(\frac{\partial w_3}{\partial r}\frac{\partial\theta}{\partial r}\right)d\Omega-\int_\Omega\left(w_3\frac{1}{r}\frac{\partial\theta}{\partial r}\right)d\Omega+\alpha^2\int_\Omega\left(\frac{1}{r}\frac{\partial w_3}{\partial z}\frac{\partial\theta}{\partial z}\right)d\Omega-\int_\Omega w_3\beta\,d\Omega=\int_\Gamma w_3\frac{\partial\theta}{\partial n}d\Gamma, \tag{7.20}$$

where $d\Gamma = \pi r dr dz$. Introducing Eqs. (6.15) and (7.14) into Eqs. (7.18) to (7.20) and considering the discretized domain, we have

$$-\sum_i B^e_{ki}\omega_i+\sum_i A^e_{ki}\psi_i=S^{k^e}_n, \tag{7.21}$$

$$Re\sum_i C^e_{kij}\psi_i\omega_i+\sum_i A^e_{ki}\omega_i+Gr\sum_i B'^e_{ki}\theta_i=S^{k^e}_n, \tag{7.22}$$

$$Re\,\mathrm{Pr}\sum_i C^e_{kij}\psi_i\theta_i+\sum_i A'^e_{ki}\theta_i=S^{k^e}_n+\beta S^{k^e}, \tag{7.23}$$

where

$$\left.\begin{aligned}
A^e_{ki}&=\int_{\Omega^e}\left(\frac{\alpha^2}{r}\frac{\partial N_k}{\partial z}\frac{\partial N_i}{\partial z}+\frac{\partial N_k}{\partial r}\left(\frac{1}{r}\frac{\partial N_i}{\partial r}\right)\right)d\Omega\\
A'^e_{ki}&=\int_{\Omega^e}\left(\alpha^2\frac{\partial N_k}{\partial z}\frac{\partial N_i}{\partial z}+\frac{\partial N_k}{\partial r}\frac{\partial N_i}{\partial r}\right)d\Omega\\
B^e_{ki}&=\int_{\Omega^e}N_kN_i\,d\Omega\\
B'^e_{ki}&=\int_{\Omega^e}N_k\frac{\partial N_i}{\partial r_i}\,d\Omega\\
C^e_{kij}&=\int_\Omega N_k\left(\frac{\partial N_i}{\partial r}\frac{\partial}{\partial z}\left(\frac{N_j}{r}\right)-\frac{\partial N_j}{\partial z}\frac{\partial}{\partial r}\left(\frac{N_i}{r}\right)\right)d\Omega\\
S^{k^e}_n&=\int_\Gamma N_k\bar{S}_k d\Gamma\ \text{and}\ S^{k^e}=\int_\Gamma N_k d\Gamma
\end{aligned}\right\}. \tag{7.24}$$

After assembly procedure, obtained resulting system (global) in the matrix arrangement is expressed as follows

$$\boldsymbol{KA} = \boldsymbol{F}, \tag{7.25}$$

in which

$$K_{ij} = \begin{bmatrix} -B^e_{ki} & A^e_{ki} & 0 \\ A^e_{ki} & ReC^e_{kij}\omega_i & GrB'^e_{ki} \\ 0 & ReC^e_{kij}\psi_i & A'^e_{ij} \end{bmatrix}, A_k = \begin{bmatrix} \omega_k \\ \psi_k \\ \theta_k \end{bmatrix}, F_k = \begin{bmatrix} S^{k^e}_n \\ S^{k^e}_n \\ S^{k^e}_n + \beta S^{k^e} \end{bmatrix}. \tag{7.25}$$

Pressure rise per wavelength plays vital role in the peristaltic flow. In order to determine the pressure within a tube, it is sufficient to determine it at the middle portion of the wave. Rise in pressure per wavelength is given by Eq. (6.14).

7.3 Validation

This section is dedicated for authentication of our own built MATLAB code of finite element method which gives the numerical solution of modeled system of nonlinear partial differential equations. Mekheimer and Abd elmaboud (2008) gave results for the analysis of heat transfer during the peristaltic transport in the vertical tube by using assumptions of lubrication theory. These results are purely analytical and hence considered to be a benchmark solution in this comparison. The obtained results of pressure distribution are compared with the results of Mekheimer and Abd elmaboud (2008) in limiting case and are shown in **Figure 7.2(a).** The graphs presented in **Figure 7.2(a)** exhibits good agreement of our results under assumptions of long wavelength along with low Reynolds number (for $Re = 0, \alpha = 0$) with corresponding results of Mekheimer and Abd elmaboud (2008). The graphs of longitudinal velocity are also plotted in limiting case of obtained results to compare with the results of Hameed et al. (2015) in **Figure 7.2(b)**. **Figure 7.2(b)** shows good agreement of obtained numerical results with results that of Hameed et al. (2015) considering long wavelength along with low Reynolds number assumptions.

7.4 Results and Discussion

For the moderate finite values of Reynolds number, a theoretical analysis of the peristaltic flow is extremely difficult because of the nonlinearity in the modeled equations which occurs by the interaction of moving wall and the flow field. The effects of Reynolds number along with other parameters of interest involved in the modeled equation are studied by plotting the velocity distribution, temperature profile, and

pressure rise per wavelength. The contours of streamlines and vorticity are plotted and the detailed discussion is provided in next subsections.

7.4.1 Velocity profile

To analyze the behavior of the velocity, longitudinal velocity is plotted at cross-section $z = 0$ for various values of participating parameters such as Reynolds number Re, wave number α, Grashof number Gr, Prandtl number Pr, heat generation parameter β and volume flow rate Q. In **Figure 7.3**, we presented the effects of Reynolds number Re on velocity distribution. We see that near the center of the tube, increase in Re causes a decrease in velocity while an opposite behavior is observed at the wall. It predicts that dominant inertial effects in the center of the tube causes decrease in velocity of the fluid, while near the wall, increase in inertial forces enhances the velocity. The same but clearer trend is observed for the velocity by varying the wave number at fixed values of other parameters as shown in **Figure 7.4**. It is also observed that for large values of wave number, the velocity attains its maximum value before entering in the region of $r = 0$. It is also interesting to note that longitudinal velocity is less sensitive to the values of Reynolds number in the range $0.2 \leq r \leq 0.4$. Similarly, longitudinal velocity varies slowly with wave number in this range and after this range rapid change is observed. In **Figure 7.5**, we observed that the longitudinal velocity rises in the vicinity of the peristaltic wall by enhancing Grashof number and it drops in neighbor of the center of the tube. It is noted from **Figures 7.6 - 7.8** that velocity profile becomes concave shaped against Reynolds number, Prandtl number and Grashof number. It is also observed that for Grashof number, change in velocity behavior is much faster in comparison with that of Reynolds number and Prandtl number. It concludes that due to increase in the temperature, the velocity of the fluid decreases and consequently more resistance appears in the flow field. We observed that when time-mean flow rate $Q \leq 1$, the velocity profile becomes negative and fluid particle at $r = 0$ moves towards opposite direction of the flow field. When time-mean flow rate $Q > 1$, the flow becomes positive and fluid particle moves in the direction of the flow field. It concludes that the particle moves along the direction of the flow field when $Q > 1$.

7.4.2 Temperature distribution

Figures 7. 9 to **7.14** shows the physical effects of all embedded parameters on temperature profile. The effects of Reynolds number Re are presented for temperature distribution in the **Figure 7.9**, as long wavelength with the low Reynolds number theory

is not able to predict such non-linear effect. It shows strong inertial effects induced by large values of Reynolds number in whole region of the tube. The opposite behavior is observed for variation of wave number α as presented in **Figure 7.10**. **Figure 7.11** shows that increase in Grashof number Gr by increasing buoyancy forces as compared to viscous forces has important role in reducing the temperature of the fluid within the tube. **Figure 7. 12** shows that temperature of the fluid can be enhanced by increasing the Prandtl number. The temperature increases when the convective heat transfer is enhanced which is evident from the **Figure 7.13**. **Figure 7.14** shows that the upsurge in time-mean flow rate encourages the rise of internal energy of the considered fluid and consequently increase in temperature is noted.

7.4.3 Trapping phenomena

The phenomena based on the circulation of the streamlines is known as trapping. Trapping is an interesting mechanism for peristaltic flows to discuss the flow properties under the influence of parameters involved in the model. We discussed this phenomenon through **Figures 7.15** to **7.18**. **Figure 7.15** shows the effects of various values of rate of time mean flow on the fluid flow. It has been observed that augmentation in the time mean flow rate causes reduction in size of the bolus. This is due to the increase of smoothness in the movement of the fluid in the central region of the tube. **Figure 7.16** shows that due to increase in Reynolds number, the flow becomes smoother in the central region. Furthermore, increase in the number of the trapped boluses is noted with a cluster of bolus showing tendency to move towards upper region of the crest. The same behavior is observed in case of wave number α as shown in **Figure 7.17**. It also reflects that we can control the smoothness of the movement of the fluid in central part of the tube by enhancing wave number. In **Figure 7.18**, we have increase the Grashof number Gr from 0.1 to 0.9 (where vanishing buoyancy effects corresponds to the Newtonian case as reported by Shapiro et. al. (1969)) where it is the point to be noted that magnitude of the trapped bolus reduces and it moves in region near the wall of tube.

7.4.4 Isothermal lines

Isothermal lines are representation of the temperature distribution in a flow field. The sketches of isothermal lines for different parameters are presented through **Figures 7.19** to **7.23**. **Figure 7.19** presents the isothermal lines for time-mean flow rate $Q = 1.2$ and $Q = 1.8$. We observed the symmetric behavior for smaller values of Q while

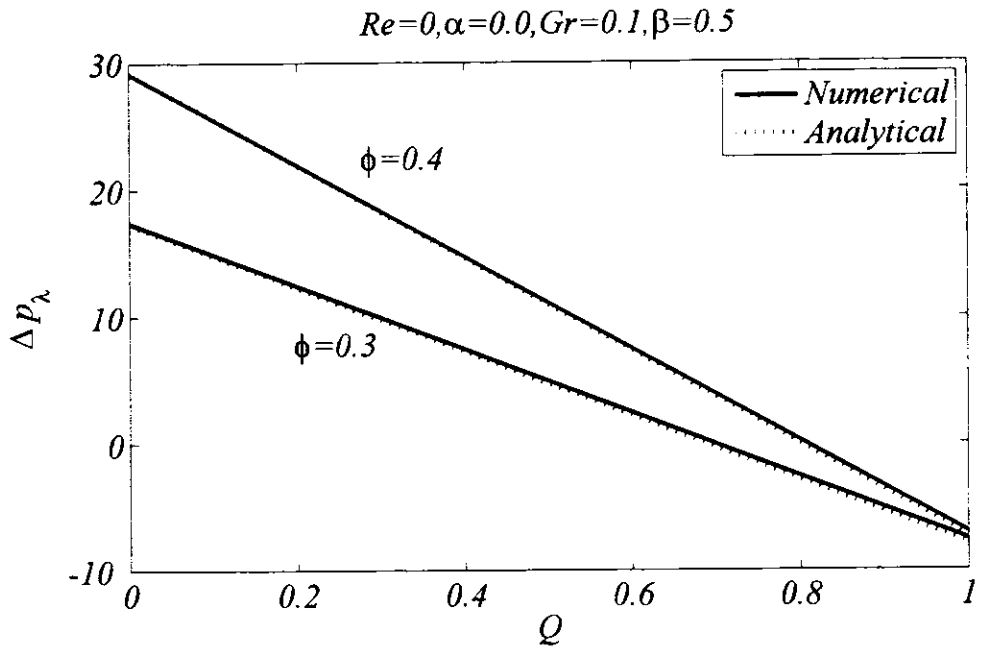

Figure 7.2(a): Comparison of pressure distribution for present numerical results with analytical results of Mekheimer and Abd elmaboud (2008)

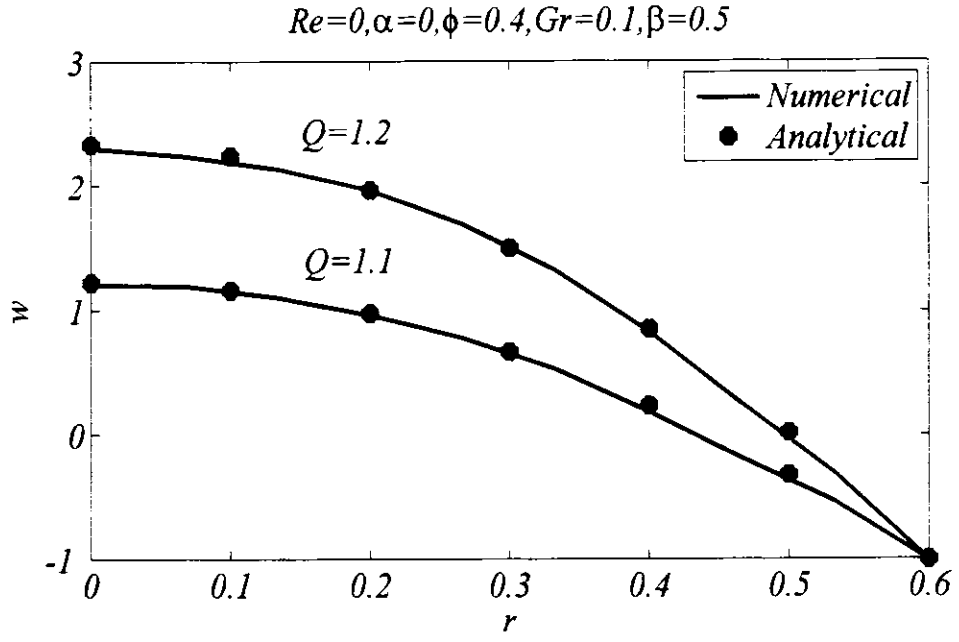

Figure 7.2(b): Comparison of longitudinal velocity for present numerical results with analytical results of Hameed et al. (2015)

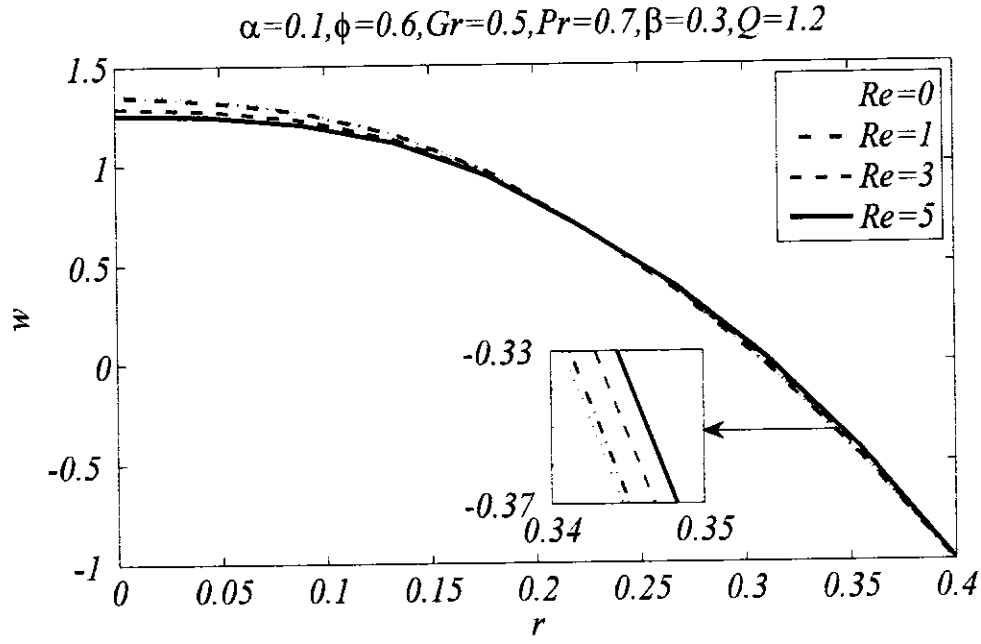

Figure 7.3: Graphs of longitudinal velocity for various values of the parameter Reynolds number *Re*

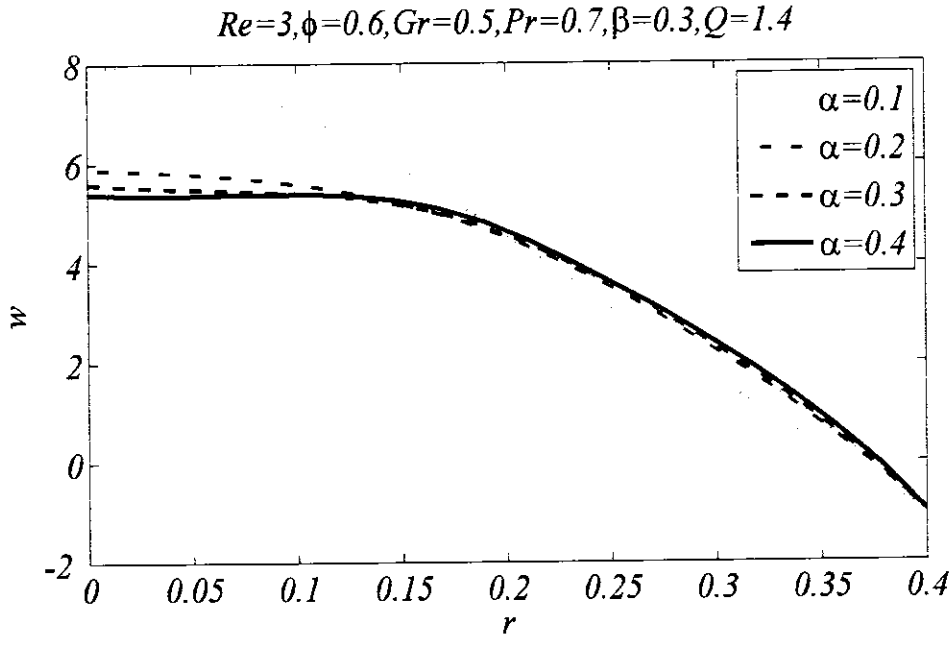

Figure 7.4: Graphs of longitudinal velocity for various values of the parameter wave number α

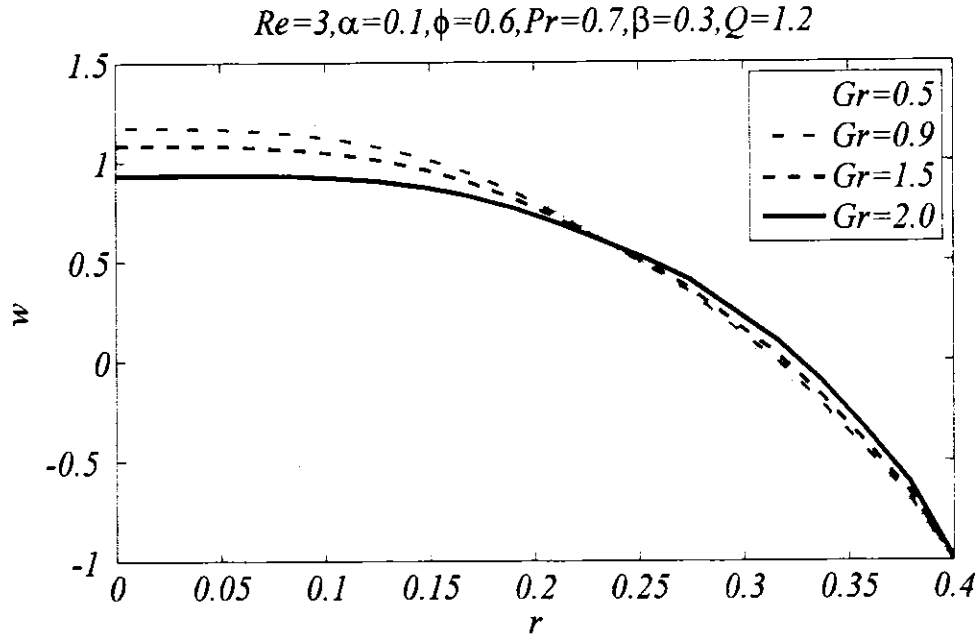

Figure 7.5: Graphs of longitudinal velocity for various values of the parameter Grashof number Gr

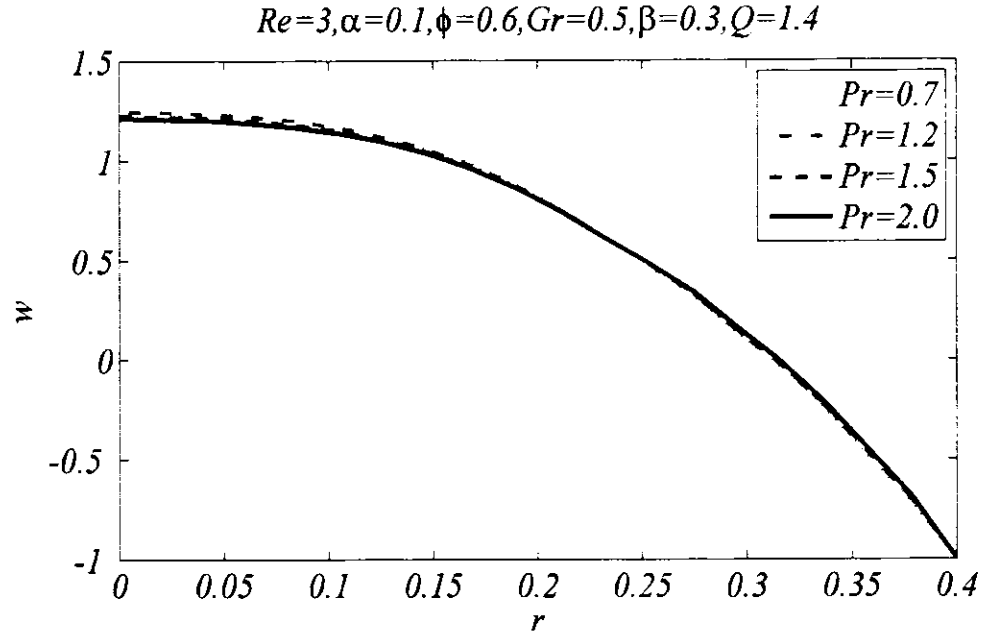

Figure 7.6: Graphs of longitudinal velocity for various values of the parameter Prandtl number Pr

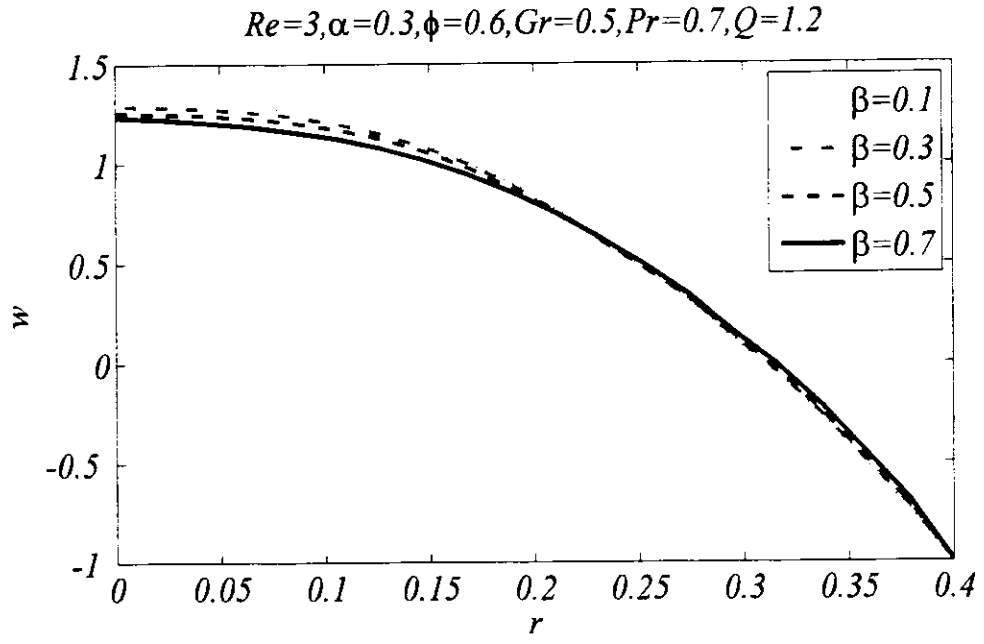

Figure 7.7: Graphs of longitudinal velocity for various values of the parameter heat generation parameter β

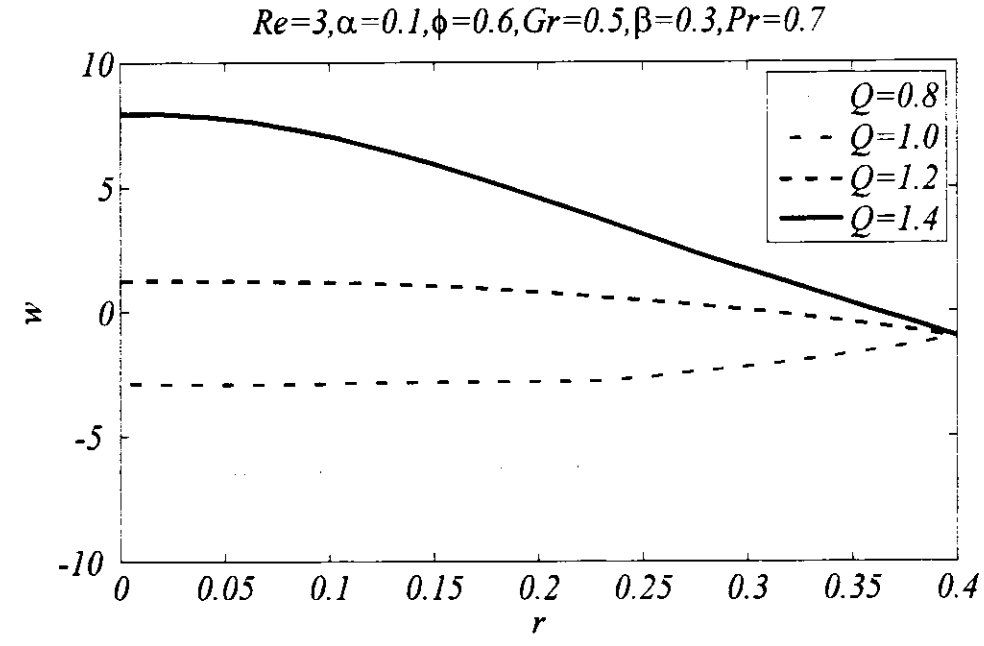

Figure 7.8 Graphs of longitudinal velocity for various values of the parameter time-mean flow rate Q

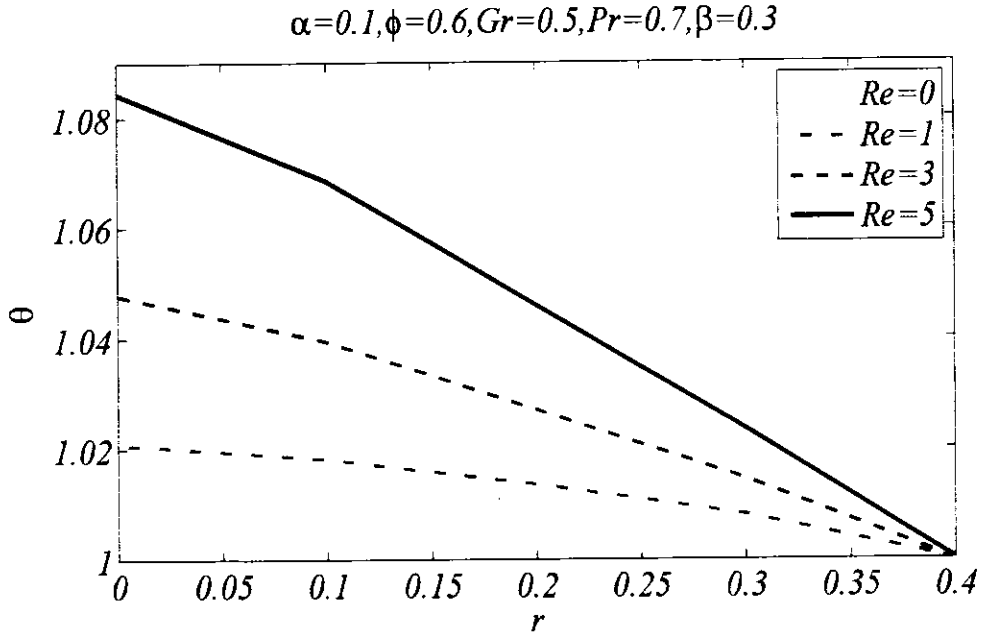

Figure 7.9: Graphs of temperature profile for various values of the parameter Reynolds number *Re* at fixed values of other parameters

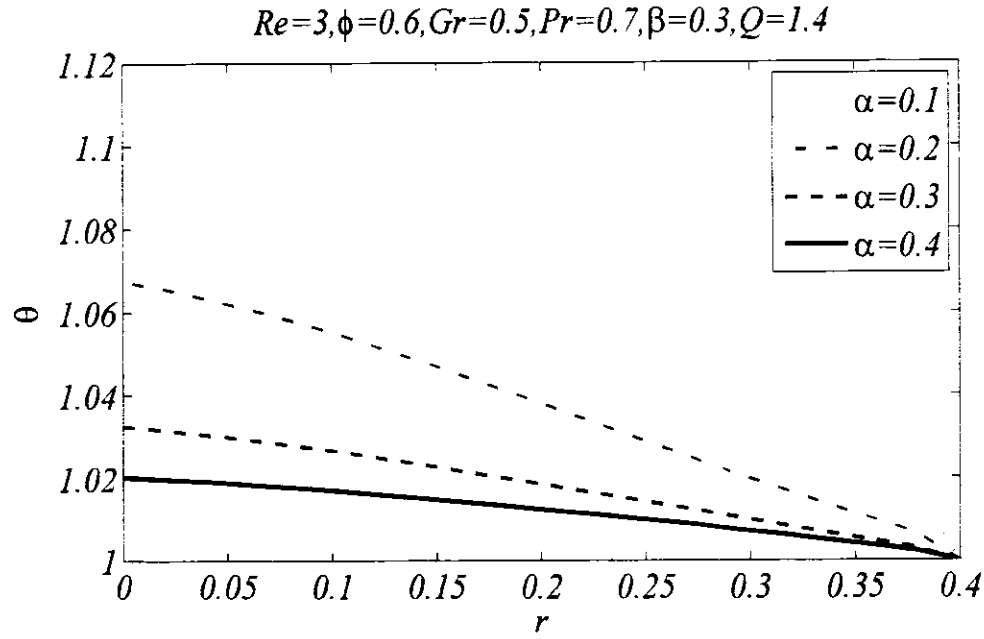

Figure 7.10: Graphs of temperature profile for various values of the paramter wave number α at fixed values of other parameters

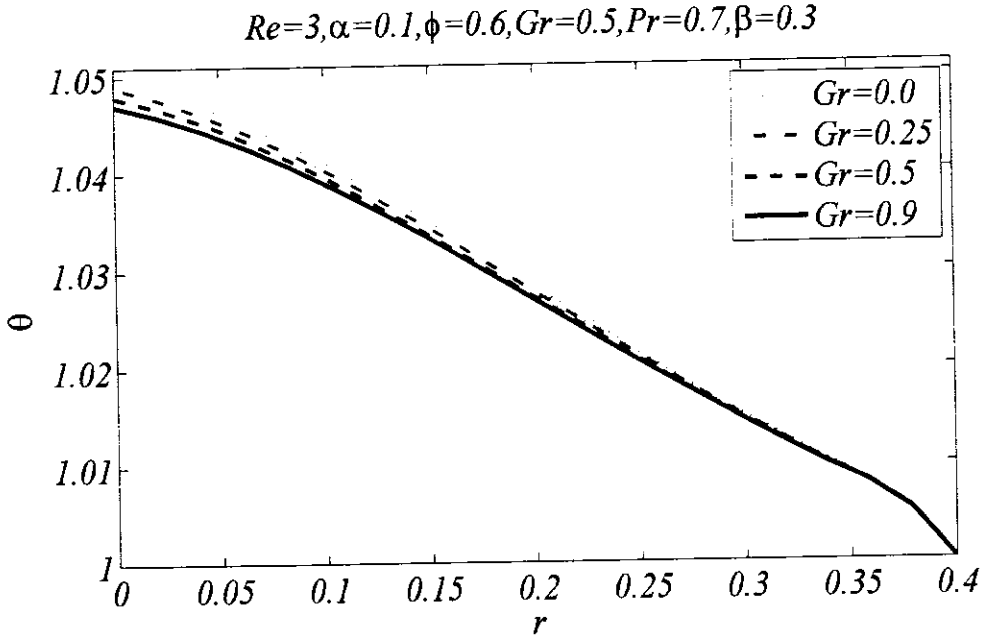

Figure 7.11: Graphs of temperature profile for various values of the paramter Grashof number Gr at fixed values of other parameters

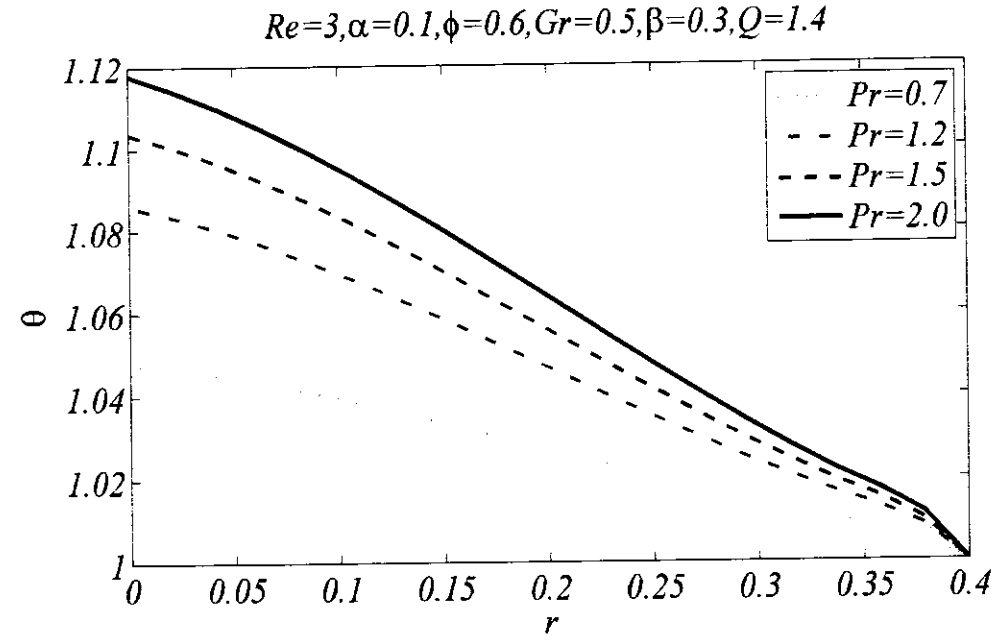

Figure 7.12: Graphs of temperature profile for various values of the parameter Prandtl number Pr at fixed values of other parameters

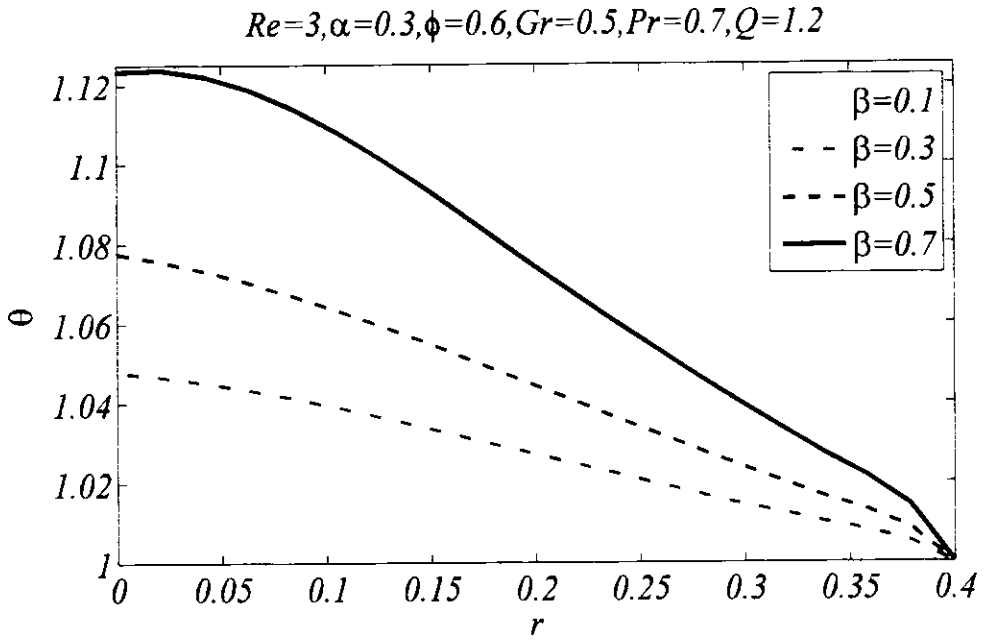

Figure 7.13: Graphs of temperature profile for various values of the paramter heat generation parameter β at fixed values of other parameters

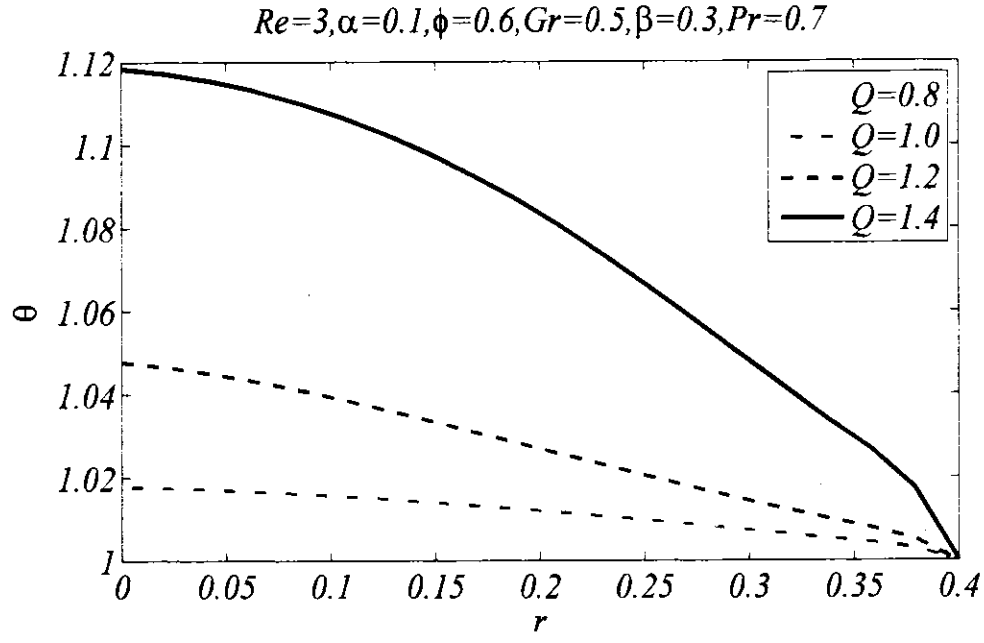

Figure 7.14: Graphs of temperature profile for various values of the parameter time-mean flow rate Q at fixed values of other parameters

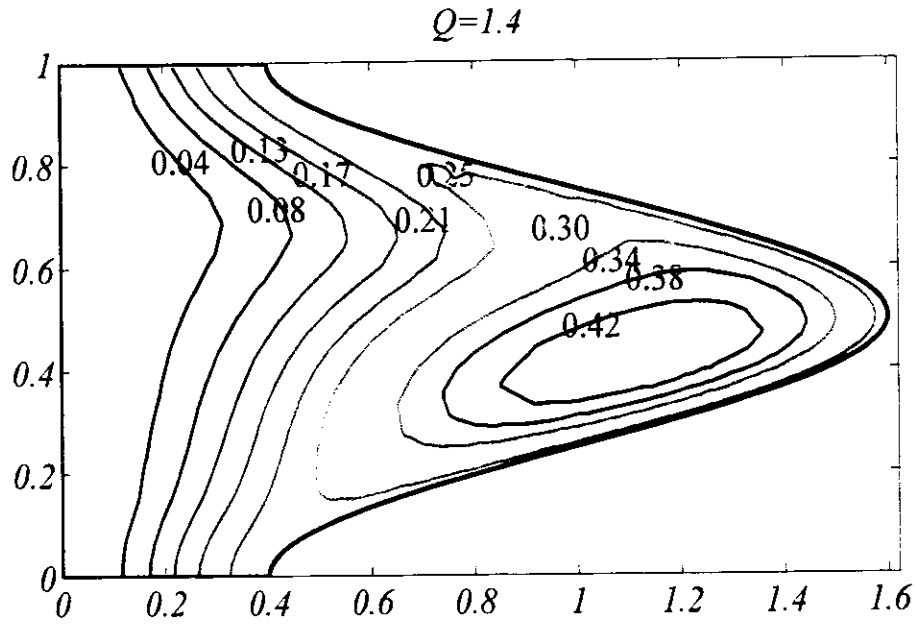

(a)

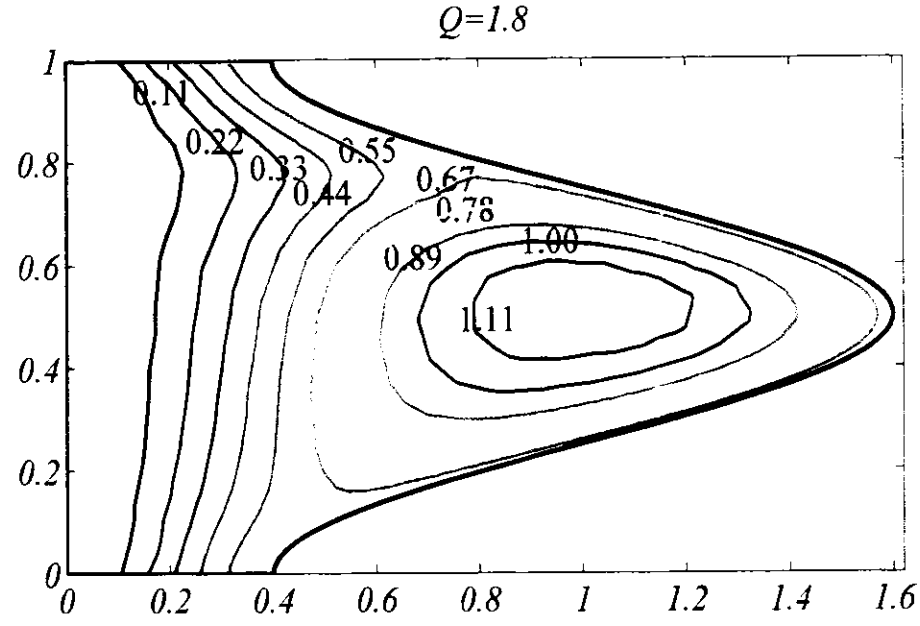

(b)

Figure 7.15: Streamlines for various values of the parameter time-mean flow rate Q at fixed values of other parameters $Re = 1, \alpha = 0.1, \phi = 0.6, Pr = 0.7, \beta = 0.3, Gr = 0.5$

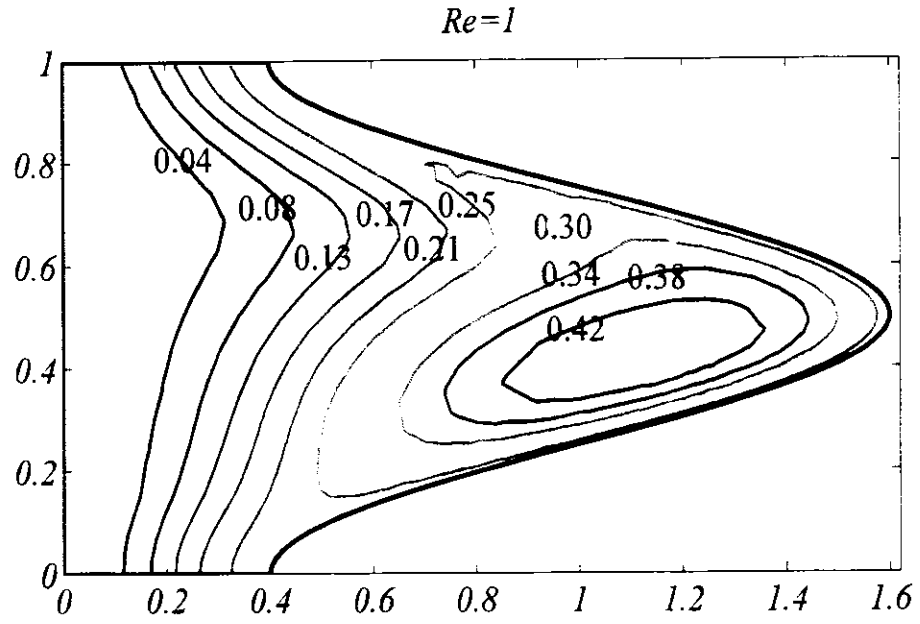

(a)

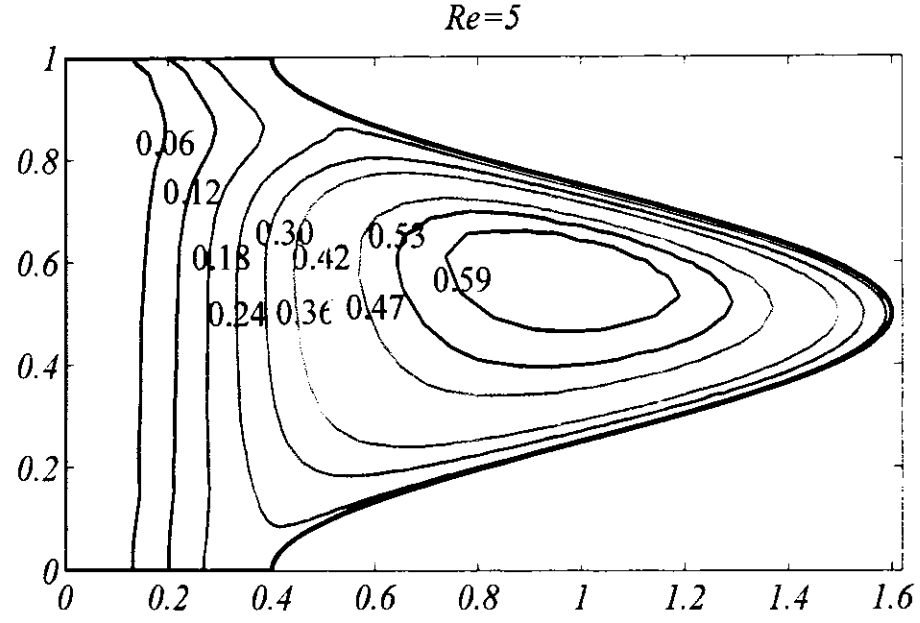

(b)

Figure 7.16: Streamlines for various values of Reynolds numbers Re at fixed values of other parameters $\alpha = 0.1, \phi = 0.6, Pr = 0.7, \beta = 0.3, Gr = 0.5, Q = 1.4$

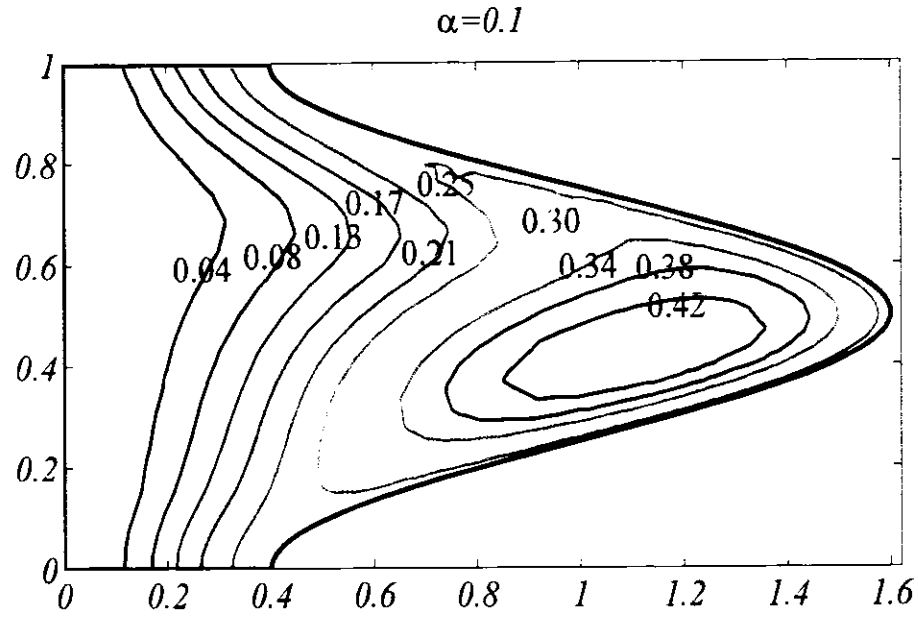

(a)

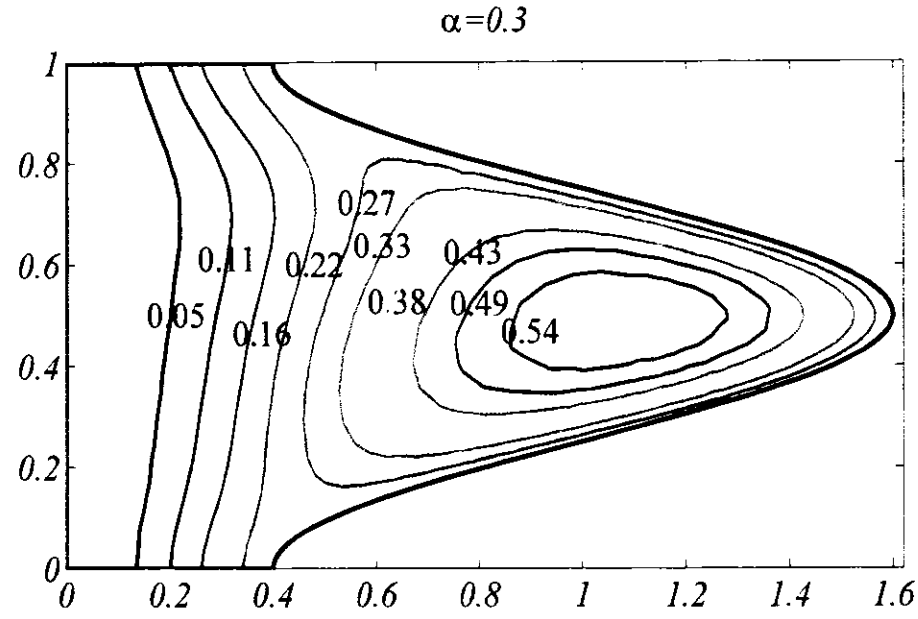

(b)

Figure 7.17: Streamline for various values of wave numbers α at fixed values of other parameters $Re = 1.0, \phi = 0.6, Pr = 0.7, \beta = 0.3, Gr = 0.5$ and $Q = 1.4$

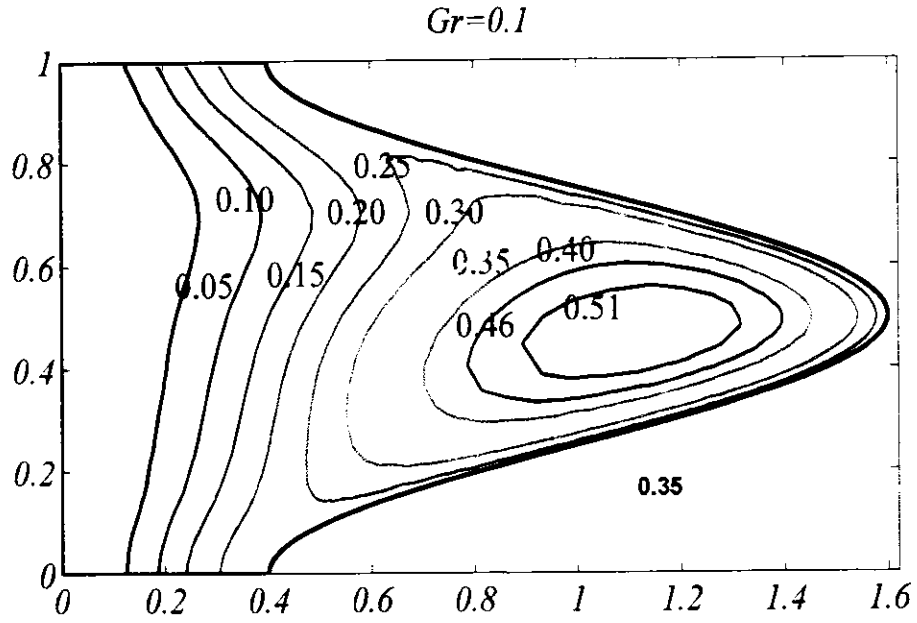

(a)

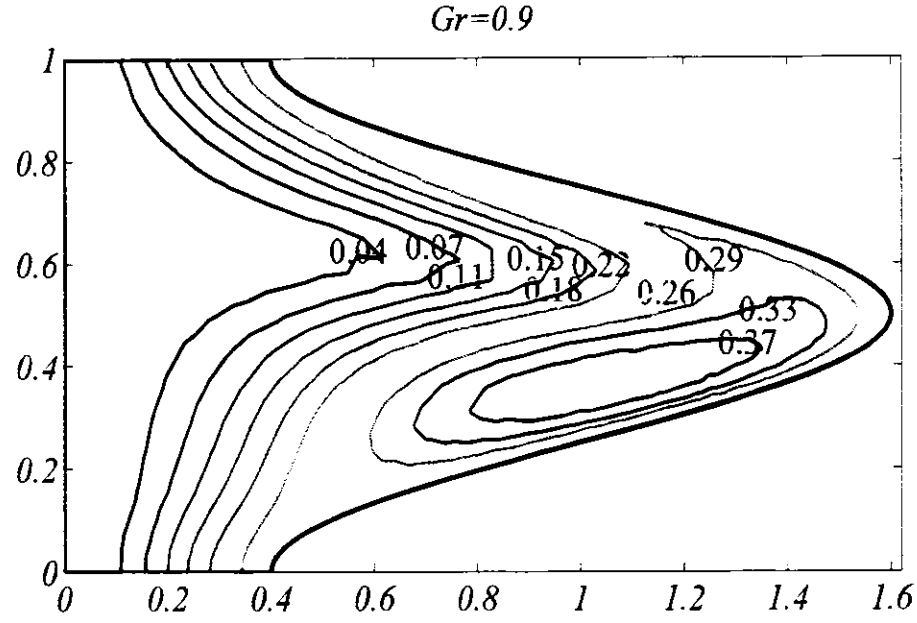

(b)

Figure 7.18: Streamline for various values of the parameter Grashof number Gr at fixed values of other parameters $Re = 1.0, \alpha = 0.1, \phi = 0.6, Pr = 0.7, \beta = 0.3, Gr = 0.5$ and $Q = 1.4$

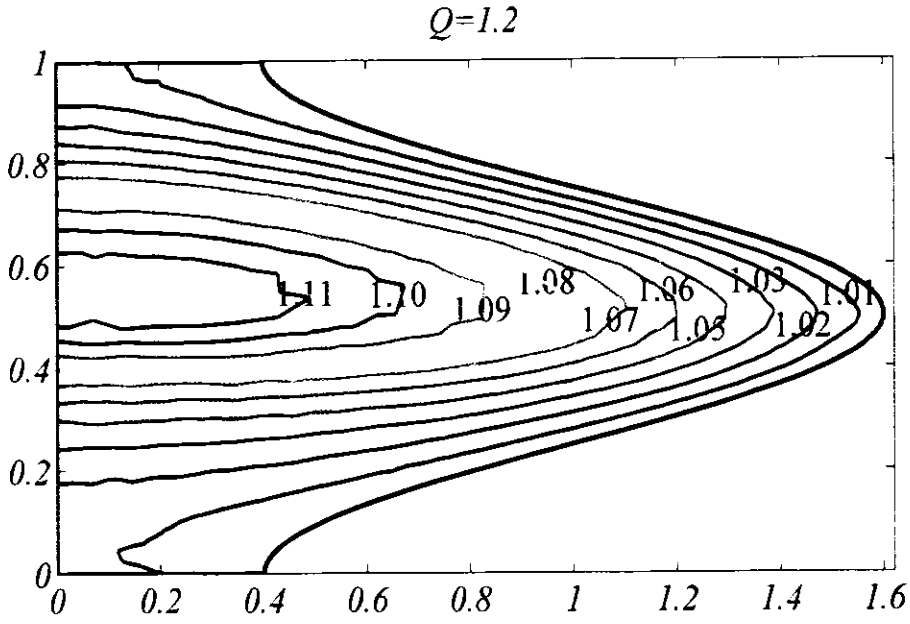

(a)

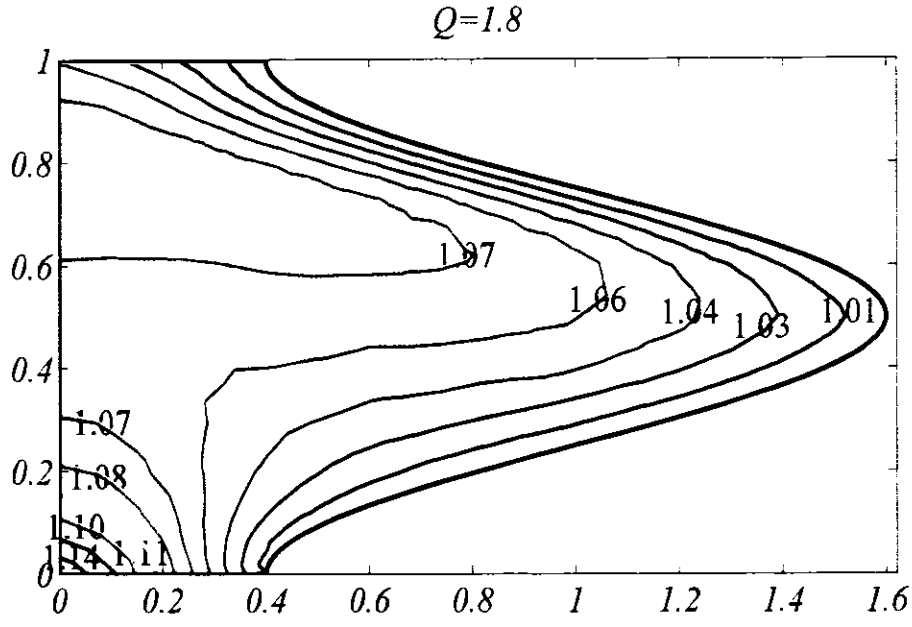

(b)

Figure 7.19: Isothermal lines for various values of time-mean flow rate Q at fixed values of other parameters $Re = 1, \alpha = 0.1, \phi = 0.6, Pr = 0.7, \beta = 0.3$ and $Gr = 0.5$

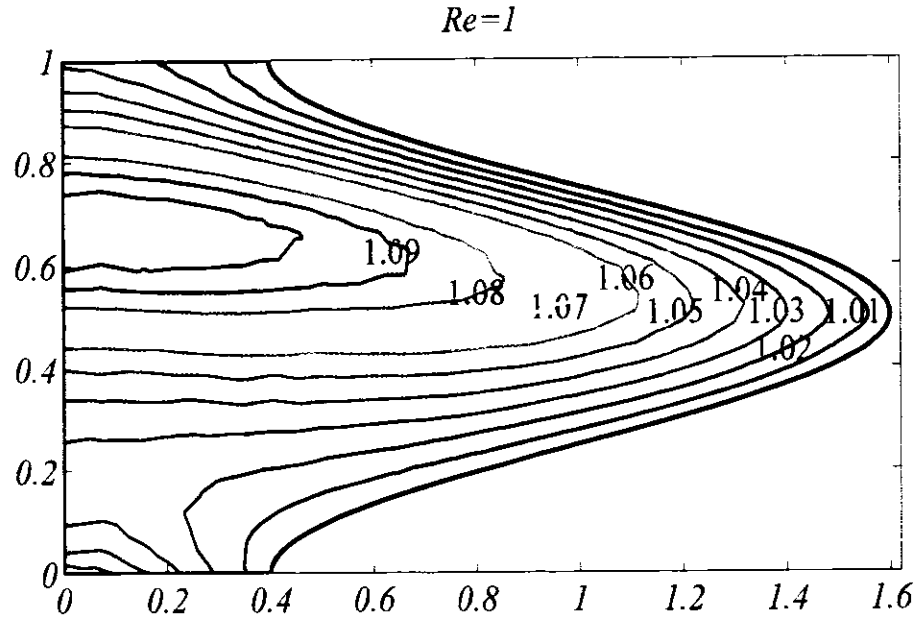

(a)

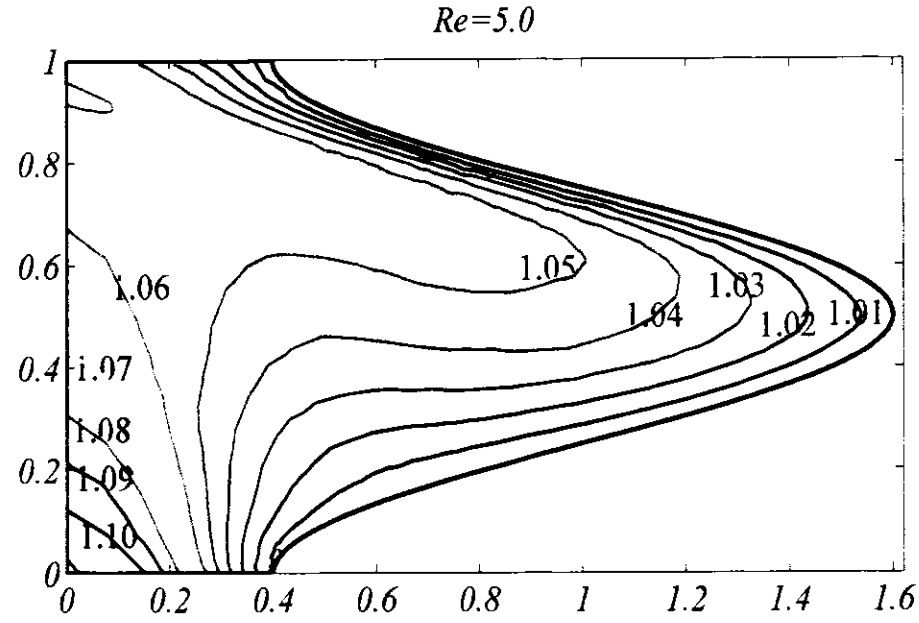

(b)

Figure 7.20: Isothermal lines for various values of Reynolds numbers Re at fixed values of other parameters $\alpha = 0.1, \phi = 0.6, Pr = 0.7, \beta = 0.3, Gr = 0.5$ and $Q = 1.4$

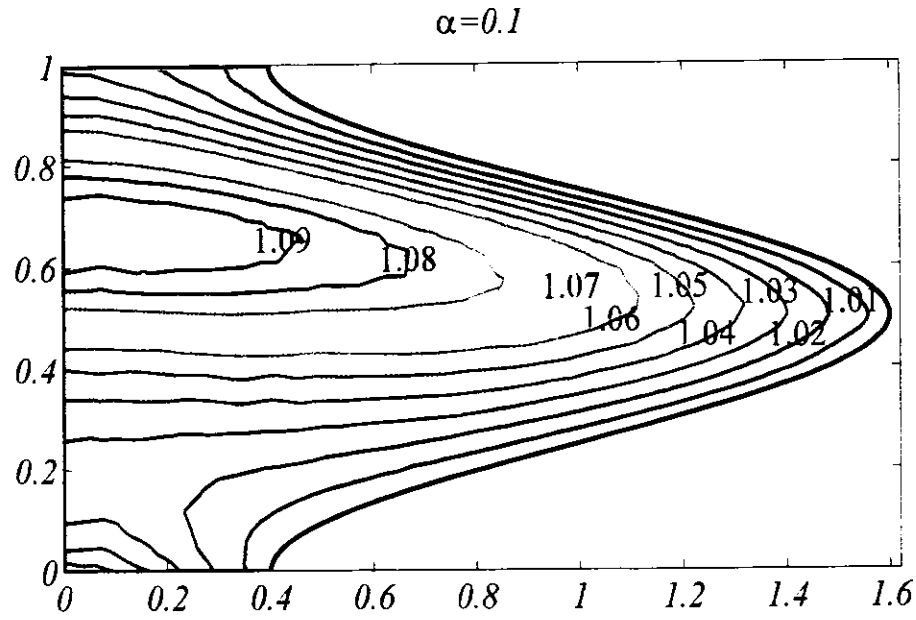

(a)

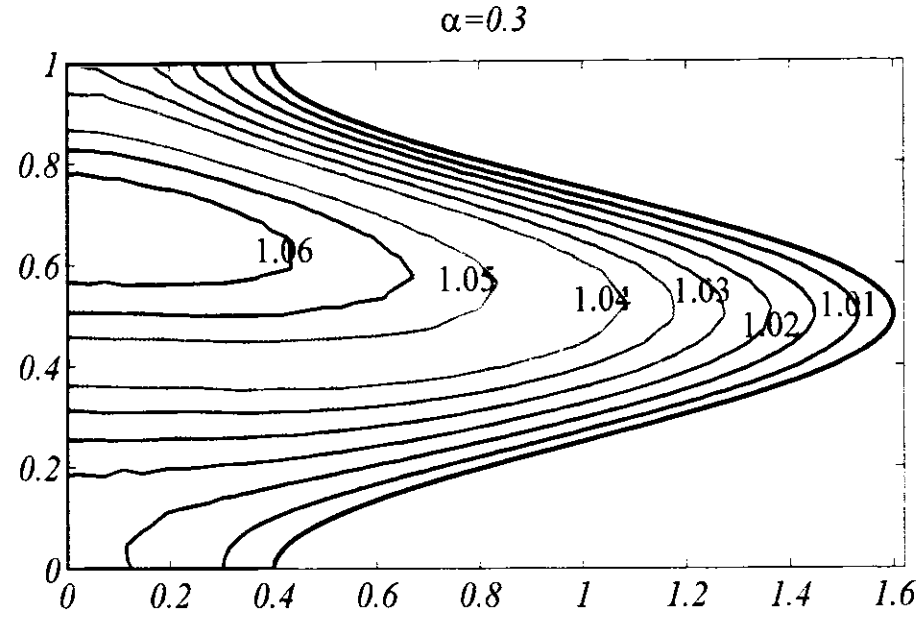

(b)

Figure 7.21: Isothermal lines for various values of wave number α at fixed values of other parameter s$Re = 1.0, \phi = 0.6, Pr = 0.7, \beta = 0.3, Gr = 0.5$ and $Q = 1.4$

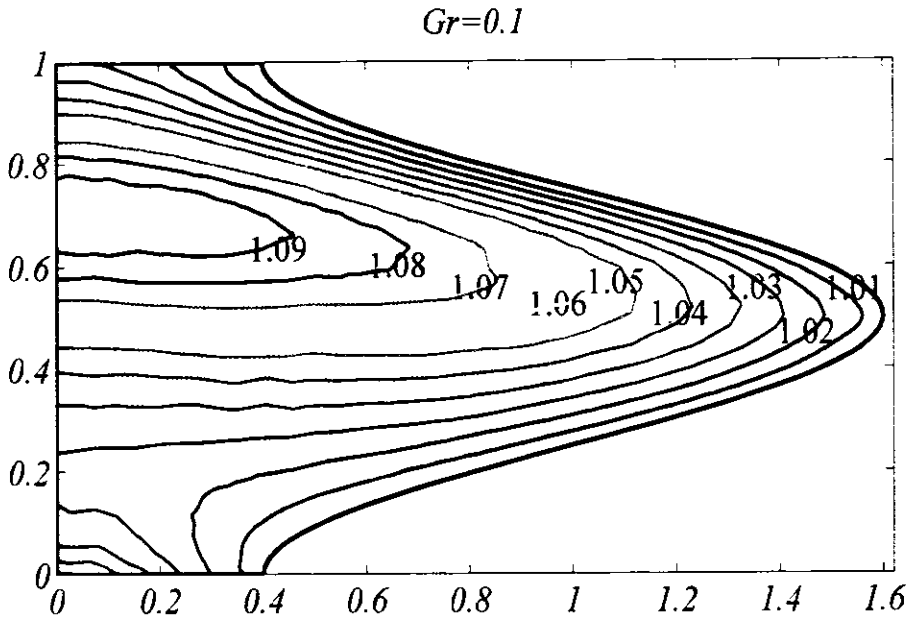

(a)

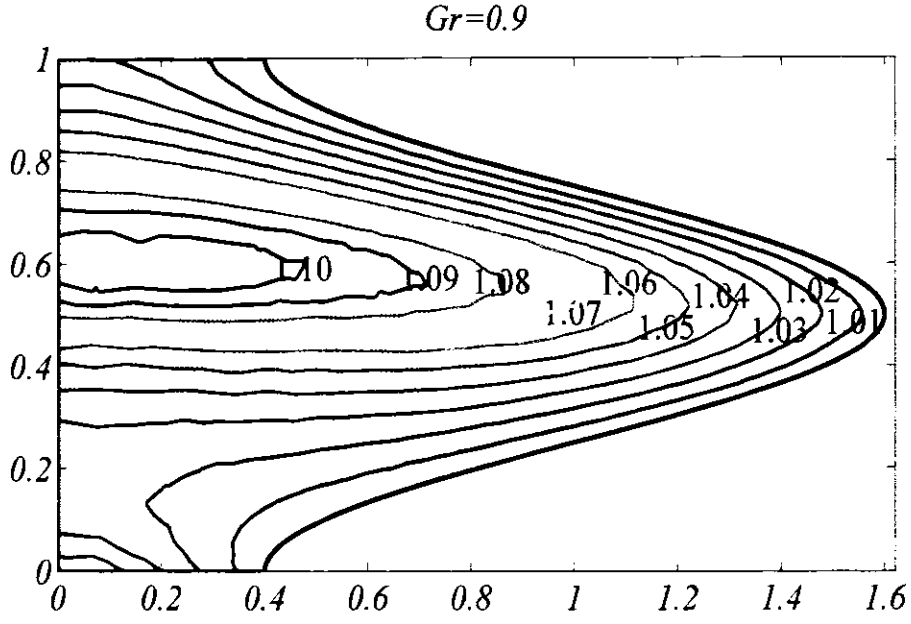

(b)

Figure 7.22: Isothermal lines for various values of the parameter Grashof number Gr at fixed values of other parameters $Re = 1.0, \alpha = 0.1, \phi = 0.6, Pr = 0.7, \beta = 0.3, Gr = 0.5$ and $Q = 1.4$

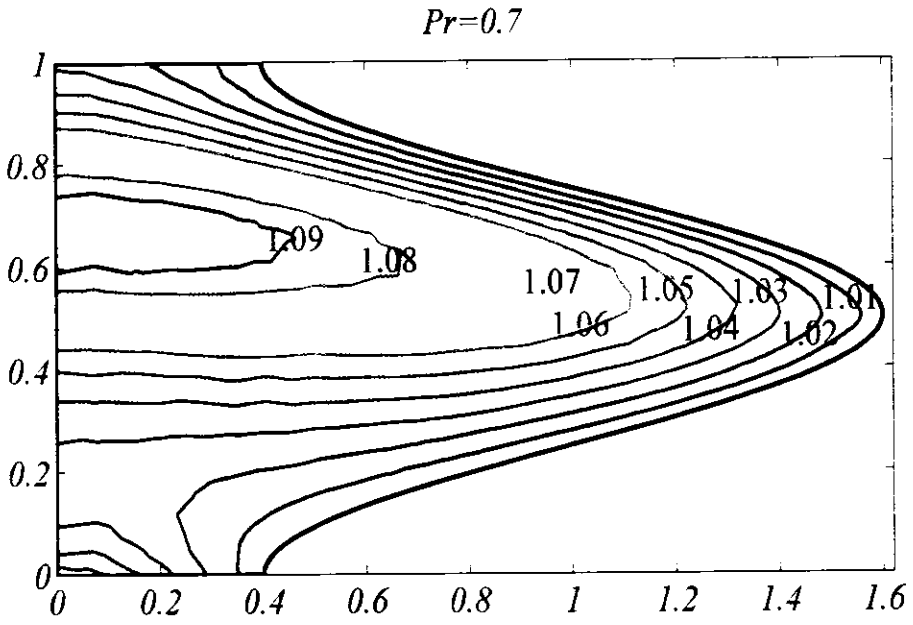

(a)

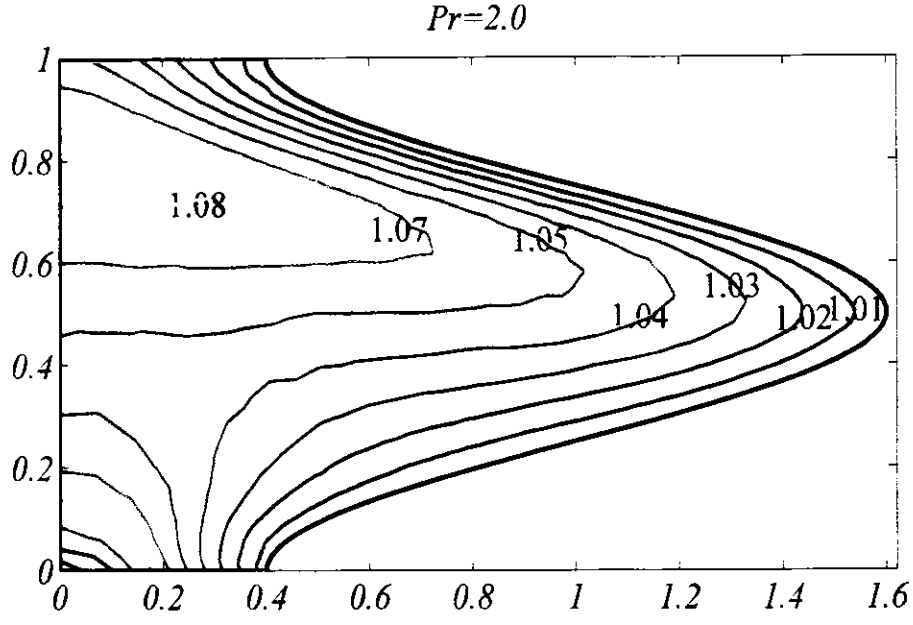

(b)

Figure 7.23: Isothermal lines for various values of Prandtl numbers Pr at fixed values of other parameters $Re = 1.0, \alpha = 0.1, \phi = 0.6, \beta = 0.3, Gr = 0.5$ and $Q = 1.4$

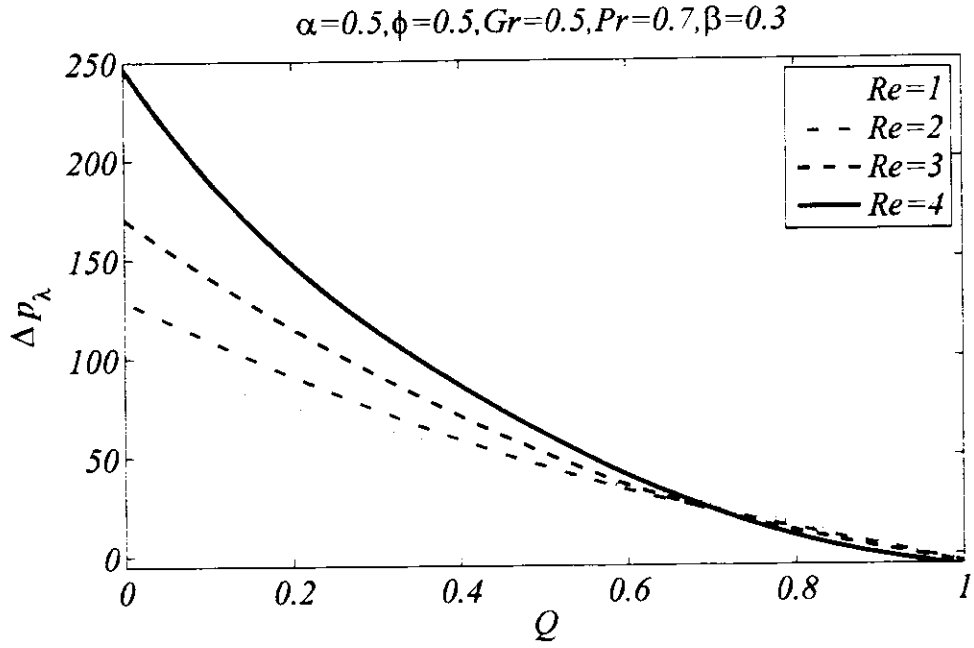

Figure 7.24: Pressure rise against time-mean flow rate Q for various values of Reynolds number Re at fixed values of other parameters

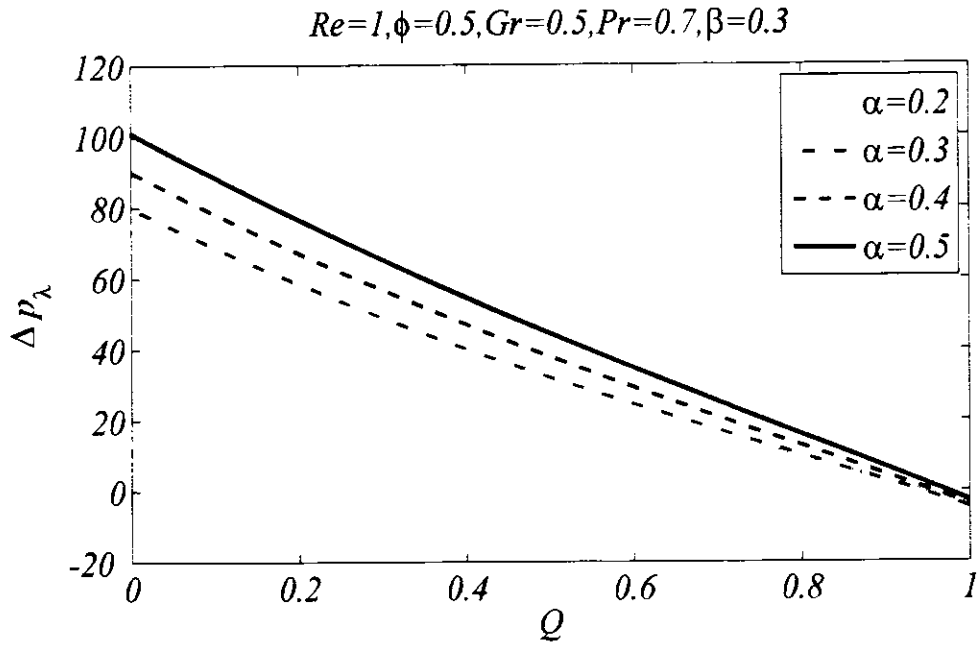

Figure 7.25: Pressure rise against time-mean flow rate Q for various values of the parameter wave number α at fixed values of other parameters

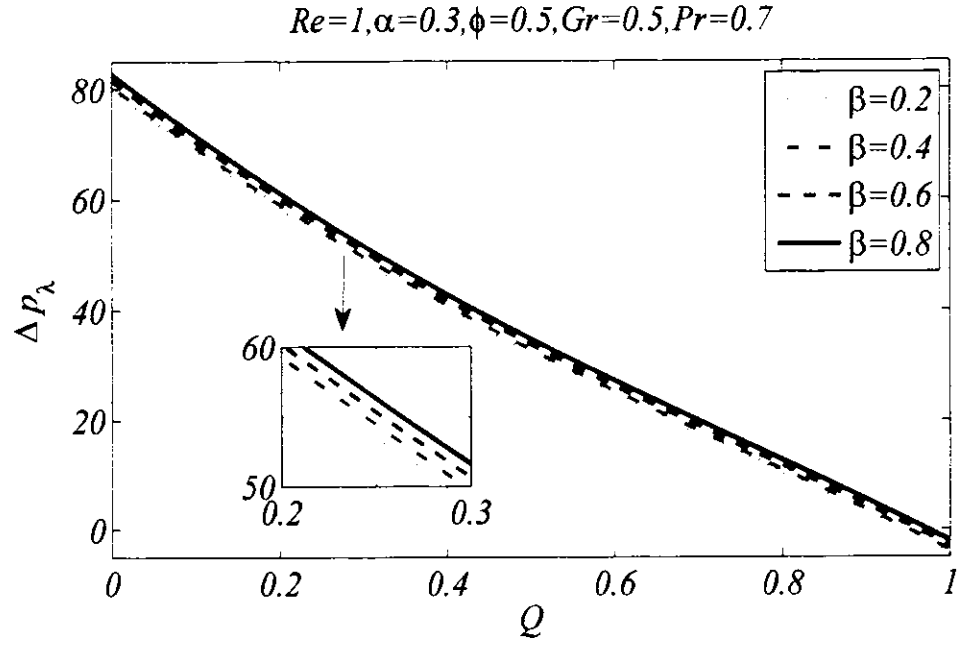

Figure 7.26: Pressure rise against time-mean flow rate Q for various values of the parameter heat generation parameter β at fixed values of other parameters

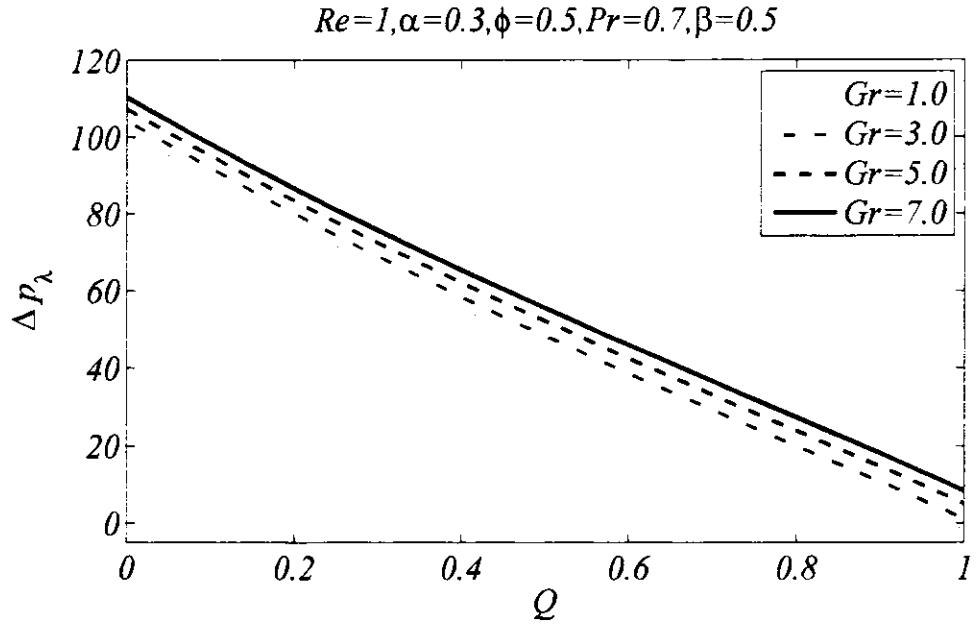

Figure 7.27: Pressure rise against time-mean flow rate Q for various values of the parameter f Grashof number Gr at fixed values of other parameters

that most rapid and remarkable increase in pressure rise is observed with the increase in Grashof number as compared to that of increase in heat generation.

7.5 Conclusions

The numerical results of streamlines and temperature distribution for mixed convective peristaltic flow passing through the vertical tube are studied and shown graphically with a suitable set of values of involved parameters by using finite element method. The key findings of this study are as follows: At the center of the tube, increasing values of Reynolds number decreases the magnitude of velocity while upsurges the temperature but increasing wave number enhances the velocity and reduces the temperature. The decrease in velocity is noted at center for increasing values of Grashof number, Prandtl number and heat generation parameter, while the slight increase is also observed for away from the center. For values of time-mean flow less than 1, velocity profile becomes negative at $z = 0$ cross section and for values greater than 1 it becomes positive. The decrease in temperature is noted for increasing values of Grashof number while Prandtl number, heat generation and time-mean flow rate supported in enhancing the temperature. Pressure rise per wavelength can be enhanced by increasing the both Reynolds number and Grashof number. Also, a decrease in pressure rise is observed by increasing values of wave number and heat generation parameter. Increase in size and number of boluses for contours of streamlines is noted for large Reynolds number and wave number while disturbance is reported for increasing Grashof number. By increasing Reynolds number, isothermal lines move along peristaltic wall and concentration in a lower part of the center of tube increases. The symmetry of isothermal lines are disturbed and saturation in the lower part is reported by increasing time-mean flow rate. Also, isotherms are generated on peristaltic wall and moves towards the center of the tube by increasing wave number, Grashof number and Prandtl number.

Chapter 8

Hydromagnetic Peristaltic Transport of Casson Fluid through a Tube

The effect of the non-zero/moderate Reynolds number on the flow by nonlinear peristaltic mechanism of a blood flow through narrow arteries, where blood flow behaves similarly to Casson fluid flow under the externally applied magnetic field with uniform strength is investigated numerically in this chapter. The governing equations for blood flow model of Casson fluid are formulated to form a system of nonlinear coupled partial differential equations, which are exposed to Galerkin's finite element method. The assumptions of lubrication theory are neglected, due to which the effects of moderate Reynolds number and wave number along with other parameters are presented. To ensure the accuracy of developed code, obtained results are compared to that of results available in the literature and found in excellent matching. The analysis shows that increasing Reynolds and Hartmann numbers enhance the velocity of the fluid. One of the findings of this study is the nonlinear behavior of pressure rise for large values of Reynolds and Hartmann numbers. Increasing wave number enhances the pressure rise in the peristaltic pumping region. In this chapter, we discussed the effect of Casson fluid parameter and time mean flow through graphs of velocity, pressure rise and contours of streamlines.

8.1 Problem Formulation

Consider the flow problem of peristaltic transport of an electrically conducting Casson fluid motion of blood flow passing through a horizontal tube of width $2a$ with speed c. Peristaltic tube is subject to the influence of applied magnetic field of uniform strength B_0 perpendicular/orthogonal to the direction of the flow. Here, due to small conductivity of fluid, the low magnetic Reynolds number R_m-approximation is assumed which allows to neglect induced magnetic field caused by applied magnetic field. Unsteady flow is considered with constant thermo-physical properties in which flow is caused by peristaltic walls along z −direction and r −direction is taken along radial direction. The symmetry of the peristaltic flow is about z-direction and schematic

diagram of the flow is presented in **Figure 6.1**. The peristaltic walls of tube moves and follows the relation given in Eq. (6.1). The governing equations that describe the flow of Casson fluid in a tube under the inducement of magnetic effects appeared through Lorentz force term are partial differential equations as follows

$$\frac{\partial W}{\partial Z}+\frac{1}{R}\frac{\partial (RU)}{\partial R}=0, \tag{8.1}$$

$$\rho\left(\frac{\partial W}{\partial t}+W\frac{\partial W}{\partial Z}+U\frac{\partial W}{\partial R}\right)=-\frac{\partial P}{\partial Z}+\mu\left(1+\frac{1}{\zeta}\right)\frac{1}{R}\frac{\partial}{\partial R}\left(R\frac{\partial W}{\partial R}\right)+\frac{\partial^2 W}{\partial Z^2}-\sigma B_0^2 W, \tag{8.2}$$

$$\rho\left(\frac{\partial U}{\partial t}+W\frac{\partial U}{\partial Z}+U\frac{\partial U}{\partial R}\right)=-\frac{\partial P}{\partial R}+\mu\left(1+\frac{1}{\zeta}\right)\frac{\partial}{\partial R}\left(\frac{1}{R}\frac{\partial (RU)}{\partial R}\right)+\frac{\partial^2 U}{\partial Z^2}. \tag{8.3}$$

The suitable boundary conditions that assist the discussed flow are

$$\left.\begin{aligned} U=0, \quad \frac{\partial W}{\partial R}=0, \quad \text{at} \quad R=0,\\ U=\frac{\partial H}{\partial t}, \quad W=0, \quad \text{at} \quad R=H. \end{aligned}\right\} \tag{8.4}$$

The defined boundary conditions in Eq. (8.4) on $\frac{\partial W}{\partial R}$ at $R=0$ corresponds to symmetry of flow and at $R=H$, $W=0$ corresponds to no-slip of the wall. While the defined boundary condition on U at $R=H$ as $U=\partial H/\partial t$ reflects that the velocity of fluid is equal to the velocity of the wall. At center of the tube, transverse velocity is zero so that we have boundary condition at $R=0$ as $U=0$. The conversion relation between the lab and wave frame of reference are given in Eqs. (6.7) and (7.7). After incorporating these transformations in Eqs. (8.1) to (8.3), we get

$$\frac{1}{r^*}\frac{\partial (r^*u^*)}{\partial r^*}+\frac{\partial w^*}{\partial z^*}=0, \tag{8.5}$$

$$\rho\left(w^*\frac{\partial w^*}{\partial z^*}+u^*\frac{\partial w^*}{\partial r^*}\right)=-\frac{\partial p^*}{\partial z^*}+\mu\left(1+\frac{1}{\zeta}\right)\frac{1}{r^*}\frac{\partial}{\partial r^*}\left(r^*\frac{\partial w^*}{\partial r^*}\right)+\frac{\partial^2 w^*}{\partial z^{*2}}-\sigma B_0^2(w^*+c), \tag{8.6}$$

$$\rho\left(w^*\frac{\partial u^*}{\partial z^*}+u^*\frac{\partial u^*}{\partial r^*}\right)=-\frac{\partial p^*}{\partial r^*}+\mu\left(1+\frac{1}{\zeta}\right)\frac{\partial}{\partial r^*}\left(\frac{1}{r^*}\frac{\partial (r^*u)}{\partial r^*}\right)+\frac{\partial^2 u^*}{\partial z^{*2}}. \tag{8.7}$$

The associated boundary conditions for the flow at center and wall of the tube are given in Eq. (6.8). Introducing the dimensionless variables defined in Eqs. (6.9) and (7.9) to above system of equations and after eliminating pressure gradient term by cross differentiation, and upon introducing the relations given in Eq. (6.10) the governing equations for the considered flow formulation are as follows

$$\frac{\alpha^2}{r}\frac{\partial^2 \psi}{\partial z^2}+\frac{\partial}{\partial r}\left(\frac{1}{r}\frac{\partial \psi}{\partial r}\right)=-\omega, \tag{8.8}$$

$$Re\left(\frac{\partial\psi}{\partial r}\frac{\partial}{\partial z}\left(\frac{\omega}{r}\right)-\frac{\partial\psi}{\partial z}\frac{\partial}{\partial r}\left(\frac{\omega}{r}\right)\right)=\left(1+\frac{1}{\zeta}\right)\frac{1}{r}\mathrm{D}^2(r\omega)+M^2\frac{\partial}{\partial r}\left(\frac{1}{r}\frac{\partial\psi}{\partial r}\right), \tag{8.9}$$

where Re is Reynolds number and M is Hartmann number. Modified form of Laplacian $(\mathrm{D}^2)$is defined as $\mathrm{D}^2=\alpha^2\frac{\partial^2}{\partial z^2}+\frac{\partial^2}{\partial r^2}-\frac{1}{r}\frac{\partial}{\partial r}$ and boundary conditions on the system modeled yield the form as

$$\left.\begin{array}{lll} \psi=0, \quad \frac{\partial}{\partial r}\left(\frac{1}{r}\frac{\partial\psi}{\partial r}\right)=0, & \frac{1}{r}\frac{\partial\psi}{\partial z}=0 & \text{at} \quad r=0 \\ \psi=q, \quad \frac{1}{r}\frac{\partial\psi}{\partial r}=-1, & \frac{1}{r}\frac{\partial\psi}{\partial z}=2\pi\phi\sin 2\pi z & \text{at} \quad r=\eta(z) \end{array}\right\}. \tag{8.10}$$

At the center of the tube $z=0$, pressure rise per wavelength is defined in wave frame is given in Eq. (6.14)

8.2 Numerical Analysis

In the present analysis, the governing equations are obtained by dropping the assumptions of lubrication theory i.e. long wavelength along with low Reynolds number assumptions. So, we obtained coupled partial differential equations which are solved numerically by using finite element method based on Galerkin's formulation. We discretize the considered domain into a mesh of triangular elements contains six nodes per element. The solution on each triangular element is found and assembled to form a global system. Finally, the solution has been obtained by using the Newton-Raphson method. In all cases, highly convergent results are obtained by our own built MATLAB code with a tolerance of 10^{-14} in $3-5$ number of iterations.

The stream function ψ and vorticity ω is approximated by the approximation given in Eq. (6.15). Galerkin's finite element approach turns Eqs. (8.8) and (8.9) as

$$\int_\Omega w_1\left(\frac{\alpha^2}{r}\frac{\partial^2\psi}{\partial z^2}+\frac{\partial}{\partial r}\left(\frac{1}{r}\frac{\partial\psi}{\partial r}\right)+\omega\right)d\Omega=0, \tag{8.11}$$

$$\int_\Omega w_2\left(Re\left(\frac{\partial\psi}{\partial r}\frac{\partial}{\partial z}\left(\frac{\omega}{r}\right)-\frac{\partial\psi}{\partial z}\frac{\partial}{\partial r}\left(\frac{\omega}{r}\right)\right)-M^2\frac{\partial}{\partial r}\left(\frac{1}{r}\frac{\partial\psi}{\partial r}\right)-\left(1+\frac{1}{\zeta}\right)\frac{1}{r}\mathrm{D}^2(r\omega)\right)d\Omega=0, \tag{8.12}$$

in which w_1 and w_2 are weight functions and $d\Omega=2\pi r dr dz$. Simplification of Eqs. (8.11) and (8.12) yields

$$\int_\Omega\left(\frac{\alpha^2}{r}\frac{\partial w_1}{\partial z}\frac{\partial\psi}{\partial z}+\frac{\partial w_1}{\partial r}\left(\frac{1}{r}\frac{\partial\psi}{\partial r}\right)-w_1\omega\right)d\Omega=\int_\Gamma w_1\frac{\partial\psi}{\partial n}d\Gamma \tag{8.13}$$

$$\int_\Omega w_2 Re\left(\frac{\partial\psi}{\partial r}\frac{\partial}{\partial z}\left(\frac{\omega}{r}\right)-\frac{\partial\psi}{\partial z}\frac{\partial}{\partial r}\left(\frac{\omega}{r}\right)\right)d\Omega+M^2\int_\Omega\left(\frac{\partial w_2}{\partial r}\frac{1}{r}\frac{\partial\psi}{\partial r}\right)d\Omega+$$

$$\left(1+\frac{1}{\zeta}\right)\int_\Omega\left(\frac{\partial w_2}{\partial r}\frac{1}{r}\frac{\partial(r\omega)}{\partial r}+\frac{\alpha^2}{r}\frac{\partial w_2}{\partial z}\frac{\partial(r\omega)}{\partial z}\right)d\Omega=M^2\int_\Gamma w_2\frac{\partial\psi}{\partial n}d\Gamma+$$

$$\left(1+\frac{1}{\zeta}\right)\int_\Gamma w_2\frac{\partial(r\omega)}{\partial n}d\Gamma \tag{8.14}$$

where $d\Gamma$ is defined as $d\Gamma=\pi r dr dz$. Introducing approximations defined in Eq. (6.15) into Eqs. (8.13) and (8.14), we get

$$-\sum_i B_{ki}^e\omega_i+\sum_i A_{ki}^e\psi_i=S_n^{k^e}, \tag{8.15}$$

$$Re\sum_i C_{kij}^e\psi_i\omega_i+\left(1+\frac{1}{\zeta}\right)\sum_i A_{ki}^e\omega_i+M^2\sum_i D_{ki}^e\psi_i=M^2S_n^{k^e}. \tag{8.16}$$

where

$$\left.\begin{aligned}
A_{ki}^e&=\int_{\Omega^e}\left(\frac{\alpha^2}{r}\frac{\partial N_k}{\partial z}\frac{\partial N_i}{\partial z}+\frac{\partial N_k}{\partial r}\left(\frac{1}{r}\frac{\partial N_i}{\partial r}\right)\right)d\Omega\\
B_{ki}^e&=\int_{\Omega^e}N_kN_i d\Omega\\
C_{kij}^e&=\int_\Omega N_k\left(\frac{\partial N_i}{\partial r}\frac{\partial}{\partial z}\left(\frac{N_j}{r}\right)-\frac{\partial N_j}{\partial z}\frac{\partial}{\partial r}\left(\frac{N_i}{r}\right)\right)d\Omega\\
D_{ki}^e&=\int_\Omega\left(\frac{\partial N_k}{\partial r}\frac{1}{r}\frac{\partial N_k}{\partial r}\right)d\Omega\\
S_n^{k^e}&=\int_\Gamma N_k\bar{S}_k d\Gamma
\end{aligned}\right\} \tag{8.17}$$

After assembly procedure, obtained resulting system (global) in the matrix arrangement is expressed as follows

$$\boldsymbol{KA}=\boldsymbol{F}, \tag{8.18}$$

where

$$K_{ij}=\begin{bmatrix}-B_{ki}^e & A_{ki}^e\\ \left(1+\frac{1}{\zeta}\right)A_{ki}^e & ReC_{kij}^e\omega_i+M^2D_{ki}^e\end{bmatrix},A_k=\begin{bmatrix}\omega_k\\ \psi_k\end{bmatrix},F_k=\begin{bmatrix}S_n^{k^e}\\ M^2S_n^{k^e}\end{bmatrix}. \tag{8.19}$$

8.3 Validation

This section is dedicated for authentication of our own build MATLAB code of finite element method which gives the numerical solution of the modeled system of nonlinear partial differential equations. Shapiro et al. (1969) presented results of peristaltic transport by applying lubrication theory. These results are purely analytical and hence considered to be a benchmark solution in this comparison. The obtained results of pressure distribution are compared with the pioneer results given by Shapiro et al. (1969) by plotting both results in **Figure 8.1**. The graphs presented in **Figure 8.1**

exhibits good agreement for $M = 0, 1/\zeta = 0$ under assumption of long wavelength along with low Reynolds number with corresponding results of Shapiro et al. (1969).

8.4 Results and Discussion

The implemented numerical scheme discussed in the previous section is implemented using MATLAB to obtain the graphs of velocity, pressure, contours of streamlines and vorticity. Influence of involved parameters like Reynolds number Re, amplitude ratio ϕ, wave number α, Hartmann number M, volume flow rate Q and Casson fluid parameter ζ on the quantities of the interest are presented graphically and discussed in detail in the following subsections.

8.4.1 Velocity profile

In this subsection, the behavior of longitudinal velocity at cross-section $z = 0$ is analyzed and discussed after plotting the graphs against Reynolds number Re, wave number α, Casson fluid parameter ζ, Hartmann number M and time mean flow rate Q. In **Figure 8.2**, the effects of numerous values of Hartmann number on the behavior of velocity for various values of Reynolds number is presented by plotting velocity profile against Reynolds number Re. We observe that increasing the Hartmann number enhances the velocity independent of the choice of the Reynolds number. It is also observed that maximum value is achieved at $Re = 99$ and solution remains smooth for large values of Reynolds number. The velocity field presented in **Figures 8.3** to **8.7** exhibits that behavior of velocity in the central region of the tube and around the vicinity of peristaltic wall is not similar for cases of different Reynolds number Re Hartmann number M, wave number α and Casson fluid parameter ζ. The longitudinal velocity field increases near the wall of tube by increasing either Hartmann number or Casson fluid parameter ζ and decreases in the central part of the tube. The wave number α shows same behavior as that of Casson fluid parameter ζ. **Figures 8.3** to **8.7** shows the behavior of velocity field by variations Reynolds number Re, wave number α, Casson fluid ζ, Hartmann number and rate of time mean flow Q. The prominent effects are noticed in the central region of the tube which shows the increase in velocity field by increasing the Reynolds number and time mean flow rate and opposite behavior is observed near wall of the tube. These effects are attributed to strong inertial force induced by high Reynolds number and reported first time as lubrication theory is not virtuous enough to report such effects. The opposite behavior is noted for wave number

parameter α and Casson fluid parameter ζ as shown in **Figure 8.4** and **8.5**. The increase in Hartmann number M reflects the dominance of electromagnetic forces over the viscous forces which cause decrease in the velocity field in central region of the tube and increases the velocity in region near the wall of the channel for non-Newtonian Casson fluid as shown in **Figure 8.6**. It is perceived from the graph that the behavior of the longitudinal velocity is same at the whole cross-section of the tube for time mean flow rate Q as shown in **Figure 8.7**. The increase in time-mean flow rate increases the longitudinal velocity of the fluid.

8.4.2 Trapping phenomenon and vorticity

Another important phenomenon of peristaltic motion is known as trapping which is mainly due to establishment of bolus by internal circulation of streamlines. The trapping phenomena for variation of different parameters involved is presented through **Figures 8.8** to **8.11**. **Figure 8.8** displays the contours of streamlines for various values of Reynolds number at $\alpha = 0.3, \phi = 0.5, M = 2.0, \zeta = 0.5, Q = 1.2$. It shows that increase in Reynolds number magnifies the size of bolus as well as increases the number of boluses. In other words, the cluster of bolus can be shifted on right side of the tube by enhancing the inertial forces, therefore by increase in Reynolds number. **Figure 8.9** shows the change of behavior of streamlines for different values of Casson fluid parameter ζ with $Re = 5, \alpha = 0.1, \phi = 0.5, M = 2.0, Q = 1.2$. The increase in number and size of bolus is noted as a result of increasing Casson fluid parameter. The influence of Hartmann number M on the streamlines are presented by plotting contours in **Figure 8.10** with fixed values of the parameters as $Re = 5.0, \alpha = 0.3, \phi = 0.5, \zeta = 0.5, Q = 1.2$. The opposite behavior is noticed as that of Casson fluid parameter. The contours of streamlines for various values of time mean flow rate Q are presented in **Figure 8.11** with fixed values of other involved parameters i.e. $Re = 5.0, \alpha = 0.3, \phi = 0.5, M = 2.0, \zeta = 0.5$. **Figure 8.11** exhibits that the flow is generated and moves along the peristaltic wall for $Q < 1$ and streamlines of almost same trajectory of peristaltic wall are appeared, while for $Q = 1$ formation of bolus are found in crest region of the tube shows circulatory motion of the fluid and some streamlines still moves along the wall and obey the same path in the vicinity of the peristaltic wall. The flow becomes smooth in the central region of the tube for $Q > 1$ and increase in number of bolus is noted. The contours of vorticity for Re are presented in **Figure 8.12** which exhibits that flow generates on the center of the tube and finished on the peristaltic wall.

8.4.3 Pressure distribution

This section is dedicated to detailed discussion on the pressure of the peristaltic transport of Casson fluid. The Casson fluid blood flow model is highly dependent on pressure for wavelength, amplitude ratio and at low shear rates blood behaves as Casson fluid. Transport of Casson fluid in the flow is presented through Figures 8.14 to 8.16. Figure 8.13 establishes the effect of Reynolds number Re on pressure rise per wavelength. It is observed that for the fixed values of Reynolds number, the rise in pressure shows more linear behavior due to strong inertial forces. It is also noted that increase in inertial forces over viscous forces causes augmentation in pressure rise and this fact is not reported in earlier investigations study. Furthermore, increasing wave number α shows analogous behavior to that of Reynolds number as shown in Figure 8.14. From Figure 8.15, it is noticed that pressure rise for pumping region is reduced due to increase in Casson fluid parameter β, as due to rise in viscosity, flow becomes slow and the pressure rise reduces. On the other hand, the increase in pressure is promoted in the increasing values of amplitude ratio M in Figure 8.16. It is noted that three ranges of the pumping in the peristalsis are possible, $\Delta P > 0$.

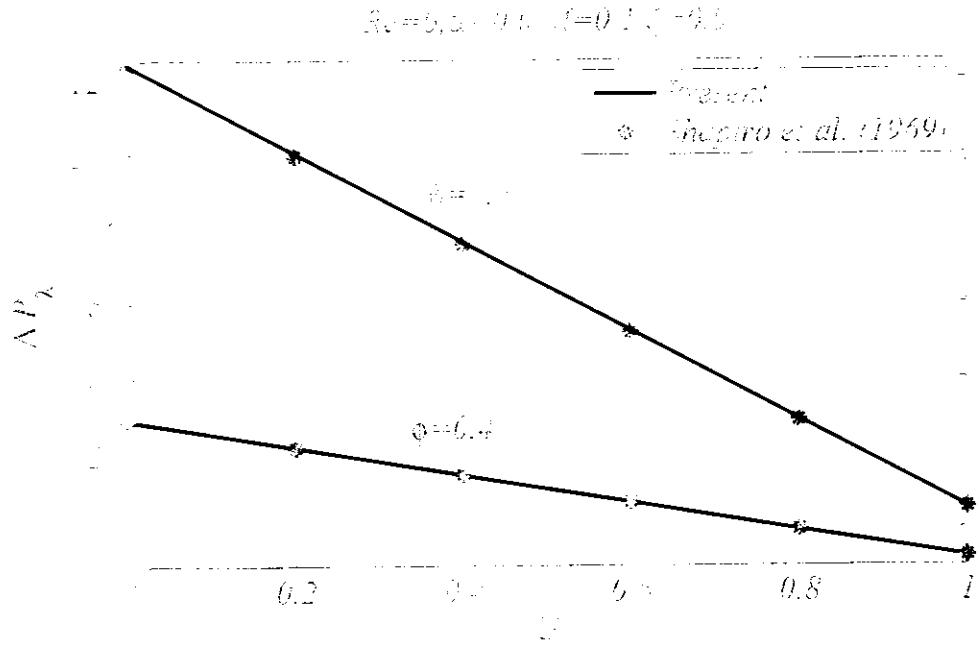

Figure 8.14: Comparison of computed pressure distributions with the results provided by Shapiro et al. (1969)

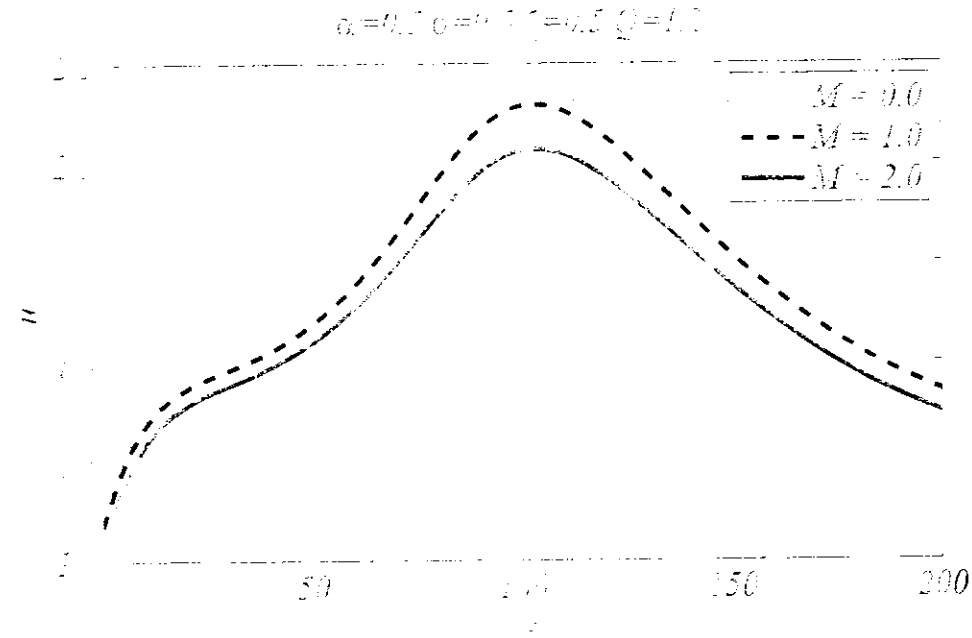

Figure [illegible] variation of velocity distribution against Re for different M at fixed values of other parameters

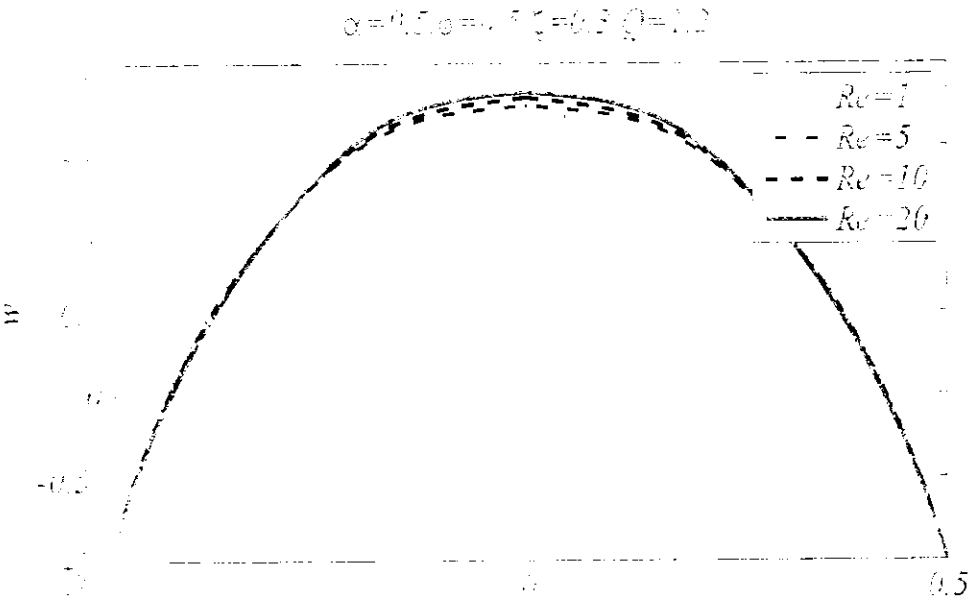

Figure [illegible] variation of longitudinal velocity distribution for various values of the parameter Reynolds number Re at fixed values of the other parameters

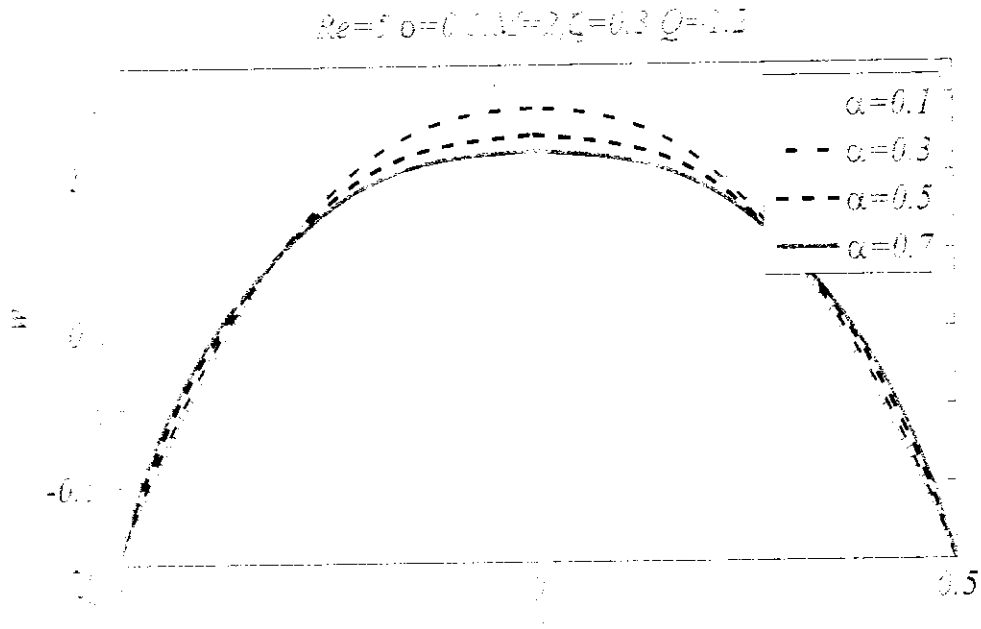

Figure 8. Graphs of longitudinal velocity distribution for various values of the parameter ... ve number α at fixed values of the other parameters

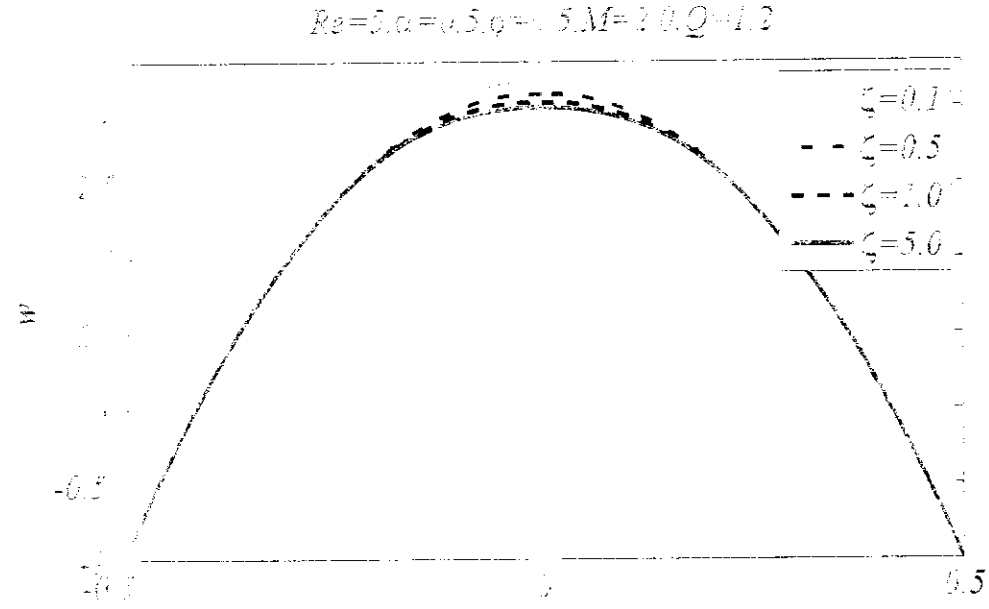

Figure 9. Graphs of longitudinal velocity distribution for various values of the parame... of Casson fluid ζ at fixed values of the other parameters

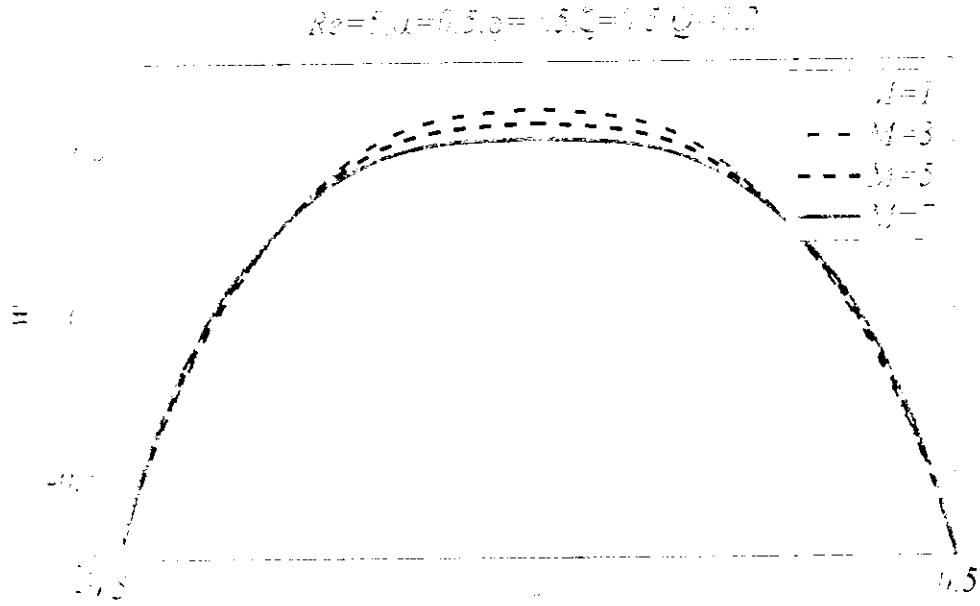

Figure 3. Profiles of the obtained magnitudes of velocity distribution for various values of the parameter of Hartmann number M at fixed values of the other parameters.

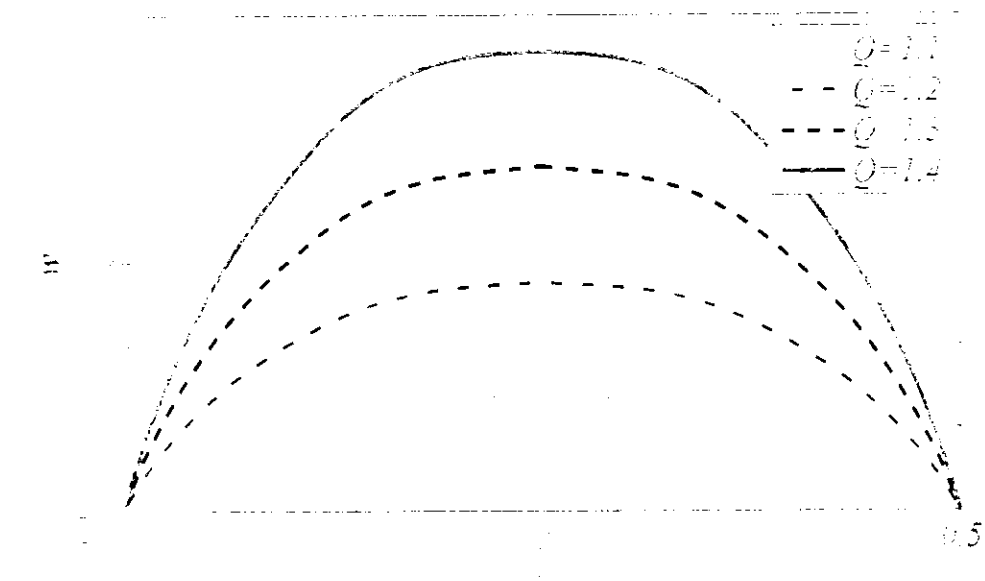

Figure 4. Profiles of longitudinal velocity distribution for various values of the parameter of the mean flow rate Q at fixed values of the other parameters.

(a)

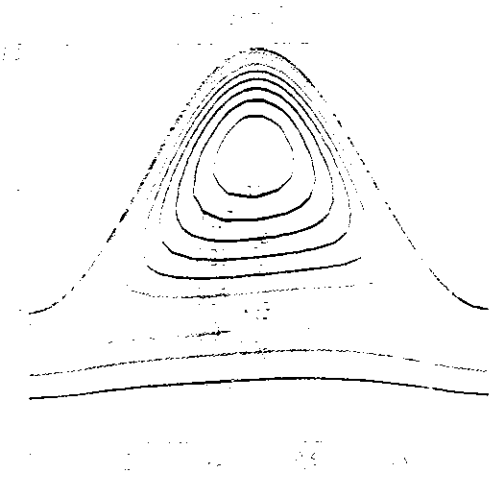

(b)

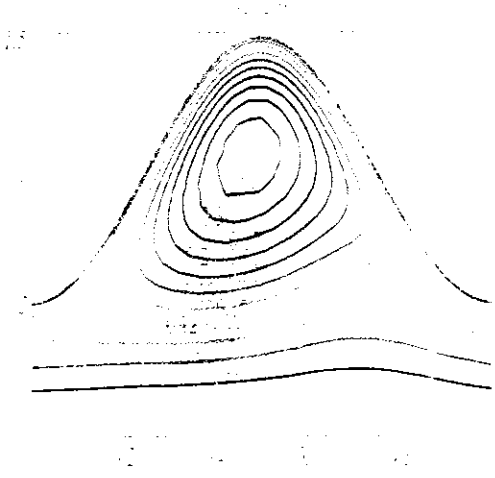

(c)

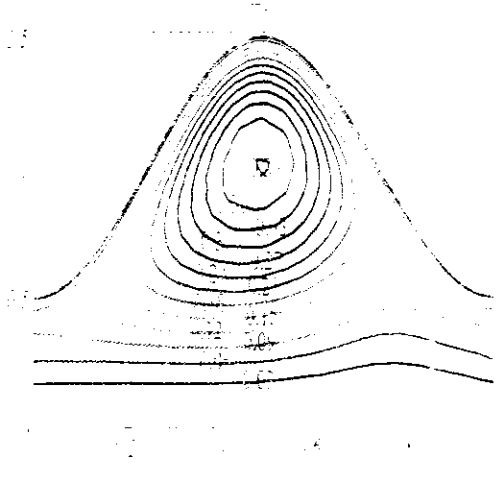

Figure 6. Streamlines for wave at time for $Pr = 1, 5$ and 10 at fixed $\alpha = 0.1, \phi = 0.1, M = 2.0, \zeta = 0.5$ and $Q = 1.2$

(a)

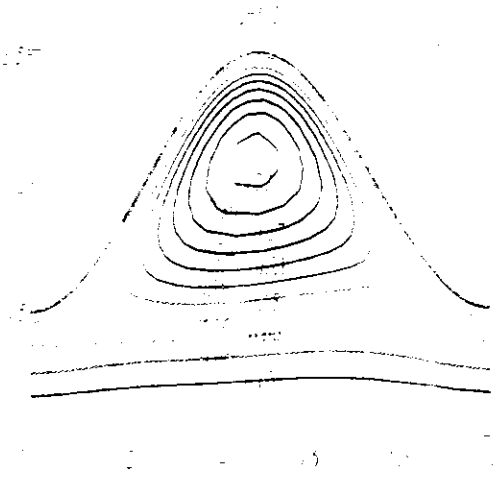

(b)

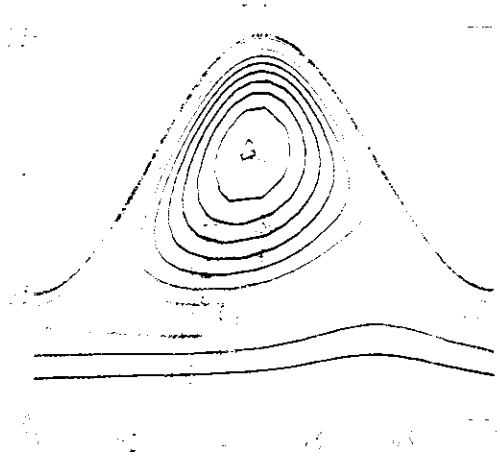

(c)

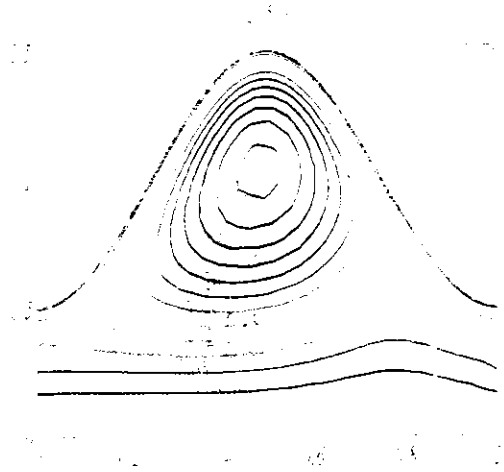

Figure 8 Contours of streamfunction [illegible] = 0.1 1.0 and 5.0 at fixed $Re = 5$, $\alpha = 0.1, \phi = 0.5, M = 2.0$ and $\varrho = 1.2$

(a)

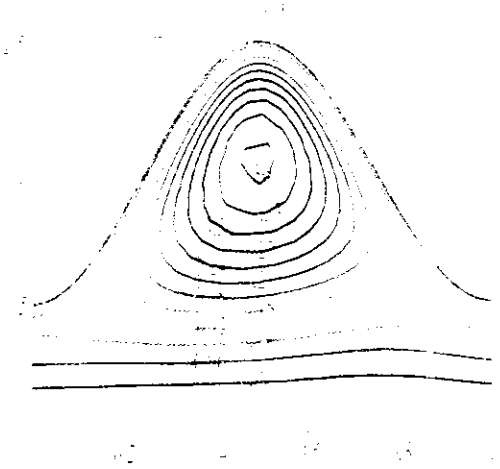

(b)

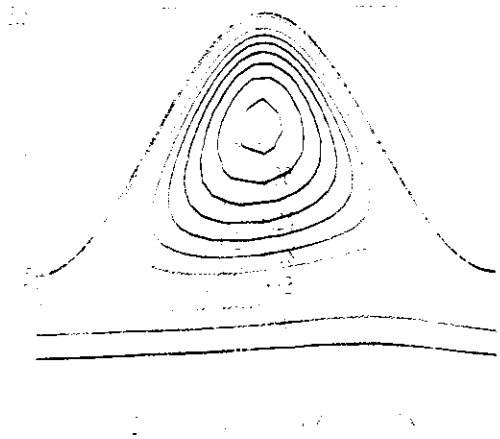

(c)

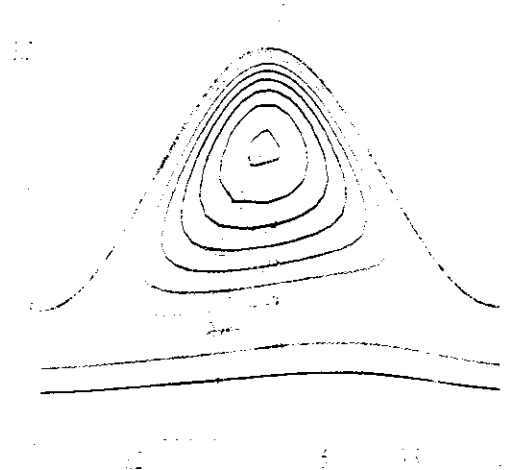

Figure 8. [illegible] streamlines [illegible] for $M = 1, 3$ and 5 at fixed $Re = 5.0$, $\alpha = 0.3$, $\phi = 0.5$, $\zeta = 0.5$ and $Q = 1.2$

(a)

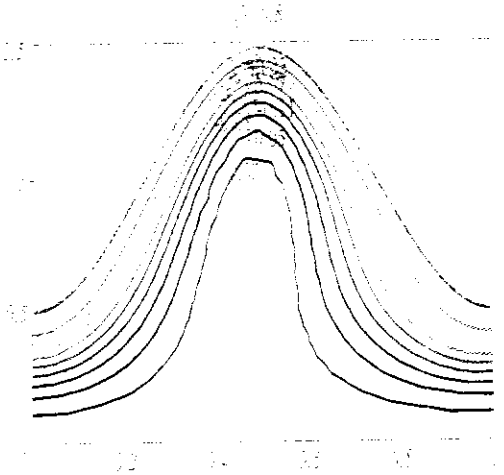

(b)

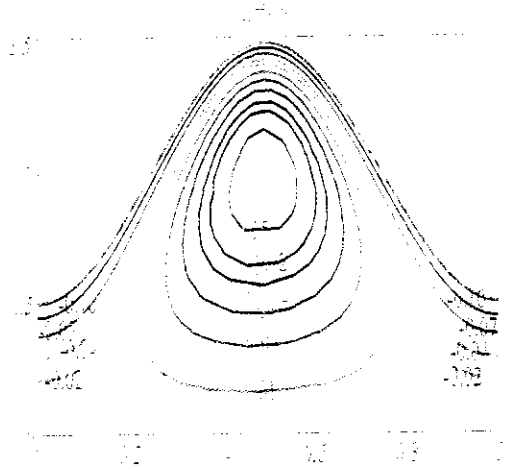

(c)

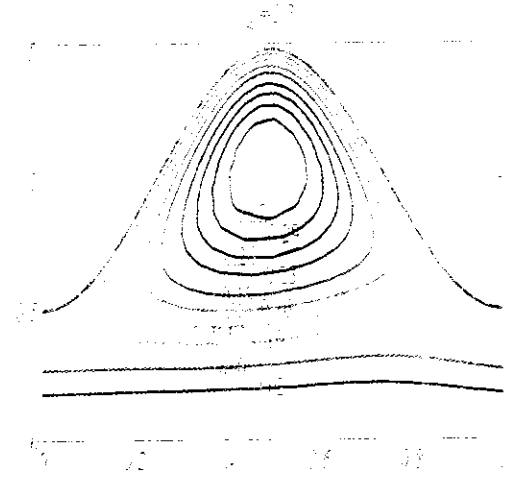

Figure 8. : Contours of streamlines in wave frame for $Q = 0.8, 1.0$ and 1.2 at fixed $Re = 5.0$, $\alpha = 0.3$, $\phi = 0.5$, $M = 2.0$ and $\zeta = 0.5$

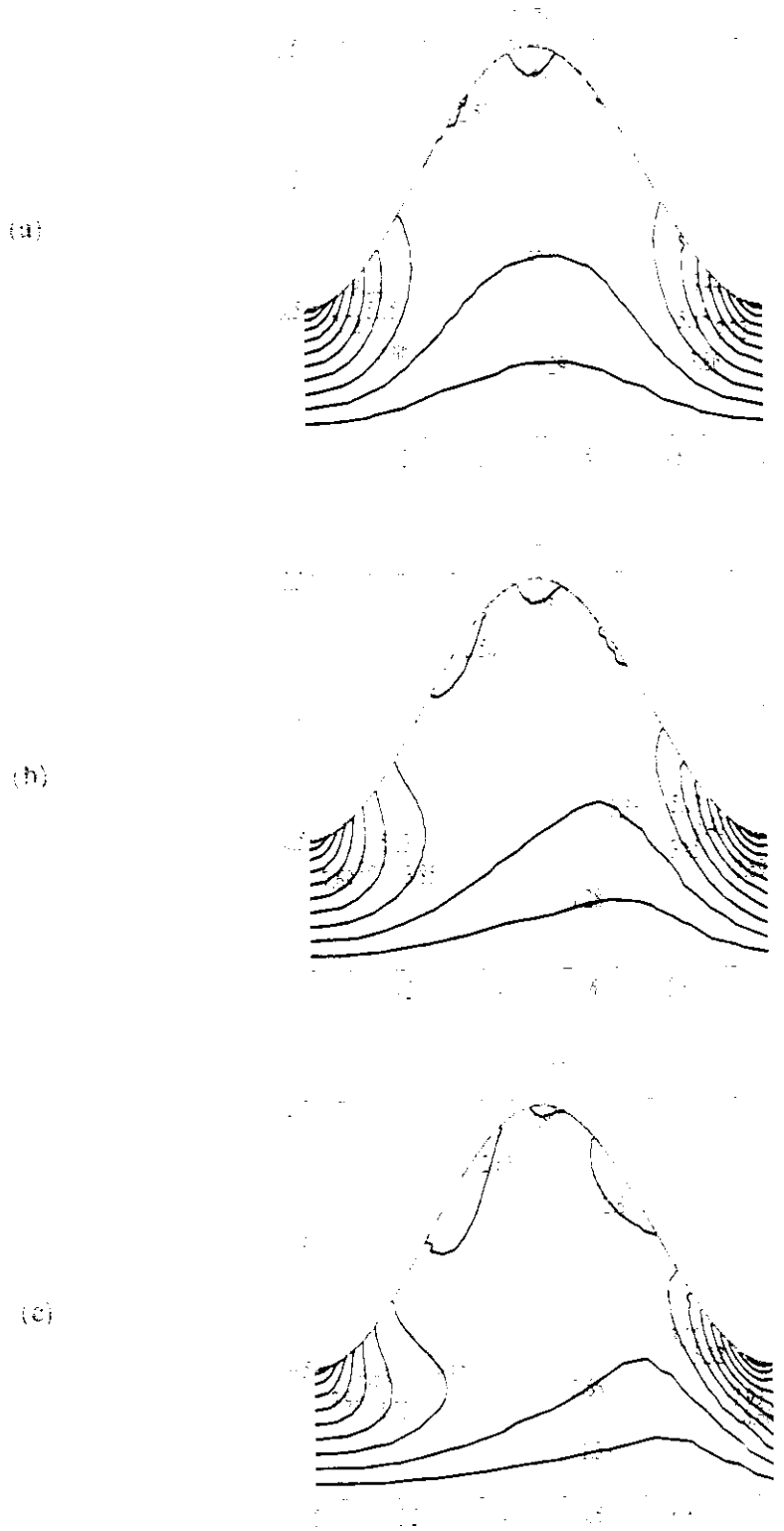

Figure 8.3.1 Contours of vertical velocity for wave trains for $Re = 1.5$ and 10 at fixed $\alpha = 0.3$, $\phi = 0.1$, $M = 2.0$, $\zeta = 0.5$ and $Q = 1.2$

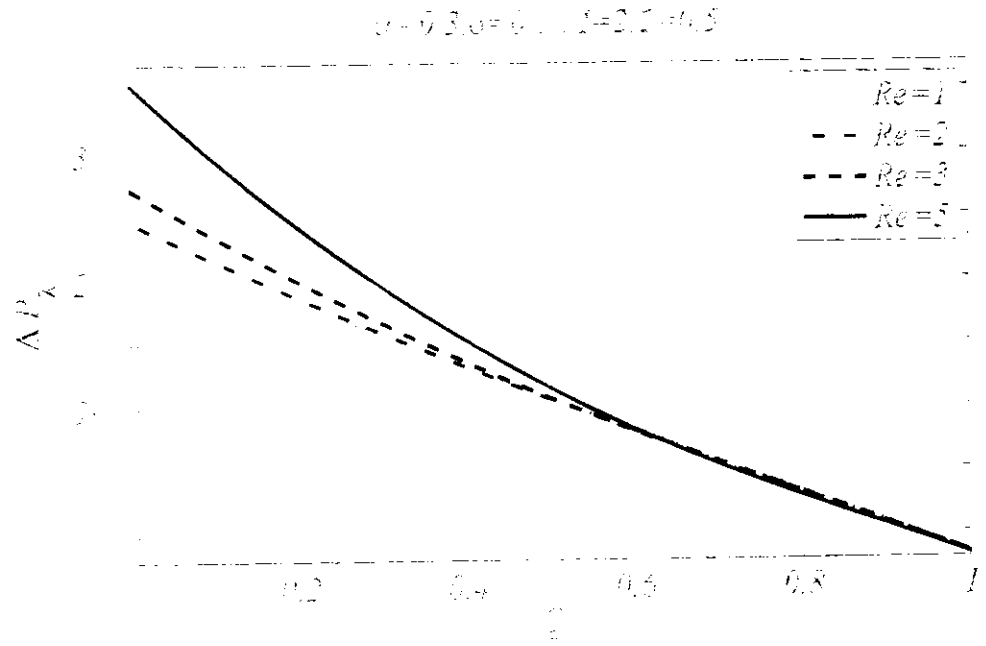

Figure 4. Pressure rise per wavelength for different values for *Re* at fixed values of other parameters.

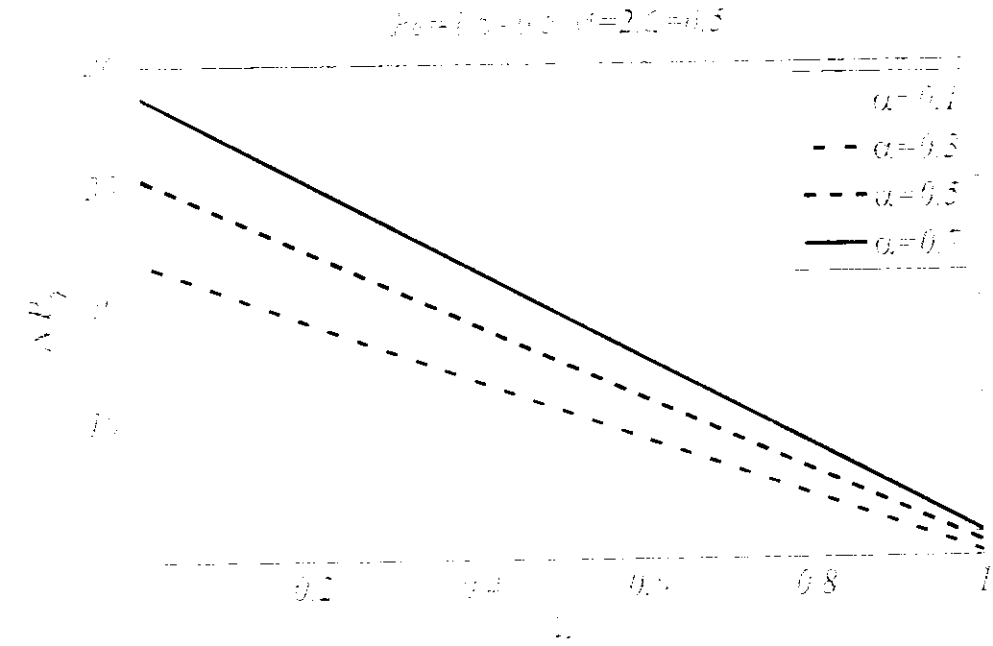

Figure 5. Pressure rise per wavelength for different values for α at fixed values of other parameters.

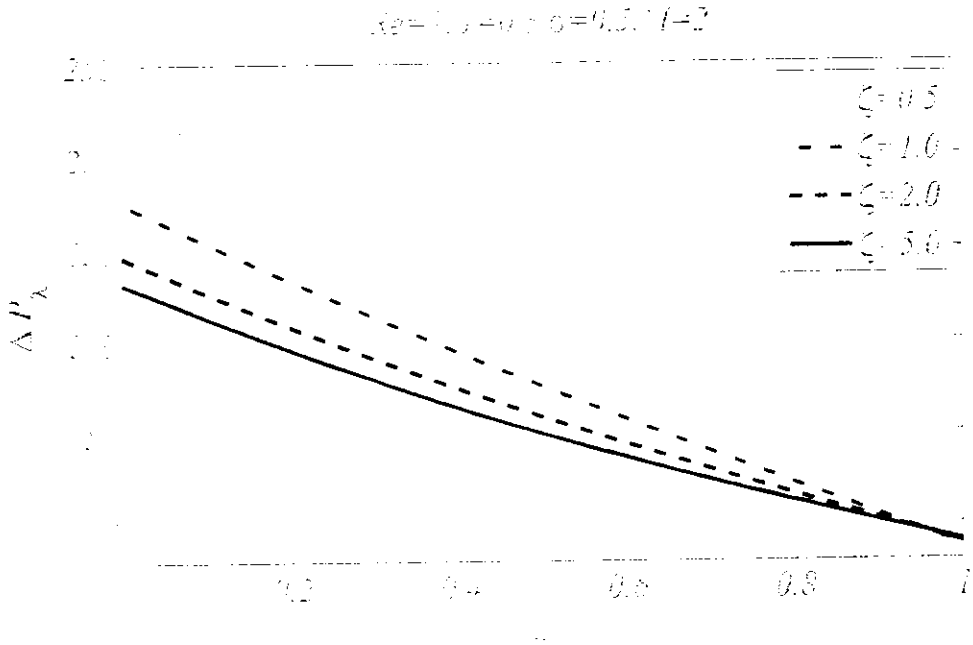

Figure 8. Pressure rise per unit length for different values of ζ at fixed values of other parameters

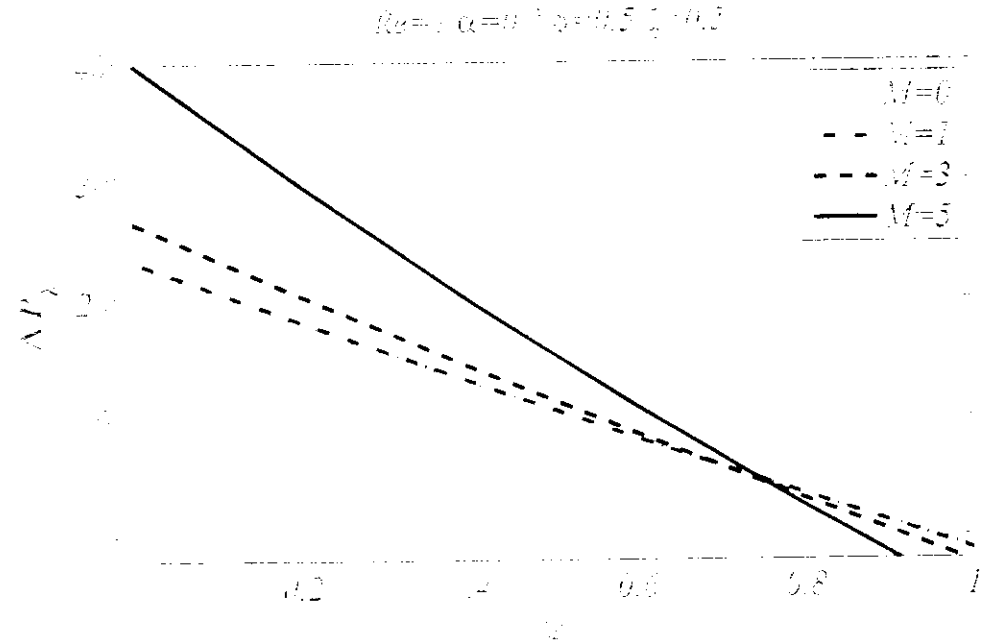

Figure 9. Pressure rise per unit length for different values of M at fixed values of other parameters

corresponds to augmented pumping region while $\Delta P = 0$ is the free pumping region and $\Delta P < 0$ is the co-pumping region. We have presented only first one which is of most interest for engineering and is vastly applicable in bio-medical sciences. The pressure rise per wavelength in peristaltic highly dependent on the applied magnetic field. So, one way to control the pressure rise of peristaltic motion of Casson fluid of blood flow by varying the strength of the applied magnetic field, this fact is widely used in MRI and other bio medical treatments. **Figure 8.16** exhibits that in the region of augmented pumping $0.7 < Q < 1$, pressure rise shows opposite behavior as compared to that of pumping region corresponding to interval $0 < Q < 0.7$. Free pumping corresponds to the relation $\Delta P = 0$ at $Q = 0.7$.

8.5 Conclusions

The effects of Reynolds number on peristaltic transportation of non-Newtonian behavior of blood has been investigated by considering blood as a Casson fluid. The governing equations modeled by dropping the long wavelength along with low Reynolds number assumptions which allow us to predict the features of peristaltic motion for moderate values of Reynolds number and wave number. The flow is subjected to the external uniform magnetic field to observe the effect of Hartmann number in different situations. Finite element method is used to solve modeled set of coupled partial differential equations. The investigation reveals that the velocity gains opposite behavior at the central region of the tube and near the wall. It is concluded that increasing values of Reynolds number enhances velocity at the center of the tube, while opposite behavior is observed for increasing wave number. Similarly opposite behavior is observed in case of Casson fluid parameter and Hartmann number. Unlike other parameters, time mean flow rate effects the velocity with the same attitude throughout the entire region.

Pressure rise per wavelength is decreased by increasing Casson flow parameter. Opposite effects are noticed for Reynolds and wave numbers while for high values of Reynolds number, pressure rise per wavelength exhibits nonlinear behavior. The increasing values of Hartman number ensure strengthening of electromagnetic forces as compared to viscous forces that cause the reduction in volume as well as number of trapping boluses. The rise in Casson flow parameter enhances the thickness of fluid and causes reduction in size and number of the bolus. The dominant inertial forces caused by an upsurge in Reynolds number increases the magnitude and number of trapped

boluses and vorticity exhibit the generation of the flow field in the narrow part of the tube in this case. It is hoped that present study will serve as a benchmark for further research on peristaltic flows of non-Newtonian fluids without applying assumption of lubrication theory.

Chapter 9

Hydromagnetic Peristaltic Flow of Micropolar Fluid through a Tube

In this chapter, modeling and simulation of peristaltic flow model of micropolar fluid passing through a uniformly saturated porous medium situated in a tube placed in the magnetic field are presented. In modeling of governing equation, the long wavelength along with low Reynolds number assumptions are not incorporated that allows to present the results that are valid for moderate Reynolds number and non-zero wave number and are modeled in terms of nonlinear partial differential equations. Finite element method based on Galerkin's weighted residual technique is implemented to the model to obtained numerical results of nonlinear partial differential equations. The obtained numerical results are presented by plotting the graphs of longitudinal velocity, pressure rise per wavelength, contours of streamlines, vorticity and microrotation and are discussed in detail. Comparison between obtained results and existing results in the literature is made which are found in good agreement. It is found that peristaltic mixing is supported by Reynolds number and permeability parameter of porous medium while Hartmann number reduces the number and size of the boluses. The pressure rise per wavelength for the considered model of micropolar fluid is better as compared to that of the case of Newtonian fluid.

9.1 Problem Formulation

Consider an unsteady electrically conducting two-dimensional peristaltic flow of micropolar fluid passing through a porous saturated tube of width $2a$ with speed c. The flow is caused by movement of peristaltic walls of the tube in the $z-$direction and uniform magnetic field of strength B_0 is applied perpendicular to the direction of the fluid. Due to small conductivity of considered fluid and to ensure that applied magnetic field is unaltered by the velocity of the fluid, we are restricted to low magnetic Reynolds number R_m . So induced magnetic field is ignored by assuming low R_m-approximation. The flow is symmetric about $r = 0$ and flow geometry is shown in **Figure 6.1**. The flow is caused by sinusoidal propagation of the walls of the tube that obeys the relation

given in Eq. (6.1). The equations that governs the peristaltic flow of micropolar fluid in porous saturated tube under the influence of magnetic field are given as

$$\nabla.\boldsymbol{V}^* = 0, \tag{9.1}$$

$$\rho(\boldsymbol{V}^*.\nabla\boldsymbol{V}^*) = -\nabla P + (\mu + \bar{\kappa})\,\nabla^2\boldsymbol{V}^* + \bar{\kappa}\nabla\times\boldsymbol{G}^* + \boldsymbol{J}\times\boldsymbol{B} - \frac{\mu}{k}\boldsymbol{V}^*, \tag{9.2}$$

$$\rho J^*(\boldsymbol{V}^*.\nabla\boldsymbol{G}^*) = -2\bar{\kappa}\boldsymbol{G}^* - \bar{\gamma}(\nabla\times\nabla\times\boldsymbol{G}^*) + \bar{\kappa}\nabla\times\boldsymbol{V}^* + (\bar{\alpha} + \bar{\beta} + \bar{\gamma})\,\nabla(\nabla.\boldsymbol{G}^*), \tag{9.3}$$

where $\boldsymbol{V}^*$is the velocity vector defined by $\boldsymbol{V}^* = (w^*, 0, u^*)$, $\boldsymbol{G}^*$ is the microrotation vector defined by $\boldsymbol{G}^* = (0, g^*, 0)$, $\boldsymbol{J}$ is the current density, $\boldsymbol{B}$ is the applied magnetic field defined by $\boldsymbol{B} = (0, B_0, 0)$, ρ is the fluid density, p^* symbolized the pressure of the fluid, J^* symbolized the microgyration parameter, μ represents classical viscosity coefficient, k represents the permeability of porous medium, $\bar{\alpha}, \bar{\beta}$ and $\bar{\gamma}$ are the coefficients of spin gradient viscosity and $\bar{\kappa}$ characterizes the coefficient of vortex viscosity. The material constraints $\mu, \bar{\kappa}, \bar{\alpha}, \bar{\beta}$ and $\bar{\gamma}$ must satisfiyes the following relations Eringen (1966) given in Eq. (1.16). To solve the considered problem in wave frame, the flow equation can be transformed from lab frame to moving frame by using following transformations given in Eqs. (6.7) and (7.7).

Eqs. (9.1) to (9.3) that govern the two-dimensional micropolar fluid flow through a uniformly saturated porous medium subject to transverse magnetic field in the wave frame yields following 1equations

$$\frac{1}{r^*}\frac{\partial}{\partial r^*}(r^*u^*) + \frac{\partial w^*}{\partial z^*} = 0, \tag{9.4}$$

$$\rho\left(w^*\frac{\partial w^*}{\partial z^*} + u^*\frac{\partial w^*}{\partial r^*}\right) = -\frac{\partial p^*}{\partial z^*} + (\mu + \kappa)\left(\frac{1}{r^*}\frac{\partial}{\partial r^*}\left(r\frac{\partial w^*}{\partial r^*}\right) + \frac{\partial^2 w^*}{\partial r^{*2}}\right) + \kappa\frac{\partial g^*}{\partial z^*} - \left(\sigma B_0^2 + \frac{\mu}{k}\right)(w^* + c), \tag{9.5}$$

$$\rho\left(w^*\frac{\partial u^*}{\partial z^*} + u^*\frac{\partial u^*}{\partial r^*}\right) = -\frac{\partial p^*}{\partial r^*} + (\mu + \kappa)\left(\frac{\partial}{\partial r}\left(\frac{1}{r^*}\frac{\partial}{\partial r^*}(r^*u^*)\right) + \frac{\partial^2 u^*}{\partial z^{*2}}\right) - \kappa\frac{\partial g^*}{\partial r^*} - \frac{\mu}{k}(u^*), \tag{9.6}$$

$$\sigma J^*\left(w^*\frac{\partial g^*}{\partial z^*} + u^*\frac{\partial g^*}{\partial r^*}\right) = -2\kappa g^* - \gamma\left(\frac{\partial^2 g^*}{\partial r^{*2}} + \frac{\partial^2 g^*}{\partial z^{*2}} + \frac{1}{r^*}\frac{\partial g^*}{\partial r^*} - \frac{g}{r^{*2}}\right) + \kappa\left(\frac{\partial u^*}{\partial z^*} - \frac{\partial w^*}{\partial r^*}\right), \tag{9.7}$$

The suitable boundary conditions for the considered flow problem are given as

$$\left.\begin{array}{llll} \dfrac{\partial w^*}{\partial r^*} = 0, & u^* = 0 & g^* = 0 & \text{at } r^* = 0 \\ w^* = -c, & u^* = -\dfrac{2\pi bc}{\lambda}\sin\left(\dfrac{2\pi z^*}{\lambda}\right) & g^* = 0 & \text{at } r^* = \eta(z^*) \end{array}\right\}. \tag{9.8}$$

Introducing the dimensionless variables defined in Eqs. (6.9) and (9.9) to the system of equations

$$g = \frac{g^*}{c}, J = \frac{J^*}{a^2}, \tag{9.9}$$

and after eliminating the pressure gradient term by cross differentiation and then using the relation given in Eq. (6.10), the governing equations stream-vorticity form in becomes

$$\frac{\alpha^2}{r}\frac{\partial^2\psi}{\partial z^2} + \frac{\partial}{\partial r}\left(\frac{1}{r}\frac{\partial\psi}{\partial r}\right) = -\omega, \tag{9.10}$$

$$Re\left(\frac{\partial\psi}{\partial r}\frac{\partial}{\partial z}\left(\frac{\omega}{r}\right) - \frac{\partial\psi}{\partial z}\frac{\partial}{\partial r}\left(\frac{\omega}{r}\right)\right) = \frac{1}{1-N}\left(\frac{1}{r}\mathrm{D}^2(r\omega) - \frac{N}{r}\mathrm{D}^2(rg)\right) + M^2\frac{\partial}{\partial r}\left(\frac{1}{r}\frac{\partial\psi}{\partial r}\right) - \frac{1}{K}\omega, \tag{9.11}$$

$$Re\, J\frac{1-N}{N}\frac{1}{r}\left(\frac{\partial\psi}{\partial z}\frac{\partial g}{\partial r} - \frac{\partial\psi}{\partial r}\frac{\partial g}{\partial z}\right) = \omega - 2g + \frac{2-N}{m^2}\frac{1}{r}\mathrm{D}^2 g. \tag{9.12}$$

The boundary conditions become

$$\left.\begin{array}{llll} \frac{\partial}{\partial r}\left(\frac{1}{r}\frac{\partial\psi}{\partial r}\right) = 0, & \frac{1}{r}\frac{\partial\psi}{\partial z} = 0, & w = 0 \quad \text{on} \quad r = 0 & \\ \frac{1}{r}\frac{\partial\psi}{\partial r} = -1, & \frac{1}{r}\frac{\partial\psi}{\partial z} = 2\pi\phi\sin 2\pi z, & w = 0 \quad \text{on} \quad r = \eta(z) & \end{array}\right\}, \tag{9.13}$$

where $\mathrm{D}^2 = \alpha^2\frac{\partial^2}{\partial z^2} + \frac{\partial^2}{\partial r^2} - \frac{1}{r}\frac{\partial}{\partial r}$ is modified Laplacian operator, coupling number is defined as $N = \kappa/(\mu+\kappa)$ that ranges between 0 to 1 i.e. $(0 < N < 1)$, and $m^2 = \alpha^2\kappa(2\mu+\kappa)/(\gamma(\mu+\kappa))$ is the micropolar parameter. The flow rate in wave frame of reference is related to time-mean flow rate in lab frame of reference by the expression $q^* = Q^* - cH^2(1+\phi^2/2)$. At the central line of the tube $z = 0$, rise in pressure per wavelength in wave frame is given in Eq. (6.14)

9.2 Numerical Analysis

In this particular section, the solution of Eqs. (9.10) to (9.12) subject to boundary conditions given in Eq. (9.13) is formulated. In the above presented modeling by dropping the assumptions of lubrication theory, we have arrived again at a system of coupled nonlinear partial differential equations along with the complex geometry. Thus, an efficient fast converging technique is required that can handle the curved geometry and nonlinearity of the equations. Galerkin's weighted residual finite element method is incorporated after discretizing the considered whole domain of the problem into a mesh of six nodal triangular elements which gives highly convergent result with

tolerance of 10^{-14} in maximum 6 to 8 number of iterations. The approximation of stream function and vorticity is given in Eq. (6.15) and approximation of microrotation function is given by

$$g = \sum_{k=1}^{n} N_k g_k, \tag{9.14}$$

where g_k are the nodal element approximation of g. In our situation, we considered quadratic triangular elements with $n = 6$. After applying Galerkin's finite element scheme to Eqs. (9.10) to (9.12) takes the following form

$$\int_\Omega w_1 \left(\frac{\alpha^2}{r}\frac{\partial^2\psi}{\partial z^2} + \frac{\partial}{\partial r}\left(\frac{1}{r}\frac{\partial\psi}{\partial r}\right) + \omega\right) d\Omega = 0, \tag{9.15}$$

$$\int_\Omega w_2 \left(Re\left(\frac{\partial\psi}{\partial r}\frac{\partial}{\partial z}\left(\frac{\omega}{r}\right) - \frac{\partial\psi}{\partial z}\frac{\partial}{\partial r}\left(\frac{\omega}{r}\right)\right) - \frac{1}{1-N}\left(\frac{1}{r}\mathrm{D}^2(r\omega) + \frac{N}{r}\mathrm{D}^2(rg)\right) - M^2\frac{\partial}{\partial r}\left(\frac{1}{r}\frac{\partial\psi}{\partial r}\right) + \frac{1}{K}\omega\right) d\Omega = 0, \tag{9.16}$$

$$\int_\Omega w_3 \left(Re\, J\frac{1-N}{N\,r}\left(\frac{\partial\psi}{\partial z}\frac{\partial w}{\partial r} - \frac{\partial\psi}{\partial r}\frac{\partial w}{\partial z}\right) - \omega + 2g - \frac{2-N}{m^2}\frac{1}{r}\mathrm{D}^2 g\right) d\Omega = 0, \tag{9.17}$$

where w_1, w_2 and w_3 represents the weight functions and $d\Omega = 2\pi r dr dz$. Upon simplification of Eqs. (9.15) to (9.17), we get

$$\int_\Omega \left(\frac{\alpha^2}{r}\frac{\partial w_1}{\partial z}\frac{\partial\psi}{\partial z} + \frac{\partial w_1}{\partial r}\left(\frac{1}{r}\frac{\partial\psi}{\partial r}\right) - w_1\omega\right) d\Omega = \int_\Gamma w_1\frac{\partial\psi}{\partial n}d\Gamma, \tag{9.18}$$

$$\int_\Omega w_2\, Re\left(\frac{\partial\psi}{\partial r}\frac{\partial}{\partial z}\left(\frac{\omega}{r}\right) - \frac{\partial\psi}{\partial z}\frac{\partial}{\partial r}\left(\frac{\omega}{r}\right)\right) d\Omega + \frac{1}{1-N}\int_\Omega \left(\frac{\partial w_2}{\partial r}\frac{1}{r}\frac{\partial(r\omega)}{\partial r} + \frac{\alpha^2}{r}\frac{\partial w_2}{\partial z}\frac{\partial(r\omega)}{\partial z}\right) d\Omega + \frac{N}{1-N}\int_\Omega \left(\frac{\partial w_2}{\partial r}\frac{1}{r}\frac{\partial(rg)}{\partial r} + \frac{\alpha^2}{r}\frac{\partial w_2}{\partial z}\frac{\partial(rg)}{\partial z}\right) d\Omega + M^2\int_\Omega \left(\frac{\partial w_2}{\partial r}\frac{1}{r}\frac{\partial\psi}{\partial r}\right) d\Omega + \frac{1}{K}\int_\Omega w_2\omega d\Omega = \frac{1}{1-N}\int_\Gamma w_2\frac{\partial\omega}{\partial n}d\Gamma + \frac{N}{1-N}\int_\Gamma w_2\frac{\partial g}{\partial n}d\Gamma + M^2\int_\Gamma w_2\frac{\partial\psi}{\partial n}d\Gamma, \tag{9.19}$$

$$Re\, J\frac{1-N}{N}\int_\Omega \frac{w_3}{r}\left(\frac{\partial\psi}{\partial z}\frac{\partial w}{\partial r} - \frac{\partial\psi}{\partial r}\frac{\partial w}{\partial z}\right) d\Omega - \int_\Omega w_3\omega\, d\Omega + 2\int_\Omega w_3 g d\Omega + \frac{2-N}{m^2}\int_\Omega \frac{\alpha^2}{r}\frac{\partial w_3}{\partial z}\frac{\partial g}{\partial z} + \frac{\partial w_3}{\partial r}\left(\frac{1}{r}\frac{\partial g}{\partial r}\right) d\Omega = \frac{2-N}{m^2}\int_\Gamma w_3\frac{\partial g}{\partial n}d\Gamma, \tag{9.20}$$

where $d\Gamma = \pi r dr dz$. After discretizing the domain and introducing the approximation given in Eqs. (6.14) and (9.14) in Eqs. (9.18) to (9.20), we get

$$-\sum_i B_{ki}^e\omega_i + \sum_i A_{ki}^e\psi_i = S_n^{k^e}, \tag{9.21}$$

$$Re\sum_i C_{kij}^e\psi_i\omega_i + \frac{1}{N-1}\sum_i A_{ki}^e\omega_i - \frac{N}{N-1}\sum_i A_{ki}^e\psi_i + M^2\sum_i D_{ki}^e\psi_i + \frac{1}{K}\sum_i B_{ki}^e\psi_i = \frac{1}{1-N}S_{n_1}^{k^e} + \frac{N}{1-N}S_{n_2}^{k^e} + M^2 S_n^{k^e}, \tag{9.22}$$

$$-\sum_i B^e_{ki}\omega_i + Re\,J\frac{N}{N-1}\sum_i C^e_{kij}\psi_i g_i + \frac{2-N}{m^2}\sum_i A1^e_{ki} g_i + 2\sum_i B^e_{ki} g_i = \frac{2-N}{m^2} S^{k^e}_{n_2} \tag{9.23}$$

where

$$\left.\begin{aligned} A^e_{ki} &= \int_{\Omega^e}\left(\frac{\alpha^2}{r}\frac{\partial N_k}{\partial z}\frac{\partial N_i}{\partial z} + \frac{\partial N_k}{\partial r}\left(\frac{1}{r}\frac{\partial N_i}{\partial r}\right)\right)d\Omega \\ B^e_{ki} &= \int_{\Omega^e} N_k N_i\, d\Omega \\ C^e_{kij} &= \int_{\Omega} N_k\left(\frac{\partial N_i}{\partial r}\frac{\partial}{\partial z}\left(\frac{N_j}{r}\right) - \frac{\partial N_j}{\partial z}\frac{\partial}{\partial r}\left(\frac{N_i}{r}\right)\right)d\Omega \\ D^e_{ki} &= \int_{\Omega}\left(\frac{\partial N_k}{\partial r}\frac{1}{r}\frac{\partial N_k}{\partial r}\right)d\Omega \\ S^{k^e}_{n_t} &= \int_{\Gamma} N_k \bar{S}_k\, d\Gamma \quad \text{where } t = 1,2 \end{aligned}\right\}. \tag{9.24}$$

After assembly procedure, obtained resulting system (global) in the matrix arrangement is expressed as follows

$$\boldsymbol{KA} = \boldsymbol{F}. \tag{9.25}$$

where

$$K_{ij} = \begin{bmatrix} -B^e_{ki} & A^e_{ki} & 0 \\ \frac{1}{N-1}A^e_{ki} & ReC^e_{kij}\omega_i + M^2 D^e_{ki} + \frac{1}{K}B^e_{ki} & -\frac{N}{N-1}A^e_{ki} \\ -B^e_{ki} & ReJ\frac{N}{N-1}C^e_{kij}g_i & \frac{2-N}{m^2}A^e_{ki} + 2B^e_{ki} \end{bmatrix},$$

$$A_k = \begin{bmatrix} \omega_k \\ \psi_k \\ g_k \end{bmatrix},\ F_k = \begin{bmatrix} S^{k^e}_n \\ \frac{1}{N-1}S^{k^e}_{n_1} + \frac{N}{N-1}S^{k^e}_{n_2} + M^2 S^{k^e}_n \\ \frac{2-N}{m^2}S^{k^e}_{n_1} \end{bmatrix}. \tag{9.26}$$

Eq. (9.25) represents the system of nonlinear algebraic equations which is solved by Newton-Raphson method. The procedure is iterated until the convergence condition is achieved.

9.3 Validation

In this section, a comparison of obtained results with the existing results available in literature is made by plotting the curves for longitudinal velocity. For this purpose, the computations of obtained results are made by applying the assumption of lubrication theory in limiting case ($1/K = 0$) and setting $q = F/2\pi$ to compare with results of Wang et al. (2011). Graph of velocity of is drawn by putting $F = 0$ and $F = 1$ it transform q as $q = 1/\pi$ and $q = 0$ and compared them with results of Wang et al.

(2011) in **Figure 9.1** and found in close agreement, hence, the solution computed is correct and the presented analysis is valid.

9.4 Results and Discussion

In this particular section, the results are obtained by implementing the above discussed numerical scheme to governing equations and shown in the arrangement of graphs that presents the effect variations of participated parameters in the governing equations such as Reynolds number Re, wave number α, permeability parameter of porous medium K, Hartmann number M, micropolar parameter m and coupling number N on the considered peristaltic flow problem and discussed in detail.

9.4.1 Velocity profile

The longitudinal velocity profile is plotted at $z = 0$ to analyze the participation of different participating parameter on the flow and shown through **Figures 9.2-9.7**. It is observed from these figures that behavior of longitudinal velocity adjacent the walls of the tube and in the central region of the tube is entirely opposite. The effects of Reynolds number on longitudinal velocity are plotted for $Re = 1, 5, 10$ and 20 with fixed values of $\alpha = 0.4, \phi = 0.4, N = 0.2, m = 1, J = 0.1, M = 2, Q = 1.4$ and $K = 0.5$ in **Figure 9.2**. It is noted that by increasing the Reynolds number that consequently enhances the dominance of inertial forces over viscous forces, increases the velocity of the fluid in the vicinity of central region of the tube. In the region near the wall, increase in Reynolds number reduces the velocity of the fluid. These results are new in the literature for peristaltic flow of micropolar fluid in a tube. In **Figure 9.3** graph of the longitudinal velocity are presented for different values of wave number $\alpha = 0.3, 0.5, 0.7$ and 0.9 with fixed $Re = 5, \phi = 0.4, N = 0.2, m = 1, J = 0.1, M = 2, Q = 1.4$ and $K = 0.5$. It exhibits that wave number shows opposite behavior as that in case of Reynolds number on longitudinal velocity. **Figure 9.4** shows the effect of numerous values of permeability of porous medium $K = 0.01,\ 0.05,\ 0.1$ and 0.5 where $Re = 5, \alpha = 0.4, \phi = 0.4, N = 0.2, m = 1, J = 0.1, M = 2$, and $Q = 1.4$ on longitudinal velocity. It reveals that increasing values of permeability parameter assists the flow in the central region of the tube while it resist the flow of the fluid near the wall. Effects of variation of Hartmann number on the velocity is plotted in **Figure 9.5** for $M = 1, 3, 5$ and 7 with $Re = 5, \alpha = 0.4, \phi = 0.4, N = 0.2, m = 1, J = 0.1, Q = 1.4$ and $K = 0.5$. It shows that increase in Hartmann number produces resistance against the flow in the region near the central line of the tube causing the decrease in the velocity due to the

fact that increase in Hartmann number strengthens the magnetic field that causes the resistance in the bulk motion of the micropolar fluid in the central part of the tube. **Figure 9.6** shows the graph of longitudinal velocity for different values of micropolar parameter $m = 2, 4$ and 6 with $Re = 5, \alpha = 0.4, \phi = 0.4, N = 0.2, J = 0.1, M = 2, Q = 1.4$ and $K = 0.5$ and for Newtonian and non-Newtonian case. It reveals that longitudinal velocity for Newtonian fluid is greater in the central region as compared to that of non-Newtonian fluid and increasing values of micropolar parameter decreases the velocity in the central part of the tube while opposite effects are noted in the section near the wall. The effects of coupling parameter on longitudinal velocity are shown in **Figure 9.7** by plotting graphs for $N = 0.2, 0.4, 0.6$ and 0.8 with $Re = 5, \alpha = 0.4, \phi = 0.4, m = 1, J = 0.1, M = 2, Q = 1.4$ and $K = 0.5$. The variation in case of coupling number is negligible as compared to that of micropolar parameter but exhibits the qualitatively same behavior in the central region and near the peristaltic wall of the tube.

9.4.2 Trapping phenomena, vorticity and microrotation

The movement of the walls of the tube in peristalsis generates the streamlines that move along the wave and sometimes these streamlines do not follow the same path but split and move in circular path, hence forms the bolus. Trapping phenomenon in the peristaltic motion includes the behavior of streamlines and trapping bolus. **Figures 9.8** to **9.10** exhibits the behavior of the streamlines along with vorticity that describes the local spinning of the fluid and microrotation of the particles for participation of various values of the prominent parameters involved in present considered model. **Figure 9.8** shows the behavior of contours of streamlines, vorticity and microrotation for variation of Reynolds number while keeping other parameters fixed at some suitable values. It reveals that increase in Reynolds number magnifies the size of bolus and increases the number of trapping boluses due to fact that as we increase the Reynolds number, inertial forces become dominant over the viscous forces and assist the velocity which increase both the size and number of the trapped boluses. The vorticity generates at the central region of the crest part of the wave and tendency to moves at the peristaltic walls of the tube with increasing values of Reynolds number which reveals that for large values of Reynolds number the fluid clustered at the peristaltic walls exhibits more rotational velocity as compared to the central region. The microrotation of the micropolar particles attributes symmetrical behavior for low Reynolds number while for large values of

Reynolds number symmetry is lost and microrotation of the micropolar particles move towards the right side of the tube in trough part of the wave. The behavior of the streamlines, vorticity and microrotation for various values of the Hartmann number are presented in **Figure 9.9** which revels that increasing values of the Hartmann number decreases the number as well as the size of the bolus. This is due to the fact that increase in Hartmann causes enhancement in the strength of the magnetic field which causes resistance against the flow of the fluid which reduces the height of the flow pattern and thus reduces the number and size of the bolus. The vorticity lines show that strong electromagnetic forces push the vorticity lines towards the peristaltic wall and exhibits the same path as that of the peristaltic walls of the tube. The physical characteristic of microrotation of the micropolar particles decreases by increasing Hartmann number. **Figure 9.10** includes the contours of streamlines, vorticity and microrotation for diverse values of permeability of porous medium. The behavior for increasing values of permeability of porous medium on streamlines, vorticity and microrotation of the micropolar particles are opposite as compared to the case of Hartmann number. Increasing values of porosity parameter magnifies the size of the bolus and increases the number of the trapped boluses. It is due to the fact that increasing permeability parameter permits rapid movement of the fluid that passes through the tube which consequently enhances the height of the flow field that made a reason for the increase in volume as well as number of the bolus. The increase in the permeability of the porous parameter enhances the vorticity lines in the central part of the tube and with increase in permeability of porous medium, vorticity lines generated at the peristaltic walls of the tube and are clustered in the central part of the tube. Furthermore, it is also noted that microrotation of the micropolar particles also enhances by the upsurge in the values of the permeability of the porous medium.

9.4.3 Pressure distribution

The pressure rise per wavelength on central line $r = 0$ is plotted against time mean flow rate to examine the effects of participating parameters involved in the governing equations on the pressure distribution for the considered modeled through **Figures 9.11** to **9.16**. In general, pumping mechanism in peristaltic flow is studied in three ranges of ΔP i.e. if $\Delta P > 0$, then that region is known as augmented pumping region while for $\Delta P < 0$ is the co-pumping region and $\Delta P = 0$ is the free pumping region. In most of the engineering and biomedical situations, researchers are interested in the results

for augmented pumping region. consequently the graphs of pressure rise per wavelength are plotted to discuss the peristaltic phenomenon in this region only. It is revealed that pressure distribution is linear when the inertial forces are balanced with the viscous forces while nonlinear behavior is observed for non-zero values of Reynolds number. In **Figure 9.11**, the effects of different Reynolds number Re = 1,2,3 and 5 with fixed values of other parameters $\alpha = 0.4, \phi = 0.6, N = 0.4, m = 2, J = 0.1, M = 2$ and $K = 0.5$ on the pressure distribution are presented. The enhancement in the dominance of inertial forces over viscous forces caused by increasing the Reynolds number [illegible] the pressure rise per wavelength. This observation for peristaltic transport [illegible] of micropolar fluid passing through a tube is presented first time in the literature the lubrication theory is not able to predict such effects. **Figure 9.12** is plotted to examine the behavior of pressure rise per wavelength for various values of wave number α = 0.1, 0.2, 0.3 and 0.4 with fixed values of other parameters $Re = 1, \phi = 0.6, N = [illegible] m = 1, J = 0.1, M = 2$ and $K = 0.5$. It is observed that increasing values of wave number which consequently increases the width of the tube in comparison to wavelength enhances the pressure distribution in the augmented pumping region. Pressure rise per wavelength for different values of permeability of porous medium

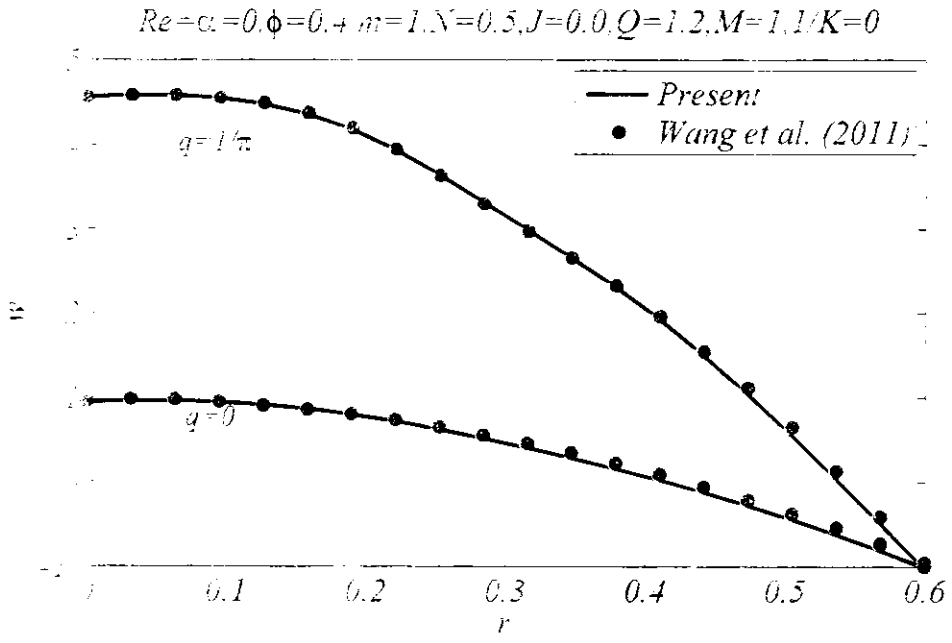

Figure [illegible] Comparison of computed results with that of Wang et al. (2011) for longitudinal velocity

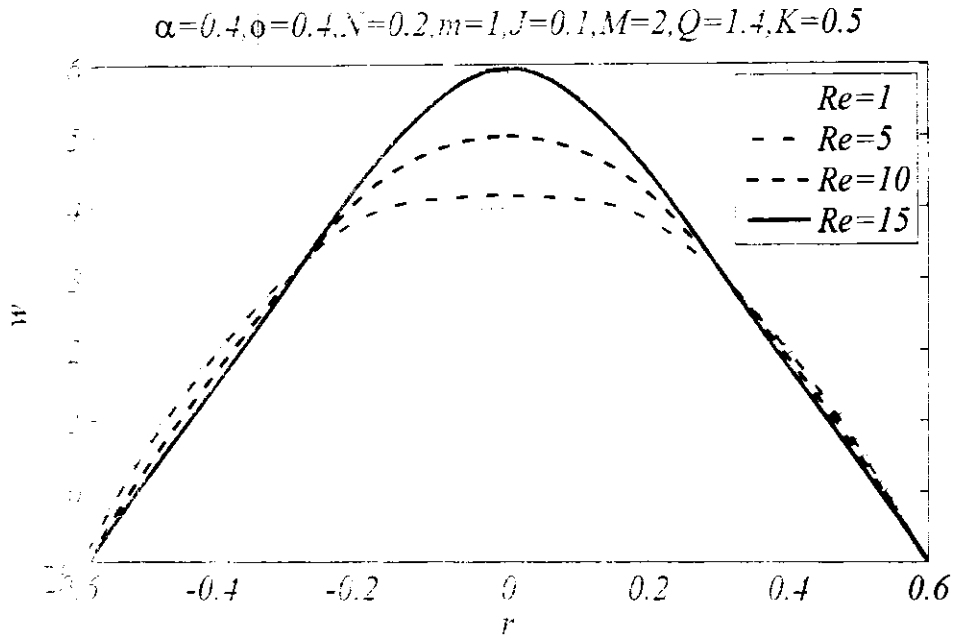

Figure 9.2: Velocity profile for variation of Reynolds number *Re* at fixed values of other parameters

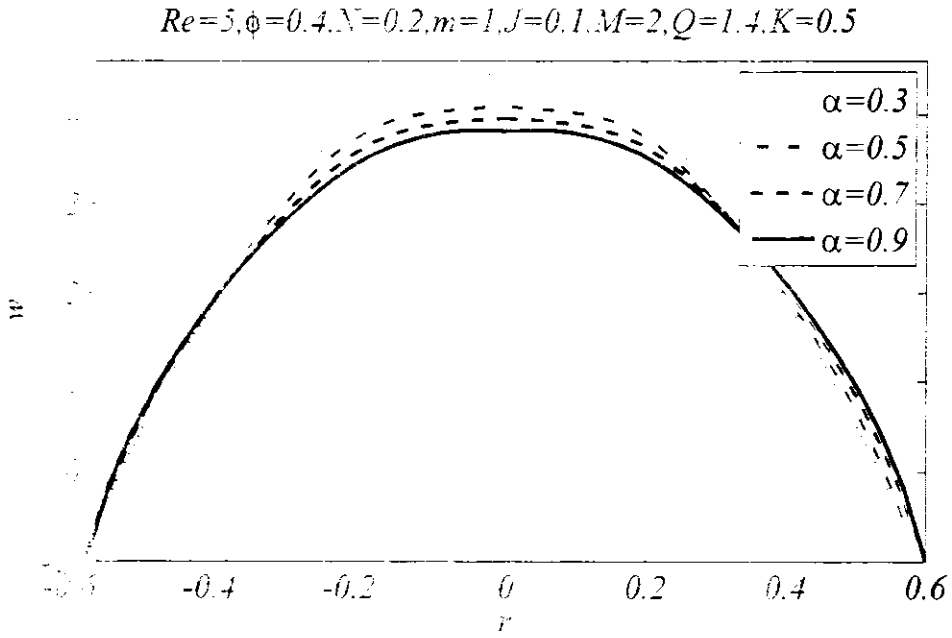

Figure 9.3: Velocity profile for variation of wave number α at fixed values of other parameters

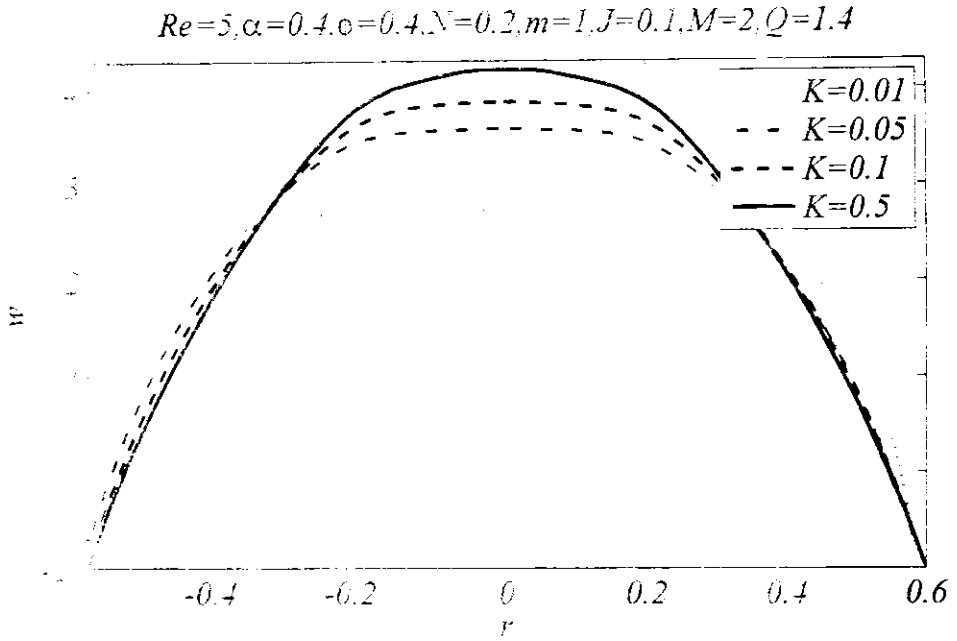

Figure 9.4: Graphs of longitudinal velocity distribution for various values of the parameter K against fixed values of other parameters

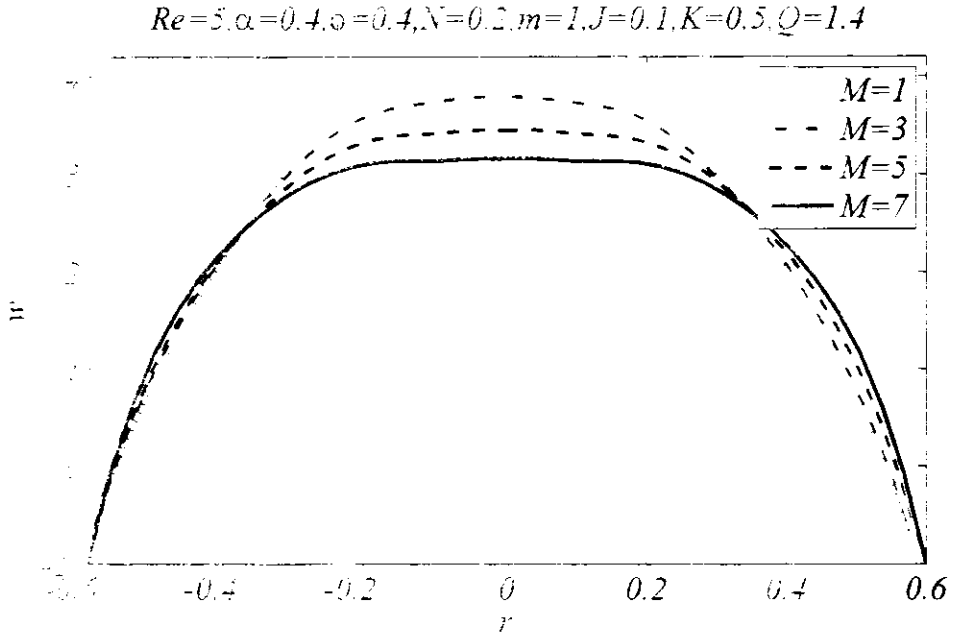

Figure 9.5: Graphs of longitudinal velocity distribution for various values of the parameter M against fixed values of other parameters

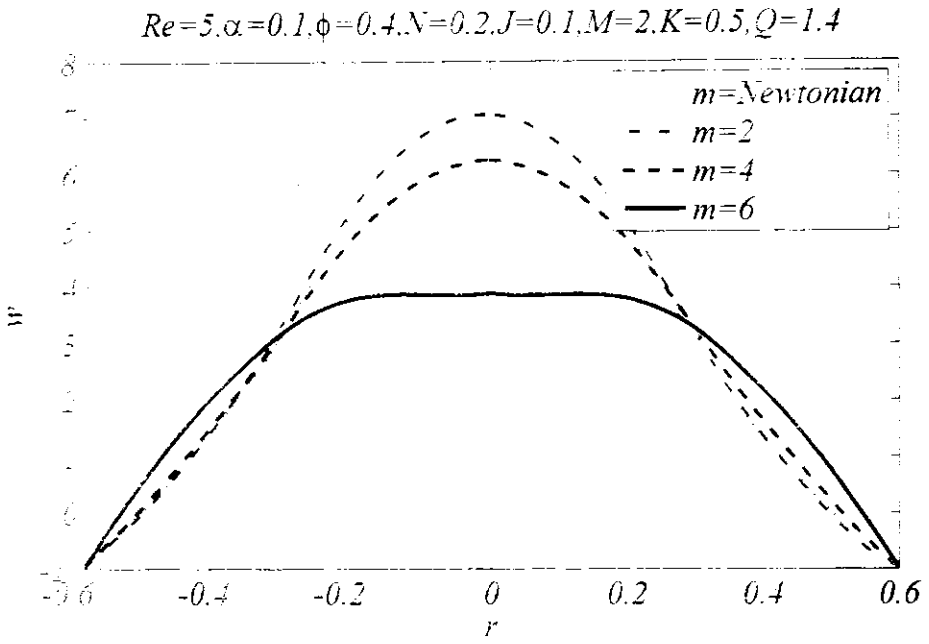

Figure 9.6: Graphs of longitudinal velocity distribution for various values of the parameter m against fixed values of other parameters

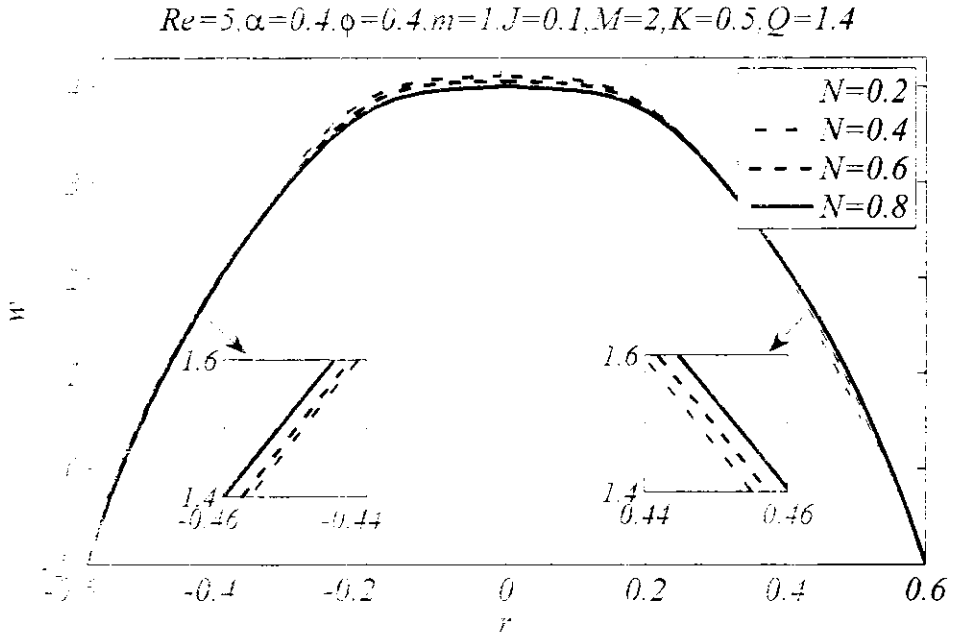

Figure 9.7: Graphs of longitudinal velocity distribution for various values of the parameter N against fixed values of other parameters

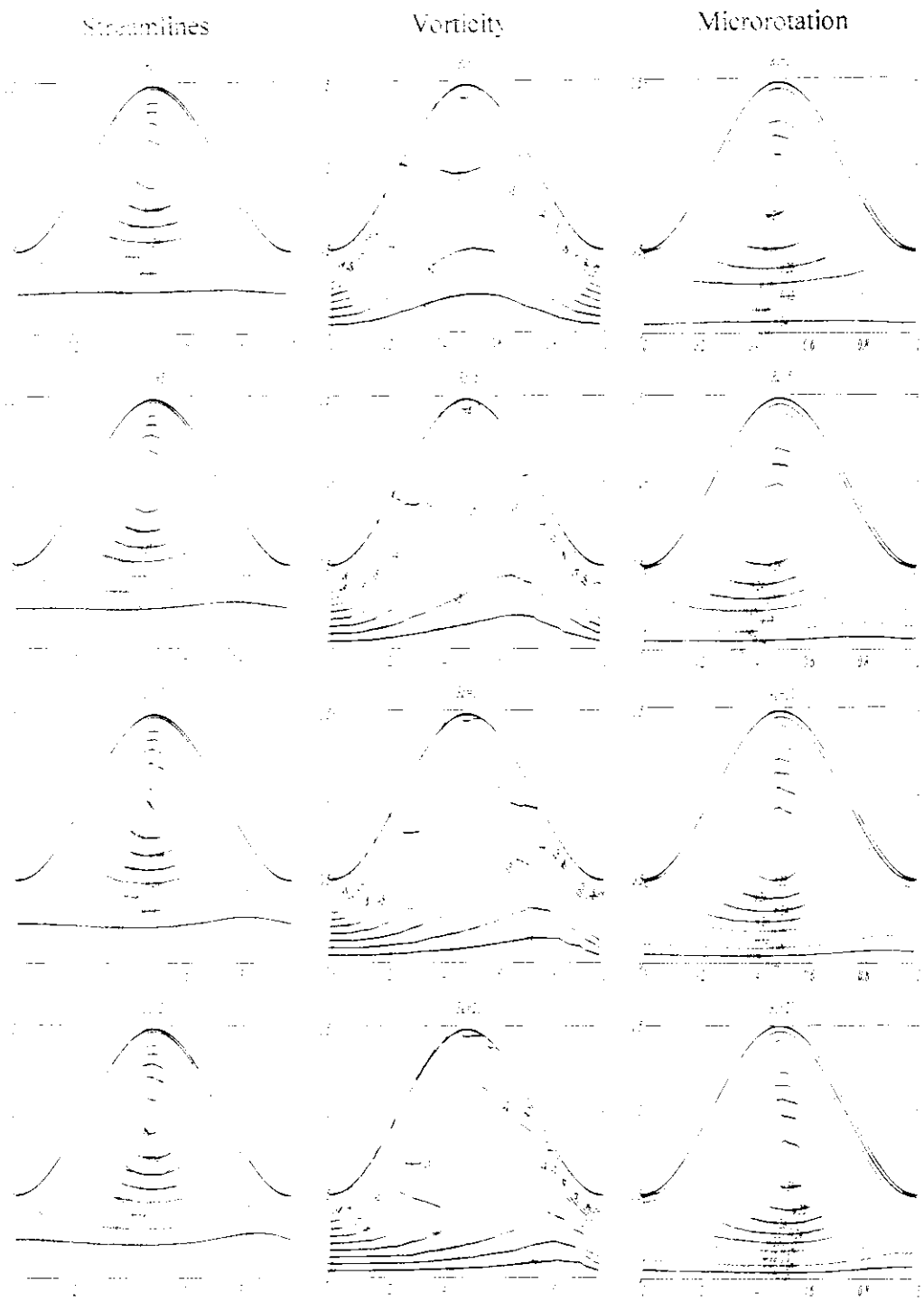

Figure 9.8. Streamlines, vorticity and microrotation for various values of Reynolds number Re against fixed values of other parameters at $\alpha = 0.5, \phi = 0.4, m = 2, n = 0.5, M = 2, K = 0.5$ and $Q = 1.2$

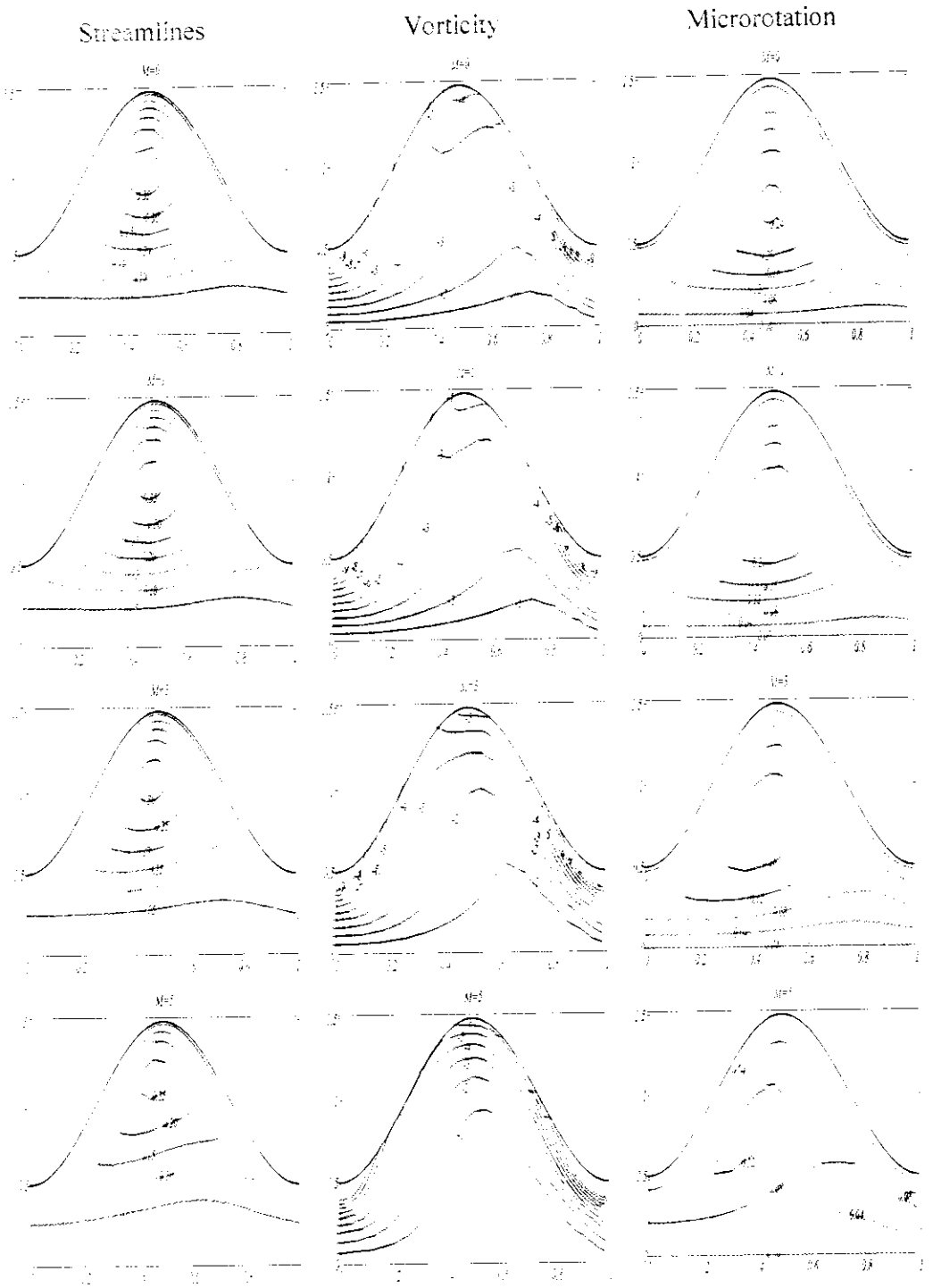

Figure 9.9: Streamlines, vorticity and microrotation for various values of Hartmann number M against fixed values of other parameters at $Re = 10, \alpha = 0.5, \phi = 0.4, m = 2, n = 0.5, K = 0.5$ and $Q = 1.2$

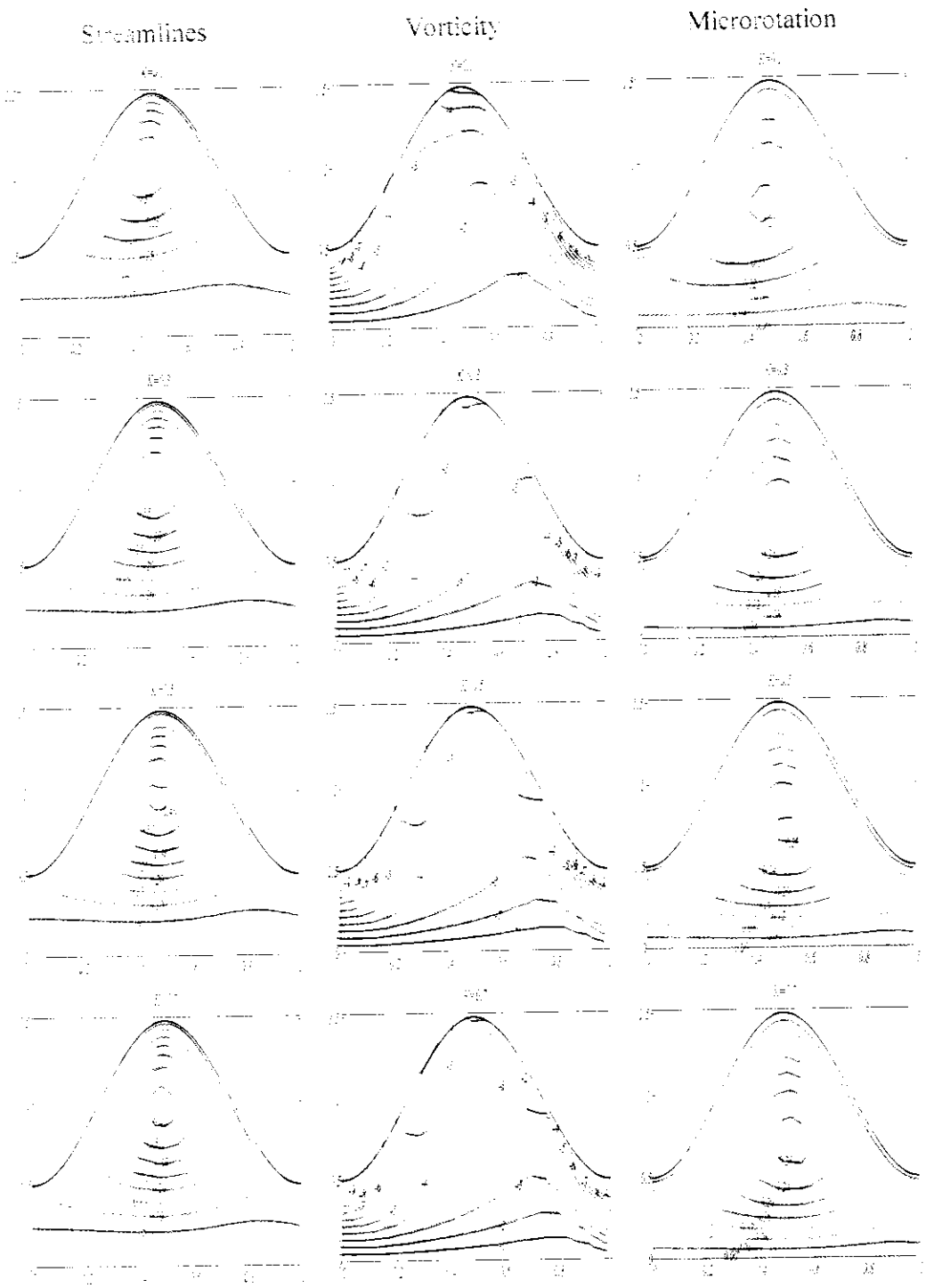

Figure 9.1c: Streamlines, vorticity and microrotation for various values of porosity parameter K against fixed values of other parameters at $Re = 10, \alpha = 0.5, \phi = 0.4, m = 2, n = 0.5, M = 2$ and $Q = 1.2$

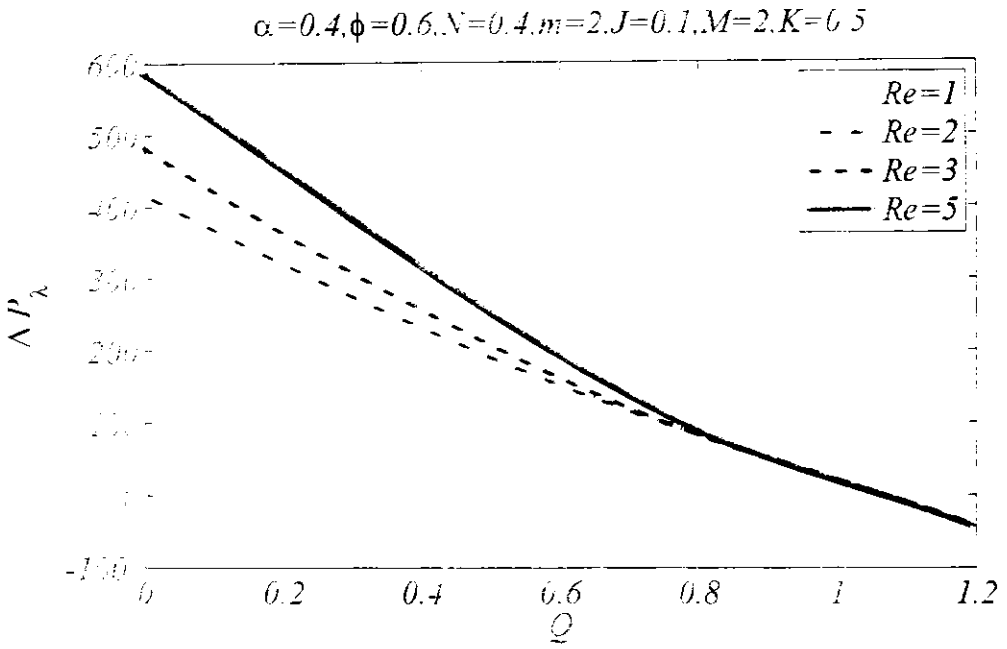

Figure 9.1: Pressure rise per wavelength for variation of Reynolds number *Re* at fixed values of other parameters

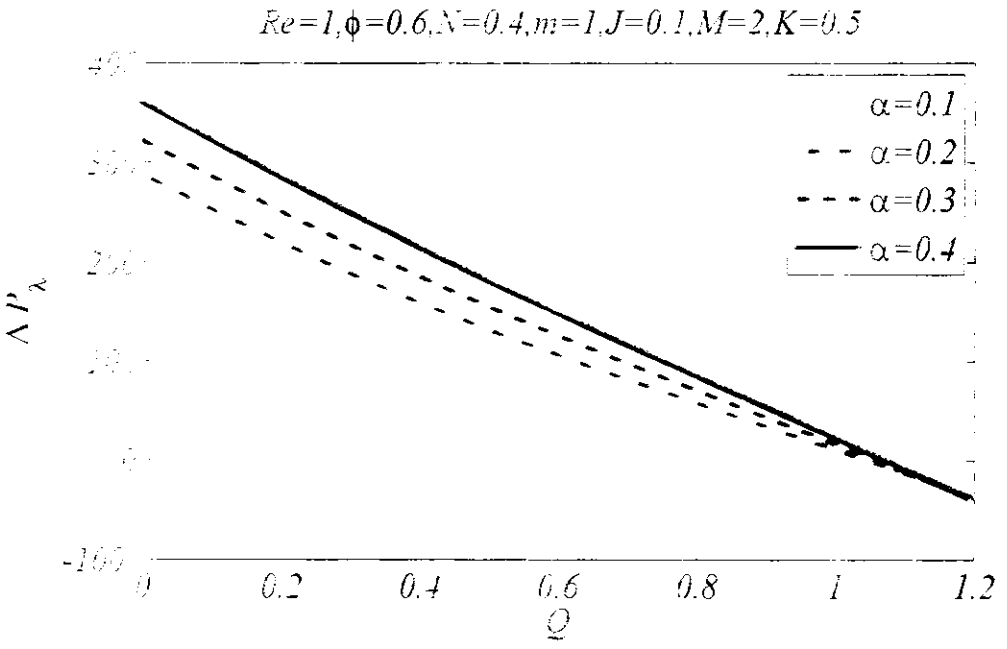

Figure 9.2: Pressure rise per wavelength for variation of wave number α at fixed values of other parameters

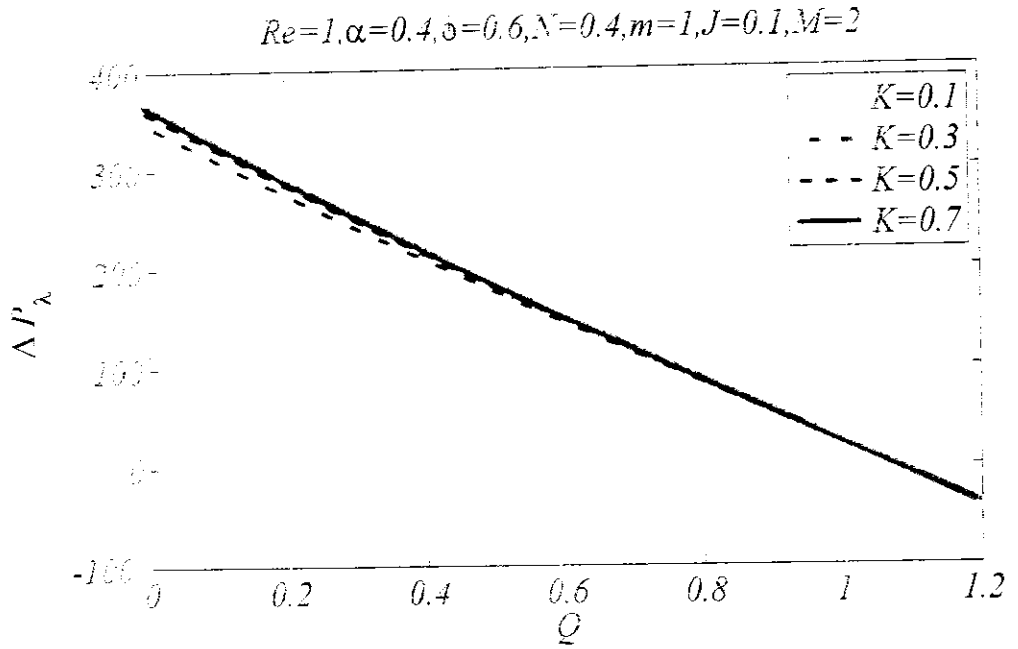

Figure 9.13: Pressure rise per wavelength for variation of permeability parameter K at fixed values of other parameters

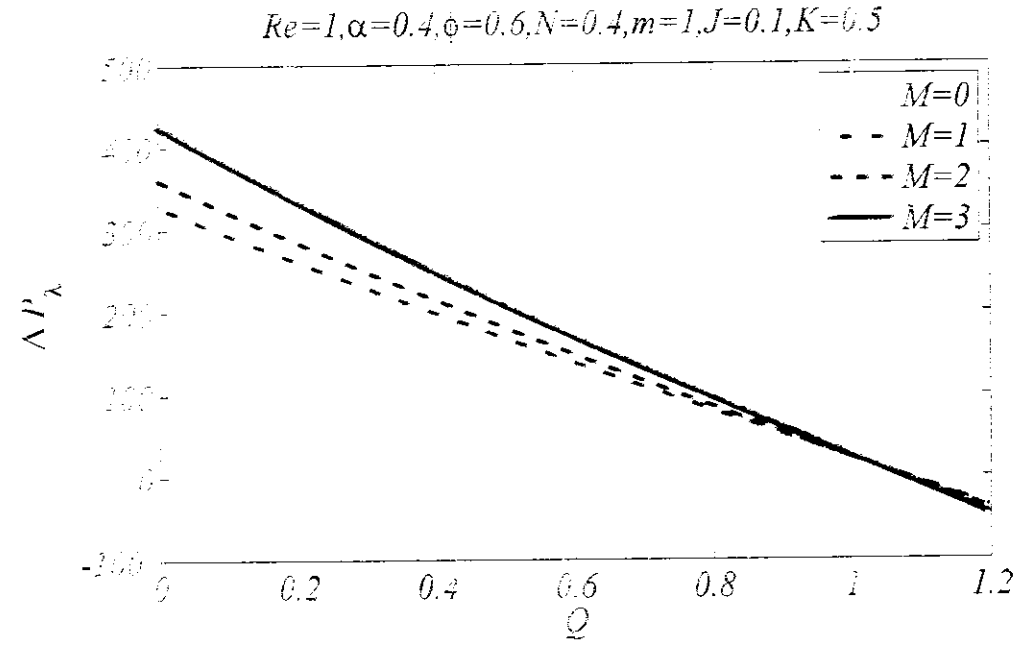

Figure 9.14: Pressure rise per wavelength for variation of Hartmann number M at fixed values of other parameters

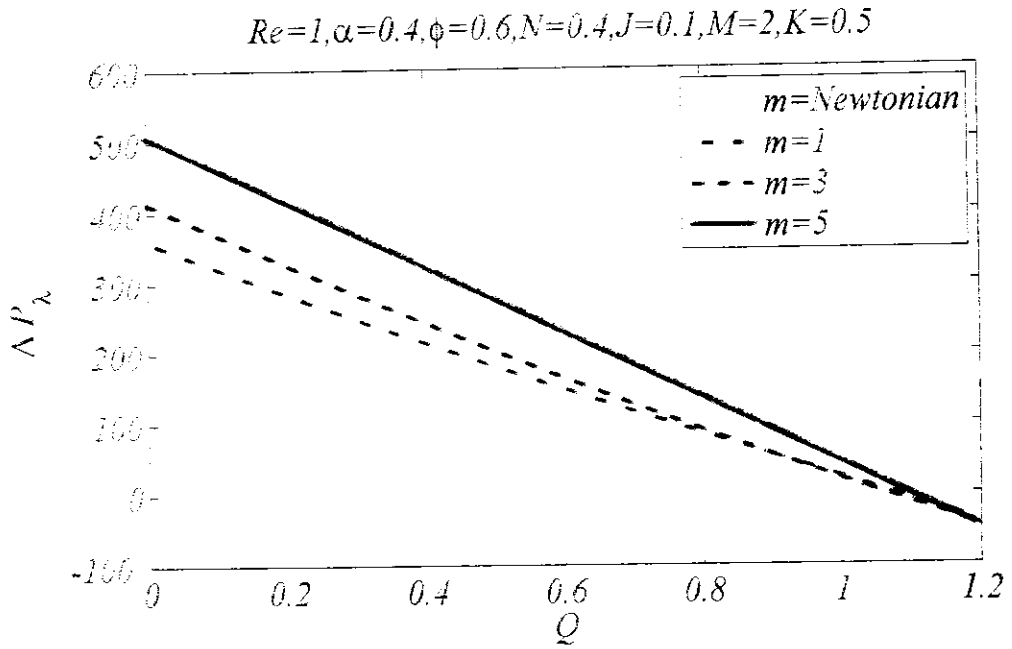

Figure 9.15: Pressure rise per wavelength for variation of micropolar parameter m at fixed values of other parameters

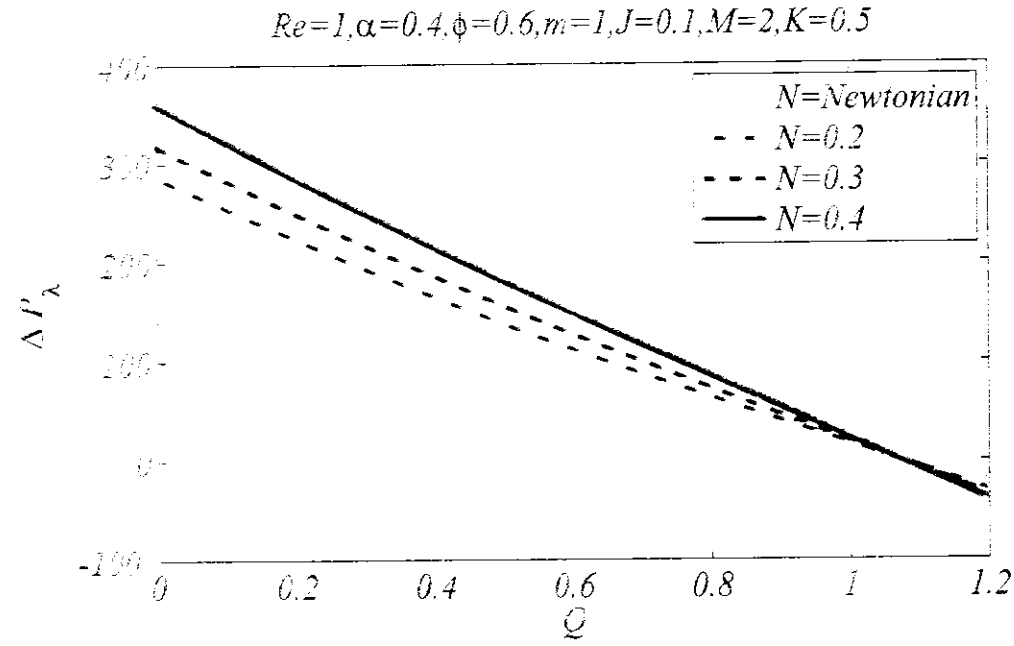

Figure 9.16: Pressure rise per wavelength for variation of coupling number N at fixed values of other parameters

$K = 0.1, 0.3, 0.5$ and 0.7 with fixed $Re = 1, \alpha = 0.4, \phi = 0.6, N = 0.4, m = 1, J = 0.1$ and $M = 2$ is shown in **Figure 9.13**. It reveals that enhancement the porous medium permeability trades increases the pressure rise per wavelength. Furthermore, for greater values of permeability parameter, comparatively less variation in the pressure is observed as compared to small values of permeability parameter. **Figure 9.14** is displayed to observe the variation of Hartmann number $M = 0, 1, 2$ and 3 with fixed values of $Re = 1, \alpha = 0.4, \phi = 0.6, N = 0.4, m = 1, J = 0.1$ and $K = 0.5$ on pressure rise per wavelength. It is observed that increase in strength of electromagnetic forces due to increase in Hartmann number assist the pressure rise per wavelength. **Figure 9.15** and **9.16** present the effects of variation of micropolar parameter and coupling number on the pressure rise per wavelength respectively. In both figures, results for Newtonian fluid are also included to compare with the pressure rise per wavelength for non-Newtonian micropolar fluid. It is noted that pressure rise per wave length exhibits the direct relation with the micropolar parameter and coupling number. Furthermore, it is perceived through graphs that pressure rise per wavelength is greater for micropolar fluid as compared to that of Newtonian fluid.

9.5 Conclusions

In this chapter, the peristaltic transportation of micropolar fluid passing through a porous medium is carried out for non-zero moderate Reynolds number in presence of an applied magnetic field. The numerical solution of a set of governing partial differential equation subject to the suitable boundary conditions is obtained by using finite element method equipped with Galerkin formulation. The current investigation is carried out without using the conventional assumptions of long wavelength and low Reynolds number which allows predicting the behavior of peristaltic motion of micropolar fluid in a tube for moderate Reynolds number. It is prominent that increase in Reynolds number assists the peristaltic flow in the central part of the tube while opposes the flow near the peristaltic wall of the tube and enhances the pressure rise per wavelength. Increasing Hartmann number is contributed by the Lorentz force diminutions the velocity in the central part of the tube and upsurges in the vicinity of the peristaltic tube and increases the pressure rise per wavelength. The rise in the permeability of the porous medium increases the velocity in the central part of the tube and support the pressure rise per wavelength. The peristaltic mixing is increased by increasing Reynolds number and permeability of porous medium, as an increase in

volume as well as number of the trapped bolus is noted. The presence of trapping bolus and its position highly depends on the Hartmann number. It is shown that for micropolar fluid in peristalsis supports the pressure rise as compared to that of Newtonian fluid. It is hoped that this investigation will encourage the researchers and will be considered as a benchmark to explore the neglected features of the peristaltic motion of micropolar fluid passing through the tube.

References

Abaid-ur-Rehman (2016). *Study of fluid flows within a square cavity by using FEM.* MS Dissertation IIUI, Pakistan.

Abbas, M. A., Bai, Y. Q., Bhatti, M. M., & Rashidi, M. M. (2016). Three dimensional peristaltic flow of hyperbolic tangent fluid in non-uniform channel having flexible walls. *Alexandria Engineering Journal, 55*(1), 653-662.

Abd-Alla, A. M., Abo-Dahab, S. M., & Al-Simery, R. D. (2013). Effect of rotation on peristaltic flow of a micropolar fluid through a porous medium with an external magnetic field. *Journal of magnetism and Magnetic materials, 348*, 33-43.

Abd-Alla, A. M., Abo-Dahab, S. M., & El-Shahrany, H. D. (2014). Effects of rotation and initial stress on peristaltic transport of fourth grade fluid with heat transfer and induced magnetic field. *Journal of Magnetism and Magnetic Materials, 349*, 268-280.

Abd-Alla, A. M., Abo-Dahab, S. M., & Kilicman, A. (2015). Peristaltic flow of a Jeffrey fluid under the effect of radially varying magnetic field in a tube with an endoscope. *Journal of Magnetism and Magnetic Materials, 384*, 79-86.

Abdelsalam, S. I., & Vafai, K. (2017). Combined effects of magnetic field and rheological properties on the peristaltic flow of a compressible fluid in a microfluidic channel. *European Journal of Mechanics-B/Fluids, 65*, 398-411.

Abou-Zeid, M. (2016). Effects of thermal-diffusion and viscous dissipation on peristaltic flow of micropolar non-Newtonian nanofluid: application of homotopy perturbation method. *Results in physics, 6*, 481-495.

Afifi, N. A. S., & Gad, N. S. (2003). Interaction of peristaltic flow with pulsatile fluid through a porous medium. *Applied Mathematics and Computation, 142*(1), 167-176.

Akbar, N. S. (2015). Influence of magnetic field on peristaltic flow of a Casson fluid in an asymmetric channel: application in crude oil refinement. *Journal of Magnetism and Magnetic Materials, 378*, 463-468.

Akbar, N. S., & Khan, Z. H. (2015). Metachronal beating of cilia under the influence of Casson fluid and magnetic field. *Journal of Magnetism and Magnetic Materials*, *378*, 320-326.

Akbar, N. S., & Nadeem, S. (2014). Exact solution of peristaltic flow of biviscosity fluid in an endoscope: A note. *Alexandria Engineering Journal*, *53*(2), 449-454.

Akbar, N. S., Tripathi, D., Bég, O. A., & Khan, Z. H. (2016). MHD dissipative flow and heat transfer of Casson fluids due to metachronal wave propulsion of beating cilia with thermal and velocity slip effects under an oblique magnetic field. *Acta Astronautica*, *128*, 1-12.

Akram, S., Mekheimer, K. S., & Elmaboud, Y. A. (2016). Particulate suspension slip flow induced by peristaltic waves in a rectangular duct: Effect of lateral walls. *Alexandria Engineering Journal*.

Akram, S., Nadeem, S., & Hussain, A. (2014). Effects of heat and mass transfer on peristaltic flow of a Bingham fluid in the presence of inclined magnetic field and channel with different wave forms. *Journal of Magnetism and Magnetic Materials*, *362*, 184-192.

Ali, N., & Hayat, T. (2008). Peristaltic flow of a micropolar fluid in an asymmetric channel. *Computers & Mathematics with Applications*, *55*(4), 589-608.

Ali, N., Javid, K., & Sajid, M. (2016). Simulations of peristaltic slip-flow of hydromagnetic bio-fluid in a curved channel. *AIP Advances*, *6*(2), 025111.

Ali, N., Sajid, M., Javed, T., & Abbas, Z. (2010). Heat transfer analysis of peristaltic flow in a curved channel. *International Journal of Heat and Mass Transfer*, *53*(15-16), 3319-3325.

ALLEN, M. (1984). Collocation techniques for modeling compositional flows in porous media.

Animasaun, I. L., Adebile, E. A., & Fagbade, A. I. (2016). Casson fluid flow with variable thermo-physical property along exponentially stretching sheet with suction and exponentially decaying internal heat generation using the homotopy analysis method. *Journal of the Nigerian Mathematical Society*, 35(1), 1-17.

Ariman, T. M. A. N. D., Turk, M. A., & Sylvester, N. D. (1973). Microcontinuum fluid mechanics—a review. *International Journal of Engineering Science*, *11*(8), 905-930.

Ariman, T. T. N. D., Turk, M. A., & Sylvester, N. D. (1974). Applications of microcontinuum fluid mechanics. *International Journal of Engineering Science*, *12*(4), 273-293.

Babu, V. R., Sreenadh, S., & Srinivas, A. N. S. (2016). Peristaltic transport of a viscous fluid in a porous channel with suction and injection. *Ain Shams Engineering Journal*.

Bang, H., & Kwon, Y. W. (2000). *The finite element method using MATLAB*. CRC press.

Basser, H., Rudman, M., & Daly, E. (2017). SPH modelling of multi-fluid lock-exchange over and within porous media. *Advances in Water Resources*, *108*, 15-28.

Böhme, G., & Friedrich, R. (1983). Peristaltic flow of viscoelastic liquids. *Journal of Fluid Mechanics*, *128*, 109-122.

Brasseur, J. G., Corrsin, S., & Lu, N. Q. (1987). The influence of a peripheral layer of different viscosity on peristaltic pumping with Newtonian fluids. *Journal of Fluid Mechanics*, *174*, 495-519.

Brown, T. D., & Hung, T. K. (1977). Computational and experimental investigations of two-dimensional nonlinear peristaltic flows. *Journal of Fluid Mechanics*, *83*(2), 249-272.

Burns, J. C., & Parkes, T. (1967). Peristaltic motion. *Journal of Fluid Mechanics*, *29*(4), 731-743.

Chetti, B. (2011). Micropolar fluids effects on the dynamic characteristics of four-lobe journal bearing. *World Academy of Science, Engineering and Technology*, *5*(11), 2155-2159.

Das, B., & Batra, R. L. (1993). Secondary flow of a Casson fluid in a slightly curved tube. *International journal of non-linear mechanics*, *28*(5), 567-577.

Davidson, P. A. (2001). *An Introduction to Magnetohydrodynamics*. Cambridge university press.

Devi, R. G., & Devanathan, R. (1975, April). Peristaltic motion of a micropolar fluid. In *Proceedings of the Indian Academy of Sciences-Section A* (Vol. 81, No. 4, pp. 149-163). Springer India.

Ebaid, A. (2008). Effects of magnetic field and wall slip conditions on the peristaltic transport of a Newtonian fluid in an asymmetric channel. *Physics Letters A, 372*(24), 4493-4499.

El Naby, A. E. H. A., El Misery, A. E. M., & El Kareem, M. A. (2006). Effects of a magnetic field on trapping through peristaltic motion for generalized Newtonian fluid in channel. *Physica A: Statistical Mechanics and its Applications, 367*, 79-92.

Eldabe, N. T. M., El-Sayed, M. F., Ghaly, A. Y., & Sayed, H. M. (2007). Peristaltically induced transport of a MHD biviscosity fluid in a non-uniform tube. *Physica A: Statistical Mechanics and its Applications, 383*(2), 253-266.

Elmabound, Y.A. and Mekheimer, K.S. (2011). Non-linear peristaltic transport of a second-order fluid through a porous medium. *Applied Mathematical Modelling*, 35(6), 2695-2710.

El-Shehawey, E. F., & Husseny, S. Z. (2002). Peristaltic transport of a magneto-fluid with porous boundaries. *Applied Mathematics and Computation, 129*(2-3), 421-440.

Elshehawey, E. F., Eldabe, N. T., Elghazy, E. M., & Ebaid, A. (2006). Peristaltic transport in an asymmetric channel through a porous medium. *Applied Mathematics and computation, 182*(1), 140-150.

Eringen, A.C. (1966) Theory of micropolar fluid, *J Math Mech*, 16.

Ervin, V. J., Lee, H., & Salgado, A. J. (2016). Generalized Newtonian fluid flow through a porous medium. *Journal of Mathematical Analysis and Applications, 433*(1), 603-621.

Fauci, L. J. (1992). Peristaltic pumping of solid particles. *Computers & fluids, 21*(4), 583-598.

Ferreira, A. J. (2008). *MATLAB codes for finite element analysis: solids and structures* (Vol. 157). Springer Science & Business Media.

Fox, R. W., McDonald, A. T., & Pritchard, P. J. (2003). Introduction to Fluid Mechanics 6th edition, *John Wiley & Sons. Inc. Hoboken, NJ.*

Fung, Y. C., & Yih, C. S. (1968). Peristaltic transport. *Journal of Applied Mechanics*, *35*(4), 669-675.

Fusi, L., & Farina, A. (2018). Peristaltic axisymmetric flow of a Bingham fluid. *Applied Mathematics and Computation*, *320*, 1-15.

Gad, N. S. (2014). Effects of hall currents on peristaltic transport with compliant walls. *Applied Mathematics and Computation*, *235*, 546-554.

Hameed, M., Khan, A. A., Ellahi, R., & Raza, M. (2015). Study of magnetic and heat transfer on the peristaltic transport of a fractional second grade fluid in a vertical tube. *Engineering Science and Technology, an International Journal*, *18*(3), 496-502.

Hamid, A. H., Javed, T., Ahmed, B., & Ali, N. (2017). Numerical study of two-dimensional non-Newtonian peristaltic flow for long wavelength and moderate Reynolds number. *Journal of the Brazilian Society of Mechanical Sciences and Engineering*, *39*(11), 4421-4430.

Hariharan, P., Seshadri, V., & Banerjee, R. K. (2008). Peristaltic transport of non-Newtonian fluid in a diverging tube with different wave forms. *Mathematical and Computer Modelling*, *48*(7-8), 998-1017.

Hayat, T., & Ali, N. (2008). Effects of an endoscope on peristaltic flow of a micropolar fluid. *Mathematical and Computer Modelling*, *48*(5-6), 721-733.

Hayat, T., & Hina, S. (2010). The influence of wall properties on the MHD peristaltic flow of a Maxwell fluid with heat and mass transfer. *Nonlinear analysis: Real world applications*, *11*(4), 3155-3169.

Hayat, T., & Noreen, S. (2010). Peristaltic transport of fourth grade fluid with heat transfer and induced magnetic field. *Comptes Rendus Mécanique*, *338*(9), 518-528.

Hayat, T., Ahmed, N., Sajid, M., & Asghar, S. (2007). On the MHD flow of a second grade fluid in a porous channel. *Computers & Mathematics with Applications*, *54*(3), 407-414.

Hayat, T., Ali, N., & Abbas, Z. (2007). Peristaltic flow of a micropolar fluid in a channel with different wave forms. *Physics letters A*, *370*(3-4), 331-344.

Hayat, T., Ali, N., & Asghar, S. (2007). Hall effects on peristaltic flow of a Maxwell fluid in a porous medium. *Physics Letters A*, *363*(5-6), 397-403.

Hayat, T., Ali, N., Asghar, S., & Siddiqui, A. M. (2006). Exact peristaltic flow in tubes with an endoscope. *Applied Mathematics and Computation*, *182*(1), 359-368.

Hayat, T., Asghar, Z., Asghar, S., & Mesloub, S. (2010). Influence of inclined magnetic field on peristaltic transport of fourth grade fluid in an inclined asymmetric channel. *Journal of the Taiwan Institute of Chemical Engineers*, *41*(5), 553-563.

Hayat, T., Farooq, S., Ahmad, B., & Alsaedi, A. (2016). Homogeneous-heterogeneous reactions and heat source/sink effects in MHD peristaltic flow of micropolar fluid with Newtonian heating in a curved channel. *Journal of Molecular Liquids*, *223*, 469-488.

Hayat, T., Farooq, S., Ahmad, B., & Alsaedi, A. (2017). Effectiveness of entropy generation and energy transfer on peristaltic flow of Jeffrey material with Darcy resistance. *International Journal of Heat and Mass Transfer*, *106*, 244-252.

Hayat, T., Farooq, S., Alsaedi, A., & Ahmad, B. (2017). Numerical study for Soret and Dufour effects on mixed convective peristalsis of Oldroyd 8-constants fluid. *International Journal of Thermal Sciences*, *112*, 68-81.

Hayat, T., Hina, S., & Ali, N. (2010). Simultaneous effects of slip and heat transfer on the peristaltic flow. *Communications in Nonlinear Science and Numerical Simulation*, *15*(6), 1526-1537.

Hayat, T., Hina, S., Hendi, A. A., & Asghar, S. (2011). Effect of wall properties on the peristaltic flow of a third grade fluid in a curved channel with heat and mass transfer. *International Journal of Heat and mass transfer*, *54*(23-24), 5126-5136.

Hayat, T., Hussain, Q., & Ali, N. (2008). Influence of partial slip on the peristaltic flow in a porous medium. *Physica A: Statistical Mechanics and its Applications*, *387*(14), 3399-3409.

Hayat, T., Javed, M., & Hendi, A. A. (2011). Peristaltic transport of viscous fluid in a curved channel with compliant walls. *International Journal of Heat and Mass Transfer*, *54*(7-8), 1615-1621.

Hayat, T., Qureshi, M. U., & Hussain, Q. (2009). Effect of heat transfer on the peristaltic flow of an electrically conducting fluid in a porous space. *Applied Mathematical Modelling*, *33*(4), 1862-1873.

Hayat, T., Qureshi, M. U., & Hussain, Q. (2009). Effect of heat transfer on the peristaltic flow of an electrically conducting fluid in a porous space. *Applied Mathematical Modelling*, *33*(4), 1862-1873.

Hayat, T., Saleem, N., Asghar, S., Alhothuali, M. S., & Alhomaidan, A. (2011). Influence of induced magnetic field and heat transfer on peristaltic transport of a Carreau fluid. *Communications in Nonlinear Science and Numerical Simulation*, *16*(9), 3559-3577.

Hayat, T., Tanveer, A., & Alsaedi, A. (2016). Mixed convective peristaltic flow of Carreau–Yasuda fluid with thermal deposition and chemical reaction. *International Journal of Heat and Mass Transfer*, *96*, 474-481.

Hayat, T., Zahir, H., Alsaedi, A., & Ahmad, B. (2017). Heat transfer analysis on peristaltic transport of Ree-Eyring fluid in rotating frame. *Chinese Journal of Physics*, *55*(5), 1894-1907.

Hayat, T., Zahir, H., Alsaedi, A., & Ahmad, B. (2017). Peristaltic flow of rotating couple stress fluid in a non-uniform channel. *Results in physics*, *7*, 2865-2873.

Hayat, T., Zahir, H., Tanveerand, A. and Alsaedi, A. (2018). Soret and Dufour effects on MHD peristaltic flow of Prandtl fluid in a rotating channel. *Results in Physics*, 8, 1291-1300.

Hill, A. A., & Straughan, B. (2009). Poiseuille flow in a fluid overlying a highly porous material. *Advances in water resources*, *32*(11), 1609-1614.

Hung, T. K., & Brown, T. D. (1976). Solid-particle motion in two-dimensional peristaltic flows. *Journal of Fluid Mechanics*, *73*(1), 77-96.

Hussain, Q., Latif, T., Alvi, N., & Asghar, S. (2018). Nonlinear radiative peristaltic flow of hydromagnetic fluid through porous medium. *Results in Physics*, *9*, 121-134.

Ikbal, M. A., Chakravarty, S., & Mandal, P. K. (2008). An unsteady peristaltic transport phenomenon of non-Newtonian fluid–A generalised approach. *Applied Mathematics and Computation, 201*(1-2), 16-34.

Jaffrin, M. Y. (1973). Inertia and streamline curvature effects on peristaltic pumping. *International Journal of Engineering Science, 11*(6), 681-699.

Javed, M., Hayat, T., & Alsaedi, A. (2014). Peristaltic flow of Burgers' fluid with compliant walls and heat transfer. *Applied Mathematics and Computation, 244*, 654-671.

Javed, T., Hamid, A. H., Ahmed, B., & Ali, N. (2017). Effect of high Reynolds number on hydromagnetic peristaltic flow in an inclined channel using finite element method. *Journal of the Korean Physical Society, 71*(12), 950-962.

Jiajan W. (2010). *Solution to incompressible Navier Stokes Equations by using finite element method.* MS Dissertation University of Texas at Arlington. USA.

Johnston, B. M., Johnston, P. R., Corney, S., & Kilpatrick, D. (2004). Non-Newtonian blood flow in human right coronary arteries: steady state simulations. *Journal of biomechanics, 37*(5), 709-720.

Khan, A. A., Farooq, A., & Vafai, K. (2018). Impact of induced magnetic field on synovial fluid with peristaltic flow in an asymmetric channel. *Journal of Magnetism and Magnetic Materials, 446*, 54-67.

Kothandapani, M., & Srinivas, S. (2008). Non-linear peristaltic transport of a Newtonian fluid in an inclined asymmetric channel through a porous medium. *Physics Letters A, 372*(8), 1265-1276.

Kothandapani, M., & Srinivas, S. (2008). On the influence of wall properties in the MHD peristaltic transport with heat transfer and porous medium. *Physics Letters A, 372*(25), 4586-4591.

Kothandapani, M., & Srinivas, S. (2008). Peristaltic transport of a Jeffrey fluid under the effect of magnetic field in an asymmetric channel. *International Journal of Non-Linear Mechanics, 43*(9), 915-924.

Kothandapani, M., Pushparaj, V., & Prakash, J. (2016). Effect of magnetic field on peristaltic flow of a fourth grade fluid in a tapered asymmetric channel. *Journal of King Saud University-Engineering Sciences.*

Kumar, B. R., & Naidu, K. B. (1995). A numerical study of peristaltic flows. *Computers & fluids, 24*(2), 161-176.

Kumari, S. V. H. N. K., Murthy, M. V., Reddy, M. C. K., & Kumar, Y. V. K. R. (2011). Peristaltic pumping of a magnetohydrodynamic Casson fluid in an inclined channel. *Adv. Appl. Sci. Res, 2*(2), 428-436.

Latham, T. W. (1966). *Fluid motions in a peristaltic pump* (Doctoral dissertation, Massachusetts Institute of Technology).

Lew, H. S., Fung, Y. C., & Lowenstein, C. B. (1971). Peristaltic carrying and mixing of chyme in the small intestine (an analysis of a mathematical model of peristalsis of the small intestine). *Journal of Biomechanics, 4*(4), 297-315.

Logan, D. (2002). *First course in finite element analysis*. Brooks/Cole.

Longo, G. A., Mancin, S., Righetti, G., & Zilio, C. (2017). Flow dynamic and energetic assessment of a commercial micro-pump for a portable/wearable artificial kidney: Peristaltic vs. diaphragm pumps. *Thermal Science and Engineering Progress, 3*, 31-36.

Longuet-Higgins, M. S. (1983). Peristaltic pumping in water waves. *Journal of Fluid Mechanics, 137*, 393-407.

Manton, M. J. (1975). Long-wavelength peristaltic pumping at low Reynolds number. *Journal of Fluid Mechanics, 68*(3), 467-476.

Mekheimer, K. S. (2003). Non-linear peristaltic transport of magnetohydrodynamic flow in an inclined planar channel. *Arabian Journal for Science and Engineering, 28*(2), 183-202.

Mekheimer, K. S. and Abd elmaboud, Y. (2008). The influence of heat transfer and magnetic field on peristaltic transport of a Newtonian fluid in a vertical annulus: application of an endoscope. *Physics Letters A, 372*(10), 1657-1665.

Mernone, A. V., Mazumdar, J. N., & Lucas, S. K. (2002). A mathematical study of peristaltic transport of a Casson fluid. *Mathematical and Computer Modelling, 35*(7-8), 895-912.

Merrill, E. W., Benis, A. M., Gilliland, E. R., Sherwood, T. K., & Salzman, E. W. (1965). Pressure-flow relations of human blood in hollow fibers at low flow rates. *Journal of Applied Physiology*, *20*(5), 954-967.

Mishra, M., and Rao, A.R. (2005). Peristaltic transport in a channel with a porous peripheral layer: model of a flow in gastrointestinal tract. *Journal of Biomechanics*, 38(4), 779-789.

Misra, J. C., & Pandey, S. K. (1995). Peristaltic transport in a tapered tube. *Mathematical and Computer Modelling*, *22*(8), 137-151.

Misra, J.C., Mallick, B., and Sinha, A. (2016). Heat and mass transfer in asymmetric channels during peristaltic transport of an MHD fluid having temperature-dependent properties. *Alexandria Engineering Journal*, 57, 391-406.

Moradi, H.V., Zandi, S., and Floryan, J.M. (2017). Algorithm for analysis of peristaltic annular flows. *Computers & Fluids*, 147, 72-89.

Mustafa, M., Abbasbandy, S., Hina, S., and Hayat, T. (2014). Numerical investigation on mixed convective peristaltic flow of fourth grade fluid with Dufour and Soret effects. *Journal of the Taiwan Institute of Chemical Engineers*, 45(2), 308-316.

Muthu, P., Kumar, B.R., and Chandra, P. (2008). Peristaltic motion of micropolar fluid in circular cylindrical tubes: Effect of wall properties. *Applied Mathematical Modelling*, 32(10), 2019-2033.

Muthuraj, R., and Srinivas, S. (2010). Mixed convective heat and mass transfer in a vertical wavy channel with traveling thermal waves and porous medium. *Computers & Mathematics with Applications*, 59(11), 3516-3528.

Muthuraj, R., Nirmala, K., and Srinivas, S. (2016). Influences of chemical reaction and wall properties on MHD peristaltic transport of a dusty fluid with heat and mass transfer. *Alexandria Engineering Journal*, 55(1), 597-611.

Myron, B., Behie, G. A., & Trangenstein, J. A. (2013). *Multiphase flow in porous media: mechanics, mathematics, and numerics* (Vol. 34). Springer Science & Business Media.

Nadeem, S., and Akram, S. (2010). Peristaltic flow of a Williamson fluid in an asymmetric channel. *Communications in Nonlinear Science and Numerical Simulation*, 15(7), 1705-1716.

Nagarani, P. (2010) "Peristaltic transport of a Casson fluid in an inclined channel", *Korea-Australia Rheology Journal*, 22(2), 105-111.

Nagarani, P., Sarojamma, G., and Jayaraman, G. (2006). Exact analysis of unsteady convective diffusion in Casson fluid flow in an annulus – application to the catheterized artery. *Acta Mechanica*, 187, 189–202.

Nield, D. A., Bejan, A., & Nield-Bejan. (2006). *Convection in porous media* (Vol. 3). New York: springer

Pandey, S.K., and Chaube, M.K. (2010). Peristaltic transport of a visco-elastic fluid in a tube of non-uniform cross section. *Mathematical and Computer Modelling*, 52(3-4), 501-514.

Pandey, S.K., and Chaube, M.K. (2011). Peristaltic flow of a micropolar fluid through a porous medium in the presence of an external magnetic field. *Communications in Nonlinear Science and Numerical Simulation*, 16(9), 3591-3601.

Poursharifi, Z., and Sadeghy, K. (2017). On the use of Lattice–Boltzmann method for simulating peristaltic flow of viscoplastic fluids in a closed cavity. *Journal of Non-Newtonian Fluid Mechanics*, 243, 1-15.

Pozrikidis, C. (1987). A study of peristaltic flow. *Journal of Fluid Mechanics* 180, 515-527.

Radhakrishnamacharya, G., and Srinivasulu, C. (2007). Influence of wall properties on peristaltic transport with heat transfer. *Comptes Rendus Mecanique*, 335(7), 369-373.

Raju, K.K., and Devanathan, R. (1972). Peristaltic motion of a non-Newtonian fluid. *Rheologica Acta*, 170-179.

Ramesh, K. (2016). Effects of slip and convective conditions on the peristaltic flow of couple stress fluid in an asymmetric channel through porous medium. *Computer methods and programs in biomedicine*, 135, 1-14.

Ramesh, K., and Devakar, M. (2015). Magnetohydrodynamic peristaltic transport of couple stress fluid through porous medium in an inclined asymmetric channel with heat transfer. *Journal of Magnetism and Magnetic Materials*, 394, 335-348.

Ramesh, K., and Devakar, M. (2017). Effect of heat transfer on the peristaltic transport of a MHD second grade fluid through a porous medium in an inclined asymmetric channel. *Chinese Journal of physics*, 55(3), 825-844.

Sankar, D. (2009). Two-fluid flow of blood through asymmetric and axisymmetric stenosed narrow arteries. *International Journal of Nonlinear Science and Numerical Simulation,* 10(11-12), 1425-1442.

Shapiro, A.H., Jaffrin, M.Y., and Weinberg, S.L. (1969). Peristaltic Pumping with Long wavelength at Low Reynolds Numbers. *Journal of Fluid Mechanics*, 37, 799-825.

Shit, G.C., and Roy, M. (2014). Hydromagnetic effect on inclined peristaltic flow of a couple stress fluid. *Alexandria Engineering Journal*, 53(4), 949-958.

Shit, G.C., Ranjit, N.K., and Sinha, A. (2016). Electro-magnetohydrodynamic flow of biofluid induced by peristaltic wave: a non-newtonian model. *Journal of Bionic Engineering*, 13(3), 436-448.

Shukla, J.B., and Gupta, S.P. (1982). Peristaltic transport of a power-law fluid with variable consistency. *Journal of Biomechanical Engineering,* 104(3), 182-186.

Shukla, J.B., Parihar, R.S., Rao, B.R.P., and Gupta, S.P. (1980). Effects of peripheral-layer viscosity on peristaltic transport of a bio-fluid. *Journal of Fluid Mechanics*, 97(2), 225-237.

Siddiqui, A.M., and Schwarz, W.H. (1994). Peristaltic flow of a second-order fluid in tubes. *Journal of non-Newtonian fluid mechanics*, 53, 257-284.

Srinivas, A.N.S., Reddy, R.H., Srinivas, S., and Sreenadh, S. (2014). Peristaltic transport of a casson fluid in a channel with permeable walls. *International Journal of Pure and Applied Mathematics*, 90(1), 11-24.

Srinivas, S., and Gayathri, R. (2009). Peristaltic transport of a Newtonian fluid in a vertical asymmetric channel with heat transfer and porous medium. *Applied Mathematics and Computation*, 215(1), 185-196.

Srinivas, S., and Kothandapani, M. (2008). Peristaltic transport in an asymmetric channel with heat transfer—a note. *International Communications in Heat and Mass Transfer*, 35(4), 514-522.

Srinivas, S., and Kothandapani, M. (2009). The influence of heat and mass transfer on MHD peristaltic flow through a porous space with compliant walls. *Applied Mathematics and Computation*, 213(1), 197-208.

Srinivas, S., and Muthuraj, R. (2011). Effects of chemical reaction and space porosity on MHD mixed convective flow in a vertical asymmetric channel with peristalsis. *Mathematical and Computer Modelling*, 54(5-6), 1213-1227.

Srinivas, S., Gayathri, R., and Kothandapani, M. (2009). The influence of slip conditions, wall properties and heat transfer on MHD peristaltic transport. *Computer Physics Communications*, 180(11), 2115-2122.

Srinivas, S., Gayathri, R., and Kothandapani, M. (2011). Mixed convective heat and mass transfer in an asymmetric channel with peristalsis. *Communications in Nonlinear Science and Numerical Simulation*, 16(4), 1845-1862.

Srinivasacharya, D., Mishra, M., and Rao, A.R. (2003). Peristaltic pumping of a micropolar fluid in a tube. *Acta Mechanica*, 161(3-4), 165-178.

Srivastava, L.M, and Srivastava, V.P. (1984). Peristaltic transport of blood: casson model–II", *J. Bio mech.* 17, 821–829.

Srivastava, L.M. and Srivastava, V.P. (1982). Peristaltic transport of a two-layered model of physiological fluid. *Journal of biomechanics,* 15(4), 257-265.

Srivsstava, L.M. (1987). Peristaltic transport of a Casson fluid. *Nig. J. Sci. Res.* 1, 71-82.

Takabatake, S., and Ayukawa, K. (1982). Numerical Study of Two-Dimensional Peristaltic Flows. *Journal of Fluid Mechanics*, 122, 439-465.

Takabatake, S., Ayukawa, K., and Mori, A. (1988). Peristaltic Pumping in Circular Tubes: A Numerical Study of Fluid Transport and Its Efficiency", *Journal of Fluid Mechanics,* 193, 267-283.

Takabatake, S., Ayukawa, K., and Sawa, M. (1990). Finite element Analysis of Two-dimensional Peristaltic flow (2nd Report, Pressure-Flow characteristics). *Japan Society of Mechanical Engineering*, 56, 3633-3637.

Tanveer, A., Hayat, T., Alsaedi, A., and Ahmad, B. (2017). Mixed convective peristaltic flow of Sisko fluid in curved channel with homogeneous-heterogeneous reaction effects. *Journal of Molecular Liquids*, 233, 131-138.

Tripathi D., and Bég, O.A. (2014). Peristaltic propulsion of generalized Burgers' fluids through a non-uniform porous medium: A study of chyme dynamics through the diseased intestine. *Mathematical biosciences*, 248, 67-77.

Tripathi, D. (2011). Peristaltic transport of fractional Maxwell fluids in uniform tubes: Applications in endoscopy. *Computers & Mathematics with Applications*, 62(3), 1116-1126.

Tripathi, D. (2013). Study of transient peristaltic heat flow through a finite porous channel. *Mathematical and Computer Modelling*, 57(5-6), 1270-1283.

Tripathi, D., Bég, O.A., Gupta, P.K., Radhakrishnamacharya, G. and Mazumdar, J. (2015). DTM simulation of peristaltic viscoelastic biofluid flow in asymmetric porous media: a digestive transport model. *Journal of Bionic Engineering*, 12(4), 643-655.

Tripathi, D., Borode, A., Jhorar, R., Bég, O.A., and Tiwari, A.K. (2017). Computer modelling of electro-osmotically augmented three-layered microvascular peristaltic blood flow *Microvascular research*, 114, 65-83.

Usha, S., & Rao, A.R. (1995). Peristaltic transport of a biofluid in a pipe of elliptic cross section. *Journal of biomechanics*, 28(1), 45-52.

Vafai, K., and Thiyagaraja, R. (1987). Analysis of flow and heat transfer at the interface region of a porous medium. *International Journal of Heat Mass Transfer*, 30, 1391-1405.

Vajravelu, K., Radhakrishnamacharya, G., and Radhakrishnamurty, V. (2007). Peristaltic flow and heat transfer in a vertical porous annulus, with long wave approximation. *International Journal of Non-Linear Mechanics*, 42(5), 754-759.

Vajravelu, K., Sreenadh, S., and Lakshminarayana, P. (2011). The influence of heat transfer on peristaltic transport of a Jeffrey fluid in a vertical porous stratum. *Communications in Nonlinear Science and Numerical Simulation*, 16(8), 3107-3125.

Vajravelu, K., Sreenadh, S., and Saravana, R. (2013). Combined influence of velocity slip, temperature and concentration jump conditions on MHD peristaltic transport of a Carreau fluid in a non-uniform channel. *Applied Mathematics and Computation*, 225, 656-676.

Vajravelu, K., Sreenadh, S., Rajanikanth, K. and Lee, C. (2012). Peristaltic transport of a Williamson fluid in asymmetric channels with permeable walls. *Nonlinear Analysis: Real World Applications*, 13(6), 2804-2822.

Venkatesan, J., Sankar, D. S., Hemalatha, K., & Yatim, Y. (2013). Mathematical analysis of Casson fluid model for blood rheology in stenosed narrow arteries. *Journal of Applied Mathematics*.

Wang, Y., Ali, N., Hayat, T., & Oberlack, M. (2011). Peristaltic motion of a magnetohydrodynamic micropolar fluid in a tube. *Applied Mathematical Modelling*, 35(8), 3737-3750.

Whitaker, S. (1986). Flow in porous media I: A theoretical derivation of Darcy's law. *Transport Porous Media*, 1, 3-25.

White, F. M. (2003). *Fluid mechanics. 5th. Boston:* McGraw-Hill Book Company.

Wilson, D.E., & Panton, R.L. (1979). Peristaltic transport due to finite amplitude bending and contraction waves. *Journal of Fluid Mechanics*, 90(1), 145-159.

Yaqing, L., and Guo, B. (2017). Effects of second-order slip on the flow of a fractional Maxwell MHD fluid. *Journal of the Association of Arab Universities for Basic and Applied Sciences*, 24, 232-241.

Yıldırım, A., and Sezer, S.A. (2010). Effects of partial slip on the peristaltic flow of a MHD Newtonian fluid in an asymmetric channel. *Mathematical and Computer Modelling*, 52(3-4), 618-625.

Yin, F.C.P., and Fung, Y.C. (1971). Comparison of theory and experiment in peristaltic transport. *Journal of Fluid Mechanics* 47(1), 93-112.

Zahir, H., Hayat, T., Alsaedi, A., and Ahmad, B. (2017). Entropy generation impact on peristaltic motion in a rotating frame. *Results in physics*, 7, 3668-3677.

Zeeshan, A., Ijaz, N., and Majeed, A. (2018). Analysis of magnetohydrodynamics peristaltic transport of hydrogen bubble in water. *International Journal of Hydrogen Energy*, 43(2), 979-985.

Zien, T.F., and Ostrach, S. A. (1970). A Long wavelength Approximation to Peristaltic Motion. *Journal of Biomechanics* 3, 63-75.